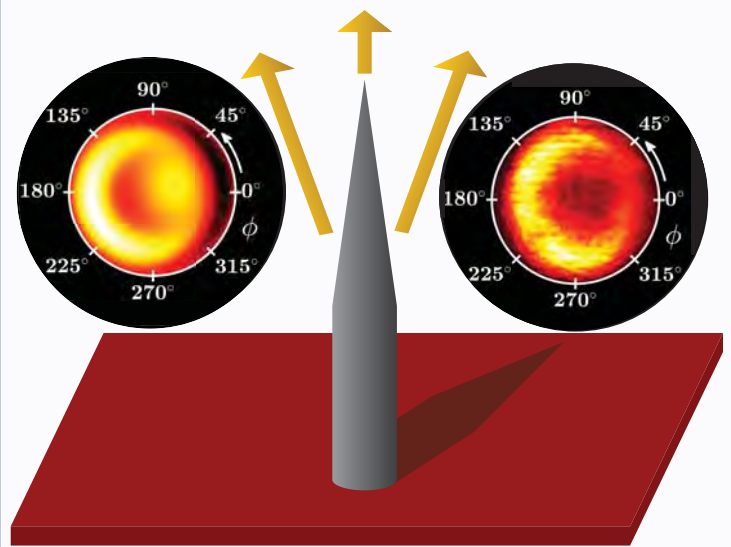


Engineering of nanophotonic structures for quantum information applications

PhD Thesis



Andreas Dyhl Østerkryger,
June 2018

Engineering of nanophotonic structures for quantum information applications

A dissertation submitted in partial fulfilment of the requirements for the degree of
philosophiae doctor

Andreas Dyhl Østerkryger
June 2018

DTU Fotonik
Department of Photonics Engineering
Technical University of Denmark

Project period:	March 2015 - June 2018
Supervisors:	Assoc. Prof. Niels Gregersen Prof. Jesper Mørk
Ph.D. defense date:	August 23, 2018
Ph.D. defense committee:	Assoc. Prof. Andrei Lavrinenko, Technical University of Denmark Post Doc Philip Trøst Kristensen, Humboldt-Universität zu Berlin Head of Research Group Sven Burger, Zuse Institute Berlin
External research stay:	February 2017 - May 2017 CEA Grenoble, France with Julien Claudon and Jean-Michel Gérard
Questions or comments:	adyhlosterkryger@gmail.com
Copyright:	©Andreas Dyhl Østerkryger, 2018

Abstract

Various nanophotonic structures are studied theoretically using the Fourier modal method (FMM), including ridge waveguides, 2D photonic crystals and nanowires.

A FMM with open boundary conditions in Cartesian coordinates is developed, implemented and tested. We find that an efficient sampling of the k -space leads to faster convergence as compared to the standard equidistant sampling.

Using a Fourier-based Bloch mode expansion technique, a photonic crystal waveguide side-coupled to a microcavity and embedded with a partially transmitting element (PTE) is investigated. We demonstrate how the symmetry of the Fano-shaped transmission spectrum is controlled by the PTE-cavity distance.

All-optical mapping of the position of single quantum dots embedded in tapered nanowires is demonstrated. We show that the far-field patterns of the quantum dots reveal their lateral position by comparison with simulations. We estimate the positioning uncertainty to be on the order of 10-15 nm.

The optimal design for obtaining a high Purcell enhancement and source efficiency of a truncated nanowire placed on a gold-silica mirror is determined using a single-mode model and a model including all optical modes. In the design process, we identify a breakdown of the single-mode model in computing both the Purcell enhancement and the source efficiency. We provide simple physical explanations of this breakdown, by analysing the influence of radiation and evanescent modes.

Finally, a quantum dot placed in a Fabry-Perot cavity realised by embedding two mirrors in a high- β waveguide is considered. We develop a quantum mechanical model, which correctly accounts for both the cavity and the waveguide effects. Our model reveals a new design strategy for solid state single-photon sources, where a quantum dot embedded in a long Fabry-Perot cavity in high- β waveguides are shown to emit photons with simultaneous high indistinguishability and efficiency.

Resumé

Diverse nanofotoniske strukturer bliver undersøgt teoretisk ved brug af Fourier modal metoden (FMM), herunder kantede bølgeledere, 2D fotoniske krystaller og cylindriske nanotråde.

En FMM med åbne grænsebetingelser i kartesiske koordinater udvikles, implementeres og testes. Vi konkluderer, at en effektiv udvælgelse af k -rummet fører til hurtigere konvergens sammenlignet med en standard ækvidistant diskretisering.

Ved brug af en formalisme baseret på en ekspansion på Bloch-modes, undersøges en fotonisk krystal bølgeleder sidekoblet til en mikrokavitet og indlejret med et delvist transmitterende element (PTE). Vi demonstrerer, hvordan symmetrien af det Fano-formede transmissionspektrum kontrolleres af afstanden mellem PTE og kavitet.

En udelukkende optisk bestemmelse af individuelle kvantepunkters position, som er indlejret i en tilspidset nanotråd, demonstreres. Vi viser, hvordan fjernfeltsmønstret af kvantepunkterne afslører deres laterale position ved sammenligning med simuleringer. Vi estimerer usikkerheden på positionsbestemmelsen til at være i omegnen af 10-15 nm.

Det optimale design for at opnå en høj Purcell forstærkning og kildeeffektivitet af en trunkeret nanotråd placeret på et guld-silica spejl bestemmes ved brug af en enkelt-mode model og en model inkluderende alle optiske modes. I designprocessen identificerede vi et sammenbrud af enkelt-mode modellen ved udregningen af både Purcell forstærkningen og kildeeffektiviteten. Vi giver simple fysiske forklaringer af dette sammenbrud ved at analysere indflydelsen af ikke-guede og uddøende optiske modes.

Til sidst undersøger vi en struktur, hvor et kvantepunkt er placeret i en høj- β bølgeleder med spejle indlejret på hver side, som udgør en Fabry-Perot kavitet. Vi udvikler en kvantemekanisk model, som på rette vis tager højde for både kavitets- og bølgeledereffekterne. Brugen af vores model fører til en ny designstrategi for faststof-enkeltfotonkilder, hvor vi viser, at et kvantepunkt placeret i en lang Fabry-Perot kavitet i høj- β bølgeledere udsender fotoner med simultant høj uskelnelighed og effektivitet.

Preface

The research presented in the present thesis has mainly been carried out at DTU Fotonik in the Quantum and Laser Photonics group¹ headed by Professor Jesper Mørk under the supervision of Associate Professor Niels Gregersen in the period from March 2015 to June 2018. The thesis is part of Niels Gregersen's LOQIT project (www.loqit.fotonik.dtu.dk) funded by a Sapere Aude grant awarded by the Danish Research Council for Technology and Production. From February 2017 to May 2017 I had an external research stay at CEA Grenoble in the "Nanophysique et Semiconducteurs"-group under supervision of Researcher Julien Claudon. The purpose of the stay was to support their experimental activities on semiconductor quantum dots embedded in nanowires with my simulations and the outcome is presented in Chapters 5 and 6.

The project has partly been affiliated with the NANophotonics for TERAbit Communications (NATEC) Centre of Excellence headed by Professor Jesper Mørk, where especially the research on Fano resonances in photonic crystal cavity-waveguide structures presented in Chapter 4 ties closely to the NATEC activities. The thesis covers both fundamental method development for simulating open nanophotonic systems as well as more device specific calculations. The experimental results presented in Chapter 5 have been carried out at CEA Grenoble by Ph.D.-student Romain Fons under supervision of Julien Claudon. I was thrilled to see the good agreement between simulations and experiments, and I am very grateful for the hard work by Romain on the experimental setup.

The work in the present thesis would not have been possible without the support by a number of people. First and foremost, I am grateful for the guidance and input by my supervisors, which kept pushing the research in an interesting direction. I thank Niels for always having time to discuss the details of my research, and for introducing me to many of his collaborators and involving me in their joint activities. It has been very inspiring to work with you. I thank Jesper for being a great group leader, whose insight in all activities in our group ranging from classical signal processing to open quantum systems theory truly amazes me.

¹Formerly known as the Theory & Signal Processing group. Our group name was changed in September 2017.

I thank all the group members of the Quantum and Laser Photonics group for making a great research environment, where there is plenty of room for non-scientific discussions during a normal working day. I always look forward to our daily 14.45 coffee break - especially the cookies. A special thank goes to Teppo for guidance on the details of the open-geometry Fourier modal method and for always being very positive and open for a discussion. I would also like to thank Jakob, who woke my interest in nanophotonics engineering through a 3-week project during the first year of my master studies.

Special thanks goes to both the players from our Friday morning football matches and all the runners participating in our (not so regular) DHL training sessions. It has been a pleasure to slow down our physical degradation with all of you.

I would like to thank my family and friends for supporting me through all three years and for trying to look interested, whenever I explained my research. Last but not least I thank my fiancé Majse for being a great girlfriend and the best mother to our lovely daughter Annika. I always look forward to get home after a long day at the office, and spend the evening with you.

Finally, I wish to acknowledge Otto Mønstedts Fond, Augustinusfonden, Marie & M.B. Richters Fond, and IDAs og Berg-Nielsens Studie- og Støttefond for economical support for my external stay and towards conference attendances.

Andreas Dyhl Østerkryger,
DTU Fotonik, Department of Photonics Engineering,
Technical University of Denmark,
June 2018

List of publications

Below we list the publications resulting from the work in the present Ph.D. project.

Journal publications

- J1 Andreas Dyhl Osterkryger, Jakob Rosenkrantz de Lasson, Mikkel Heuck, Yi Yu, Jesper Mørk and Niels Gregersen, "Spectral symmetry of Fano resonances in a waveguide coupled to a microcavity", *Opt. Lett.* **41**, 2065-2068 (2016)
- J2 Andreas Dyhl Osterkryger and Niels Gregersen, "Efficient formalism for treating tapered structures using the Fourier modal method," *Proc. SPIE 9889, Optical Modelling and Design IV*, 988917 (2016)
- J3 Teppo Häyrynen, Andreas Dyhl Osterkryger, Jakob Rosenkrantz de Lasson and Niels Gregersen, "Modelling open nanophotonic systems using the Fourier modal method: generalization to 3D Cartesian coordinates", *J. Opt. Soc. Am. A* **34**, 1632-1641 (2017)

Submitted manuscripts

- J4 Emil Vosmar Denning, Jake Iles-Smith, Andreas Dyhl Osterkryger, Niels Gregersen and Jesper Mørk, "Fundamental cavity-waveguide interplay in cavity QED", (arXiv:1804.01364 [quant-ph]) in review at *Physical Review B (Rapid Communications)*.
- J5 Romain Fons, Andreas Dyhl Osterkryger, Petr Stepanov, Eric Gautier, Joël Bleuse, Jean-Michel Gérard, Niels Gregersen and Julien Claudon, "All-optical mapping of the position of single quantum dots embedded in a nanowire antenna", in review at *Nano Letters*.

Manuscripts in preparation

- J6 Andreas Dyhl Østerkryger, Julien Claudon and Niels Gregersen, "Breakdown of single-mode model for calculating the Purcell factor and far-field emission pattern of truncated nanowires"

Conference contributions

- C1 Andreas Dyhl Østerkryger, Jakob Rosenkrantz de Lasson, Yi Yu, Jesper Mørk and Niels Gregersen, "Investigations on the parity of Fano resonances in photonic crystals", Poster presentation at CLEO/Europe-EQEC (2015)
- C2 Andreas Dyhl Østerkryger and Niels Gregersen, "Efficient formalism for treating tapered structures using the Fourier modal method," Poster presentation at SPIE Photonics Europe (2016). Proceeding published in J2.
- C3 Andreas Dyhl Østerkryger, Teppo Häyrynen, Jakob Rosenkrantz de Lasson and Niels Gregersen, "Modelling open nanophotonic structures using the Fourier modal method in infinite domains", Oral presentation at OWTNM (2017)
- C4 Andreas Dyhl Østerkryger, Teppo Häyrynen, Jakob Rosenkrantz de Lasson and Niels Gregersen, "Modelling open nanophotonic structures using the Fourier modal method in infinite domains", Oral presentation at CLEO/Europe-EQEC (2017)
- C5 Andreas Dyhl Østerkryger, Niels Gregersen, Romain Fons, Petr Stepanov, Tomasz Jakubczyk, Jöel Bleuse, Jean-Michel Gérard and Julien Claudon, "Determination of radial quantum dot position in trumpet nanowires from far field measurements", Poster presentation at CLEO/Europe-EQEC (2017)
- C6 Andreas Dyhl Østerkryger, Niels Gregersen, Romain Fons, Petr Stepanov, Tomasz Jakubczyk, Jöel Bleuse, Jean-Michel Gérard and Julien Claudon, "Optical localization of quantum dots in tapered nanowires", Oral presentation at NUSOD (2017)

Contributions to journal publications by the author

All research in J1, J2 and J6 has been done by the author, including the development and implementation of the used numerical code. All three manuscripts were written by the author and discussed with the co-authors.

For J3 the theoretical formalism was developed in collaboration with the co-authors. The implementation of the numerical code has been carried out by the

author. All figures for the manuscript has been made by the author as well as parts of the text.

For J4 the optical Greens function was derived by the author. Other than that, the author took part in discussions on the manuscript, and revised the manuscript before submission.

For J5 the development and implementation of the used numerical code has been carried out by the author, as well as the comparison between the simulated and measured far-fields. For the manuscript the author has contributed with comments and feedback.

Contents

Abstract	i
Resumé	iii
Preface	v
Publications	vii
Contents	xi
Acronyms	xv
I Background, theoretical foundation and methodology	1
1 Introduction	3
2 Theory of nanophotonics engineering	9
2.1 Maxwell's equations	10
2.2 Modelling techniques	11
2.3 The modal method	13
2.4 Boundary conditions	15
2.5 Spontaneous emission rate and β -factor	17
2.6 Near-field to far-field transformation	18
3 Modelling open nanophotonic systems using the Fourier modal method: Generalization to 3D Cartesian coordinates	21
3.1 3D open-geometry Fourier modal method	23
3.2 Discretization scheme	28
3.3 3D oFMM simulations	31
3.4 Discussion	37
3.5 Conclusion	37
II Applied nanophotonics engineering	39
4 Spectral symmetry of Fano resonances in a waveguide coupled to a microcavity	41
4.1 Computational framework	44

4.2	Single- versus multi-mode model	46
4.3	Parity of Fano resonances	49
4.4	Conclusion	51
5	All-optical mapping of the position of single quantum dots embedded in a nanowire antenna	53
5.1	Nanowire physics	55
5.2	Near-field to far-field transformation	59
5.3	Experimental setup	62
5.4	Comparison between simulations and experiments	65
5.5	Conclusion	74
6	Breakdown of single-mode model for computing source efficiency and Purcell enhancement for nanopost structures	77
6.1	Single-mode and full model	79
6.2	Optimal geometry of nanopost	80
6.3	Single-mode versus full model	83
6.4	Conclusion	91
7	Cavity–waveguide interplay in lossy resonators and its role in optimal single photon sources	93
7.1	LDOS for Fabry-Perot cavity in waveguide	96
7.2	Green’s function	100
7.3	Optimal single-photon source	104
7.4	Conclusion	107
8	Conclusion and outlook	109
	Appendix A Near-field to far-field transformation	113
A.1	Derivation of Eqs. (2.24)	113
A.2	Derivation of Eqs. (5.4) and (5.5)	116
	Appendix B Modelling open nanophotonic systems using the Fourier modal method: Generalization to 3D Cartesian coordinates	125
B.1	Direct factorization rule	125
B.2	Inverse factorization rule	127
B.3	Relationship between open and periodic boundary conditions . . .	130
B.4	Field emitted by a point dipole	131
B.5	Waveguide on substrate	133
	Appendix C All-optical mapping of the position of single quantum dots embedded in a nanowire antenna	137
C.1	Photoluminescence spectrum	137
C.2	Polarization study	138
C.3	Lifetime measurement	138
C.4	The role of the emitter type for the far-field radiation pattern . . .	141

C.5 Simulated far-fields of the needle nanowire	150
Appendix D Breakdown of single-mode model for computing source efficiency and Purcell enhancement for nanopost structures	155
D.1 Convergence study of Purcell enhancement	155
D.2 Division of radiation modes into TE and TM polarization	157
Appendix E Far-field of tapered nanowires	161
Bibliography	165

Acronyms

1D	One-dimensional.
2D	Two-dimensional.
3D	Three-dimensional.
AR	Anti-reflective.
BC	Boundary condition.
DoP	Degree of parity.
EM	Electromagnetic.
FDTD	Finite-difference time-domain.
FEM	Finite element method.
FMM	Fourier modal method.
FSR	Free spectral range.
fs	Fine structure splitting.
FWHM	Full-width at half-maximum.
GFIEM	Green's function integral equation method.
HPC	High-performance computer.
KLM	Knill, Laflamme and Millburn.
MM	Modal method.
NA	Numerical aperture.
NV	Nitrogen vacancy.
oFMM	Open-geometry Fourier modal method.
PhC	Photonic crystal.
PL	Photoluminescence.
PML	Perfectly matched layer.
PTE	Partially transmitting element.
QD	Quantum dot.
PSB	Phonon side band.
SE	Spontaneous emission.
SPDC	Spontaneous parametric down-conversion.
SPS	Single-photon source.
TE	Transverse electric.
TM	Transverse magnetic.
ZPL	Zero-phonon line.

Part I

Background, theoretical foundation and methodology

Introduction

In 1865 James Clerk Maxwell published his famous Maxwell's equations in the article entitled 'A Dynamical Theory of the Electromagnetic Field' [1], and in 1884-1885 these equations were reformulated to the differential form we know today by Oliver Heaviside [2]. Maxwell's equations implies that light propagates as electromagnetic waves, and in 1905 Albert Einstein added that a beam of light actually consists of a stream of individual wave packets [3] (these were later named *photons*), which lead to the wave-particle duality that initiated the development of quantum mechanics. Today a whole range of technologies exists, which are build on the physical laws formulated by Maxwell and Einstein from over a century ago. In the pursuit of making these technologies more efficient and compact, the devices are structured on a decreasingly smaller scale.

Nanophotonic devices

Nanophotonic devices are a broad term covering numerous technologies, where the structuring of the materials on the nanometer scale is important for the performance of the device. Within classical applications these includes vertical-cavity surface-emitting lasers (VCSEL) [4–6], photonic crystal (PhC) lasers [7–9], signal-processing such as switching [10] and pulse carving [11], and the whole field of integrated photonics.

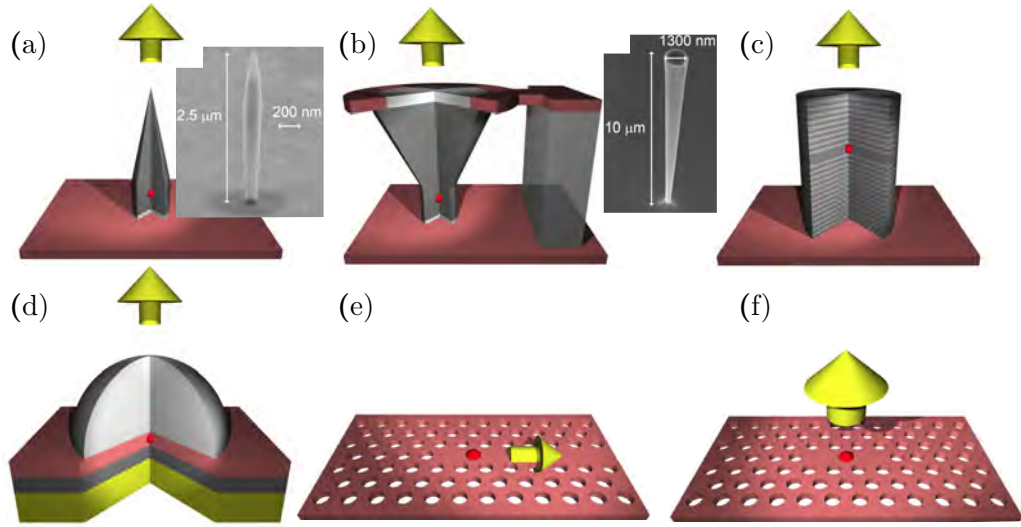


Figure 1.1: Illustration of different designs of single photon sources (SPS). Nanowire with (a) a needle out-coupling taper and (b) a trumpet out-coupling taper, (c) micropillar, (d) planar dielectric antenna, (e) terminated PhC W1 waveguide and (f) PhC L3 cavity. The illustrations are from Ref. [22] and the SEM images in (a-b) are from Ref. [23]

Due to the continuous improvement of the fabrication techniques, nanophotonic devices are believed to be a key technology in the development of the optical quantum computer [12–15], proposed by Knill, Laflamme and Millburn (KLM) in 2001 [16]. Here they showed that quantum computing is possible using only linear optical elements, such as beam splitters, phase shifters and mirrors, together with single-photon sources (SPSs) and photo-detectors. However, the KLM scheme suffers from being probabilistic and several ways to improve the scheme has been suggested, which are discussed in the review article Ref. [13]. The optical quantum computer is a technology for the future, however, quantum cryptography is already on the market. One way to realize quantum cryptography is to use quantum key distribution as suggested by Bennett and Brassard in 1984 with their BB84 protocol [17]. Entangled photon pairs are central to their scheme, and thus an efficient source producing these are needed [18–20]. Thus both the optical quantum computer and quantum cryptography relies on efficient sources of quantum light, for which the performance is characterised by the indistinguishability, purity and efficiency. Thus the development of efficient quantum light sources are key for both the optical quantum computer, quantum cryptography and for the quantum internet [21].

The indistinguishability of photons is a quantum mechanical property describing how well the wave-packets overlap in energy, space, time and polarization [24]. The efficiency of quantum light sources is a measure of how many of the

emitted photons are collected by a lens or a waveguide, whereas the brightness is defined as the number of photons collected per excitation pulse into the first lens [25]. Single-photons are emitted by atoms and atomic like structures such as molecules [26], semiconductor quantum dots (QDs) [25, 27–29] and NV-centres [30], or are generated by non-linear processes such as spontaneous parametric down-conversion (SPDC) [31]. Only the semiconductor QD micropillar structures have demonstrated simultaneous high indistinguishability, efficiency and brightness [25, 29]. In order to enhance both the efficiency and indistinguishability of QD semiconductor structures, several design strategies have been investigated and some of these are illustrated in Fig. 1.1, where a quantum emitter is embedded in different photonic structures such as nanowires in (a-b) [27, 32], (c) micropillar cavities [25, 29], (d) planar dielectric antennas [26, 33], (e) PhC waveguides [28] and (f) PhC L3 cavities [34]. Generally the best approach is not known, and for both the classical and quantum nanophotonic devices, optimal designs are not identified in the laboratory, since this would be both very inefficient and expensive. Instead numerical simulations and modelling of the devices are necessary, and for that a range of different techniques exist.

Topics of thesis

In the Quantum and Laser Photonics group at DTU Fotonik ¹, we have a close collaboration between our theoretical and experimental activities, where the theorists in general design and model nanophotonic devices. In my master and the beginning of my Ph.D.-project, I investigated a photonic crystal Fano structure (to be presented in Chapter 4), which for now has primarily classical applications within e.g. signal processing [11] and self-pulsing nanolasers [9, 35]. My Ph.D. is part of the LOQIT-project², where our aim is to develop high efficiency single-photon and entangled photon pair sources for quantum cryptography and quantum information processing. Specifically, we want to establish the physical understanding needed for engineering sources with simultaneous high indistinguishability and near-unity efficiency. Thus I have moved from classical applications towards quantum applications during my studies, however without changing the methodology, which remains classical. Initially, my primary task was to develop on the Fourier model method, both in terms of the computational efficiency, boundary conditions and expanding the range of structures it can handle. However, during my Ph.D., we got a lot of requests for calculations from experimental groups outside DTU on specific nanophotonic devices with applications within quantum information technology. This shifted our focus from method development to more device specific calculations, since we find the interplay between experiments and simulations/theory both very interesting and important. Thus

¹Formerly, known as the Theory & Signal-Processing group. Our group is part of the Nanophotonics section, which consists of four research groups.

²Linear optics for quantum information technology. Website: loqit.fotonik.dtu.dk

we only develop on the existing simulation tools in Chapter 3, whereas Chapters 4-7 are concerned with the physics and performance of specific devices.

My external stay at CEA in Grenoble with Julien Claudon is a result of our close collaboration with their experimental activities, where we deliver the theory and modelling of their devices. During my stay, I shared office with fellow Ph.D.-student Romain Fons, who carried out the experiments presented in Chapter 5. Sharing office with him was extremely fruitful, since we had very different views on the same physical phenomena, which lead to interesting discussions on the physics in the needle nanowires investigated in Chapter 5.

Commonly for all the chapters is that the workhorse is the Fourier modal method (FMM), due to the physical insight inherently provided by the technique³. The method will be used on ridge waveguides (3D structure), 2D photonic crystals (PhC, 2D structure) and on nanowires (rotationally symmetric structure), underlining the diversity of problems the FMM is able to solve. The FMM also has some drawbacks, including convergence difficulties for resolving large discontinuities, and that tapers and PhC holes are described with a staircase approximation reducing the computational efficiency. Furthermore, the FMM is not universal, meaning that it will be very efficient for structures with rotational and/or translational symmetry, and very inefficient for more advanced structures, e.g. topology optimized structures [36], and L5 and L9 PhC cavities as recently reported in Ref. [37].

Overview

The present thesis, as stated above, contains both method development, which adds to the functionality of the FMM, and applied nanophotonics engineering, where specific structures are investigated using the FMM in different forms. The thesis is therefore divided into two parts and eight chapters as listed below.

Part 1: Background, theoretical foundation and methodology In this part we introduce nanophotonic engineering on a general basis and develop new simulations tools. The part consists of the current chapter, and Chapters 2 and 3:

Chapter 2 We present the theoretical concepts central for the thesis. The chapter starts at the true foundation of nanophotonic engineering by presenting Maxwell's equations and the Lorentz reciprocity theorem. Thereafter we briefly review different techniques for solving Maxwell's equations followed by a section presenting the FMM in general terms. We provide an overview of the different types of boundary conditions, which are important to consider for especially open systems. The β -factor and Purcell

³In Chapter 7 the FMM plays a minor role as compared to the other chapters.

enhancement is presented and the chapter ends with the near-field to far-field transformation in cylindrical coordinates.

Chapter 3 Open boundary conditions are the ideal choice for open systems, and here we present our open-geometry Fourier modal method (oFMM) in 3D Cartesian coordinates. We show the importance of sampling the k -space in a clever way for faster convergence, and demonstrate our technique by calculating the emission rates and β -factor for a dipole embedded in a ridge waveguide, as well as the reflectivity of a metallic mirror.

Part 2: Applied nanophotonics engineering Specific nanophotonics structures are modelled using the FMM, in order to obtain insight on the physics of the devices.

Chapter 4 Using a Fourier-based Bloch mode expansion technique we consider a photonic crystal waveguide structure coupled to a microcavity. In the waveguide, we place a partly transmitting element (PTE) and we show how the spectral symmetry (parity) of the resulting Fano resonance depends on the distance between the PTE and the microcavity.

Chapter 5 InGaAs QDs embedded in GaAs nanowires are positioned randomly in the lateral plane due to the growth method. In this chapter, we present an all-optical mapping technique for determining the position of the QDs from far-field measurements.

Chapter 6 The source efficiency and Purcell enhancement of a dipole embedded in a truncated nanowire placed on a gold-silica mirror is investigated using a single-mode model and a model including all modes. We identify a breakdown of the single-mode model for computing both the Purcell enhancement and source efficiency, and provide simple physical explanations for this.

Chapter 7 When computing the indistinguishability and efficiency of single-photon sources (SPS), one needs to include the interaction with phonons, which is only possible with a quantum mechanical description. We present a model, which correctly accounts for the inherently high β -factor of nanowire SPSs not included in the current models, and identify a new design strategy for obtaining simultaneous high indistinguishability and efficiency.

The thesis ends with Chapter 8, where we will summarize the conclusions of the thesis and provide an outlook.

Theory of nanophotonics engineering

In this chapter, the theoretical foundation for the rest of the thesis will be laid. The purpose of the chapter is to introduce the general concepts, which the present thesis is based upon, rather than deriving all equations from first principles. In Section 2.1 Maxwell's equations are presented, as they form the basis of all photonics engineering. In the same section the Lorentz reciprocity theorem is presented, since it is the starting point for calculating the coupling of a dipole emitter to the surrounding photonic environment. Numerical techniques are often needed for solving Maxwell's equations and a brief review of the most common methods are found in Section 2.2. The workhorse for all the optical simulations presented throughout the thesis is the modal method in different formats. Thus we present an overview of the modal method in Section 2.3. Section 2.4 presents different types of boundary conditions as these are essential for the convergence of optical simulations. In Section 2.5 the spontaneous emission rate and the β -factor will be introduced in general terms, and the chapter ends with Section 2.6, where the near-field to far-field transformation is presented in cylindrical coordinates.

2.1 Maxwell's equations

Most of the work presented in the present thesis relies on solving Maxwell's equations in different nanophotonic structures. Maxwell's equations in the basic differential form are [38, 39]

$$\nabla \times \mathbf{E}(\mathbf{r}, t) = -\partial_t \mathbf{B}(\mathbf{r}, t), \quad (2.1a)$$

$$\nabla \times \mathbf{H}(\mathbf{r}, t) = \partial_t \mathbf{D}(\mathbf{r}, t) + \mathbf{J}(\mathbf{r}, t), \quad (2.1b)$$

$$\nabla \cdot \mathbf{D}(\mathbf{r}, t) = \rho(\mathbf{r}, t), \quad (2.1c)$$

$$\nabla \cdot \mathbf{B}(\mathbf{r}, t) = 0, \quad (2.1d)$$

where \mathbf{E} , \mathbf{B} , \mathbf{H} and \mathbf{D} are the electric field, the magnetic induction, the magnetic field and the electric displacement, respectively, while \mathbf{J} and ρ are the free current density and free charge, respectively. Using the harmonic time dependence

$$\mathbf{F}(\mathbf{r}, t) = \mathbf{F}(\mathbf{r}) \exp(-i\omega t), \quad (2.2)$$

for all fields and functions in Eqs. (2.1), Maxwell's equations in the frequency domain are obtained

$$\nabla \times \mathbf{E}(\mathbf{r}) = i\omega \mathbf{B}(\mathbf{r}), \quad (2.3a)$$

$$\nabla \times \mathbf{H}(\mathbf{r}) = -i\omega \mathbf{D}(\mathbf{r}) + \mathbf{J}(\mathbf{r}), \quad (2.3b)$$

$$\nabla \cdot \mathbf{D}(\mathbf{r}) = \rho(\mathbf{r}), \quad (2.3c)$$

$$\nabla \cdot \mathbf{B}(\mathbf{r}) = 0. \quad (2.3d)$$

For now the spatial dependence of the fields and functions in Eqs. (2.3) is suppressed in the interest of a leaner notation. The constitutive relations for non-magnetic and non-dispersive media relates the electric field with the electric displacement, and the magnetic field with the magnetic induction as

$$\mathbf{D} = \varepsilon_0 \varepsilon \mathbf{E}, \quad (2.4a)$$

$$\mathbf{B} = \mu_0 \mathbf{H}, \quad (2.4b)$$

where ε_0 and μ_0 are the vacuum permittivity and permeability, and ε is the relative permittivity (also known as the dielectric function), which in general is a function of both space and frequency. However, in this thesis the frequency

dependence of the dielectric function is generally neglected unless otherwise specified. Inserting Eqs. (2.4) into Eqs. (2.3) leads to the following form of Maxwell's equations

$$\nabla \times \mathbf{E} = i\omega\mu_0\mathbf{H}, \quad (2.5a)$$

$$\nabla \times \mathbf{H} = -i\omega\varepsilon_0\varepsilon\mathbf{E} + \mathbf{J}, \quad (2.5b)$$

$$\varepsilon_0\nabla \cdot \varepsilon\mathbf{E} = \rho, \quad (2.5c)$$

$$\nabla \cdot \mathbf{H} = 0. \quad (2.5d)$$

For all structures considered in this thesis there are no free charges i.e. $\rho = 0$. The energy flux density (energy per unit area per unit time) carried by an electromagnetic field is given by the Poynting vector [40]

$$\mathbf{S} = \mathbf{E} \times \mathbf{H}. \quad (2.6)$$

In general, we are often more interested in the time-averaged Poynting vector describing the average power per unit area given as [41]

$$\langle \mathbf{S} \rangle = \frac{1}{2} \text{Re}(\mathbf{E} \times \mathbf{H}^*). \quad (2.7)$$

Lorentz reciprocity theorem

Lorentz' reciprocity theorem follows from Maxwell's equations and reads as follows [39]

$$\int_S (\mathbf{E}_1 \times \mathbf{H}_2 - \mathbf{E}_2 \times \mathbf{H}_1) \cdot \hat{\mathbf{n}} dS = \int_V (\mathbf{J}_1 \cdot \mathbf{E}_2 - \mathbf{J}_2 \cdot \mathbf{E}_1) dV, \quad (2.8)$$

where the electromagnetic fields $[\mathbf{E}_{1(2)}, \mathbf{H}_{1(2)}]$ are produced by the current source $J_{1(2)}$ at frequency ω . This theorem is used for determining the dipole excitation of eigenmodes in photonic structures. It will be used for the Fourier modal method in both Cartesian and cylindrical coordinates.

2.2 Modelling techniques

There are numerous numerical methods for solving Maxwell's equations (2.1) in nanophotonic structures. Depending on which properties one wish to compute each method has its advantages and disadvantages. In the present thesis we are especially interested in the following very specific properties of the nanophotonic structures: the scattering coefficients, the spontaneous emission rate into both

guided and radiation modes, and the spatial distribution of the guided modes. Below the ability of the most common numerical techniques to compute these properties will be reviewed, which will serve as the motivation for using the Fourier modal method (FMM) throughout the present thesis.

The finite-difference time-domain (FDTD) technique [42] is the most commonly used method for simulating nanophotonic structures¹. It is often being described as a *brute force* method, since it directly solves Maxwell's equations with no further approximations. It is only the differential operators that are approximated as *finite-differences*. FDTD has the advantage of being available in commercial software packages such as Lumerical, however, this has the downside of often being a *black box*, where you risk losing physical insight. To my knowledge it is quite difficult to get modal information using FDTD, meaning that scattering coefficients, modal spontaneous emission rates and modal spatial distributions are not easily accessible using FDTD.

Another commonly used technique is the finite element method (FEM)² [43]. In contrast to FDTD the differential operators of Maxwell's equations are intact. Instead the solution space is approximated as consisting of small patches on which a number of basis functions³ are provided for approximating the solution. The patches with the local basis functions are called *finite elements*. These patches are pieced together assuring the continuity of the tangential components of the electric and magnetic fields. As for FDTD, commercial software packages based on FEM like COMSOL and JCMwave are available, which is a huge advantage of this technique. Using FEM it is possible to obtain the spatial distributions of optical modes and thus also model knowledge of the spontaneous emission rates. However, scattering coefficients are not straightforwardly extracted using FEM. Both FDTD and FEM rely on discretizing the solution space, which makes them quite memory demanding for 3D problems, especially for open systems where a region outside the structure needs to be included with absorbing boundary conditions.

The Green's function integral equation method (GFIEM) is also a commonly used technique, however to my knowledge no commercial software exists for this method. GFIEM is especially useful for scattering problems, where the field at all positions can be described as a sum of a field incident on the scatterer and a scattered field [44, 45]. The scattered field is described as a sum of fields emitted by a continuum of point sources located either inside or on the surface of the scatterer, where the strength of each source is determined by the fields at that position. By construction the GFIEM has open boundaries, meaning that it is an ideal method for open systems. Whether you can extract modal information

¹This is at least the impression I get at conferences.

²This assumption is again based on my conference participations.

³E.g. polynomials.

regarding the spontaneous emission rates and scattering coefficients probably depend on how you describe the Green's function of the scatterer.

The last class of methods to be summarised here are the modal methods (MM), where the structure is divided into uniform layers in a chosen propagation direction [46]. In each of these layers the electric and magnetic fields are described as a superposition of eigenmodes, which can be determined semi-analytically⁴ or numerically by expanding these on a set of basis functions, which leads to an eigenvalue problem easily solvable in Matlab. The electromagnetic field in each layer is then coupled together via the scattering matrix formalism. One of the big advantages of using a MM is the direct access to each individual mode and all the scattering coefficients associated with each mode. This enables easy calculation of the Purcell enhancement and β -factor in nanophotonic structures. In the following section we will provide a bit more details on the modal method.

2.3 The modal method

Throughout the present thesis, we will use the Fourier modal method (FMM) in Cartesian coordinates for 3D (Chapter 3) and 2D systems (Chapter 4), and in cylindrical coordinates for rotationally symmetric structures (Chapter 5 and 6). In Chapter 7 the modal method will be used in general terms, thus it will not be specific to one coordinate system. Here we will not go into the details of the FMM for each coordinate system with each type of boundary condition (see Section 2.4), however, regardless of these the FMM is build on the same basis, which we will provide here.

The basic assumption of the modal methods, is that the total electromagnetic field can be described in a z -invariant section of the structure as a superposition of forward and backward propagating eigenmodes [46]

$$\mathbf{F}(\mathbf{r}, \omega) = \sum_j a_j \mathbf{f}_j^+(\mathbf{r}, \omega) \exp(i\beta_j z) + b_j \mathbf{f}_j^-(\mathbf{r}, \omega) \exp(-i\beta_j z), \quad (2.9)$$

where \mathbf{F} is either the electric (\mathbf{E}) or magnetic (\mathbf{H}) field, \mathbf{f}_j is the j 'th eigenmode, $a_j(b_j)$ is the modal expansion coefficient of the j 'th forward (backward) propagating eigenmode and β_j is the propagation constant for the j 'th eigenmode. The superscript $+(-)$ indicate the propagation direction of the eigenmode.

In order to determine the field in Eq. (2.9) the eigenmodes and the modal expansion coefficients needs to be determined. The first step is to divide the optical structure into uniform layers in the propagation direction, meaning that the refractive index does not change along that direction [46, 47], as illustrated in Fig. 2.1. The eigenmodes are expanded on a set of basis functions, and insertion

⁴At least for 2D and rotationally symmetric structures

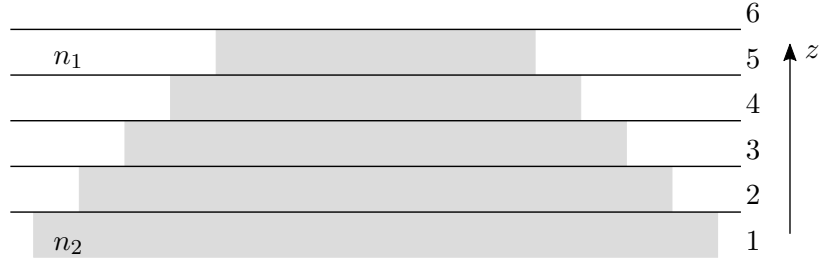


Figure 2.1: Division of a photonic structure into six layers of uniform refractive index along the z -direction. The grey (white) area has refractive index $n_2(n_1)$.

of this expansion into Maxwell's Eqs. (2.5a) and (2.5b) assuming no free currents ($\mathbf{J} = 0$), leads to an eigenvalue problem, whose solutions gives the eigenmodes and their propagation constants.

Having determined the eigenmodes, the modal expansion coefficients needs to be found. These are found in 2 steps. First the reflection and transmission matrices between adjacent layers are found by matching the electromagnetic field at the interface. Here we require that the tangential electric and magnetic fields are continuous across the interface [46]. This condition leads to a transmission and a reflection matrix that couples the eigenmodes in the adjacent layers across the interface.

The next step is to take the scattering at all interfaces into account. For simplicity, we consider the structure in Fig. 2.1 and illuminate it from the bottom with the fundamental mode of the first layer (i.e. $\mathbf{a} = \delta_{1j}$). At the first interface between layer 1 and 2, it will be partly reflected and partly transmitted. The transmitted part will reach the second interface between layer 2 and 3, where it is again partly transmitted and reflected. The reflected part travels backwards towards the interface between layer 1 and 2, where it is partly reflected and transmitted. The result is that in each layer we have in principle an infinite number of roundtrips of light that is partly transmitted and reflected at the interfaces. In order to describe this correctly we use the scattering matrix formalism [46], which is a cyclic procedure for computing the reflection and transmission matrices relating layer q and q' . We start by finding the scattering matrices for layer 1 and 2, then for layer 1 and 3, layer 1 and 4, and so on, until we have repeated the procedure for all interfaces. This gives us access to all the modal excitation coefficients through the structure, and thus also the coupling between all modes. As will be shown throughout the present thesis, this feature is advantageous for obtaining a physical intuition and understanding of the observed phenomena.

In Chapter 3 the Fourier modal method in 3D Cartesian coordinates and with open boundary conditions will be derived, implemented and tested. Chapter 4 uses a Fourier-based Bloch mode expansion technique in order to exploit the periodicity of the photonic crystal structure under investigation. This technique

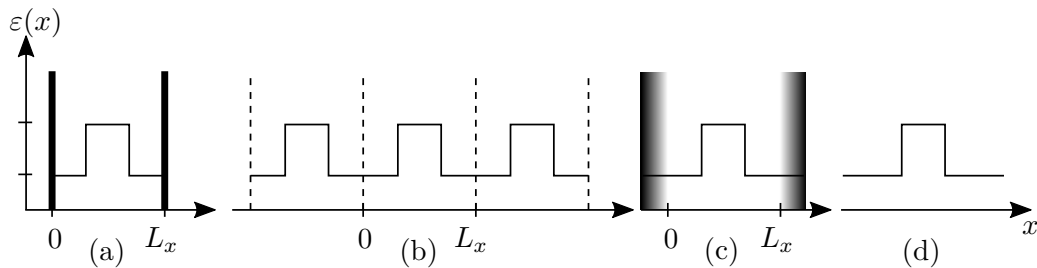


Figure 2.2: The dielectric profile of a waveguide in a geometry with (a) closed boundary conditions, (b) periodic boundary conditions, (c) absorbing boundary conditions and (d) open boundary conditions.

is well established, and a good description of the details is found in Ref. [46]. For Chapters 5 and 6 we use the Fourier modal method in cylindrical coordinates and with open boundary conditions, which was recently developed in Ref. [48], where the derivation of the formalism and the eigenvalue problem is found.

2.4 Boundary conditions

In computational photonics it is very important to consider the right choice of boundary conditions for the computational domain. In this section a small overview of the different types of boundary conditions will be provided. Extensive details on the implementation of open boundary conditions in the Fourier modal method using Cartesian coordinates will be given in Chapter 3.

Closed boundary conditions

Closed boundary conditions is probably the simplest boundary condition, where it is required that the electric (magnetic) field is zero at the boundary of the computational domain. The structure of interest is placed in a box of length L_x with walls being a perfect electric (magnetic) conductor such that [39]

$$\mathbf{E}(\mathbf{H})_{\parallel}(0) = \mathbf{E}(\mathbf{H})_{\parallel}(L_x) = 0. \quad (2.10)$$

Fig. 2.2(a) illustrates the closed geometry for a slab waveguide. Care should be taken when using closed boundary conditions since these leads to artificial reflections from the boundary of the computational domain.

Periodic boundary conditions

Periodic boundary conditions is normally used in the Fourier modal method, where the eigenmodes are expanded on Fourier series [46]. For a periodic structure

the Bloch theorem is employed, which requires that the field after one period reproduces itself multiplied with a phase term as [39, 49]

$$\mathbf{E}(x + L_x) = \mathbf{E}(x) \exp(i\alpha), \quad (2.11)$$

where α can be freely chosen from the outset [46]. Fig. 2.2(b) illustrates a periodic geometry. Again if you are to perform computations on an open system, care should be taken when using periodic boundary conditions, since you will have interference between the neighbouring structures in your computational domain.

Absorbing boundary conditions

Implementing an absorbing boundary condition is a way to reduce the artificial reflections from the computational boundaries inherent for periodic and closed boundary conditions in open systems [50]. The mostly used absorbing boundary are the perfectly matched layer (PML) [42], which was proposed in Ref. [51] in 1994 for the finite-difference time-domain technique. For eigenmode expansion techniques PMLs are still the standard boundary condition for open systems [47, 52–54]. In short, PMLs are absorbing boundary regions surrounding the computational domain in which out-going electromagnetic energy is dissipated. The PMLs are perfectly matched to the computational domain in order to reduce reflections at the interface between the PML domain and the computational domain. However, it should be noted that PMLs are an artificial boundary and convergence issues has been reported for a FMM implementation [50]. For correctly implemented PMLs these converge towards the true open boundary conditions. Fig. 2.2(c) sketches a PML for a waveguide geometry.

Open boundary conditions

Open boundary conditions allows outgoing waves to propagate to infinity with no artificial reflection, as illustrated in Fig. 2.2(d). For simulation techniques relying on a spatial discretization such as FEM and FDTD, open boundaries are not possible. However, for the FMM, where the fields are expanded on Fourier series it is possible to expand these on Fourier integrals instead, which in principle gives the exact description of the fields. Extensive details on the implementation of open boundaries in the FMM for 3D Cartesian coordinates will be given in Chapter 3, which is based on the same ideas of an efficient discretization of k -space for the Fourier integrals as was first proposed in Ref. [48].

2.5 Spontaneous emission rate and β -factor

Until Purcell's analysis in 1946 [55] spontaneous emission by a quantum emitter was considered an intrinsic property independent of the surrounding photonic environment [56]. He discovered that the spontaneous emission rate, γ , of an emitter in a resonant cavity is enhanced by a factor proportional to the ratio between the quality factor Q and the mode volume V of the cavity as compared to the emission rate in a bulk medium, γ_0 . This factor is the well-known Purcell factor and is given as

$$F_P = \frac{\gamma}{\gamma_0} = \frac{3}{4\pi^2} \left(\frac{\lambda_c}{n}\right)^3 \frac{Q}{V}, \quad (2.12)$$

where λ_c is the resonant wavelength of the cavity and n is the refractive index of the cavity medium. However, Eq. (2.12) only holds at the cavity resonance and for an emitter located exactly at the field maximum [57].

A general expression for the spontaneous emission rate is given by Fermi's golden rule [56, 58] in the dipole approximation

$$\gamma = \frac{2\pi}{\hbar} \sum_f \left| \langle f | \hat{H}_I | i \rangle \right|^2 \delta(\omega_i - \omega_f), \quad (2.13)$$

where $|i\rangle$ denotes the initial state of the emitter with emission frequency ω_i and $|f\rangle$ any possible final state with frequency ω_f . \hat{H}_I is the interaction Hamiltonian between the initial and final state of the emitter and is in the dipole approximation given as [56, 59]

$$\hat{H}_I = -\hat{\mathbf{p}} \cdot \hat{\mathbf{E}}, \quad (2.14)$$

where $\hat{\mathbf{p}}$ and $\hat{\mathbf{E}}$ are the dipole moment and electric field operators respectively. In the present thesis, however, all calculations are done classically by use of the dipole approximation, as the structures considered will be in the weak coupling regime, where classical theory and quantum electrodynamics have shown to agree on the effects of a cavity on the spontaneous emission rate [56, 60]. An exception is made in Chapter 7, where we will use a quantum mechanical model to calculate the indistinguishability and efficiency of a nanowire single-photon source, since a classical model is not adequate in this case. In the dipole approximation, the quantum emitter is treated as a classical dipole, and the light-matter coupling is only dependent on the electric field strength at the emitter position. The spontaneous emission rate cannot be computed directly using the FMM, instead the equality between the spontaneous emission rate and radiated power normalized to their bulk values is used [56]

$$\frac{\gamma}{\gamma_0} = \frac{P}{P_0}, \quad (2.15)$$

where $\gamma_0(P_0)$ is the spontaneous emission rate (radiated power) in a bulk medium. The radiated power by a harmonically oscillating dipole in bulk is given analytically as [56]

$$P_0 = \frac{|\mathbf{p}|^2}{4\pi\epsilon_0\epsilon} \frac{n^3\omega^4}{3c^3}, \quad (2.16)$$

and the emitted power by a dipole in any linear medium is given by [56]

$$P = \frac{\omega}{2} \text{Im} [\mathbf{p}^* \cdot \mathbf{E}(\mathbf{r}_0)]. \quad (2.17)$$

Using a modal expansion technique Eq. (2.17) can be modified to provide the power emitted into a specific optical mode (eigenmode) m by only evaluating the electric field strength of the specific mode at the dipole position [48]

$$P_m = \frac{\omega}{2} \text{Im} [\mathbf{p}^* \cdot \mathbf{E}_m(\mathbf{r}_0)]. \quad (2.18)$$

The access to all modes provided by the FMM is a very strong feature, since we can easily compute the power emitted into each mode. This is especially advantageous for computing the β -factor, which is defined as the ratio of the total emission going into the fundamental mode of a waveguide structure

$$\beta = \frac{P_m}{P_{\text{Tot}}}. \quad (2.19)$$

The β -factor is an important parameter for the performance of a whole range of nanophotonic devices e.g. lasers and SPSs, and therefore precise computations of this is very important.

2.6 Near-field to far-field transformation

The FMM is usually used within nanophotonics to compute scattering coefficients, optical modes and near-fields of dipoles embedded in optical structures. However, for nanowire structures with an out-coupling taper [27, 32, 61, 62] the far-field is often of interest, since the shape and size of the far-field defines the collection efficiency [23, 62, 63]. In Chapters 5 and 6 the far-field is investigated for a needle nanowire and a truncated nanowire (denoted a nanopost). This section provides the basic formulas for the near-field to far-field transformation in a cylindrical coordinate system supported by derivations in Appendix A.

In a spherical coordinate system the radial components of the far-field from a point source are negligible [56, 64], such that $E_r \simeq H_r \simeq 0$. The remaining components of the far-field in free space are [64]

$$E_\theta \simeq -\frac{ik_0 \exp(-ik_0 r)}{4\pi r} (L_\phi + \eta_0 N_\theta), \quad (2.20a)$$

$$E_\phi \simeq \frac{ik_0 \exp(-ik_0 r)}{4\pi r} (L_\theta - \eta_0 N_\phi), \quad (2.20b)$$

$$H_\theta \simeq \frac{ik_0 \exp(-ik_0 r)}{4\pi r} \left(N_\phi - \frac{L_\theta}{\eta_0} \right), \quad (2.20c)$$

$$H_\phi \simeq -\frac{ik_0 \exp(-ik_0 r)}{4\pi r} \left(N_\theta + \frac{L_\phi}{\eta_0} \right), \quad (2.20d)$$

where $\eta_0 = \sqrt{\mu_0 \varepsilon_0^{-1}}$ is the free space wave impedance. The functions N_θ , N_ϕ , L_θ and L_ϕ are given by the equivalent currents on a surface S , which in a cylindrical coordinate system are related as [64]

$$N_\theta = \int_S [J_r \cos \theta \cos(\phi - \phi') + J_\phi \cos \theta \sin(\phi - \phi') - J_z \sin \theta] \exp(-ik_0 r' \sin \theta \cos(\phi - \phi')) ds', \quad (2.21a)$$

$$N_\phi = \int_S [-J_r \sin(\phi - \phi') + J_\phi \cos(\phi - \phi')] \exp(-ik_0 r' \sin \theta \cos(\phi - \phi')) ds', \quad (2.21b)$$

$$L_\theta = \int_S [M_r \cos \theta \cos(\phi - \phi') + M_\phi \cos \theta \sin(\phi - \phi') - M_z \sin \theta] \exp(-ik_0 r' \sin \theta \cos(\phi - \phi')) ds', \quad (2.21c)$$

$$L_\phi = \int_S [-M_r \sin(\phi - \phi') + M_\phi \cos(\phi - \phi')] \exp(-ik_0 r' \sin \theta \cos(\phi - \phi')) ds'. \quad (2.21d)$$

Here the observation point in the far-field is at (r, θ, ϕ) in spherical coordinates and the source point on the surface S is given by the coordinates (r', ϕ') in cylindrical coordinates. The equivalent currents J_r , J_ϕ , M_r and M_ϕ are all functions of (r', ϕ') and are related to the electric and magnetic field by the relations [64]

$$\mathbf{J} = \hat{\mathbf{n}} \times \mathbf{H}, \quad \mathbf{M} = -\hat{\mathbf{n}} \times \mathbf{E}, \quad (2.22)$$

where $\hat{\mathbf{n}}$ is the unit vector normal to the surface S . Eqs. (2.21) are simplified by assuming a cosine/sine angular dependence of the equivalent currents such that

$$J_r(r', \phi') = J_r(r') \cos(n\phi'), \quad J_\phi(r', \phi') = J_\phi(r') \sin(n\phi'), \quad (2.23a)$$

$$M_r(r', \phi') = M_r(r') \sin(n\phi'), \quad M_\phi(r', \phi') = M_\phi(r') \cos(n\phi'). \quad (2.23b)$$

Using this assumption and assuming that the surface is plane i.e. $J_z = M_z = 0$, Eqs. (2.21) are simplified to

$$N_\theta = - \int \cos \theta \cos(n\phi) [H_p(r') J_{n-1}(-k_0 r' \sin \theta) + H_m(r') J_{n+1}(-k_0 r' \sin \theta)] i^{n-1} \pi r' dr', \quad (2.24a)$$

$$N_\phi = \int \sin(n\phi) [H_p(r') J_{n-1}(-k_0 r' \sin \theta) - H_m(r') J_{n+1}(-k_0 r' \sin \theta)] i^{n-1} \pi r' dr', \quad (2.24b)$$

$$L_\theta = - \int \cos \theta \sin(n\phi) [E_m(r') J_{n-1}(-k_0 r' \sin \theta) + E_p(r') J_{n+1}(-k_0 r' \sin \theta)] i^{n-1} \pi r' dr', \quad (2.24c)$$

$$L_\phi = \int \cos(n\phi) [-E_m(r') J_{n-1}(-k_0 r' \sin \theta) + E_p(r') J_{n+1}(-k_0 r' \sin \theta)] i^{n-1} \pi r' dr', \quad (2.24d)$$

where

$$H(E)_m = H(E)_r - H(E)_\phi, \quad H(E)_p = H(E)_r + H(E)_\phi. \quad (2.25)$$

In Appendix A the derivation of Eqs. (2.24) is found as well as the similar expressions (Eqs. (A.7)) for the reverted cosine/sine dependence in Eqs. (2.23), which has to be used for TE polarized light. More details on this matter will be given in Chapter 5, where the far-field of a needle nanowire is used to determine the approximate position of the emitting quantum dot. The far-field power is computed using the time-averaged Poynting vector in Eq. (2.7).

Modelling open nanophotonic systems using the Fourier modal method: Generalization to 3D Cartesian coordinates

A lot of nanophotonic devices such as microcavity resonators [25, 29, 65], slow-light waveguides [66–68] and single-photon sources [14, 22, 23] are open systems with properties strongly dependent on their leakage of light into the surroundings, which in principle extend to infinity. As mentioned in Section 2.2 only the Green’s function integral equation approach has open boundaries [45], whereas the finite-difference time-domain (FDTD) [42, 69] and the finite element method (FEM) [43] inherently rely on a limited computational domain with efficient absorbing boundary conditions (BCs) for treating open systems. Thereby, the widely used FDTD and FEM techniques cannot fully account for the openness of a system, and thereby correctly model radiative losses. Thus, careful treatment of the computational domain boundaries is needed for simulations of open systems, in order to avoid artificial reflections from the domain wall [51, 53, 54, 70].

The Fourier modal method (FMM) has until recently also relied on selecting proper artificial absorbing BCs [50], and to circumvent this problem a new com-

combination of an open BC and an efficient discretization scheme was developed in Ref. [48] for the FMM, called open-geometry FMM (oFMM) in the following. In Ref. [48] the formalism presented was limited to rotationally symmetric structures, and in this chapter we expand this formalism to model 3D structures in Cartesian coordinates. For now the formalism is limited to handle structures with layers surrounded by a bulk material, and the reason for this will be discussed later in Section 3.4 and in Appendix B.5. As discussed in Sections 2.2 and 2.3 modal methods have some advantages regarding physical insight in nanophotonic structures, and thus a modal method with open boundaries is a very powerful tool, since you in principle can obtain a precise and correct description of all modes in the structure.

Usually the basis functions in the FMM are plane waves expanded in a Fourier series [71–73], which inherently assumes periodic BCs. Instead the open boundary of the computational domain is obtained by using basis functions (plane waves in Cartesian coordinates) that expand the whole infinite space and by using the Fourier transform. This gives an exact description in the limit of *continuous* k -space sampling, however the numerical implementation requires a *discrete* sampling. In contrary to using Fourier series, we are free to choose the k -space discretization, which enables a more efficient mode sampling. Using integrals instead of series is not a novel approach, and has been used for both 2D [74] and rotationally symmetric 3D structures [75–77], but without applying efficient k -space discretization schemes. In [48] the oFMM approach based on open BCs and a Chebyshev grid [78, 79] was developed for rotationally symmetric structures, a formalism we will expand to 3D Cartesian structures (3D oFMM) in this chapter.

Due to the discretization of the k -space, Li’s factorization rules [71–73] should ideally be applied in our 3D oFMM formalism. It turns out that in contrast to the rotationally symmetric case, where Li’s factorization rules are straightforwardly applied for any k -space discretization [48, 75], the inverse factorization rule can only be applied for the conventional equidistant discretization scheme in our 3D approach. However, we will show that an efficient sampling of the k -space and using the direct factorization rule still leads to faster convergence compared to traditional schemes using the correct factorization rules.

The present chapter has been published in Ref. [80] (J3), and thus any citations should be directed to the journal publication. The author have contributed to developing, implementing and testing the formalism and to writing the article. The chapter is thus a slightly modified version of Ref. [80] in order to fit it into the present thesis.

The chapter is organized as follows. Section 3.1 outlines the theory of the oFMM approach. The details of the new discretization scheme are discussed in Section 3.2. The method is tested by calculating the dipole emission in a waveguide and the reflection of the fundamental mode from a waveguide-metal interface in

Section 3.3. After a discussion of advantages and limitations of the method in Section 3.4, conclusions are drawn in Section 3.5, and detailed derivations of our theory are provided in Appendix B.

3.1 3D open-geometry Fourier modal method

In this section, we follow the approach of Ref. [48] and generalize the results for the 3D Cartesian coordinate system. We outline the derivation of the open BC formalism and introduce the theoretical concepts required to understand the results of the following sections. As important examples, we show how the oFMM approach is applied to calculate the emission from a dipole placed inside a waveguide and to compute the reflection from a waveguide-metal interface. In Appendix B, we give the detailed derivations of the open geometry formalism, discuss the applicability of Li's factorization rules and show why our formalism is currently limited to treating structures laterally surrounded by a bulk material.

Open boundary condition formalism

We use a complete vectorial description of Maxwell's equations based on Fourier expansion and open BCs to describe the electromagnetic (EM) fields in a z -invariant material layer. The z dependence is treated in the standard way by combining z -invariant layers using the scattering matrix formalism [46, 81]. It is only the calculation of the lateral electric and magnetic field components of the eigenmodes in each layer that is altered by the new oFMM formalism. The eigenmodes then form the expansion basis for the EM field.

In the conventional FMM [46], the eigenmodes are computed by expanding its field components as well as the permittivity profile in Fourier *series* in the lateral coordinates (x, y) on a *finite-sized* computational domain, implying that these functions vary *periodically* in these coordinates. In the open boundary formalism, we instead consider an *infinite-sized* computational domain and employ expansions in Fourier *integrals*. We use a plane-wave expansion as basis functions. In the following, we describe the general steps and equations required to expand the field components and to solve for the expansion coefficients and the propagation constant. The specific equations and derivations are given in Appendix B and are referred to throughout this section.

We start by considering a z -invariant part of the space where the lateral structure is defined by the relative permittivity $\varepsilon(x, y)$ and impermeability $\eta(x, y) \equiv 1/\varepsilon(x, y)$. For simplicity, we consider a non-magnetic material having vacuum permeability μ_0 and with no current sources and assume a harmonic time depen-

dence on the fields. In such a region of space, Maxwell's equations (2.5a) and (2.5b) are written as

$$\nabla \times \mathbf{E}(x, y, z) = i\omega\mu_0\mathbf{H}(x, y, z), \quad (3.1a)$$

$$\nabla \times \mathbf{H}(x, y, z) = -i\omega\varepsilon_0\varepsilon(x, y)\mathbf{E}(x, y, z), \quad (3.1b)$$

where ω is the angular frequency and \mathbf{E} and \mathbf{H} are the vectorial electric and magnetic fields respectively. We then write the fields in a component-wise representation and introduce a z dependence of the form $\exp(i\beta z)$, where β is the propagation constant of a particular eigenmode

$$\partial_y E_z - i\beta E_y = i\omega\mu_0 H_x, \quad (3.2)$$

$$i\beta E_x - \partial_x E_z = i\omega\mu_0 H_y, \quad (3.3)$$

$$\partial_x E_y - \partial_y E_x = i\omega\mu_0 H_z, \quad (3.4)$$

$$\partial_y H_z - i\beta H_y = -i\omega\varepsilon_0\varepsilon E_x, \quad (3.5)$$

$$i\beta H_x - \partial_x H_z = -i\omega\varepsilon_0\varepsilon E_y, \quad (3.6)$$

$$\partial_x H_y - \partial_y H_x = -i\omega\varepsilon_0\varepsilon E_z, \quad (3.7)$$

The individual field components and the permittivity and impermittivity functions are then expanded on basis functions $g(k_x, k_y, x, y) = \exp[i(k_x x + k_y y)]$ (corresponding to a plane wave expansion basis for harmonic time dependence) as

$$\begin{aligned} f(x, y) &= \int_{-\infty}^{\infty} c_f(k_x, k_y) g(k_x, k_y, x, y) dk_x dk_y \\ &\simeq \sum_m \sum_l c_f(k_x^m, k_y^l) g(k_x^m, k_y^l, x, y) \Delta k_x^m \Delta k_y^l, \end{aligned} \quad (3.8)$$

where the basis function $g(k_x, k_y, x, y)$ satisfy the following orthogonality condition

$$\int_{-\infty}^{\infty} g(k_x, k_y, x, y) g^*(k'_x, k'_y, x, y) dx dy = (2\pi)^2 \delta(k_x - k'_x) \delta(k_y - k'_y). \quad (3.9)$$

The expansion coefficients in Eq. (3.8) are obtained by multiplying with $g^*(k'_x, k'_y)$, integrating over the transverse plane and using the orthogonality relation Eq. (3.9) leading to

$$c_f(k_x, k_y) = \frac{1}{(2\pi)^2} \int_{-\infty}^{\infty} \int_{-\infty}^{\infty} f(x, y) g^*(k_x, k_y, x, y) dx dy. \quad (3.10)$$

In the last row of Eq. (3.8) the integral expansions are discretized using a Riemann sum on a (k_x^m, k_y^l) grid for numerical calculations. The double summation over the indices m and l in Eq. (3.8) is valid for the conventional *separable* discretization scheme, where the discretization grid coordinates along the k_x and k_y axes in k -space are defined *independently* of each other. However, when using a non-separable representation as we will do in the following, the Riemann sum is instead written as

$$f(x, y) \simeq \sum_{\xi} c_f(k_x^{\xi}, k_y^{\xi}) g(k_x^{\xi}, k_y^{\xi}, x, y) \Delta k_{\xi}, \quad (3.11)$$

where a single index ξ is used to describe the discretization points in the 2D k -space and Δk_{ξ} is the discretization area for the ξ 'th k point. In the particular case of the separable discretization in Eq. (3.8), we have $\Delta k_{\xi} = \Delta k_x^m \Delta k_y^l$. This discretization area Δk_{ξ} will generally vary as function of ξ . Furthermore, as will be discussed in detail in Section 3.2, the selection of the wave number values k_x^{ξ} and k_y^{ξ} defines the Fourier expansion basis. The computational efficiency of our approach depends crucially on the choice of this expansion basis, as will be apparent from the convergence analysis in Section 3.3.

The material properties of the structure are described by the permittivity and impermeability functions, which are written as a sum of a constant background value and a position dependent deviation from the background value, as

$$\varepsilon(x, y) = \varepsilon_B + \Delta\varepsilon(x, y), \quad (3.12)$$

$$\eta(x, y) = \frac{1}{\varepsilon(x, y)} = \eta_B + \Delta\eta(x, y), \quad (3.13)$$

where $\Delta\varepsilon(x, y)$ and $\Delta\eta(x, y)$ are functions with compact support, such that $\Delta\varepsilon = \Delta\eta = 0$ outside a finite domain. This description of the permittivity and impermeability functions can only be used for homogeneous backgrounds. If the background consists of a substrate and air, this formalism breaks down as discussed in Appendix B.5.

The expansion coefficients of the Fourier transform of the permittivity function can then be written as

$$c_{\varepsilon}(k_x, k_y) = \varepsilon_B \delta(k_x) \delta(k_y) + c_{\Delta\varepsilon}(k_x, k_y), \quad (3.14)$$

where

$$c_{\Delta\varepsilon}(k_x, k_y) = \frac{1}{(2\pi)^2} \int_{-\infty}^{\infty} \int_{-\infty}^{\infty} \Delta\varepsilon(x, y) g^*(k_x, k_y, x, y) dx dy. \quad (3.15)$$

The Fourier transforms of the position dependent deviations, $\Delta\varepsilon$ and $\Delta\eta$, are thus obtained by calculating finite integrals, whereas the constant ε_B and η_B contributions are handled analytically using Dirac delta functions.¹

In order to factorize Eqs. (3.2)-(3.7) by insertion of the expansion in Eq. (3.8), Li's factorization rules [71, 73, 81] should be considered. Eqs. (3.2)-(3.4) and Eq. (3.7) do not contain any products between two functions with concurrent jumps (discontinuities) and therefore the direct rule applies in these equations. Considering a rectangular waveguide in free space the product $\varepsilon E_{x,y}$ in Eq. (3.5) and (3.6) will be discontinuous when the field is parallel to an interface and continuous for the direction perpendicular to an interface. In the latter case both $\varepsilon(x, y)$ and $E_{x,y}(x, y)$ have concurrent jumps and the inverse rule should - ideally - be used.

When expanding the field components using the separable discretization, we treat the product of the permittivity function and the electric field components in Eq. (3.1b) using Li's factorization rules [71, 73, 81]. However, as discussed in Appendix B.1 and B.2, this is not possible when using a non-separable discretization. The details of the expansions are given in Eqs. (B.1)-(B.3), (B.7)-(B.8) and (B.12)-(B.18).

After inserting the expansions into Maxwell's equations and eliminating the z -components of the EM fields, we arrive at two sets of equations coupling the lateral field components (Eqs. (B.11) and (B.21) in Appendix B.1 and B.2)

$$\begin{bmatrix} \mathbf{k}_x \varepsilon_{\text{Tot}}^{-1} \mathbf{k}_y & -\mathbf{k}_x \varepsilon_{\text{Tot}}^{-1} \mathbf{k}_x + k_0^2 \mathbf{I} \\ \mathbf{k}_y \varepsilon_{\text{Tot}}^{-1} \mathbf{k}_y - k_0^2 \mathbf{I} & -\mathbf{k}_y \varepsilon_{\text{Tot}}^{-1} \mathbf{k}_x \end{bmatrix} \begin{bmatrix} \mathbf{h}_x \\ \mathbf{h}_y \end{bmatrix} = \omega \varepsilon_0 \beta \begin{bmatrix} \mathbf{e}_x \\ \mathbf{e}_y \end{bmatrix}, \quad (3.16)$$

$$\begin{bmatrix} -\mathbf{k}_x \mathbf{k}_y & \mathbf{k}_x^2 - k_0^2 \varepsilon_y \\ k_0^2 \varepsilon_x - \mathbf{k}_y^2 & \mathbf{k}_y \mathbf{k}_x \end{bmatrix} \begin{bmatrix} \mathbf{e}_x \\ \mathbf{e}_y \end{bmatrix} = \omega \mu_0 \beta \begin{bmatrix} \mathbf{h}_x \\ \mathbf{h}_y \end{bmatrix}, \quad (3.17)$$

where \mathbf{e}_x , \mathbf{e}_y , \mathbf{h}_x and \mathbf{h}_y are the vectors of the expansion coefficients of E_x , E_y , H_x , and H_y , respectively, and \mathbf{k}_x and \mathbf{k}_y are diagonal matrices of the discretized k_x^ξ and k_y^ξ values. Furthermore, $\varepsilon_{\text{Tot}} = \Delta\varepsilon \Delta\mathbf{k} + \varepsilon_B \mathbf{I}$ with $\Delta\varepsilon$ being the Toeplitz matrix defined below Eq. (B.9) in Appendix B.1, \mathbf{I} is the identity operator and $\Delta\mathbf{k}$ is the diagonal matrix containing the elements Δk_ξ . When using a separable discretization grid, ε_x and ε_y are given by Eqs. (B.17) and (B.18) in Appendix B.2 respectively, and for a non-separable discretization grid $\varepsilon_x = \varepsilon_y = \varepsilon_{\text{Tot}}$.

Combining Eqs. (3.16) and (3.17) allows us to compute, for example, the lateral electric field components $E_{x,j}(x, y)$ and $E_{y,j}(x, y)$ of the eigenmode j and its propagation constant β_j , after which the lateral magnetic field components $H_{x,j}(x, y)$ and $H_{y,j}(x, y)$ and the longitudinal field components $E_{z,j}(x, y)$ and $H_{z,j}(x, y)$ can be derived using Eqs. (B.4) and (B.6). In Appendix B.1 and B.2, we show how

¹Note that $c_{\Delta\varepsilon}(k_x, k_y)$ does not have the same physical dimensions as ε_B .

Li's factorization rules are correctly used with the oFMM based on equidistant discretization. However, our non-separable "dartboard" discretization introduced in Section 3.2 is not compatible with the inverse factorization rule, and for this reason we employ only the direct factorization rule, which means that we use $\varepsilon_x = \varepsilon_y = \varepsilon_{\text{Tot}}$.

Field emitted by a point dipole

In the modal expansion method, the emission from a point dipole placed in a photonic structure can be described [46] as an expansion of eigenmodes with expansion coefficients proportional to the electric field strength of the corresponding eigenmode obtained from Eqs. (3.16)-(3.17) at the emitter position. The total field emitted by a point dipole \mathbf{p} placed at \mathbf{r}_{pd} inside a z -invariant structure is

$$\begin{aligned} \mathbf{E}(x, y, z) &= \sum_j a_j(\mathbf{r}_{\text{pd}}, \mathbf{p}) \mathbf{E}_j(x, y, z) \\ &= \sum_j \sum_{\xi} a_j(\mathbf{r}_{\text{pd}}, \mathbf{p}) c_{j,\xi} \mathbf{g}(k_x^{\xi}, k_y^{\xi}, x, y) \Delta k_{\xi} e^{i\beta_j(z-z_{\text{pd}})}, \end{aligned} \quad (3.18)$$

where $a_j(\mathbf{r}_{\text{pd}}, \mathbf{p})$ is the dipole coupling coefficient to mode j given in Eq. (B.33) in Appendix B.4, where it is derived using the Lorentz reciprocity theorem (Eq. (2.8)) as in Ref. [46]. The coupling coefficient depends on the dipole position \mathbf{r}_{pd} and dipole moment \mathbf{p} through a dot product $\mathbf{p} \cdot \mathbf{E}_j(\mathbf{r}_{\text{pd}})$. For the sake of notational clarity, we omit these dependencies in the following. Furthermore, $c_{j,\xi}$ are the expansion coefficients for mode j , and $\mathbf{g}(k_x^{\xi}, k_y^{\xi}, x, y)$ are the vectorial plane wave basis functions.

The emitted field (3.18) consists of three contributions [82]: guided modes, radiating modes, and evanescent modes. For a waveguide surrounded by air each mode is classified based on their propagation constant β_j as

$$k_0^2 < \beta_j^2 \leq n_w^2 k_0^2, \quad \text{Guided mode}, \quad (3.19a)$$

$$0 < \beta_j^2 \leq k_0^2, \quad \text{Radiation mode}, \quad (3.19b)$$

$$\beta_j^2 \leq 0, \quad \text{Evanescent mode}, \quad (3.19c)$$

where n_w is the refractive index of the waveguide. We will apply this classification in Section 3.3 when we investigate the performance of the discretization schemes, and in Chapters 5 and 6 for modes in rotationally symmetric structures.

Using Eqs. (2.15), (2.16), (2.18) and (3.18) the normalized power emitted by a dipole to a selected mode j can be expressed as [56]

$$\frac{P_j}{P_0} = \frac{\omega \operatorname{Im}\{\mathbf{p}^* \cdot a_j \mathbf{E}_j(\mathbf{r}_{\text{pd}})\}}{2 P_0} \quad (3.20)$$

$$= \frac{\omega \operatorname{Im}\{\mathbf{p}^* \cdot \sum_{\xi} a_j c_{j,\xi} \mathbf{g}_{\xi}(\mathbf{r}_{\text{pd}}) \Delta k_{\xi}\}}{2 P_0}, \quad (3.21)$$

where P_0 is the emitted power in a bulk medium of refractive index n_B and is given in Eq. (2.16). The normalized power is equal to the normalized spontaneous emission rate [56] as stated in Eq. (2.15) $\gamma_j/\gamma_0 = P_j/P_0$, where γ_j and γ_0 are the spontaneous emission rates to the mode j and to a bulk material, respectively. In the following and throughout the thesis we will mainly use the normalized unitless quantity $\Gamma_j = \gamma_j/\gamma_0$ for the emission rates.

Reflection at an interface

While the theory above holds for a structure with uniformity along the z -axis, most geometries of interest consist of several z -invariant sections. The full structure can be described by combining the solutions of Eqs. (3.16)-(3.17) using a scattering matrix approach [46, 72]. Since our oFMM is based on expanding the fields in each layer using the same basis function, the reflections and transmission of the eigenmodes can be calculated conveniently using the expansion coefficients as described in the following.

Let \mathbf{C}_i^E and \mathbf{C}_i^H , where $i = 1, 2$ is the layer index, be matrices whose columns contain the vector expansion coefficients for the lateral electric and magnetic fields respectively computed using (3.16) and (3.17). Then, at the interface of material layers 1 and 2, the transmission and reflection matrices are given as [46]

$$\mathbf{T}_{12} = 2 \left[(\mathbf{C}_1^E)^{-1} \mathbf{C}_2^E + (\mathbf{C}_1^H)^{-1} \mathbf{C}_2^H \right]^{-1}, \quad (3.22)$$

$$\mathbf{R}_{12} = \frac{1}{2} \left[(\mathbf{C}_1^E)^{-1} \mathbf{C}_2^E - (\mathbf{C}_1^H)^{-1} \mathbf{C}_2^H \right] \mathbf{T}_{12}. \quad (3.23)$$

3.2 Discretization scheme

We have now, via the modal representation in Eq. (3.11), developed a formalism capable of using a non-uniform k -space discretization, which is a generalization of the uniform k -space discretization traditionally used in the Fourier modal method. In this section, we describe the important point of how to efficiently sample the k -space, before proceeding to example calculations.

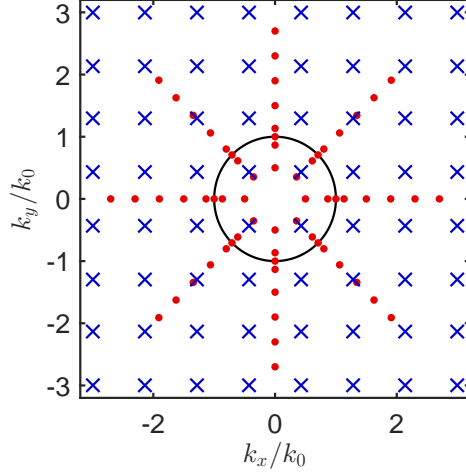


Figure 3.1: Examples of the discrete mode distributions \mathbf{k}_\perp used with 3D oFMM. The blue crosses show the conventional equidistant discretization which may have different discretization step size for x and y directions, i.e. $\Delta k_x \neq \Delta k_y$. The red dots represent the dartboard discretization used with the open BC formalism. The solid line shows a unit circle $|\mathbf{k}_\perp|/k_0 = 1$. In this simple example, we have used $k_{\text{cut-off}}/k_0 = 3$ and 64 modes for both discretization schemes so that $N_x = N_y = 8$, and $N_\phi = 8$, $N_s = 5$ and $\Delta k_{\text{tail}}/k_0 = 0.4$.

The lateral expansion basis function $g(k_x, k_y, x, y) = \exp[i(k_x x + k_y y)]$ are plane waves defined entirely by the discretized values of the lateral wavenumbers k_x and k_y . To discretize the transverse expansion basis efficiently in a general 3D approach, we generalize the non-uniform strategy used in the rotational symmetric case [48].

First, in the conventional equidistant mode discretization approach, the spatial grid in k -space is given by

$$(k_x^m, k_y^l) = (-k_{\text{cut-off},x} + m\Delta k_x, -k_{\text{cut-off},y} + l\Delta k_y), \quad (3.24)$$

where $\Delta k_\alpha = 2k_{\text{cut-off},\alpha}/(N_\alpha - 1)$ and $m, l = 0, \dots, (N_\alpha - 1)$, with $k_{\text{cut-off},\alpha}$ being the cut-off value of the wavenumber and N_α the number of modes along the $\alpha = x, y$ -axis, see Fig. 3.1. In the following, when we apply the equidistant discretization scheme, we will use identical cut-off values $k_{\text{cut-off},x} = k_{\text{cut-off},y}$ and modes $N_x = N_y$ along the k_x and k_y axes.

Now, the proposed non-uniform circular non-separable discretization approach, which we in the following refer to as the "dartboard" scheme, is defined as follows. We consider the in-plane wavevector in polar coordinates and set N_ϕ rays on equidistantly placed angles, cf. Fig. 3.1. Along each of the rays, the wavenumber

values are sampled so that we use dense sampling in the interval $[0, 2k_0]$ symmetrically placed around k_0 , and in the interval $[2k_0, k_{\text{cut-off}}]$ a fixed step-size Δk_{tail} is used. The symmetric dense mode sampling is defined using a Chebyshev grid [78, 79] as

$$\begin{aligned} k_m &= k_0 \sin(\theta_m), & 1 \leq m \leq N_s/2 \\ k_m &= k_0[2 - \sin(\theta_m)], & N_s/2 + 1 \leq m \leq N_s, \end{aligned} \quad (3.25)$$

where $\theta_m = \frac{m\pi}{N_s+1}$ and N_s is the number of modes in the interval $[0, 2k_0]$. Thus, in the dartboard discretization approach we have four parameters N_ϕ , N_s , Δk_{tail} , and $k_{\text{cut-off}}$. The motivation of using symmetric dense sampling around k_0 is to accurately account for the radiating modes as discussed in detail in [48], and the sampling is further motivated by plotting the contribution to the total emitted field by each wavenumber, similar to Fig. 2 in [48]. Such a plot for an x -oriented dipole embedded in a square waveguide with $w = 1.15\lambda/n_w$ is seen in Fig. 3.2 (see the inset in Fig. 3.3 for a sketch of the structure), where it should be noted that the wavenumbers contributing the most to the emitted field are located on a ring with radius k_0 , which motivates the dense sampling of k -values around the free space wavenumber.

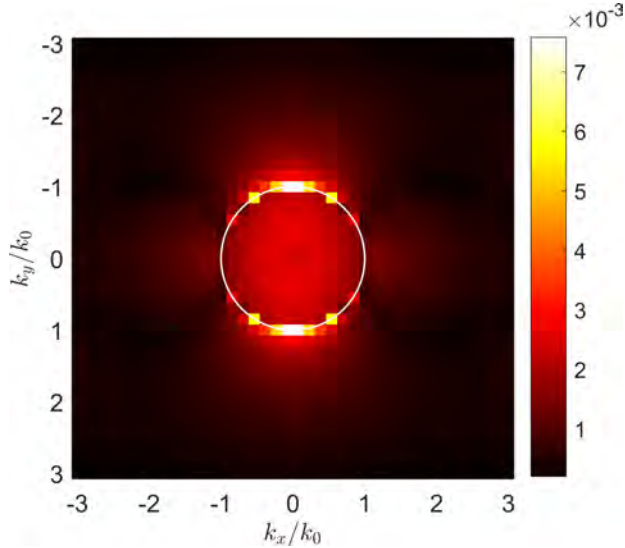


Figure 3.2: The contribution of the wavenumbers to the total emitted field from a point dipole embedded in a square waveguide with side length $w = 1.15\lambda/n_w$. The white ring has a radius of 1, corresponding to the free space wave number. The figure was made using the standard equidistant grid.

In the next section, we show that the dartboard discretization approach outperforms the conventional equidistant mode sampling. As pointed out in [48], the dartboard mode sampling approach described here is not necessarily the universally optimal, and geometry specific variations may be adopted instead. However,

with the proposed approach significant improvement is achieved in terms of the required number of modes and thus of the required computational power. For any geometry a similar plot as in Fig. 3.2 can be made in order to see where a dense sampling of k -values is needed.

3.3 3D oFMM simulations

Now that we have introduced the principles of the oFMM formalism and the non-uniform mode sampling scheme, we will test the performance of our method for two cases: 1) for light emission by a dipole in a square waveguide and 2) the reflection of the fundamental guided mode at a waveguide-metal interface. Both examples are interesting in a nanophotonic engineering perspective, since optimizing the β -factor and the mirror reflection coefficients are important tasks for realising an efficient single-photon source. Furthermore, both examples depend critically on a correct and accurate implementation of the open BCs. We will compare the performance of the dartboard discretization scheme with the equidistant discretization used with Li's factorization rules, and our results will demonstrate that even without the inverse factorization rule the dartboard discretization outperforms the equidistant discretization implemented using Li's factorization rules. As already mentioned, in Appendix B we show how Li's factorization rules are correctly used with the oFMM based on equidistant discretization, whereas the equations implementing the non-separable dartboard discretization used in this chapter are not compatible with the inverse factorization rule.

Dipole emission in a square waveguide

We first investigate light emission in a square waveguide by calculating the emission rates to the guided modes and to the radiation modes. Additionally, we compute the spontaneous emission factor β (not to be confused with the propagation constant β_j) describing the ratio of emitted light coupled to the fundamental guided mode. While typical nanophotonic waveguides support only a few guided modes, the total emission rate and thus the β factor depend on the emission into the continuum of radiation modes leaking out of the waveguide. The strength of the oFMM method becomes apparent when determining the light emission to the radiation modes.

Similar to the investigations presented in [83], we consider a dipole emitter oriented along the x -axis placed on the axis of an infinitely long square waveguide with varying edge length $w_x = w_y$ and refractive index $n_w = 3.5$ surrounded by air. Figure 3.3(a) presents the β factor and the emission rates to the guided modes and to the radiation modes as functions of the waveguide size calculated using the dartboard discretization. The rates are normalized to the bulk emission

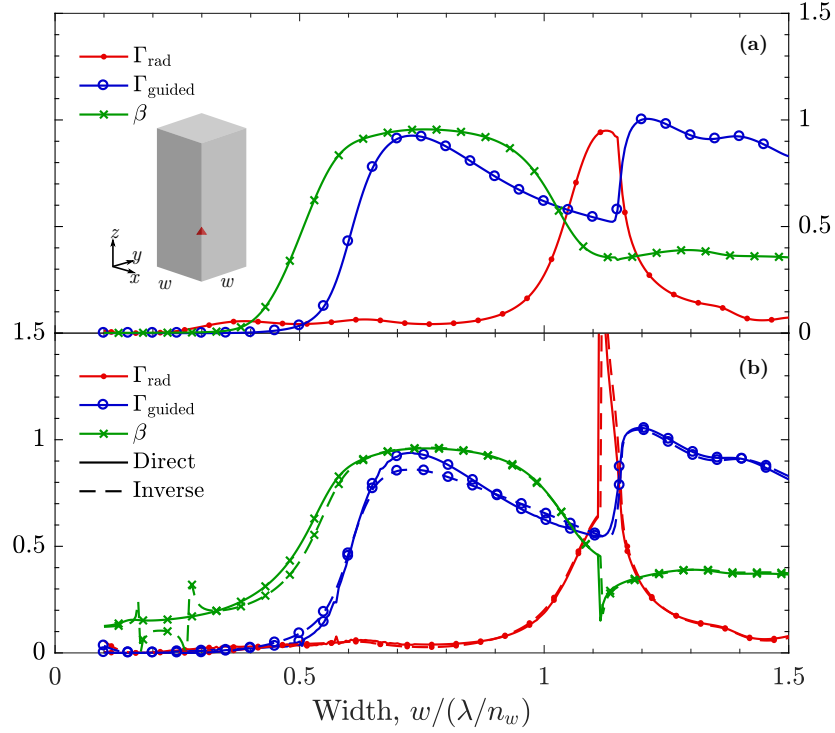


Figure 3.3: Emission from a point dipole placed on-axis of an infinitely long square waveguide having widths $w_x = w_y = w$. The dipole is oriented along the x -axis. (a) The normalized emission to the radiation modes, to the guided modes, and the β factor calculated using the dartboard discretization scheme with $N_\phi = 14$, $N_s = 180$, $k_{\text{cut-off}}/k_0 = 15$, and $\Delta k_{\text{tail}}/k_0 = 0.06$. (b) The corresponding data calculated using conventional square sampling and applying both the direct and Li’s inverse factorization rules with $N_x = N_y = 80$ and $k_{\text{cut-off}}/k_0 = 15$. The wavelength used in the calculations is $\lambda = 1 \mu\text{m}$. The total number of modes are (a) 5558, and (b) 6400.

rate (see Section 2.5). Figure 3.3(b) shows the same properties of the waveguide calculated using an equidistant square sampling using either the direct or the inverse factorization rules. The emission rate to the guided modes calculated with the three approaches agree well, however, a clear difference is seen in the emission rate to the radiation modes and therefore also in the β factor. In particular, the coupling to the radiation modes exhibit a spike around a normalized width of 1.15 with the square sampling, which gives an unphysical kink in the β factor. The discretization parameters used in Fig. 3.3 are given in the figure caption and were selected as a result of the convergence investigations presented in the following.

To further investigate the performances of the three approaches we fix the waveguide geometry by setting the width to $w = 1.15\lambda/n_w$ and vary the cut-off value of the transverse wavenumber as well as the number of modes. This waveguide size

is selected for the convergence investigations since a clear difference of the results is seen for this diameter in Fig. 3.3. Figures 3.4(a) and (b) show the convergence investigations of the total emission rate as a function of the cut-off value with several different mode numbers for the equidistant and dartboard discretization respectively, while Fig. 3.4(c) shows the convergence of the total emission rate as a function of the number of modes N_s in the interval $[0, 2k_0]$ for the dartboard discretization scheme. The dartboard approach shows clear convergence around a cut-off of $\approx 15k_0$. In contrast, the equidistant discretization scheme does not guarantee convergence even with cut-off value of $30k_0$. We have set a soft limit on the memory requirement to 30 gigabyte (Gb) in order for our simulations to start fairly quickly on our HPC cluster. The maximum number of modes used in the calculation of Fig. 3.4(a,b,c) roughly correspond to this limit, however, in Figs. 3.4(b,c) the convergence is obtained before the maximum number of modes is used.

When using the equidistant discretization, numerical artifacts in the form of large oscillations are observed at particular values of the number of modes and cut-off as displayed in Figs. 3.3(b) and 3.4(a) (as well as in Figs. 3.5(b) and 3.6(a)). As discussed in Appendix B.3, the oFMM together with the equidistant square discretization scheme mathematically corresponds to having periodic BCs and to using a Fourier series expansion, where the periodic lengths of the computational domain are inversely proportional to Δk_x and Δk_y^2 . For geometries with periodic BCs, destructive or constructive interference due to light emission in the neighboring periodic elements may occur leading to the observed large oscillations of the emission rates, that thus are an inherent consequence of the equidistant discretization scheme.

A common approach to circumvent these artifacts due to periodic BCs is to use artificial absorbing BCs, often in the form of the so-called perfectly matched layers (PMLs) [51, 53]. However, for the modal method with a PML BC, the convergence of the emission properties with the PML parameters towards the open geometry limit [54, 70] is not well-established with errors in some cases as high as $\approx 20\%$ [50]. In contrast, the oFMM with the efficient discretization scheme relies on a truly open computational domain, and therefore avoids using artificial or periodic BCs leading to improved accuracy and convergence towards the true open geometry limit.

Reflection from a dielectric waveguide-metal interface

As a second example, we investigate convergence of the method for a structure consisting of an infinite waveguide standing on top of a metallic mirror by computing the reflection coefficient of the fundamental guided mode from the

²You could argue that our open boundary conditions are actually periodic for the equidistant grid.

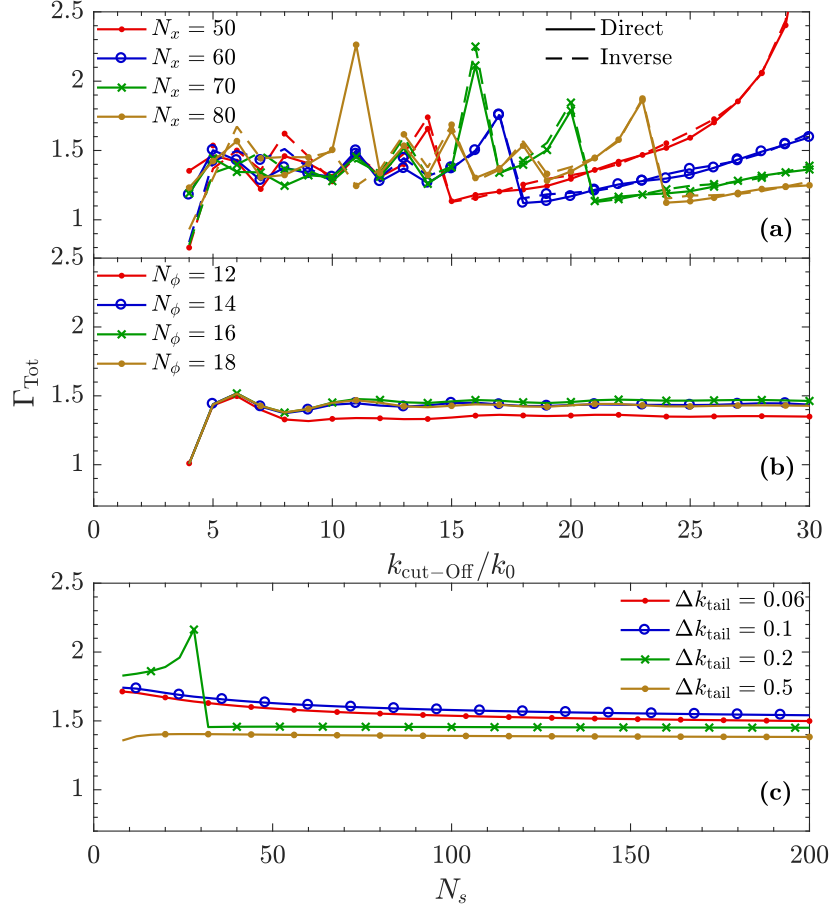


Figure 3.4: Convergence comparison of the total emission rate using the three approaches for a waveguide $w/(\lambda/n_w) = 1.15$. (a) The total emission rate for the equidistant discretization as a function of the cut-off value computed with the number of modes shown in the legend using the direct factorization rule (solid line) and the inverse factorization rule (dashed line). (b) The emission rate as a function of the cut-off value computed using the dartboard mode sampling and the number of angles shown in the legend with $N_s = 140$ modes on the symmetric radial part with $\Delta k_{\text{tail}}/k_0 = 0.2$. (c) The emission rate as function of the number of modes N_s in the symmetric sampling part computed using the dartboard mode sampling with a fixed number of angles $N_\phi = 16$ and cut-off value $k_{\text{cut-off}}/k_0 = 13$.

waveguide-metal interface. The refractive indices of the waveguide and metal are $n_w = 3.5$ and $n_{\text{Ag}} = \sqrt{-41 + 2.5i}$ at the wavelength $\lambda = 1 \mu\text{m}$.

Figure 3.5 shows the calculated reflection coefficient as a function of the waveguide size $w_x = w_y$ using (a) the dartboard sampling and (b) the equidistant discretization employing the direct and inverse factorization rules with several different number of discretization modes. The cut-off in all cases is $k_{\text{cut-off}}/k_0 =$

14. Furthermore, for the dartboard discretization fixed values of $N_\phi = 14$ and $\Delta k_{\text{tail}}/k_0 = 0.2$ were used and only N_s was varied. These parameters were chosen to achieve convergence according to the investigations discussed in the next paragraph. In narrow waveguides, the reflection coefficients are essentially determined by the air-metal reflection ($R_{\text{Air-Ag}} \approx 0.98$) since in this limit the fundamental mode is mainly localized in the air surrounding the waveguide. In contrast, in the limit of large waveguides the fundamental mode is primarily confined in the GaAs waveguide ($R_{\text{GaAs-Ag}} \approx 0.95$). A dramatic difference in the results is seen in the region around $w/(\lambda/n_w) \approx 0.6$, where the reflectivity drops due to a surface-plasmon mediated coupling predominantly to radiation modes [84]. When a substantial amount of light is propagating in the x - y plane, the performance of the open boundary conditions becomes critical, and comparison of Figs. 3.5(a) and 3.5(b) clearly demonstrates that this scattering is better resolved using the dartboard discretization.

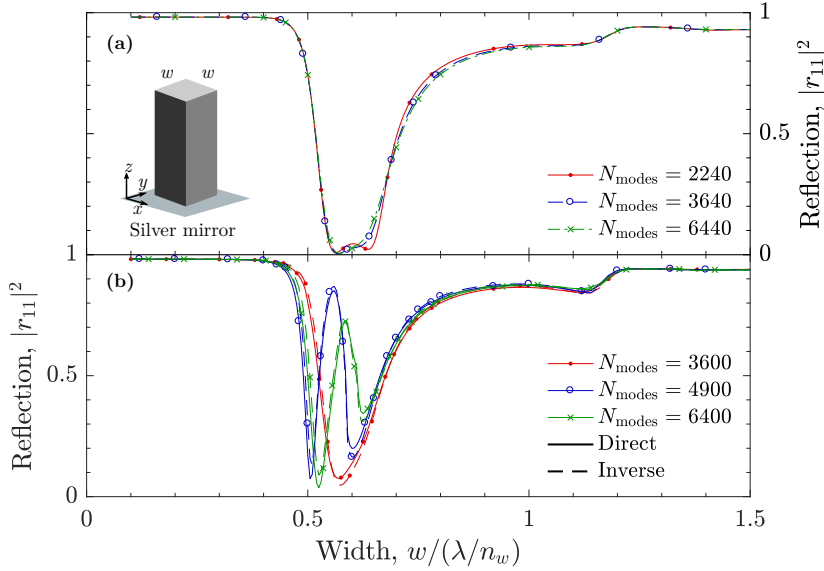


Figure 3.5: The reflection of the fundamental waveguide mode from a metal mirror calculated using (a) the dartboard discretization and (b) the equidistant discretization. The cut-off in both cases is $k_{\text{cut-off}}/k_0 = 14$, and for the dartboard discretization fixed values of $N_\phi = 14$ and $\Delta k_{\text{tail}}/k_0 = 0.2$ were used. The legends show the total number of modes used.

Whereas the reflection coefficients in Figs. 3.5(a) and (b) are obtained for a fixed cut-off value, we now fix the geometry and study the effect of the cut-off value of k_m . We select a waveguide width of $w_x = w_y = 0.63\lambda/n_w$, since Fig. 3.5(b) reveals this to be a challenging computational point. The convergence investigation is shown in Fig. 3.6. The dartboard discretization (Figs. 3.6(b,c)) again leads to convergence with respect to all of the four discretization parameters. In contrast, no clear convergence is seen when using the equidistant discretization, while we

also in this case approach the performance limit of our HPC cluster computer. As discussed in the previous section, the peaks observed in Figs. 3.5(b) and 3.6(a) are a consequence of the periodicity of the computational domain when using the equidistant discretization scheme.

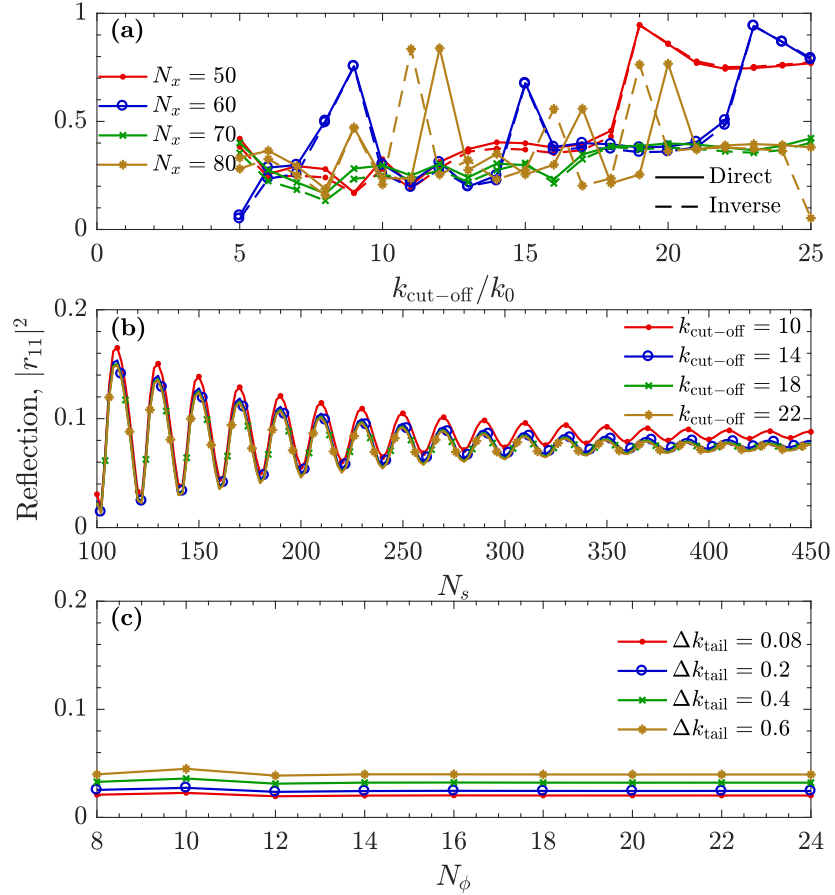


Figure 3.6: Convergence of the reflection of the fundamental waveguide mode from a metal mirror. (a) The reflection as function of the cut-off value with number of modes shown in the legend using the direct factorization rule (solid line) and the inverse factorization rule (dashed line). (b) The reflection as function of the number of modes in the symmetric sampling part using the dartboard mode sampling with fixed $N_\phi = 14$ and $\Delta k_{\text{tail}}/k_0 = 0.2$, and cut-off value shown in the legend. (c) The reflection as function of the number of angles using the dartboard mode sampling with fixed $k_{\text{cut-off}}/k_0 = 14$ and $N_s = 100$, and $\Delta k_{\text{tail}}/k_0$ shown in the legend. Note the different scaling between (a) and (b-c).

3.4 Discussion

The convergence checks in the selected waveguide examples presented in Figs. 3.4 and 3.6 show that our method converges for the investigated waveguide sizes and structures. The non-separable nature of our discretization scheme prevents the use of Li's factorization rules, but even when using the standard direct factorization, a clear improvement in the performance is obtained using the proposed dartboard discretization scheme compared to the conventional equidistant discretization of the basis functions. Although these examples do not guarantee the convergence of our method for all imaginable waveguide sizes and geometries, we generally expect our method to deliver improved performance for various types of waveguides, possibly with additional geometry specific modifications to the discretization scheme.

In high-index-contrast structures as the examples presented here, the FMM, due to the difficulty of resolving large discontinuities using a plane wave expansion, generally requires a significant amount of modes to achieve convergence. Whereas this may not be a computational difficulty in a rotational symmetric case which in the lateral plane reduces to a 1D problem, the size of the eigenvalue problem in the general planar 2D case rapidly explodes when the number of modes are increased [50]. Thus, we expect that a further improvement in terms of computational efficiency could be obtained by combining the dartboard discretization scheme with an adaptive spatial coordinate scheme [85] or by introducing a semi-analytical approach for defining the eigenmodes. In the rotationally symmetric case, exact analytical descriptions of the eigenmodes exist [82], while in the rectangular case approximate solutions [86] could be used.

Additionally the formalism as presented in this chapter is limited to handle ridge waveguides surrounded by a bulk material. As shown in Appendix B.5 the formalism cannot correctly handle a ridge waveguide on a substrate, which experimentally is a very interesting structure, due to its very low transmission losses [87] and potentially large β -factor [88]. This limits the applications of our formalism in its current form, however we have an ongoing project on how to develop our formalism to handle substrate supported structures.

3.5 Conclusion

We have generalized the recently reported open geometry Fourier modal method formalism relying on open boundary conditions and a non-uniform circular "dartboard" k -space sampling for general 3D systems with a uniform background material, allowing e.g. the modeling of rectangular waveguides. By applying open boundary conditions, we avoid using the artificial absorbing BCs. We have demonstrated the efficiency of the approach by investigating dipole emission in

a square waveguide structure and by studying the reflection coefficient of the fundamental waveguide mode for a waveguide-metal mirror interface, that both are problems of fundamental interest when designing nanophotonic devices. We expect that our new method will prove useful in accurate modeling of a variety of nanophotonic structures, for which correct treatment of an open boundary is crucial.

Part II

Applied nanophotonics engineering

Spectral symmetry of Fano resonances in a waveguide coupled to a microcavity

In the previous chapter, we considered a ridge waveguide surrounded by air in order to develop an open-geometry Fourier modal method for the 3D Cartesian coordinate system. However, in this chapter we consider a photonic crystal (PhC) membrane structure consisting of a waveguide-coupled microcavity blocked by a partly transmitting element (PTE) (see Fig. 4.1) using a 2D Fourier modal method with periodic BCs [46].

This structure represent an attractive platform for applications that can exploit the strong sensitivity of the transmission to the resonance frequency of the cavity. Due to the large ratio of quality factor to mode volume of PhC cavities [89], even small refractive index perturbations within the volume occupied by the cavity mode lead to significant transmission changes. This fact has been used to demonstrate ultra-low energy all-optical signal processing [90] as well as chemical- and biological sensing [91]. It was shown in 2002 [92] how a Fano resonance [93] can be achieved in PhC structures, which further improves the wavelength sensitivity, due to the asymmetric lineshape (see. Fig. 4.2) of the transmission/reflection spectrum. The interference between a discrete and con-

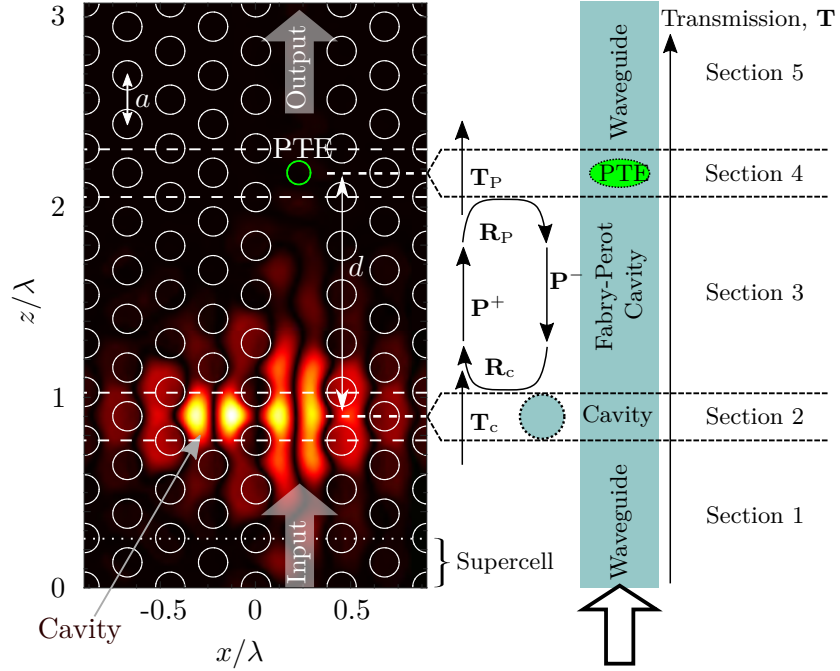


Figure 4.1: Left: PhC structure and field plot ($|H_y|$) at the minimum transmission frequency for the PhC Fano structure with hole radius $r = 0.30a$, PTE radius $r_{PTE} = 0.80r$, Fabry-Perot length $d = 5a$, refractive index of background material $n_b = 3.1$ and refractive index of air holes $n_h = 1$. The supercell for the first section is illustrated by the dotted white line, and the section interfaces are indicated with the dashed white lines. Right: Schematic of the structure with transmission, reflection and propagation matrices indicated, where the full PhC structure is divided into five sections.

tinuum of states, which leads to Fano resonances, was implemented with a low- and high- Q cavity structure for switching purposes [94]. Recently a simpler geometry [95] was proposed, and it was demonstrated that the shape and amplitude of the transmission can be controlled [10]. Furthermore, carving-out short pulses from long duration input pulses has been demonstrated in PhC Fano structures as reported in Ref. [11], without the use of any control signal.

In this chapter, we expand on these results by showing how both the parity and shape may be manipulated in a way that is easily controlled experimentally. We define the parity to denote whether the minimum of the transmission spectrum is red or blue shifted relative to the maximum, as illustrated in Fig. 4.2. It is generally not well understood what determines the parity of a Fano resonance, so in this chapter we determine the decisive parameter for a specific case. The case is the situation where the PTE and microcavity form a Fabry-Perot resonator, where we demonstrate that the roundtrip phase determines the parity. This conclusion arises from treating the structure with a single-mode model. However, as we will show, the single-mode description breaks down, when the PTE is moved

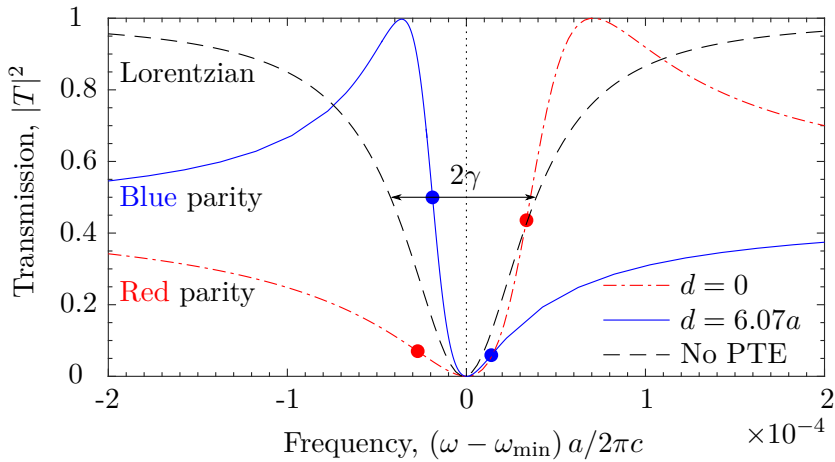


Figure 4.2: Transmission spectra for $d = 0a$ (red parity), $d = 6.07a$ (blue parity) and for the microcavity only, where the geometry of the PhC structure is seen in Fig. 4.1. The point with maximum slope on each side of the transmission minimum are indicated with solid markers for the two Fano spectra. The linewidth of the Lorentzian spectrum is 2γ .

close to the microcavity due to the influence of evanescent modes. In that case, a simple model for determining the parity of the Fano resonance is currently not available.

The results presented in the following chapter have been published in Ref. [96] (J1), and thus all citations of the chapter should be directed towards the journal article. In the work presented the author implemented the 2D Fourier modal method in Matlab, conducted all simulations, and wrote the first draft of the manuscript. The work is a continuation of the author's M.Sc. thesis [97], where the modal method was implemented in Matlab and the first initial results were produced. However, all figures and results presented in Ref. [96] and in this chapter have been produced during the author's Ph.D. studies and are thus not found in the M.Sc. thesis [97].

The chapter is organized as follows. In Section 4.1 we briefly introduce the Fourier-based Bloch mode expansion technique used for computing the transmission spectra of the structure. Section 4.2 compares the results obtained by using the numerically exact multi-mode (full) model with the approximative single-mode model. We pinpoint what controls the parity (symmetry) of the Fano transmission spectra in Section 4.3 and end the chapter with a conclusion.

4.1 Computational framework

As stated above, we define the parity to denote whether the minimum of the transmission from the input to the output waveguide is red or blue shifted relative to the maximum, as demonstrated in Fig. 4.2. Different physical mechanisms cause the cavity resonance shift to be either positive or negative. In optical signal processing, it is essential whether the resonance shift causes an increase or decrease in transmission, depending on the preferred modulation format. Since this is determined by the parity of the resonance, our investigated structure is easily transferred between applications, where different signs of the resonance shift are demanded.

Figure 4.1 shows the investigated structure consisting of a microcavity adjacent to a waveguide containing a partially transmitting element (PTE), which was also a key element in previous proposals [10, 92, 95]. By shifting the position of the PTE, both the parity and shape of the transmission spectrum can be controlled. The PTE is realized by a hole placed in the center of the waveguide and the microcavity is here realized as a simple point defect, i.e., a missing hole¹. The distance between the microcavity and the PTE is d , and a is the PhC lattice constant. In [92] a different structure consisting of a microcavity placed in the center of a Fabry-Perot cavity composed of two PTEs was investigated with a single-mode transfer matrix formalism. It was concluded that whether the transmission spectrum is asymmetric (Fano-shaped) or symmetric (Lorentzian-shaped) depends on the spectral position of the microcavity resonance frequency relative to the Fabry-Perot background. In this chapter, we consider a different structure without a Fabry-Perot background. We describe the shape of the transmission spectrum as a function of the distance d using a full multi-mode model, and we show that the single-mode transfer matrix model in [92] breaks down in the short distance limit.

The structure investigated here is two-dimensional (2D) (invariant along y), and we use a Fourier-based Bloch mode expansion technique for simulating the transmission [46, 50, 98, 99]. Though convergence issues for this technique was recently reported in Ref. [37] for calculating Q -factors and resonance wavelengths of L5 and L9 PhC cavities, we can safely use the technique for our 2D structure, since we only need to resolve refractive index discontinuities in one dimension². The structure is divided into periodic sections as shown in the right part of Fig. 4.1, each with a distinct supercell and set of Bloch modes, and the expansions are coupled together with a Bloch mode S-matrix algorithm [46]. Thus, we have direct access to the individual Bloch modes and their reflection and transmission

¹The microcavity can be realized in different ways. For example by displacing the PhC holes or by reducing the size of one hole.

²As opposed to the previous chapter, where we had to resolve the discontinuities in both the x - and y -direction.

coefficients, which plays a key role in the analysis to be presented here. The Bloch modes are determined in each section as in [46, 99] and the electromagnetic field is expanded on these Bloch modes as

$$\mathbf{F}_w(r) = \sum_m \left(a_{wm} \Psi_{wm}^{F+}(\mathbf{r}_\perp, z) + b_{wm} \Psi_{wm}^{F-}(\mathbf{r}_\perp, z) \right), \quad (4.1)$$

where $\mathbf{F}_w(r)$ is either the electric ($\mathbf{E}_w(r)$) or magnetic ($\mathbf{H}_w(r)$) field in the w th section and a_{wm} [b_{wm}] is the amplitude of the m th forward (+ z) [backward ($-z$)] propagating Bloch mode, $\Psi_{wm}^{F+[-]}(\mathbf{r}_\perp, z)$. The Bloch modes are expanded on backward and forward travelling eigenmodes at position z' [46, 50] as

$$\Psi_{wm}^{F\pm} = \sum_j^N \left[c_{mj}^\pm \mathbf{f}_{qj}^+ \exp[i\beta_j(z - z')] + d_{mj}^\pm \mathbf{f}_{qj}^- \exp[-i\beta_j(z - z')] \right], \quad (4.2)$$

where q is the layer index within section w and $c_{mj}(d_{mj})$ are the expansion coefficients for the j 'th forward (backward) travelling eigenmode ($\mathbf{f}_{qj}^{+(-)}$). This equation holds for z -values within the q 'th layer. In order to get the full Bloch mode for all z -values we refer to [46, 50], where the method is discussed in more detail. The eigenmodes in Eq. (4.2) are expanded as Fourier series, which inherently leads to periodic boundary conditions in contrast to the method developed in Chapter 3 and the method used in Chapters 5 and 6, where open boundary conditions are used. However, for a PhC waveguide periodic boundary conditions in the x -direction are sufficient due to the photonic bandgap. This ensures that the field has decayed before reaching the computational boundary, thereby minimizing the influence of the boundary on the computational results. Furthermore, since the computations presented in this chapter is for a 2D PhC we do not have any boundaries in the y -direction.

The transmission and reflection of the microcavity (PTE) section are computed by considering sections 1-3 (3-5), and using the scattering matrix formalism on this reduced geometry. This effectively reduces the full five-section geometry to a three-section geometry consisting of three waveguide sections (1, 3 and 5) coupled through the transmission and reflection matrices of the microcavity ($\mathbf{T}_c, \mathbf{R}_c$) and PTE ($\mathbf{T}_P, \mathbf{R}_P$) sections. Thereby, the total transmission from input to output in Fig. 4.1 is given as [46]

$$\mathbf{T} = \mathbf{T}_P \mathbf{P}^+ (\mathbf{I} - \mathbf{R}\mathbf{T})^{-1} \mathbf{T}_c, \quad (4.3)$$

$$\mathbf{R}\mathbf{T} \equiv \mathbf{R}_c \mathbf{P}^- \mathbf{R}_P \mathbf{P}^+, \quad (4.4)$$

where the matrices \mathbf{P}^+ and \mathbf{P}^- represent propagation in section 3 by the length of an integer number of supercells in the forward and backward direction, respectively. From Eq. (4.3) it is clear that the structure in Fig. 4.1 can be thought

of as a Fabry-Perot cavity, where the microcavity constitutes a highly dispersive mirror, and this interpretation was previously used to propose an ultra-high speed laser structure [35, 100] and recently the self-pulsing of a photonic crystal Fano laser was demonstrated experimentally [9] and explained theoretically in [101]. When the mirror distance, d , is small enough for the PTE to lie inside the neighbouring supercell of the microcavity, the Fabry-Perot interpretation no longer makes sense, since this interpretation requires a waveguide supercell to be in-between the supercells of the PTE and the microcavity. In this case the structure will instead be divided into 3 or 4 sections (see Fig. 4.1) and the total transmission matrix takes a different form.

The transmission spectra for different cavity-PTE distances, d , are computed using Eq. (4.3) and a measure of the degree of parity, DoP, is defined as the difference between the numerical maximum slope of the transmission spectrum before and after the transmission minimum (see the solid markers on the spectra in Fig. 4.2):

$$\text{DoP} = \frac{2\pi c}{a} \left[\max \left(\left| \frac{\partial T}{\partial \omega} \right|_{\omega < \omega_{\min}} \right) - \max \left(\left| \frac{\partial T}{\partial \omega} \right|_{\omega > \omega_{\min}} \right) \right]. \quad (4.5)$$

With this definition, a positive (negative) DoP corresponds to blue (red) parity, and in Fig. 4.3, the DoP is plotted for different cavity-PTE distances, where the points are color-coded according to the parity. It is apparent that the parity and shape of the transmission spectrum can be engineered by the position of the PTE relative to the microcavity, and very large slopes are achievable. An example of this is seen in Fig. 4.2 with $d = 6.07a$, where the spectral distance between the maximum and minimum is seen to not be limited by the microcavity linewidth, 2γ , as is the case for previously proposed structures with $d = 0$ [10, 95]. A shorter spectral distance between the maximum and minimum can be obtained, but not while requiring $\max(|T|^2) = 1$ for our investigated structure.

4.2 Single- versus multi-mode model

The relative position of the transmission maximum and minimum results from the interference between many Bloch modes bouncing back and forth between the mirrors, as described by Eq. (4.3). Generally, it is not obvious how to determine the parity by direct inspection of this matrix equation. However, for sufficiently large d , the coefficients in \mathbf{P}^\pm corresponding to evanescent modes are exponentially damped. For single-mode PhC waveguides, which we restrict the following analysis to, only one element from the propagation matrices has a significant contribution and therefore all other elements can be neglected. This

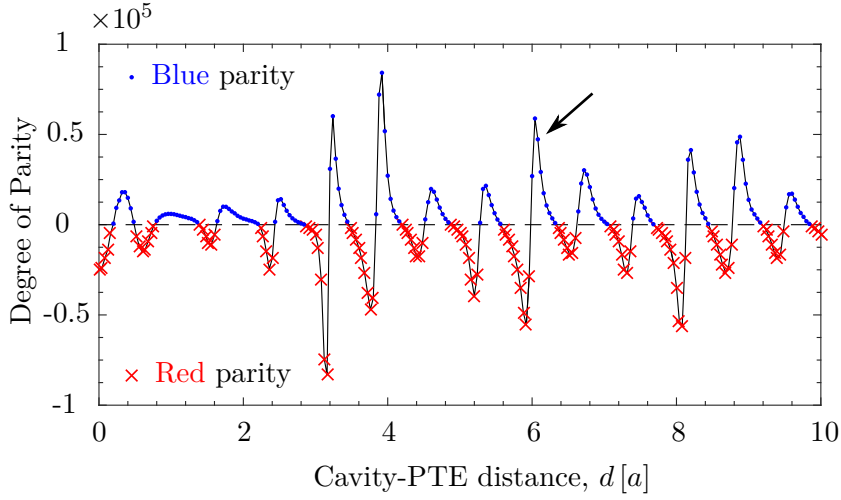


Figure 4.3: The degree of parity, DoP, (defined in Eq. (4.5)) as function of the cavity-PTE distance, d . The data points are color-coded according to the parity and the black curve connecting the points serves as a guide to the eye. The arrow indicates the DoP for the transmission spectrum with $d = 6.07a$ in Fig. 4.2.

reduces the transmission Eqs. (4.3) and (4.4) to scalar equations:

$$T = T_P P^+ (1 - RT)^{-1} T_c, \quad (4.6)$$

$$RT = R_c P^- R_P P^+, \quad (4.7)$$

where the (1,1) matrix elements are taken from the full matrices in Eqs. (2) and (3), since these couple and propagate the guided mode in the three waveguide sections³.

In Fig. 4.4, the transmission spectra found from Eqs. (4.3) - (4.4) (full model) and from Eqs. (4.6) - (4.7) (single-mode) are compared for four different cavity-PTE distances. At the smallest distances (top panel), the single-mode model predicts the correct parity, but otherwise deviates visibly from the numerically preciser spectra, e.g. with a clear offset of the spectral position of the transmission minimum. As the distance is increased to $d = 4a$ (bottom panel, blue curves), the agreement between the numerically exact and the single-mode model becomes substantially better, and at the largest distance considered here, $d = 5a$, (bottom panel, magenta curves) the agreement is almost perfect. The mismatch between the full and the single-mode model is due to the influence of evanescent Bloch modes in the Fabry-Perot region. A similar behavior was observed in [102] in describing transmission between a ridge waveguide and a slow light PhC waveguide, and in [103] in analyzing PhC Ln cavities. In Chapter 6 we show the breakdown of a single-mode model in describing the Purcell enhancement of

³The same enumeration of the modes as in [46] has been used.

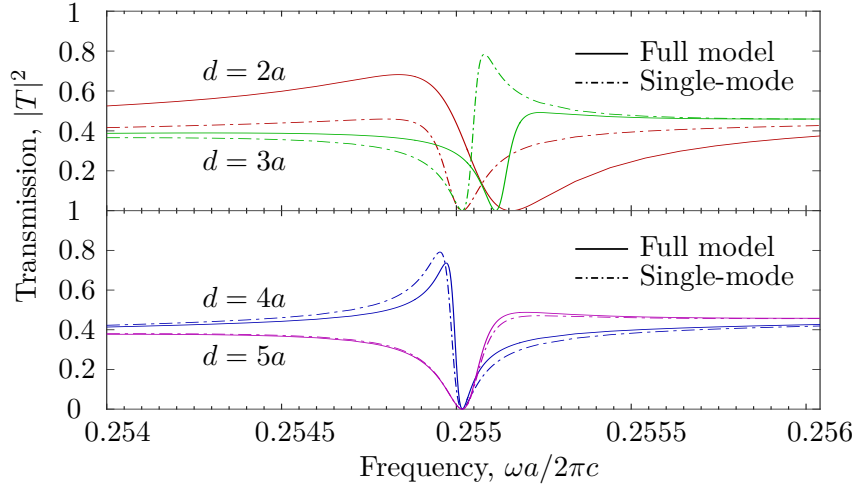


Figure 4.4: Transmission spectra for cavity-PTE distances $d = 2, 3, 4$ and $5a$ using Eq. (4.3) (full model, solid curves) and Eq. (4.6) (single-mode, dash-dotted curves).

a dipole emitter placed in a truncated nanowire (nanopost) standing on a gold-silica mirror, and for that system we find that the breakdown is due to coupling to both radiation modes⁴ and evanescent modes.

The minimum transmission frequency is shifted for $d = 2a$ and $d = 3a$ compared to $d = 4a$ and $d = 5a$ in Fig. 4.4, which does not seem intuitive, since the transmission of the guided Bloch mode through the microcavity section is zero at the resonance frequency of the microcavity for all $d \geq 2a$. However, the scattering of the guided Bloch mode at the microcavity section will populate evanescent Bloch modes in the Fabry-Perot section. For large Fabry-Perot lengths the population of the evanescent Bloch modes will vanish before reaching the PTE and no scattering will occur. But for small distances there will be a finite population of the evanescent Bloch modes at the PTE, where they will scatter and populate the guided Bloch mode in section 5, resulting in a finite overall transmission of the guided Bloch mode from section 1 to 5 at the resonance frequency of the microcavity. This effect causes the shift of the transmission minimum for structures with small cavity-PTE distances.

To render Eqs. (4.6) - (4.7) more easily interpretable, we write the propagation constants and T - and R -coefficients as follows:

$$P^+(\omega) = P^-(\omega) = \exp(ik(\omega)L), \quad (4.8)$$

$$T_P(\omega) = t_P(\omega) \exp(i\phi_{t,P}(\omega)), \quad (4.9)$$

$$R_P(\omega) = r_P(\omega) \exp(i\phi_{r,P}(\omega)), \quad (4.10)$$

$$R_c(\delta) = \frac{\gamma}{-i\delta + \gamma} = \frac{\gamma}{\sqrt{\delta^2 + \gamma^2}} \exp(i\phi_{r,c}(\delta)), \quad (4.11)$$

⁴We do not have any radiation modes in our 2D PhC structure.

$$T_c(\delta) = \frac{-\delta}{-i\delta + \gamma} = \frac{-\delta}{\sqrt{\delta^2 + \gamma^2}} \exp(i\phi_{t,c}(\delta)), \quad (4.12)$$

where L is the distance between the microcavity and PTE sections, $k(\omega)$ is the dispersion of the guided Bloch mode in the PhC waveguide, $\phi_{t(r),P}$ are the phases related to transmission and reflection at the PTE, $t_P = |T_P|$ and $r_P = |R_P|$ are the transmission and reflection amplitudes for the PTE, and $\delta = \omega - \omega_{\min}$ is the detuning. Finally γ is half the linewidth of the transmission spectrum of the microcavity (see Fig. 4.2), which equals the coupling rate between the microcavity and the waveguide. The microcavity reflection phase is derived from Eq. (4.11) and the result is $\phi_{r,c} = \arctan(\delta/\gamma)$. Using this and Eq. (4.6) we find:

$$\begin{aligned} |T|^2 &= \frac{|T_P|^2 |T_c|^2}{1 + |R_P|^2 |R_c|^2 - 2|R_P||R_c| \cos(2kL + \phi_{r,P} + \phi_{r,c})} \\ &= \frac{t_P^2 \delta^2}{\delta^2 + (1 + r_P^2)\gamma^2 - 2r_P\gamma\sqrt{\gamma^2 + \delta^2} \cos(\Phi_{RT})}, \end{aligned} \quad (4.13)$$

where the frequency dependence of all parameters has been suppressed, and $\Phi_{RT} = 2K\delta L + 2k(\omega_{\min})L + \phi_{r,P} + \arctan(\delta/\gamma)$ is the phase of the roundtrip as a function of detuning for a waveguide with *linear* dispersion, where $1/K$ is the group velocity

$$v_g = \frac{1}{K} = \frac{\partial\omega}{\partial k} = \frac{\delta}{\Delta k}. \quad (4.14)$$

In the single-mode limit, the transmission vanishes exactly at the resonance frequency of the microcavity, i.e. at zero detuning $\delta = 0$, which is evident from Eqs. (4.12) and (4.13).

4.3 Parity of Fano resonances

Figure 4.5 shows the phase of the roundtrip element RT in Eq. (4.7) at the frequency of minimum transmission, ω_{\min} , as a function of d . The blue (red) dots (crosses) correspond to the structure having blue (red) parity, where the parity is found from the full computation using Eq. (4.3). From our definition of parity in Eq. (4.5) it follows that the transition between blue and red parity occurs when the transmission spectrum is an even function of the detuning, δ . Eq. (4.13) shows that this can only be achieved, if $\cos(\Phi_{RT}(\delta))$ is also even, which occurs when $\Phi_{RT}(\delta)$ is odd, corresponding to $\Phi_{RT}(\omega_{\min}) = 0 + p\pi, p \in \mathbb{Z}$. Since the transition only happens at these values, the parity must have the same sign in the intervals $\Phi_{RT} \in]0; \pi[$ and $]-\pi; 0[$, which Fig. 4.5 confirms. The parity of the transmission spectrum is therefore completely determined by the roundtrip phase at the transmission minimum.

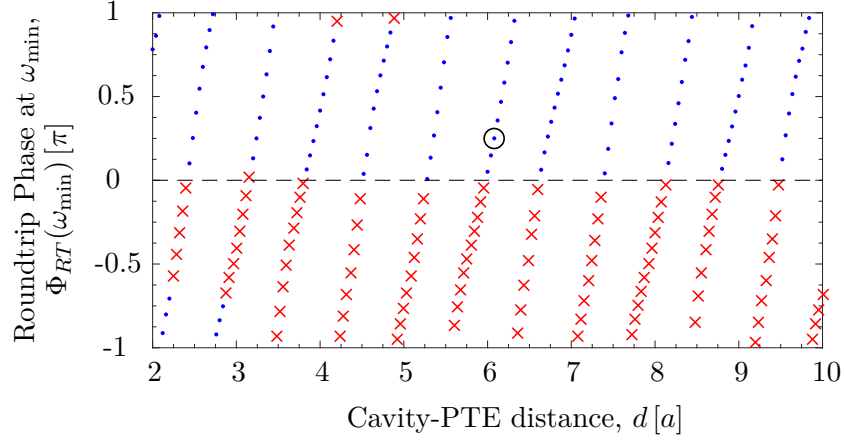


Figure 4.5: Phase of the roundtrip matrix element given in Eq. (4.7) for different cavity-PTE distances. Each point has been color coded according to the parity of the numerically exact transmission spectrum (obtained from Eqs. (4.3-4.4)), such that **red** parity structures are marked by **red** crosses and **blue** parity structures are marked with **blue** dots. The black circle indicates the chosen cavity-PTE distance used for Fig. 4.6.

However, the above explanation assumes that the transmission and reflection coefficients for the PTE, $t_p(\omega)$ and $r_p(\omega)$, are independent of frequency, which is generally not the case. This frequency dependence contributes to the asymmetry of the transmission spectra, but as seen in Fig. 4.5 the effect is very small, since the roundtrip phase at ω_{\min} predicts the right parity for all simulations with $d > 5a$. Furthermore, the above explanation assumes a linear dispersion, and thus a frequency independent group velocity. If, in turn, the structure is operated closer to the band edge of the waveguide, where the group velocity depends strongly on frequency, this would also affect the symmetry and could potentially be used as an additional parameter to engineer the shape of the transmission spectrum.

Since the parity depends on the roundtrip phase, it is possible to flip the sign of the DoP by changing $\Phi_{RT}(\omega_{\min})$, which can be done by applying a pump pulse to the waveguide region in the Fabry-Perot cavity as in [104]. This is shown in Fig. 4.6, where the transmission computed from Eq. (4.13) is plotted using the parameters for $d = 6.08a$ for $\Phi_{RT}(\omega_{\min}) = 0$ and $\pm\pi/4$. For this to be possible in an efficient way, the spectral distance between the maximum and minimum transmission points should be as small as possible. The investigated structure is not optimal, since it requires a total phase shift of $\sim \pi/2$ for switching the DoP and maintain $\max(|T|^2) = 1$. Reducing the linewidth, 2γ would increase the slope and thus reduce the required phase shift for flipping the DoP, while maintaining $\max(|T|^2) = 1$.

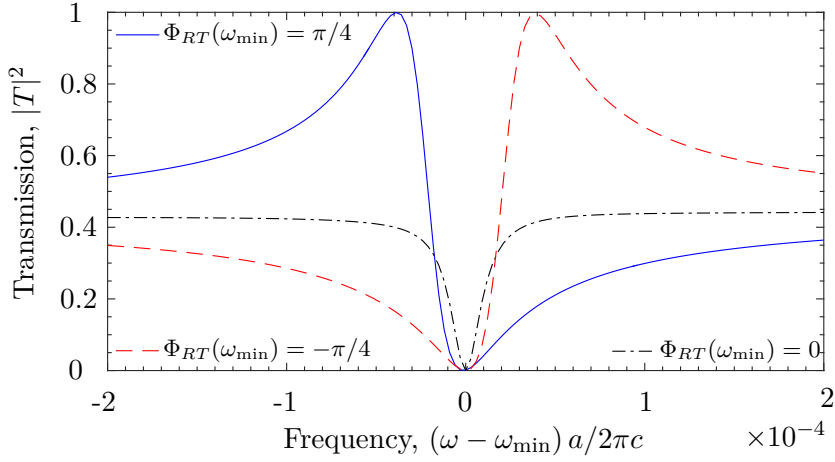


Figure 4.6: Transmission spectrum for $\Phi_{RT}(\omega_{\min}) = \pi/4$ (blue solid), $\Phi_{RT}(\omega_{\min}) = 0$ (black dot-dashed) and $\Phi_{RT}(\omega_{\min}) = -\pi/4$ (red dashed), where all other parameters are those for $d = 6.08a$.

4.4 Conclusion

We have analyzed the transmission spectrum of a photonic crystal microcavity coupled to a partially-blocked waveguide using a 2D Fourier-based Bloch mode expansion technique. We showed that the structure displays Fano resonances and that the symmetry of these can be controlled by varying the distance between the microcavity and the partially transmitting element. For sufficiently large distances, a single-mode description accurately describes the shape of the transmission spectrum, and in this limit it was shown that the phase of the roundtrip within the Fabry-Perot cavity determines the parity of the Fano resonance. This limit was identified to be at $d \simeq 5a$ for the investigated structure. The breakdown of the single-mode description for $d < 5a$ is due to the increasing influence of evanescent Bloch modes for smaller Fabry-Perot cavities. The possibility of fully tailoring the Fano resonance in photonic crystal microcavity-waveguide structures might find applications in, for example, optical signal processing and sensing.

Our results suggest that the shape of the transmission can be made extremely sensitive to changes in the roundtrip phase. It is therefore interesting to investigate whether the structure is more susceptible to refractive index changes in the waveguide, rather than in the microcavity, which is conventionally used [10, 90, 92, 94, 95].

All-optical mapping of the position of single quantum dots embedded in a nanowire antenna

Up to this point in the present thesis, we have considered structures with Cartesian geometry. In this chapter we turn our attention to rotationally symmetric structures. Thus neither the 3D oFMM developed in Chapter 3 or the 2D Fourier-Based Bloch mode expansion technique used in Chapter 4 is suitable. Therefore we will use the oFMM method for cylindrical structures developed in Ref. [48] as the work horse for the numerical simulations in the present chapter.

As briefly touched upon in the introduction to the present thesis (Chapter 1), quantum emitters, such as semiconductor quantum dots (QDs), embedded into photonic nanostructures form the basis of modern solid-state quantum optics [12]. Semiconductor QDs embedded into tapered nanowires has been demonstrated as a promising platform for obtaining bright quantum light emission, due to its efficient out-coupling into a directive Gaussian shaped free-space beam [27, 32, 105–107]. As opposed to cavity based single-photon sources (SPS), this waveguide approach offers a broad operation bandwidth enabling widely strain-tunable SPS [105, 108], as well as bright sources of entangled photon pairs [18, 109]. The Gaussian shaped output beam delivered by tapered single-mode nanowires [61, 62]

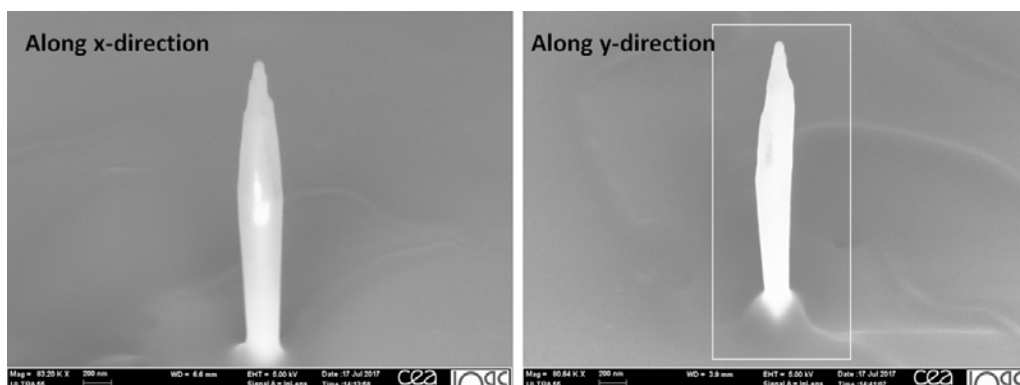


Figure 5.1: SEM image of the needle structure under study in this chapter. The needle is not perfectly rotational symmetric, however we model it as being so. It will be apparent later in the chapter, that even with this approximation a good agreement between our simulations and experimental results is obtained.

enables efficient coupling to a single-mode fiber, either using free-space optics [62] or through direct 'butt' coupling [110].

The emitter position in a photonic nanowire has a huge impact on the device performance. Besides governing the strength of the light-matter interaction it affects the coherence properties of the emitter as well. Recently, a strong dependence of the optical linewidth of QD emission on thermal vibrations of the nanowire was demonstrated [111]. In particular, the coupling to flexural modes features a steep spatial dependence, which was used for position mapping of QDs in trumpet nanowires in [112]. Furthermore, the potential impact of surface states is still to be explored for nanowire structures, and this likely depends on the distance between the QD and the sidewall. Thus, precise mapping of the QD position is crucial for further understanding and optimization of this light-matter interface. Conventional optics is not applicable here since the dimensions of the structure are below the diffraction limit, and thus other methods such as the one presented in [112] should be considered. The QD mapping technique in [112] relies on the coupling of QDs to flexural modes, however this technique will strongly rely on the specific mechanical properties of the nanowire structure, and is probably not as precise for nanowires with needle out-coupling tapers as compared to nanowires with trumpet out-coupling tapers.

In this chapter, we present a novel all-optical technique to precisely map the position of individual self-assembled InAs QDs embedded in a needle nanowire (a SEM image of the structure under investigation is seen in Fig. 5.1). Our approach is non-destructive and exploits interferences associated with the simultaneous excitation of two guided modes¹ having different transverse field profiles. Through

¹One mode is actually a semi-guided radiation mode.

spectrally-resolved Fourier microscopy, we resolve this interference in the far-field angular profile for individual QDs. Comparing the experimental data with numerical simulations based on an approximative model geometry yields the emitter position with uncertainties of 8-15 nm on the distance to the nanowire axis and 9-14 nm for the azimuthal position of the QDs under investigation. These numbers are way below the diffraction limit.

The present chapter is a product of my external stay at CEA Grenoble with Julien Claudon. All experimental results presented in the chapter is a result of the hard work by Romain Fons, Joël Bleuse and Julien Claudon at CEA, whereas all simulations and the comparison between the simulated and experimental results has been carried out by the author. A joint publication is currently in review at Nano Letters (J5).

The chapter is organized as follows. In Section 5.1, we briefly present the open-geometry Fourier modal method (oFMM) in cylindrical coordinates [48], which is the workhorse for all simulations presented in this chapter. Furthermore, we present the basic physics of the nanowire. Section 5.2 presents our near-field to far-field transformation implementation in the oFMM formalism, as well as a discussion on how to treat the far-field from different excitonic complexes in a QD. The experimental setup used for the far-field measurements is presented in Section 5.3, and in Section 5.4, we outline the simulation procedure followed by a numerical comparison between the simulated and measured far-fields. Based on this, we conclude on the position of the QDs. The chapter ends with an overall conclusion of the work presented.

5.1 Nanowire physics

A nanowire is in this thesis generally defined as a cylindrical semiconductor wire supporting up to a few guided modes. The number of guided modes in a nanowire is determined by the diameter, the refractive index contrast to the environment and the wavelength [113].

Open-geometry Fourier modal method for cylindrical geometries

We model cylindrical structures using the open-geometry Fourier modal method (oFMM) in cylindrical coordinates presented in Ref. [48], where the electromagnetic field is expanded on a set of eigenmodes. This method is ideal for treating nanowires, since each angular momentum is treated separately giving access to all modes of the nanowire. An emitter placed in the nanowire will through emission produce a field, which is a superposition of the eigenmodes in the nanowire. In the oFMM the emitted field is written as

$$\mathbf{F}(r, \phi, z) = \sum_{n=-N}^N \sum_j a_{nj}(r_{\text{PD}}) \mathbf{f}_{nj}(r) \exp(in\phi) \exp(i\beta_{nj}z), \quad (5.1)$$

where \mathbf{F} is either the total electric (\mathbf{E}) or magnetic (\mathbf{H}) field, n is the order of the angular momentum, j is the mode index, a_{nj} is the dipole coupling coefficient of each mode, $\mathbf{f}_{nj}(r)$ is the electric ($\mathbf{e}_{nj}(r)$) or magnetic ($\mathbf{h}_{nj}(r)$) field for the j 'th eigenmode with angular momentum n and r_{PD} is the position of the point dipole (emitter). The dipole coupling coefficient is calculated as in [48] by using the Lorentz reciprocity theorem [46] and is for orthonormal eigenmodes given as

$$a_{nj}(r_{\text{PD}}) = \frac{i\omega \mathbf{p} \cdot \mathbf{e}_{nj}(r_{\text{PD}})}{2}, \quad (5.2)$$

where \mathbf{p} is the dipole moment. Here it should be noted that the dipole coupling coefficient is dimensionless, and thus a unit of watts has been thrown away through normalization.² The eigenmodes in each z -invariant layer are expanded on a Bessel function basis as [48, 75]

$$f_{r,nj}(r) = i \sum_{m=1}^M k_m \Delta k_m [b_{njm}^f J_{n+1}(k_m r) - c_{njm}^f J_{n-1}(k_m r)], \quad (5.3a)$$

$$f_{\phi,nj}(r) = \sum_{m=1}^M k_m \Delta k_m [b_{njm}^f J_{n+1}(k_m r) + c_{njm}^f J_{n-1}(k_m r)], \quad (5.3b)$$

where $b(c)_{njm}^f$ are the eigenmode expansion coefficients and J_n is the n 'th order Bessel function of the first kind. The eigenmode mode expansion coefficients are computed for each z -invariant layer using the technique outlined in [48] and [75], which is similar to the Cartesian case presented in Chapter 3. The normalized spontaneous emission (SE) rate of the dipole emitter is computed using Eq. (3.20) with the dipole coupling coefficients in Eq. (5.2) and the eigenmodes in Eqs. (5.3). For a structure varying along the propagation direction (i.e. the z -direction) the eigenmodes in each z -invariant layer are coupled through the scattering matrix formalism [46], and the reflection and transmission matrices between adjacent layers are found by matching the boundary conditions as in Chapter 3 [46].

Modes of the nanowire

Three classes of modes exist in the nanowire, which are classified by their propagation constant as listed in Eq. (3.19). There is always a discrete number of guided modes, however there is a continuous set of radiation and evanescent

²If you go through the derivation in Ref. [46], you will see that the units are lost through evaluation of integrals of delta functions.

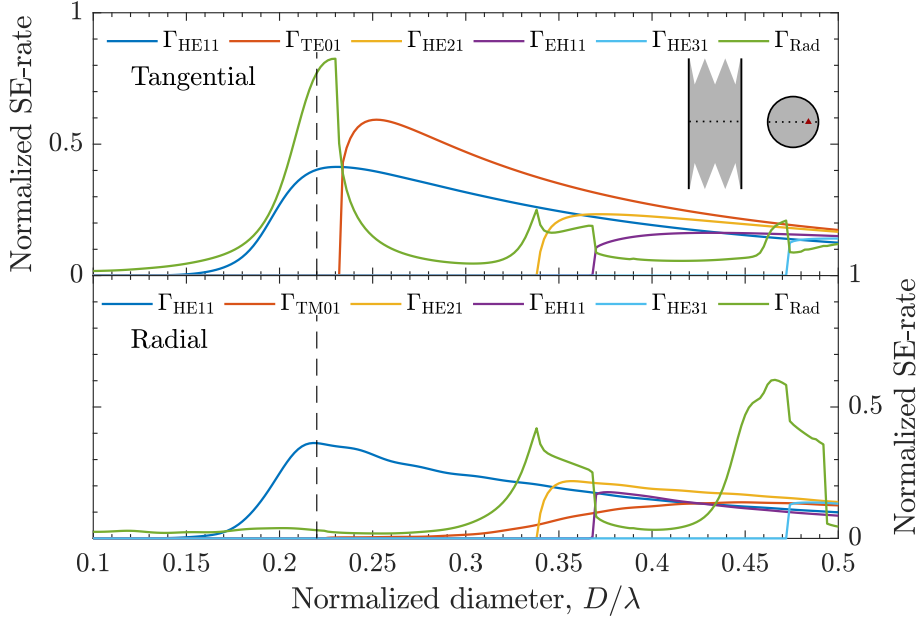


Figure 5.2: The normalized spontaneous emission rate into the guided and radiating modes of a tangential (top) and radial (bottom) oriented dipole in a GaAs nanowire with $n_{\text{GaAs}} = 3.46$ as function of the diameter normalized to the emission wavelength. The dipole is placed $0.6R$ off axis, where $R = D/2$, as indicated in the inset. The black dashed line indicate $D/\lambda = 0.22$, which is roughly the ratio of the QDs embedded in the needle nanowire in Fig. 5.1.

modes. One way to characterize the nanowire is to embed a point dipole and calculate the SE rate into each mode of the nanowire. From Eqs. (5.1-5.3) it is seen that a dipole placed on-axis (i.e. $r_{\text{PD}} = 0$) will only couple to modes with angular momentum $n = \pm 1$ ³, whereas an off-axis dipole will couple to all modes with all angular momenta and thus provide a good overview of which modes are confined in the nanowire. The spontaneous emission (SE) rate for a dipole emitter at $r_{\text{PD}} = 0.6R_{\text{NW}}$ as function of the diameter-wavelength ratio D/λ of a GaAs nanowire with $n_{\text{GaAs}} = 3.46$ is seen in Fig. 5.2, where R_{NW} is the radius of the nanowire.

An important thing to notice in Fig. 5.2 is that the SE rate into radiation modes rises just before the next guided mode is supported by the nanowire and quickly drops again after the guided mode has been dragged into the nanowire. This feature was also seen in Chapter 3 in Fig. 3.3 and in Refs. [48, 80, 114] and is an important aspect, when computing the far-field emission pattern of single-mode tapered nanowires, since the radiation modes are not always emitting directly

³This is realized by setting $r = 0$ in Eqs. (5.3), and use that only Bessel functions of order $n = \pm 1$ is non-zero, when evaluated at $r = 0$: $J_n(0) = 1$ for $n = \pm 1$ and $J_n(0) = 0$ for $n \neq \pm 1$.

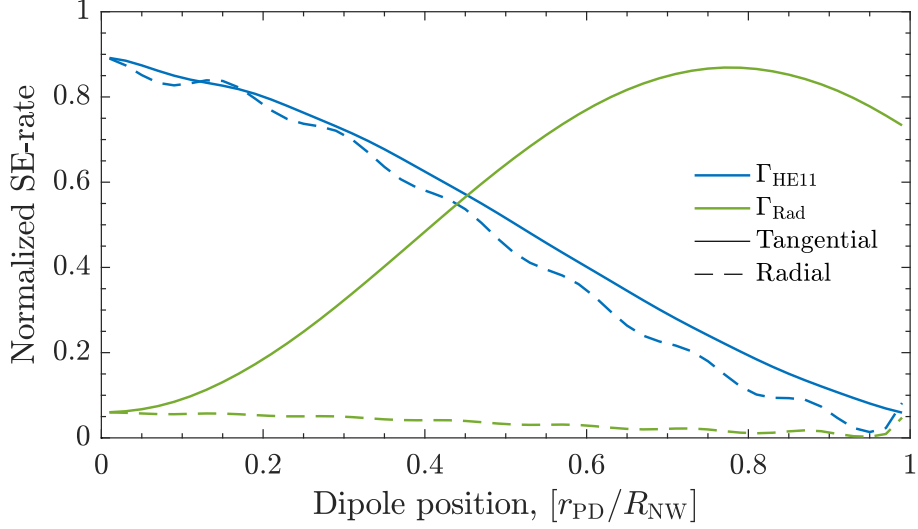


Figure 5.3: The normalized SE rate for a dipole emitter at 910 nm in a nanowire with a diameter of 200 nm as function of the radial position of the dipole. The SE rate is plotted for radially and tangentially oriented dipole moments.

to the sides of the nanowire, but can also be semi-guided by the nanowire and thus contribute significantly in the far-field. The same feature has been observed experimentally in Ref. [115] for ZnO needle nanowires, where the total radiation intensity was found to oscillate with increasing diameter of the nanowire.

In this study we are investigating the GaAs needle nanowire shown in Fig. 5.1 with a diameter D of around 200 nm and emission wavelengths $\lambda = 891.5, 907$ and 912 nm, meaning that $D/\lambda \approx 0.22$ in Fig. 5.2, which is indicated with the black dashed line. As seen only the HE11 mode is guided, however the large SE rate into the radiation modes are mostly into what we denote a TE01-like radiation mode, which at a slightly larger diameter becomes the guided TE01 mode. The normalized SE rate as function of the dipole position r_{PD} is seen in Fig. 5.3, and here it is evident that the radiation modes are TE01-like showing a similar dependence on the radial position of the dipole. Thus a QD placed at two different radial positions in the nanowire will couple differently to the HE11 mode and the radiation modes, and this should be visible in their far-field radiation pattern. However, the far-field pattern is not only dependent on the radial position of the QD, but also on the height of the nanowire, due to the different propagation constants of the modes, which will change their interference pattern along the nanowire. This point will be evident later in the present chapter.

5.2 Near-field to far-field transformation

The oFMM method used in this study is used to compute the near-field of the needle in Fig. 5.1. In order to compute the far-field we need to use the near-field to far-field transformation out-lined in Section 2.6 and use the field expansions in Eqs. (5.3). We consider the two cases $n \neq 0$ and $n = 0$ separately, and for $n \neq 0$ insertion of Eqs. (5.3) into Eqs. (2.24) lead to the following very simple equations

$$N_{\theta,nj} = 4(-i)^n \pi \cos \theta \cos(n\phi) \sum_{m=1}^M \Delta k_m (b_{mjn}^H - c_{mjn}^H) \delta(k_m - k_0 \sin \theta), \quad (5.4a)$$

$$N_{\phi,nj} = 4(-i)^n \pi \sin(n\phi) \sum_{m=1}^M \Delta k_m (b_{mjn}^H + c_{mjn}^H) \delta(k_m - k_0 \sin \theta), \quad (5.4b)$$

$$L_{\theta,nj} = -4(-i)^{n-1} \pi \cos \theta \sin(n\phi) \sum_{m=1}^M \Delta k_m (b_{mjn}^E - c_{mjn}^E) \delta(k_m - k_0 \sin \theta), \quad (5.4c)$$

$$L_{\phi,nj} = 4(-i)^{n-1} \pi \cos(n\phi) \sum_{m=1}^M \Delta k_m (b_{mjn}^E + c_{mjn}^E) \delta(k_m - k_0 \sin \theta), \quad (5.4d)$$

where $\delta(k_m - k_0 \sin \theta) = 1/\Delta k_m$, when $k_m = k_0 \sin \theta$ and zero otherwise. Insertion of Eqs. (5.4) into Eqs. (2.20) gives the far-field for each mode j with angular momentum $n \neq 0$. The total far-field is computed in the standard way as a summation over all modes weighted by the modal excitation coefficient a_{nj} . In Eqs. (5.4) it is apparent that each in-plane k_m value corresponds to one angle in the far-field. The full derivation of Eqs. (5.4) is found in Appendix A.2. For the case of $n = 0$, we have two different polarizations that need to be treated separately as discussed in Appendix A.2, and in the end we arrive at these expressions for TE and TM polarization

$$N_{\theta,j,\text{TM}} = 2i\pi \cos \theta \sum_{m=1}^M \Delta k_m [b_{m,j}^H - c_{m,j}^H] \delta(k_m - k_0 \sin \theta), \quad (5.5a)$$

$$N_{\phi,j,\text{TE}} = 2\pi \sum_{m=1}^M \Delta k_m [b_{m,j}^H + c_{m,j}^H] \delta(k_m - k_0 \sin \theta), \quad (5.5b)$$

$$L_{\phi,j,\text{TE}} = -2i\pi \cos \theta \sum_{m=1}^M \Delta k_m \left[b_{m,j}^E - c_{m,j}^E \right] \delta(k_m - k_0 \sin \theta), \quad (5.5c)$$

$$L_{\phi,j,\text{TM}} = -2\pi \sum_{m=1}^M \Delta k_m \left[b_{m,j}^E + c_{m,j}^E \right] \delta(k_m - k_0 \sin \theta). \quad (5.5d)$$

The remaining components are $N_{\theta,j,\text{TE}} = N_{\phi,j,\text{TM}} = L_{\phi,j,\text{TM}} = L_{\phi,j,\text{TE}} = 0$. Using these expressions in Eqs. (2.20) gives the far-field for TE and TM polarization. It should be stressed that the above equations are only valid for dipoles emitting linearly polarized light, since these couple equally to modes with opposite angular momentum, i.e. the excitation of a mode with $+n$ equals the excitation of the same mode with angular momentum $-n$. However, for emitters producing circularly polarized light (as is the case for a trion state [12]) the dipole does not couple equally to $\pm n$ angular momentum, and the far-field equations presented in this thesis are no longer valid. If a dipole producing circularly polarized light is to be treated correctly, the angular momentum with opposite sign should be treated individually by using an angular dependence of the form $\exp(in\phi)$ in Eqs. (2.23) and the derivations in Appendix A should be redone.

Far-field from quantum dot exciton

Due to the epitaxial growth of the QDs embedded in the needle nanowire in Fig. 5.1, their dipole moment is oriented in the transversal plane [116], and thus in the oFMM formalism we only need to consider tangentially and radially oriented dipoles. As seen from Eq. (5.2), the dipole coupling coefficient is given by a dot product between the dipole moment and the electric field of the eigenmode, and thus depends on the dipole orientation of the exciton state in the QD.

Several excitonic states exist in a QD, and the photons emitted through the corresponding radiative recombination processes have different frequencies and polarizations [12]. If a neutral exciton recombines, the emitted photon will be linearly polarized, however if a charged exciton (trion state) recombines, it will lead to circularly polarized light, where the helicity is determined by the spin of the additional carrier [12, 117]. The spin state of the excitons and trions in Fig. 5.4 are [12]

$$|X_b\rangle = \frac{1}{\sqrt{2}} (|\uparrow\downarrow\rangle + |\downarrow\uparrow\rangle), \quad (5.6a)$$

$$|Y_b\rangle = \frac{1}{\sqrt{2}} (|\uparrow\downarrow\rangle - |\downarrow\uparrow\rangle), \quad (5.6b)$$

$$|X^-\rangle_{\alpha_h} = |u_v\rangle^* |\alpha_h\rangle \otimes \frac{1}{\sqrt{2}} (|\uparrow\downarrow\rangle - |\downarrow\uparrow\rangle), \quad (5.6c)$$

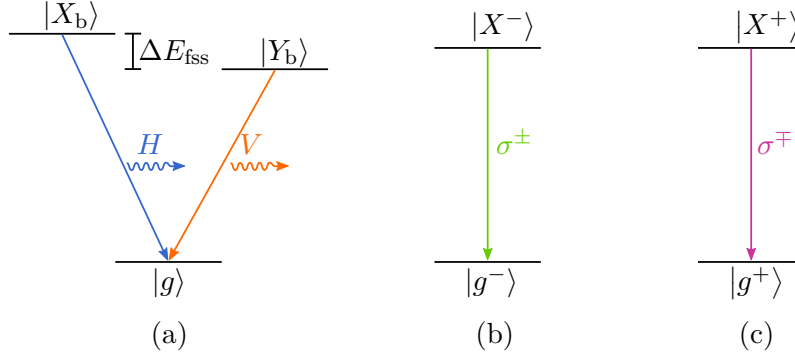


Figure 5.4: A few of the radiative transitions in a QD. (a) Recombination of an electron-hole pair in an exciton leads to emission of either a horizontally or vertically polarized photon. The two energies are separated by the fine structure splitting ΔE_{fss} . A circularly polarized photon is emitted through recombination of an electron-hole pair in (b) a negative trion state or (c) a positive trion state.

$$|X^+\rangle_{\alpha_e} = \frac{1}{\sqrt{2}} (|\uparrow\downarrow\rangle - |\downarrow\uparrow\rangle) \otimes |u_c\rangle |\alpha_e\rangle, \quad (5.6d)$$

where $|\alpha_{e(h)}\rangle$ is the spin state of the electron (hole) in the positive (negative) trion state, and $|u_{c(v)}\rangle$ is the electronic Bloch function evaluated at the Γ point of the conduction (valence) band [12]. Thus it seems, that our technique for determining the position of the QDs depend on the addressed exciton in the needle nanowire. However, in the experiment each emitted photon is either the result of one particular relaxation process (e.g. $|X_b\rangle$ to $|g\rangle$) or the orthogonal process (e.g. $|Y_b\rangle$ to $|g\rangle$), and never the coherent superposition of the two. When the far-field is detected, the image is built up as the ensemble average of many detection events, which then is the balanced (50/50) incoherent sum of the detected power profile resulting from two orthogonally polarised dipoles. The balance between the two orthogonal states is due to our non-resonant excitation scheme and the large spin relaxation rate in InAs QDs [118] (the experimental details will be given in the following section). This means that the far-field consists of an incoherent sum of the two emitter polarizations, and as derived in Appendix C.4 the incoherent sum of the two trion states produces the same far-field as the incoherent sum of the two bright excitons

$$P_{\text{Tot}} = P_{X^+}^{\downarrow} + P_{X^+}^{\uparrow} = P_{X^-}^{\downarrow} + P_{X^-}^{\uparrow} = P_{X_b} + P_{Y_b} = P^{p^r} + P^{p^\phi}, \quad (5.7)$$

where P_{Tot} is the total emitted power, $P_{X(Y)}$ is the power emitted by each excitonic state and $P^{p^{r(\phi)}}$ is the power emitted by a radially (tangentially) oriented dipole. Strictly speaking, the power emitted from the different transitions are not necessarily the same, since their transition frequency will differ. However, the expression suggests, that they can be modelled in the same way using a radial and

tangential dipole, and thus we only need to know the wavelength of the emitted photon and not which exciton transition it originates from. This fact proves a certain generality to our position mapping technique, meaning that we are not limited by, whether the emission originates from recombination of trion or neutral exciton states, since both are treated in the same way in the simulations.

5.3 Experimental setup

The needle nanowire is placed in a cryostat at 4K in order to reduce thermal fluctuations of the energy levels in the QDs. The QDs are excited non-resonantly with a CW laser at $\lambda_{\text{Exc}} = 825 \text{ nm}$. The population of the QD levels are thus not controlled, and after non-radiating relaxation processes we have populated biexcitons, neutrally charged excitons or charged trion states in the QD. A photon is emitted through a recombination of an electron and a hole, and the polarization of the emitted photon depends on the excited quantum state [12].

The emitted photon is guided by the GaAs nanowire and adiabatically leaves the nanowire through the tapered needle section [27, 63] and is collected by an objective with a numerical aperture (NA) of 0.75. The emitted light is directed by a lens towards a half-wave plate and a polarizer, for polarization controlled measurements. Then a band-pass filter enables measurement at specific wavelengths, such that each transition in each QD can be addressed individually ⁴. A second lens focusses the emitted light onto a CCD camera, where the far-field emission pattern is measured. The experimental setup is schematically shown in Fig. 5.5.

A standard photoluminescence (PL) experiment reveals the spectrum of the QDs in the needle nanowire, and the spectrum is seen in Fig. 5.6. Based on the PL spectrum we have chosen to focus this study on three QDs with emission wavelengths 891.5 nm (QD1), 907 nm (QD2) and 912 nm (QD3). Due to the non-resonant excitation of the QDs we have no control over which states are populated, and thus when we filter out a single peak in the PL spectrum we do not know which transition it originates from. The fine structure splitting (fss) of the energy levels in a neutral exciton can be found through polarization controlled PL measurement, by exploiting the orthogonal polarizations of the two bright exciton transitions. Thus if the peak of the PL spectrum changes, when rotating the polarizer, it is a good indication that the transition stems from a neutral exciton, however if the peak is independent of the polarizer angle additional experiments are needed to conclude on the origin of the emission.

The PL spectra for different rotations of the polarizer are seen in Figs. C.2-C.4 in Appendix C.2 for QD1, QD2 and QD3. A fss is observed for QD1 and

⁴This is of course in the ideal case. It happens, that the QD transitions are practically inseparable if their energies are too close to each other.

QD2 indicating that the emission from these QDs are from a neutral exciton - this conclusion is supported by the biexponential trend of the time-resolved PL measurement seen in Figs. C.6(a-b) in Appendix C.3. However, we do not observe any fss for QD3, which is either because the transition we measure is not from a neutral exciton or because the fss is too small to resolve in the polarized PL spectrum shown in Fig. C.4 in Appendix C.2. A vanishing fss is possible if the QD is laterally very symmetric, and is thus not a unique indicator of the exciton transition. The time-resolved PL measurement of QD3 in Fig. C.6(c) shows a quasi-exponential behaviour⁵, however the lifetime is a factor 2 larger than for QD1 and QD2. A trion state should have a shorter lifetime than a neutral exciton [119]. The longer lifetime can be explained by a fast spin-flip rate within QD3, which makes the slow decay rate dominant and dilutes the biexponential behaviour [118, 120]. Thus we conclude that the QD3 emission probably originates from a neutral exciton. The details of this analysis is found in Appendix C.3.

We measure the far-field radiation pattern by adding two images taken for two waveplate angles that differ by 45° in order to account for the strongly polarization dependent transmission of the band-pass filter in Fig. 5.5. Furthermore, due to the non-resonant excitation scheme, the two bright excitons (or the two spin configurations of each trion state) will be equally populated, since any polarization memory of the excitation laser is lost, due to our non-resonant excitation scheme [118]. As derived in Appendix C.4 the contributions from the two bright excitons (or trions) should be added incoherently, meaning that the far-field *power* from the two in-plane dipole orientations are added, when computing the far-field

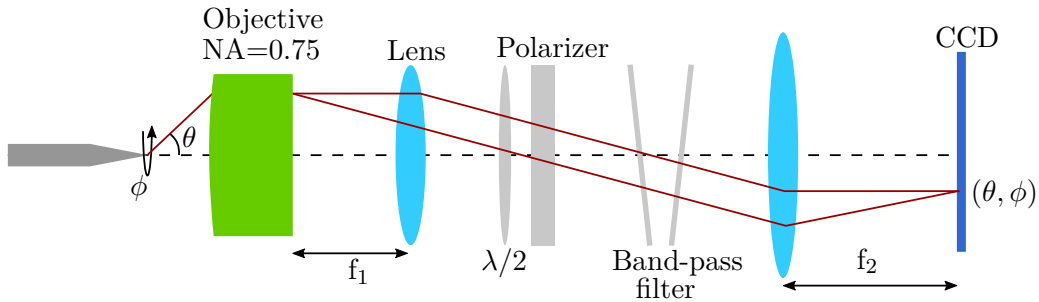


Figure 5.5: Illustration of the experimental setup for measuring the far-field emission pattern of the needle nanowire. The needle nanowire is placed inside a cryostat, and the QDs are excited non-resonantly at 825 nm. The emitted light is collected with an objective and focused onto a CCD camera, where the far-field pattern is measured. The half-wave plate and the polarizer are for polarization controlled measurements and the band-pass filter is used for measuring on a single transition in a single QD.

⁵Quasi-exponential meaning that the biexponential behaviour is dominated by one decay rate.

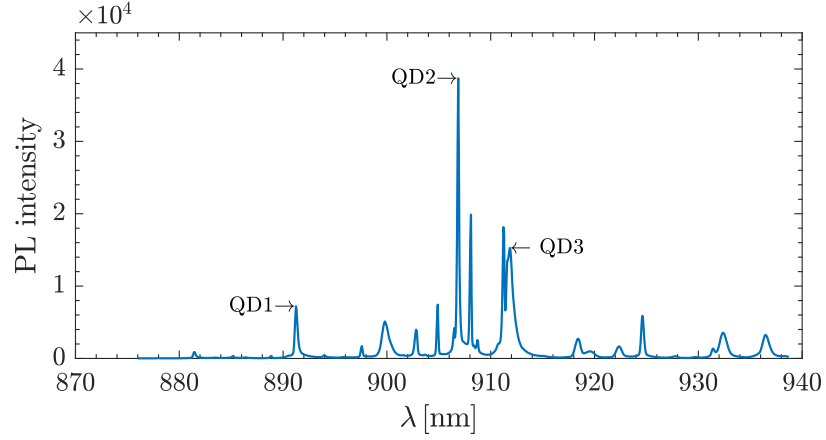


Figure 5.6: PL spectrum of the needle nanowire. As seen several QD transitions are visible in the spectrum. We have chosen to focus this study on QD1, QD2 and QD3.

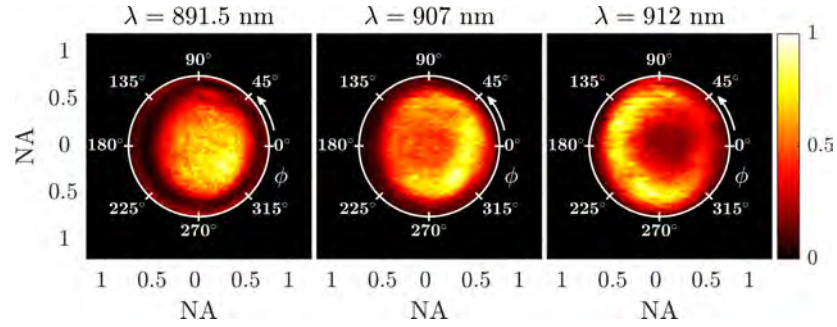


Figure 5.7: The raw measured far-field for QD1 (891.5 nm), QD2 (907 nm) and QD3 (912 nm) normalized with their maximum pixel value. The white circle indicate a numerical aperture of 0.75. The x - and y -axes are given in $NA = |\sin \theta|$.

in the oFMM formalism. Due to the large spin relaxation rate in InAs QDs and our non-resonant excitation scheme [118], the population of the $|X_b\rangle$ and $|Y_b\rangle$ excitons will be equal and thus the two dipole orientations in the oFMM formalism has the same amplitude, meaning that we can use the expression given in Eq. (5.7) when computing the far-field. Fig. 5.7 shows the far-field for the three QD transitions. The diversity of the measured far-fields patterns indicate different positions of the QDs in the nanowire, providing a first hint of the extreme sensitivity of this physical property on the QD position. In the following section, we will compare the measured far-fields with our simulations and conclude on the position of each of the QDs.

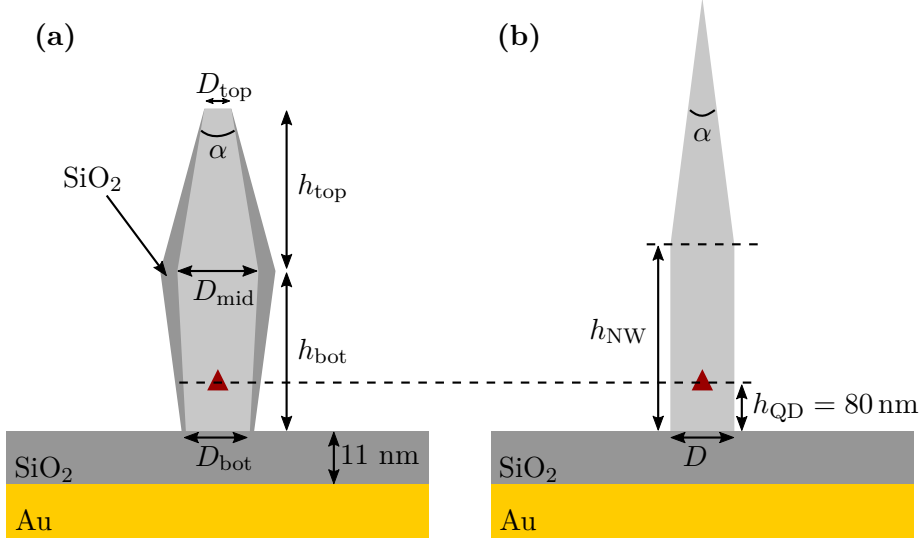


Figure 5.8: (a) Model description of the exact geometry assuming rotational symmetry, where $D_{\text{bot}} = 200$ nm, $D_{\text{mid}} = 218$ nm, $D_{\text{top}} = 74$ nm, $h_{\text{bot}} = 1450$ nm, $h_{\text{top}} = 1365$ nm and $\alpha = 6^\circ$. The thickness of the passivation layer is 2 nm at the bottom, 37 nm in the middle and 0 nm at the top. The QDs are placed 80 nms above the bottom mirror and the thickness of the SiO₂-layer is 11 nm. (b) Sketch of the simulated structure emulating the model structure in (a). h_{NW} is the length of the straight nanowire section and the diameter, D , is 200 nm.

5.4 Comparison between simulations and experiments

Before we compare the measured and simulated far-field radiation patterns, we will outline the simulation procedure, since it has not been a straightforward task to get a good agreement between simulations and experiments.

Simulation procedure

The investigated needle structure is not completely rotationally symmetric as seen in the SEM image in Fig. 5.1, however we model it as being so for three reasons: 1) It is a good approximation of the actual structure, 2) it hugely simplifies the computational task and 3) it allows us to use the open-geometry Fourier model method developed in Ref [48] giving us access to the individual modes of the structure. The GaAs needle nanowire is covered with a thin passivation layer of SiO₂, of which the thickness has been estimated by cutting a similar structure (i.e. not the same structure for which we performed the far-field measurements) with a focused ion beam at different heights, and measuring the thickness of the

passivation layer from SEM images. This procedure lead to a model description of the structure sketched in Fig. 5.8(a), where the diameter of the structure increases slightly from 200 nm at the bottom to 218 nm in the middle, where it is tapered to a top diameter of 74 nm. The opening angle is estimated to 6 degrees, and the thickness of the passivation layer is 2 nm at the bottom, 37 nm in the middle and 0 nm at the top. Of course these numbers are associated with some uncertainty, and simulating the model geometry did not produce far-fields with convincing agreement with the measurements. Furthermore, there are quite a lot of parameters, which could be varied in order to get a better agreement, however, studying the effect of all these would be extremely time consuming, and in the end the model geometry is an approximation of the true geometry. In order to keep things a bit simpler, we chose to look at the simplified geometry sketched in Fig. 5.8(b) consisting of a straight nanowire with an out-coupling taper neglecting the SiO₂ passivation layer.

By considering the simplified structure in Fig. 5.8(b) instead of the model geometry in Fig 5.8(a) we have reduced the number of variables in the model, and thus we have decreased the number of simulations needed for learning the role of each variable. As seen from Fig. 5.2 the curve for the SE rate into the TE01 like radiation mode is quite steep around our diameter and emission wavelengths of interest, and thus the far-field radiation pattern is quite sensitive towards both parameters. However, after several simulations we chose to fix the diameter to 200 nm (which is also the estimated average diameter of the nanowire), and since the tapering angle mainly affects the spot size in the far-field we found that the critical variable to tune for obtaining agreement is the height of the straight nanowire section. The HE11 mode and the TE01-like radiation mode have different propagation constants and thus by changing the height of the nanowire, the relative propagation phase between these are varied, which leads to a change in their interference pattern observable in the far-field.

For each height of the nanowire we simulated the far-field of a radially and a tangentially oriented dipole placed in 10 different positions along the radial axis, $r_{\text{PD}} = (0, 1, 2, 3, \dots, 9)R_{\text{NW}}/10$. The wavelength of the dipole was chosen to match the wavelength of QD1 (891.5 nm), QD2 (907 nm) or QD3 (912 nm). We added the far-fields of the two dipole orientations incoherently as discussed in the previous section, and in this way we obtained a far-field radiation pattern for 10 different positions of the QD in the needle nanowire as shown in Fig. 5.9 for QD1. The point dipoles are placed along the y -axis from the centre ($r_{\text{PD}} = 0$) to the upper edge ($r_{\text{PD}} = 0.9$) in the figure. As seen, the far-field pattern changes as the dipole position is changed, due to the change of the relative power between the HE11 and the TE01-like radiation mode, which is seen from the SE rates in Fig. 5.3. Furthermore it should be noted, that the far-field pattern is mirror symmetric with respect to the radial axis (y -axis in Fig. 5.9), and thus the pattern contains information on the exact QD position and not just the radial position.

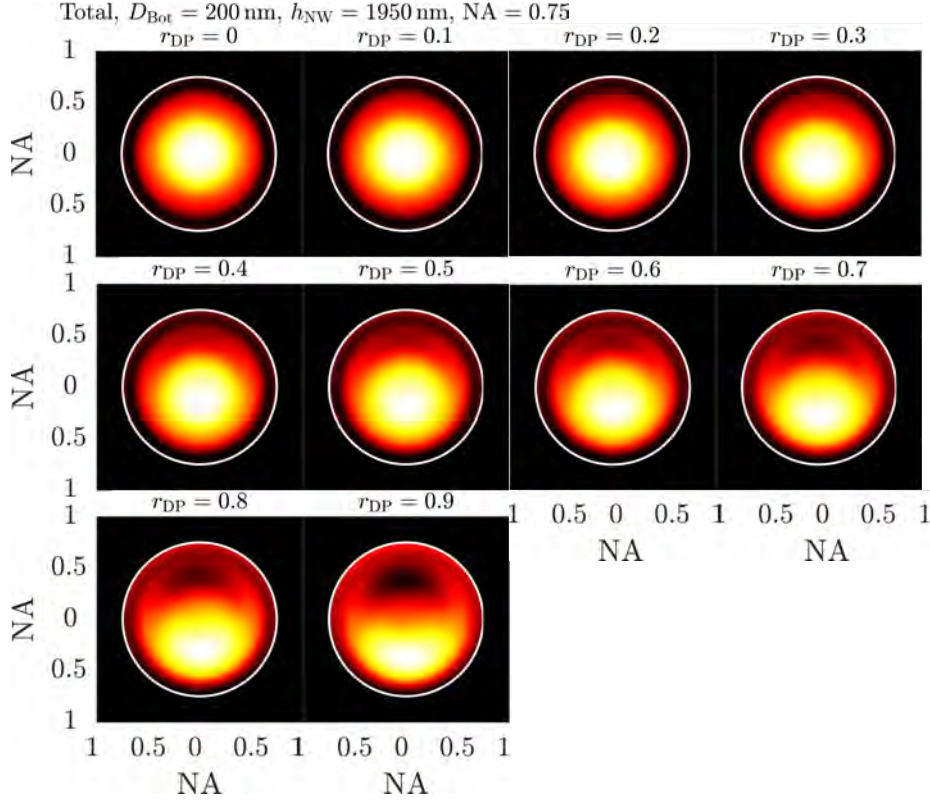


Figure 5.9: Simulated far-field radiation pattern for 10 different QD positions on the the y -axis starting from the centre towards the upper edge of the nanowire. The emission wavelength is 891.5 nm corresponding to QD1, and the height of the nanowire section in Fig. 5.8(b) is 1950 nm. The white circle indicates $\text{NA} = 0.75$.

In Appendix C.5 the simulated far-fields for all three emission wavelengths 891.5 nm (Fig. C.9), 907 nm (Fig. C.10) and 912 nm (Fig. C.11) are shown for three different nanowire heights: 1900 nm, 1950 nm and 2000 nm. We have investigated the far-field for additional heights of the nanowire, however, we found that these heights came closest to reproducing the experimental results, while being close to the real geometry. As discussed in Appendix C.5 the height of the nanowire determines the phase difference between the HE11 and TE01-like radiation mode, and thus greatly influences the far-field pattern.

Far-field comparison and deduced QD positions

We will compare the measured far-fields in Fig. 5.7 to the simulated far-fields shown in Figs. C.9-C.11 in Appendix C.5 both numerically and through visual inspection in order to deduce the position of the three QDs in the needle nanowire.

The numeric comparison is carried out by interpolating the simulated far-fields, such that we can compare these with the measured far-fields pixel-by-pixel. We initialize the far-fields by normalizing them with their maximum pixel value. In this way all far-fields have pixel values between 0 and 1. After these initializing procedures, we developed an algorithm for minimizing the mean pixel difference between the simulations and the measurements. The algorithm have two free parameters - the radial position of the QD and a far-field power scaling factor.

Before using the algorithm for determining the radial position, we turn our attention to the azimuthal position of the QDs. We determine the azimuthal position by exploiting that the far-fields should be close to mirror symmetric⁶. From symmetry, we know that the QDs are placed along the mirror axis of the far-fields, and we determine this axis by calculating the mean pixel difference between two halves of the far-fields shown in Fig. 5.7, separated by a mirror axis tilted with an angle of ϕ_{tilt} . The mean pixel difference is plotted as function of the mirror axis tilt in Fig. 5.10 and is formally calculated as

$$\Delta P_{mn}(\phi_{\text{tilt}}) = \left| P_{mn}^{\phi_{\text{tilt}+}} - P_{mn}^{\phi_{\text{tilt}-}} \right|, \quad (5.8a)$$

$$P_{\Delta}^{\text{mean}}(\phi_{\text{tilt}}) = \frac{\sum_{mn} \Delta P_{mn}(\phi_{\text{tilt}})}{\#\text{Pixels}}, \quad (5.8b)$$

where $P_{mn}^{\phi_{\text{tilt}+(-)}}$ is the power in pixel mn on the positive(negative) side of the mirror axis⁷.

The minima in Fig. 5.10 provides one of two possible azimuthal positions of the QDs - the other position is found by addition of 180 degrees, however from the simulated far-fields in Figs. C.9-C.11 we know that the QD is placed oppositely of the far-field maximum power for our nanowire heights, and thus we conclude the following azimuthal positions for the QDs

$$\phi_{\text{QD1}}^{\text{pos}} = 163^{\circ} \pm 12^{\circ}, \quad (5.9a)$$

$$\phi_{\text{QD2}}^{\text{pos}} = 180^{\circ} \pm 6^{\circ}, \quad (5.9b)$$

$$\phi_{\text{QD3}}^{\text{pos}} = 14^{\circ} \pm 6^{\circ}, \quad (5.9c)$$

where the uncertainty has been estimated as the $\pm 5\%$ deviation from the minima in Fig. 5.10. Choosing a $\pm 5\%$ deviation gives us a 90% confidence interval, and should cover the inherent numerical uncertainties, which are likely much smaller than the uncertainty on the exact experimental structure.

⁶They would be perfectly mirror symmetric, if the nanowires had perfect cylindrical symmetry.

⁷Positive side meaning the side in the positive rotation direction.

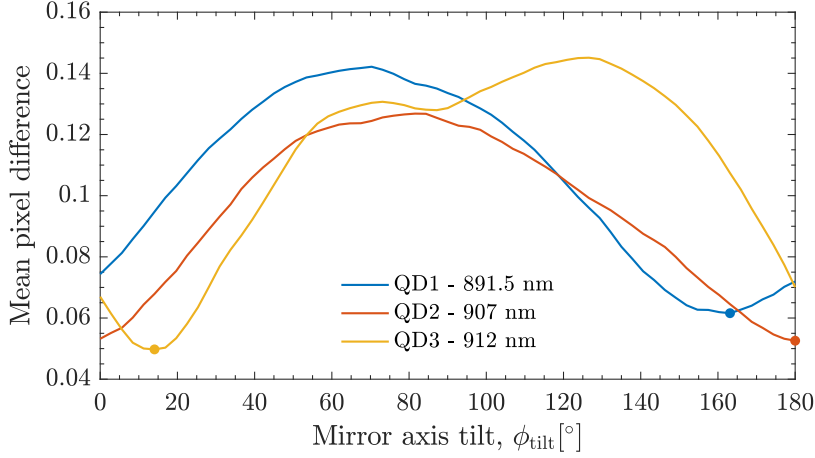


Figure 5.10: The mean pixel difference between the two halves of the far-fields in Fig. 5.7 separated by a mirror axis tilted by ϕ_{tilt} for each QD.

Having determined the azimuthal position of the QDs, we will now find the radial position. This we do by comparing the measured far-fields in Fig. 5.7 with the simulated far-fields in Appendix C.5. The comparison is done in the following way. As mentioned above there are two parameters to vary for obtaining the best agreement between simulations and measurements: 1) the radial dipole position in the simulations, and 2) a scaling factor. The first parameter is self-explaining, and the second is a simple scaling factor multiplied on the measured far-fields after the pixels has been normalised to the range between 0 and 1. The purpose of the scaling factor is to reduce the influence of bright spots on the measurements, which could affect the interpreted radial position in the wrong way. We use the scaling factor, which leads to the global minimum in the mean pixel difference for each QD. The optimal scaling factors was found to be

$$c_{\text{scale}}^{\text{QD1}} = 1.30, \quad (5.10a)$$

$$c_{\text{scale}}^{\text{QD2}} = 1.35, \quad (5.10b)$$

$$c_{\text{scale}}^{\text{QD3}} = 1.10. \quad (5.10c)$$

Using these scaling factors we determine the mean pixel difference between the simulated and measured far-fields as

$$\Delta P_{mn}(r_{\text{PD}}) = \left| P_{mn}^{\text{sim}}(r_{\text{PD}}) - P_{mn}^{\text{exp}} c_{\text{scale}} \right|, \quad (5.11a)$$

$$P_{\Delta}^{\text{mean}}(r_{\text{PD}}) = \frac{\sum_{mn} \Delta P_{mn}(r_{\text{PD}})}{\#\text{Pixels}}, \quad (5.11b)$$

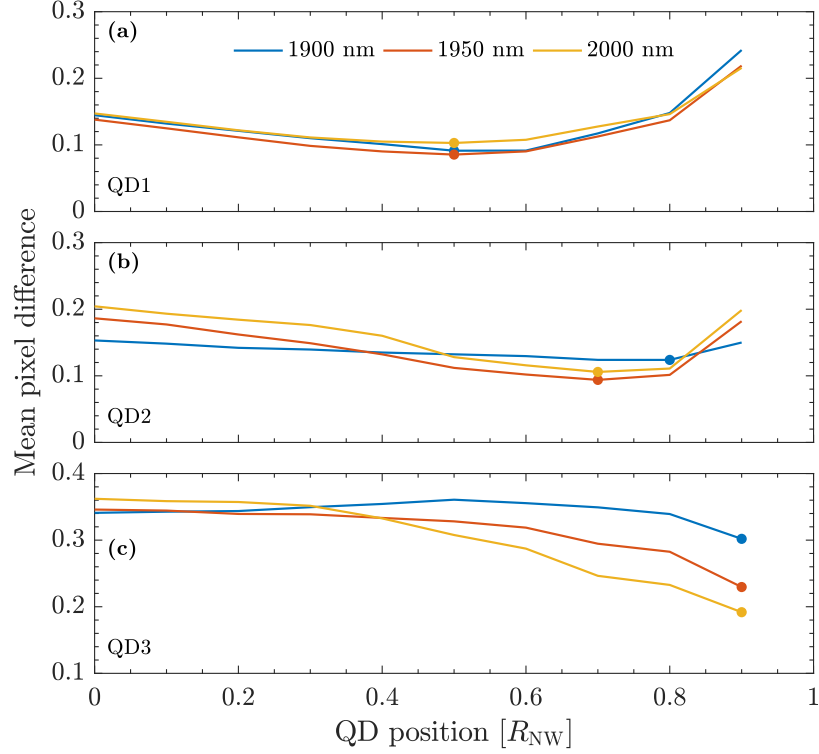


Figure 5.11: The mean pixel difference between the simulated and measured far-fields calculated for nanowire heights of 1900, 1950 and 2000 nm for (a) QD1 (891.5 nm), (b) QD2 (907 nm) and (c) QD3 (912 nm) as function of the radial dipole position of the simulated far-fields. For these curves we used the optimal azimuthal position of the QDs found in Fig. 5.10.

where r_{PD} is the radial dipole position in the simulations in units of the nanowire radius. Using this expression, we compute the mean pixel difference as function of the dipole position for each QD for nanowire heights of 1900, 1950 and 2000 nm. The results are presented in Fig. 5.11.

The predicted radial position of the QDs is found as the minima in Fig. 5.11, and as above we determine the uncertainty by finding the QD positions with a 5% deviation from the minimum mean pixel difference for all three nanowire heights. We deduct the following positions for each of the nanowire heights

$$\begin{aligned}
 r_{\text{QD1}}^{1900\text{nm}} &= [0.5; 0.6], & r_{\text{QD2}}^{1900\text{nm}} &= [0.6; 0.8], & r_{\text{QD3}}^{1900\text{nm}} &= 0.9, \\
 r_{\text{QD1}}^{1950\text{nm}} &= 0.5, & r_{\text{QD2}}^{1950\text{nm}} &= 0.7, & r_{\text{QD3}}^{1950\text{nm}} &= 0.9, \\
 r_{\text{QD1}}^{2000\text{nm}} &= [0.4; 0.6], & r_{\text{QD2}}^{2000\text{nm}} &= [0.7; 0.8], & r_{\text{QD3}}^{2000\text{nm}} &= 0.9,
 \end{aligned} \tag{5.12}$$

where all numbers have been normalised with $R_{\text{NW}} = 100$ nm. From these numbers we conclude the following radial positions of the QDs

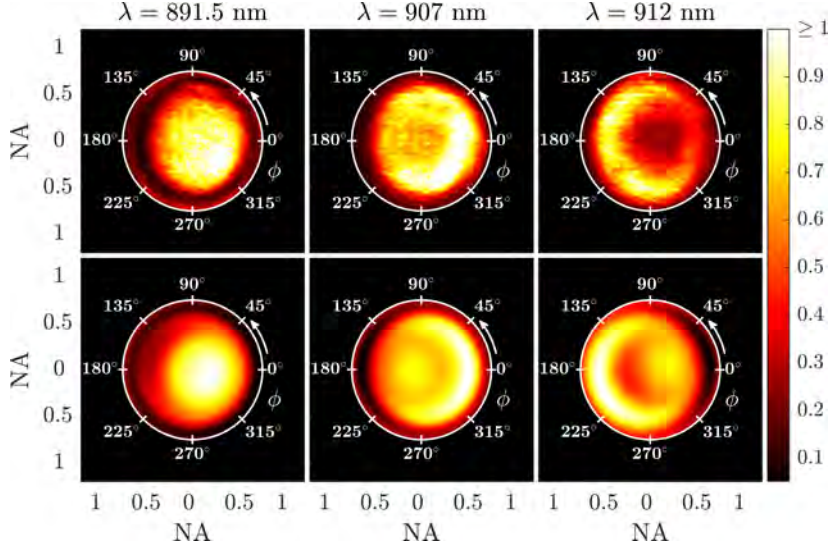


Figure 5.12: Top row: Measured far-fields for the three QDs. Bottom row: Simulated far-fields for $h_{\text{NW}} = 1950$ nm, where the far-fields has been rotated in order to obtain the best agreement with the measured far-fields. The dipole position used in the simulation is $0.5R_{\text{NW}}$, $0.7R_{\text{NW}}$ and $0.9R_{\text{NW}}$ for the three emission wavelengths respectively.

$$r_{\text{QD1}}^{\text{cyl}} = [50 \pm 15] \text{ nm}, \quad (5.13a)$$

$$r_{\text{QD2}}^{\text{cyl}} = [70 \pm 15] \text{ nm}, \quad (5.13b)$$

$$r_{\text{QD3}}^{\text{cyl}} = [90 \pm 5] \text{ nm}, \quad (5.13c)$$

where the superscript 'cyl', means assuming cylindrical symmetry. These uncertainty estimates are approximated from the intervals in Eq. (5.12) and our resolution on the radial QD position. Our simulations has been made in steps of 10 nm, so each position has an inherent uncertainty of ± 5 nm. In Fig. 5.12 we show the measured far-fields in the top row scaled with the scaling factors in Eq. (5.10), and the simulated far-fields with the best overlap found by the above analysis in the bottom row. This enables visual comparison between simulations and measurements, and as seen the simulations replicate well the features of the measured far-fields. The error estimates in Eq. (5.13) is purely estimated from the agreement between the simulations and the measurements, assuming a rotationally symmetric structure. However, we know our needle structure has some ellipticity, and in the following we will estimate the error arising from our assumption of rotational symmetry.

To do this, we used an in-house code, which is able to compute spontaneous emission rates in to the confined modes of an infinite elliptical nanowire. Since it is the ratio between the emitted power into the HE11 and the TE01 mode that

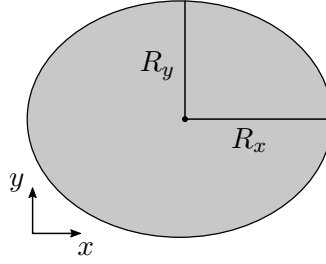


Figure 5.13: Approximate elliptical cross-section of the nanowire in Fig. 5.1, where $R_x = 112.5 \text{ nm}$ and $R_y = 87.5 \text{ nm}$. For the TE01 mode, we have used $R_x = 1.25 \cdot 112.5 \text{ nm} = 140.6 \text{ nm}$ and $R_y = 1.25 \cdot 87.5 \text{ nm} = 109.4 \text{ nm}$.

determines the interference pattern, the uncertainty on this ratio translates into the uncertainty on the radial dipole position. We consider the infinite elliptical nanowire sketched in Fig. 5.13, and compute the spontaneous emission rates into the HE11 and the TE01 mode for dipole positions along the semi-major axis ($R_x = 112.5 \text{ nm}$) and the semi-minor axis ($R_y = 87.5 \text{ nm}$). However, our elliptical code is only able to treat guided modes, and the TE01 mode is technically a radiation mode for our structure. Therefore, we approximate the emission rates for the TE01 mode by computing these for a slightly larger elliptical cross-section ($R_{x(y)}^{\text{TE01}} = 1.25R_{x(y)}$) and scale these with the ratio between the emission rates for a cylindrical nanowire with diameters of 200 and 250 nm as

$$\Gamma_{\text{TE01}}^{\text{Ellip}}(R_x, R_y) = \Gamma_{\text{TE01}}^{\text{Ellip}}(1.25R_x, 1.25R_y) \frac{\Gamma_{\text{TE01}}^{\text{Cyl}}(R)}{\Gamma_{\text{TE01}}^{\text{Cyl}}(1.25R)}, \quad (5.14)$$

where $R = \frac{R_x + R_y}{2} = 100 \text{ nm}$.

Fig. 5.14 plots the SE rate ratio between the TE01 mode and the HE11 mode for a tangentially oriented dipole as function of the dipole position along the major and minor axis of the elliptical nanowire sketched in Fig. 5.13, as well as along the radial axis of a cylindrical nanowire with a diameter of 200 nm. We estimate the lower and upper bound of the dipole position, as the positions, where the SE rate ratio on the major and minor axis of the elliptical nanowire equals the cylindrical nanowire SE rate ratio for the QD positions found above as shown in Fig. 5.14. In this way, we include the elliptical shape of the nanowire in our error estimate on the found QD positions. From Fig. 5.14, we find that the radial positions of the QDs are within the following intervals

$$r_{\text{QD1}}^{\text{ellip}} = [0.42; 0.53] R_{\text{NW}}, \quad (5.15a)$$

$$r_{\text{QD2}}^{\text{ellip}} = [0.60; 0.74] R_{\text{NW}}, \quad (5.15b)$$

$$r_{\text{QD3}}^{\text{ellip}} = [0.79; 0.93] R_{\text{NW}}. \quad (5.15c)$$

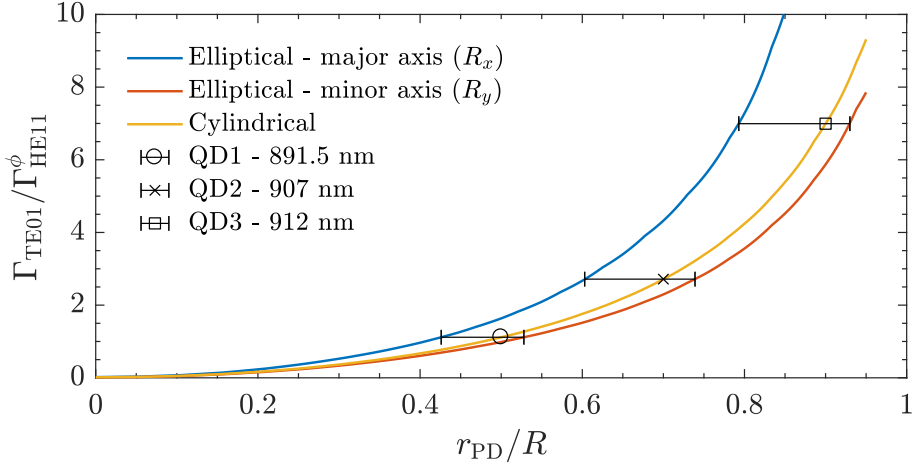


Figure 5.14: Ratio between the spontaneous emission rate into the TE01 mode and the HE11 mode for a tangentially oriented dipole for a dipole moved along the major axis (blue curve) and minor axis (red curve) for the elliptical nanowire sketched in Fig. 5.13, and for a dipole moved along the radial axis for a cylindrical nanowire (yellow curve). The position of the three QDs are shown with the deduced error bars.

Comparing these intervals with the error estimates in Eq. (5.13), we see that the uncertainty on the radial position of QD3 is larger than our first estimate, due to the ellipticity of our structure. This leads us to the following radial positions of the QDs

$$r_{\text{QD1}} = [50 \pm 15] \text{ nm}, \quad (5.16a)$$

$$r_{\text{QD2}} = [70 \pm 15] \text{ nm}, \quad (5.16b)$$

$$r_{\text{QD3}} = [87 \pm 8] \text{ nm}. \quad (5.16c)$$

The QD position map, including the estimated uncertainties, is shown in Fig. 5.15. Thus for the structure under investigation we are predicting the QD positions with an uncertainty of ± 15 , ± 15 and ± 8 nm on the radial position, and ± 14 , ± 9 and ± 10 nm on the azimuthal position for QD1, QD2 and QD3 respectively. In Ref. [112] the uncertainty on the positioning was reported to be ± 1 nm for QDs placed close to what they denote a neutral line and ± 35 nm for QDs placed close to the edge of the NW. In our case it seems we get better precision for QDs placed close to the edge. For QDs placed close to the axis, the SE rate into the HE11 and TE01 mode varies quite slowly as function of the QD radial position as seen in Fig. 5.3, and thus the far-field interference pattern does not change drastically for small changes in the radial position. However, as the QD is moved further off-axis the slope of the SE rate increases, thus increasing our sensitivity towards the radial position. Similarly for the azimuthal position, we

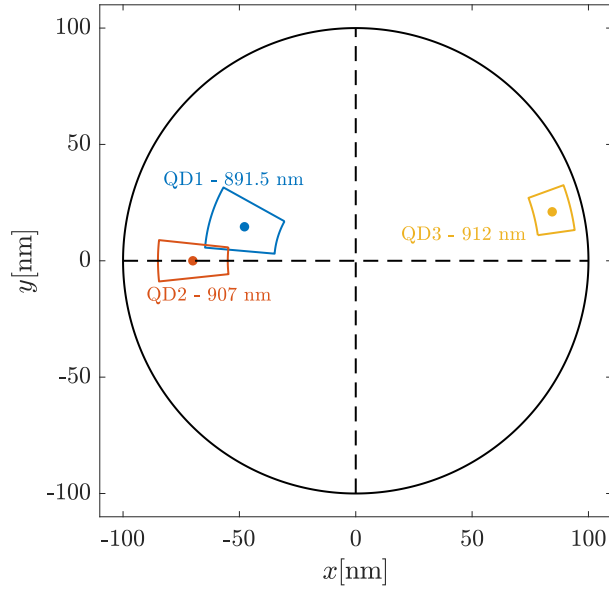


Figure 5.15: The concluded QD positions from the analysis of the far-field radiation pattern. The dots mark the QD positions predicted by the model and the enclosed area indicate the uncertainty on the actual position. We thus expect to find the QDs within the enclosed areas.

expect the largest uncertainty for QDs close to the axis, since finding the mirror axis in a far-field with no or very weak interference patterns will be more sensitive towards fabrication imperfections and thus associated with larger uncertainties.

The precision of our position mapping technique strongly depends on the fabricated structure, and how rotationally symmetric it is. Furthermore, our technique is limited to handle nanowires, where the only guided modes are the HE₁₁ and TE₀₁ modes. Thus for GaAs nanowires with QDs emitting at 900 nm, our technique should be applicable to diameters between roughly 180 and 270 nm corresponding to $D/\lambda = 0.2$ and 0.3 in Fig. 5.2. Our technique should be applicable to handle nanowires with trumpet out-coupling tapers as well.

5.5 Conclusion

We have shown that using an open-geometry Fourier modal method and a far-field transformation, we are able to reverse engineer the position of quantum emitters embedded in a needle nanowire with a reasonable precision. One of the strong features of the presented technique, is the ability to implement it on a standard micro-photoluminescence setup. This is in contrast to the proposed technique in Ref. [112], where mechanical driving and detection is required, adding to the experimental complexity.

In this study, we used the oFMM method for the numerical modelling, however with a careful treatment of the open boundaries required for convergence, one could use more widely known techniques such as FDTD (e.g. Lumerical) or FEM (e.g. Comsol or JCMwave) for simulating the far-fields. The drawback will be the loss of easy access to the optical modes of the nanowire, especially to the radiation modes, but an advantage would be the possibility to account for fabrication deviations from the ideal cylindrical nanowire.

Since the correct modelling of the far-fields is the core of our method and, unfortunately, not an easy and straightforward task, our mapping technique would be more accessible to others if a simple two-mode model could be developed. Eq. (C.11b) in Appendix C.4 describes the power distribution for the TE₀₁ and HE₁₁ modes in a cross-section of the nanowire, where the defining parameters are the difference in propagation constant, Δ_β , and the transverse profile of the modal fields $E(H)_{\text{HE11}}$ and $E(H)_{\text{TE01}}$. It is well-known, how to determine both the propagation constants and the modal fields in a nanowire,[113] and thus the power distribution in the straight nanowire section is easily computed, especially if the TE₀₁ mode is a truly guided mode, and not radiating as in our structure. However, the challenge arises in describing the interference along the out-coupling taper. The propagation constants will change differently for the two modes as well as the confinement of the modal fields, and thus you need a continuous description of both. This poses an on-going research challenge of how to efficiently model both needle and trumpet tapers with the FMM, which we touched upon in Ref. [121] (J2). However, the work we presented in this SPIE Proceedings did not reach a conclusion, and thus an efficient model for treating tapers is still to be developed. One idea which was pursued in this Ph.D.-study was to combine the oFMM method with the cross-section method [122, 123], however due to time constraint and other priorities, the project was put on-hold. Thereby formulating a simple 2-mode model describing the emitted far-fields by QDs in tapered nanowires would be an interesting future research project.

Breakdown of single-mode model for computing source efficiency and Purcell enhancement for nanopost structures

In the previous chapter, we considered a nanowire with a needle out-coupling taper. The out-coupling taper secures a good coupling to a Gaussian mode in the far-field for an on-axis QD [27, 62, 63], however at the cost of Purcell enhancement due to the negligible reflectivity of the needle tip. With a trumpet out-coupling taper [23, 32, 61], it is possible to introduce some reflectivity by a Bragg mirror in the trumpet region as proposed in [57], and thereby introduce some Purcell enhancement. The Purcell enhancement is needed for accelerating the photon emission rate in order to reduce phonon-induced decoherence and spectral diffusion, and thereby enhancing the indistinguishability of the emitted photons [57]. The state-of-the-art platform within semiconductor single-photon sources (SPS) is currently the micropillar structure [25, 29, 124, 125], which uses DBR mirrors in order to increase the Purcell enhancement through cavity effects. However, since the micropillar structures rely on a large Purcell effect both the spectral alignment of the emitter and the cavity, as well as the spatial alignment of the

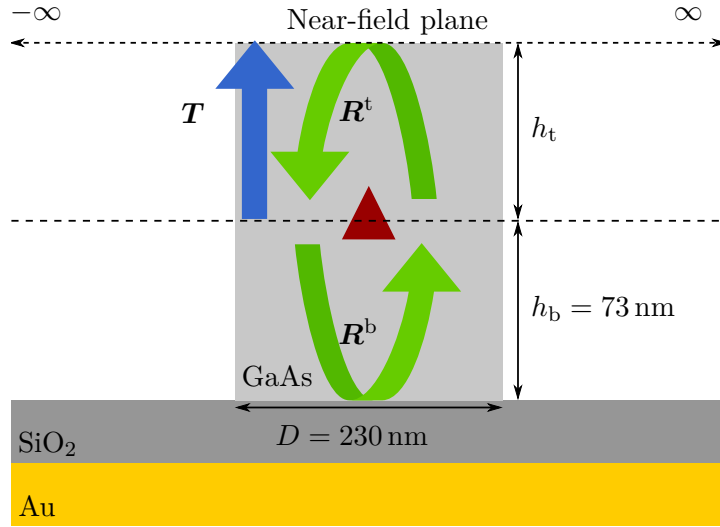


Figure 6.1: GaAs nanopost on a silica-gold mirror. The distance from the QD to the mirror is kept fixed at 73 nm, which correspond to the first antinode of the HE₁₁ mode.

emitter and the cavity field maximum needs to be very precise. This results in a narrow operating bandwidth preventing large tuning of the QD emission lines [57]. The advantage of using nanowires instead of micropillars as SPS is their broad operating bandwidth, however implementing efficient top and bottom mirrors in order to enhance the SE rate is still an on-going research field. In Ref. [57] they introduce DBRs in the out-coupling trumpet, however an experimental demonstration of this design is still to be realised.

The fabrication of trumpet nanowires with DBR mirrors embedded in the taper part is thus quite complex, and therefore we set out to study the simplest possible nanowire design - a truncated nanowire (denoted a nanopost). In the present chapter, we investigate the properties of the nanopost with two different models based on the oFMM formalism[48]: a single-mode model and the full model including all modes (see Section 6.1). From a modelling point of view it is interesting to investigate, whether the single-mode model is applicable, since it is widely used in the literature for treating nanowire structures as in [22, 23, 57, 63], where it is in general shown to be a good model. From a fabrication point of view it is interesting to investigate the performance of such a simple structure, and see how well it performs compared to more complex structures. For sure the nanopost design (see Fig. 6.1) will not break any records regarding pure performance, however, the complexity of the fabrication of the design is also of importance, when designing quantum optical experiments.

The nanopost design is seen in Fig. 6.1, where the bottom mirror consists of a silica-gold mirror, which is the current state-of-the-art mirror type for nanowire structures [84]. The work presented in the present chapter was initiated during my

external stay at CEA in collaboration with Julien Claudon. So far the project is purely theoretical, and all modelling, method development and simulations have been performed by the author. Julien and his team are currently working on reproducing the theoretical predictions experimentally. We have a manuscript focussing only on the theoretical modelling and the discovered breakdown of the single-mode model in preparation (J6). This chapter is based on the manuscript.

The chapter is organized as follows. In Section 6.1, we introduce the single-mode and full model, which we use and compare throughout the chapter. We summarize the design strategy for finding the optimal geometrical parameters of the nanopost in Section 6.2, where we focus on optimizing the Purcell enhancement - later in the chapter we will also look at the source efficiency. In Section 6.3, we compare the results obtained by the single-mode and full model, and provide simple physical explanations for why the single-mode model breaks down. We finish the chapter with a conclusion and an outlook for the nanopost design.

6.1 Single-mode and full model

Due to the rotational symmetry of the nanopost, we are using the oFMM formalism in cylindrical coordinates (as in the previous chapter) described in details in Ref. [48] for computing the eigenmodes instead of the 3D oFMM formalism presented in Chapter 3. All reflection and transmission matrices for the structure in Fig. 6.1 are found in the standard FMM way using the boundary conditions at the interfaces between z -independent layers and the scattering matrix formalism [46]. The full electromagnetic field is given as in the previous chapter by Eq. (5.1), and the Purcell enhancement is given in Eq. (3.20). Both of these quantities depend on the dipole coupling coefficient, which in an infinite nanowire is computed using Eq. (5.2). The scattering reflection matrices of the top facet and bottom mirror in Fig. 6.1 both include the propagation phase from the QD position to the interface. The cavity effects are included in the dipole coupling coefficient by using the scattering matrix formalism as [46]

$$\mathbf{a}_{\text{tot},n} = (\mathbf{I} - \mathbf{R}^b \mathbf{R}^t)^{-1} (\mathbf{a}_{\infty\text{NW}} + \mathbf{R}^b \mathbf{b}_{\infty\text{NW}}), \quad (6.1)$$

where $\mathbf{a}_{\infty\text{NW}}$ ($\mathbf{b}_{\infty\text{NW}}$) is the dipole coupling coefficient into the forward (backward) propagating modes in an infinite nanowire, and \mathbf{R}^b (\mathbf{R}^t) is the reflection matrix for the bottom mirror (top facet). Eq. (6.1) is referred to as the full model, since it includes all modes and their mutual coupling. Since we are only considering in-plane dipole orientations,¹ the nanowire is mirror symmetric with respect to the QD plane, and thus couple equally to modes propagating upwards

¹As discussed in Chapter 5, the InGaAs QDs in GaAs nanowires will always have a dipole orientation in the plane due to the fabrication technique.

and downwards: $\mathbf{a}_{\infty\text{NW}} = \mathbf{b}_{\infty\text{NW}}$. The single mode model comes forth by rewriting Eq. (6.1) into a scalar version using only the matrix elements for the HE11 mode:

$$a_{\text{tot,HE11}} = \frac{1 + r_{\text{HE11}}^b}{1 - r_{\text{HE11}}^b r_{\text{HE11}}^t} a_{\infty\text{NW,HE11}}, \quad (6.2)$$

where $a_{\infty\text{NW,HE11}}$ is the first element of $\mathbf{a}_{\text{tot},n=1}$. In this study we consider a dipole placed on-axis in the nanopost structure, and thus we only need to consider modes with angular momentum $n = \pm 1$, since the QD will not couple to modes with other angular momenta as discussed in Section 5.1.

The near-field to far-field transformation outlined in Section 5.2 is re-used in this chapter for computing both the far-field and the source efficiency of the nanopost structure. The near-field will be computed using the transmission matrix from the QD position to the near-field plane in Fig. 6.1 as

$$\mathbf{a}_{\text{NF},n} = \mathbf{T}\mathbf{a}_{\text{tot},n}. \quad (6.3)$$

In the single-mode model $\mathbf{a}_{\text{tot},n}$ is replaced with the vector $\mathbf{a}_{\text{tot,HE11}}(j) = \delta_{1j}a_{\text{tot,HE11}}$. The source efficiency of the nanopost is computed as the ratio between the power collected in a lens with numerical aperture NA and the emitted power as

$$\text{Source efficiency} = \frac{P_{\text{Collected}}}{P_{\text{Emitted}}}, \quad (6.4)$$

where the emitted power is computed using Eq. (3.20) and Eq. (2.16), whereas the collected power is computed by integrating the time-averaged Poynting vector (see Eq. (2.7)) of the far-field, \mathbf{S}_{far} , over the area of the NA as

$$P_{\text{Collected}} = \int_0^{2\pi} \int_0^{\theta_{\text{NA}}} \langle \mathbf{S}_{\text{far}} \cdot \hat{\mathbf{r}} \rangle R^2 \sin \theta d\theta d\phi, \quad (6.5)$$

where $\text{NA} = \sin \theta_{\text{NA}}$, R is the distance from the center of the near-field plane to the observation point, and $\hat{\mathbf{r}}$ is the radial unit vector for the spherical coordinate system in which, we compute the far-field.

In Section 6.3 we compare the results of the two models, where the limitations of the single-mode model will be apparent, and provide physical arguments for why it breaks down.

6.2 Optimal geometry of nanopost

There are several design parameters for the GaAs nanopost to optimize. We fix the emission wavelength in this study to $\lambda = 920 \text{ nm}$, and the first task is to

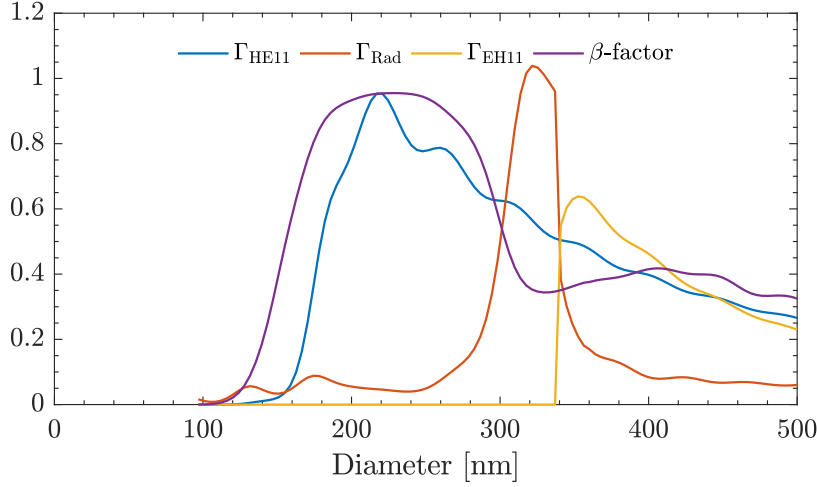


Figure 6.2: Normalized SE rates and β -factor of an on-axis emitter in an infinite nanowire.

determine the diameters with a good β -factor and inherent Purcell enhancement. We place an emitter with emission wavelength $\lambda = 920$ nm on-axis in an infinite nanowire. The SE rates and the β -factor of this configuration as function of the diameter are plotted in Fig. 6.2. A similar plot is found in Ref. [48]. A β -factor above 0.9 is obtained for diameters between 190 nm and 260 nm, and thus we expect the optimal geometry to be found in this interval. We observe a peak for the Purcell enhancement of the HE11 mode around 220 nm, and the β -factor peaks at around 230 nm.

We now consider the silica-gold bottom mirror, where the thickness of the silica layer can be chosen freely. In Fig. 6.3 the reflectance of the HE11 mode, $R = |r|^2$, is plotted as function of the nanowire diameter for various thicknesses of the silica layer. As seen, the optimal thickness depends on the diameter, however for the diameter range with high β -factor and large Purcell enhancement in Fig. 6.2 a thickness of either 7 or 9 nm seems to be the optimal choice. Note that the silica layer reduces the reflection dip of the metal mirror that we studied for the square nanowire in Chapter 3 in Fig. 3.5, by reducing the coupling to surface plasmons [84].

The QD should be placed in an antinode of the cavity mode meaning that the reflected light at the bottom mirror and the top facet should be in phase at the QD position, i.e. $\arg(R_{\text{HE11}}^b) = \arg(R_{\text{HE11}}^t) = 2\pi n$, where $n = 0, 1, 2, \dots$. Thus the distances h_b and h_t may only be varied discretely in order to match the phase condition, and they will both depend on the diameter of the nanopost. Now we consider the shortest possible nanopost geometry and place the QD in the antinode of the cavity mode, and use both the full and single-mode model described in the previous section to compute the Purcell enhancement of the

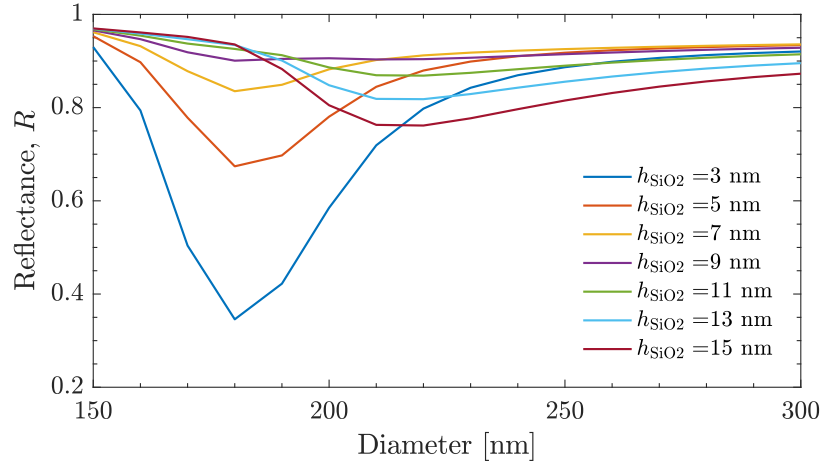


Figure 6.3: Reflectance of the HE11 mode as function of the nanowire diameter for various thicknesses of the silica layer.

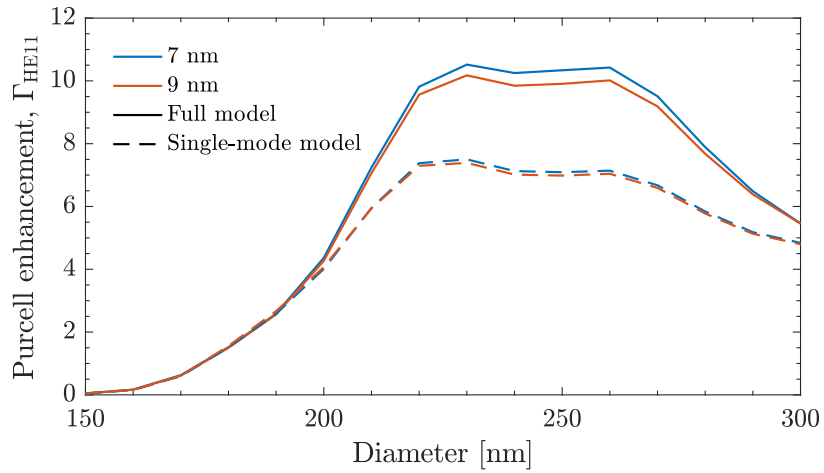


Figure 6.4: Purcell enhancement of the HE11 mode as function of diameter of the full structure sketched in Fig. 6.1. The nanopost is designed as short as possible and the dipole emitter is placed in the antinode.

HE11 mode. We use a silica thickness of 7 and 9 nm for the bottom mirror. This leads to the plot shown in Fig. 6.4, where a remarkable Purcell enhancement of around 10 is obtained for diameters between 220 and 260 nm. The single-mode model predicts a somewhat lower Purcell enhancement of around 7 in the same range. The disagreement between these two models will be analysed and explained throughout the remaining of the chapter. It seems from Fig. 6.4 that the largest Purcell enhancement is obtained for a silica thickness of 7 nm and a diameter of 230 nm, and thus we will use these parameters for the nanopost

geometry in our analysis. We will keep the distance between the QD and the bottom mirror fixed to the shortest possible, and vary the distance from the QD to the top facet discretely still satisfying the phase criteria, such that the QD is always placed in an antinode of the cavity mode.

6.3 Single-mode versus full model

In this section, we compute the Purcell enhancement, the source efficiency and the far-field using the single-mode model and the full model presented in Section 6.1. We show that the single-mode model is adequate for computing the Purcell enhancement for all nanopost heights except for the shortest possible, and that it in general is a bad approximation for computing the source efficiency and the far-field radiation pattern due to the scattering at the top facet.

Purcell enhancement and source efficiency

In Fig. 6.5(a) the Purcell enhancement for the geometry in Fig. 6.1 is computed using the full model and the single-mode model as function of the distance between the emitter and the top facet, h_t . As long as the dipole is placed in a field anti-node, there is no dependence on h_t in the single-mode model, and the full model generally agrees with the single-mode prediction. However, for the smallest possible nanopost, where a true anti-node exist, the full model predicts a Purcell enhancement of $F_p = 10 \pm 2$, where as the single-mode model predicts a Purcell enhancement of $F_p = 7.3 \pm 0.3$. This result is rather surprising so thorough convergence checks have been carried out and the result in Fig. 6.5(a) is not an artefact from convergence issues. In Appendix D.1 you will find the discretization strategy of the in-plane k_m -values used in Eqs. (5.3) as well as the convergence study on the Purcell enhancement computed using the full model and single-mode model for the shortest nanopost geometry (i.e. the first point in Fig. 6.5(a)).

The enhanced Purcell effect for the shortest nanopost is a consequence of a complex coupling at the bottom mirror and the top facet between the fundamental mode, radiation modes and evanescent modes.² The reflectivity of the bottom mirror for the HE11 mode is: $R_{\text{HE11}} = 0.92$, and thus 8% of the power in the fundamental mode goes into radiation and evanescent modes at the bottom mirror. For the smallest nanopost, however, the radiation and evanescent modes can couple back in to the HE11 mode at the top facet and thereby enhance the Purcell effect. The evanescent modes, though not carrying any power, have not completely decayed before reaching the top facet making their contribution to the HE11 mode non-negligible. Fig. 6.6 shows the Purcell enhancement as function

²Here we use the same classification of modes as in Chapter 3 in Eq. (3.19).

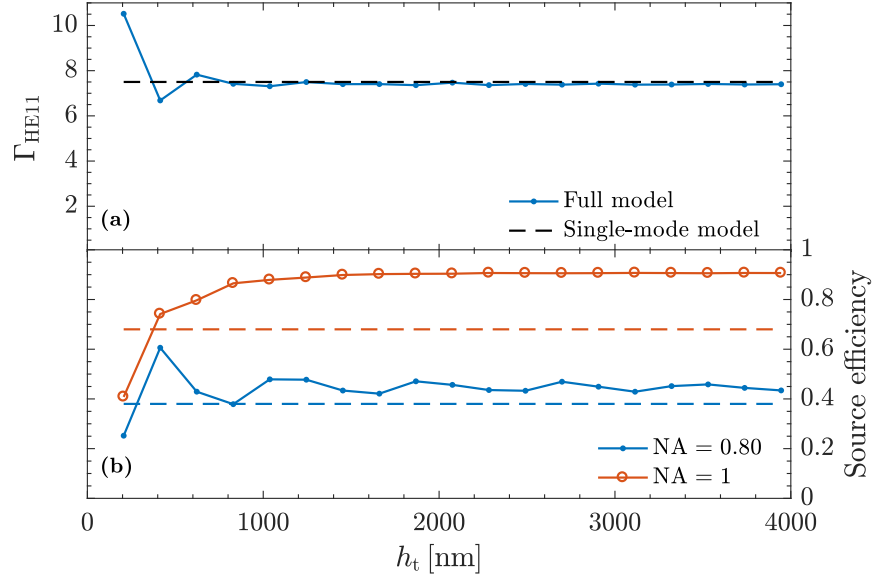


Figure 6.5: (a) Purcell enhancement for the nanopost sketched in Fig 6.1 computed using the full model and the single-mode model as function of the distance between the dipole and the top facet. (b) The source efficiency with a numerical aperture of 0.80 and 1 for the nanopost as function of h_t . The dashed line in both plots are computed using the single-mode model.

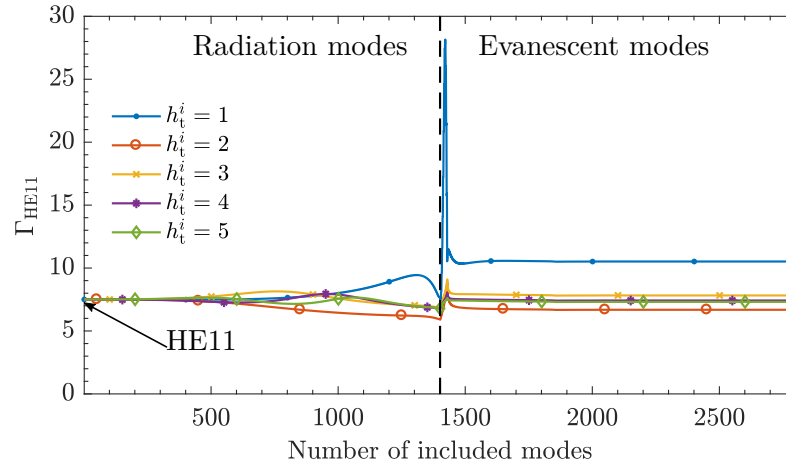


Figure 6.6: The Purcell enhancement for the five shortest nanoposts as function of the number of included modes in the full model. The first mode is the HE11 mode, followed by radiation modes and from 1400 the modes included are evanescent.

of the number of included modes in the full model for the five shortest nanoposts. As seen, using all modes or only the HE11 mode gives approximately the same result except for the shortest nanopost. For the shortest nanopost all radiation modes and the first 30-40 evanescent modes should be included before the Purcell enhancement converges. This supports the argument that the evanescent modes cannot be neglected for very small structures. That the coupling between evanescent modes and the fundamental mode can break-down a single-mode model for short propagation distances was also shown in 2D photonic crystal Fano structures in Chapter 4 [96].

From Fig 6.5(b) it seems that the enhanced Purcell effect comes at a cost of lower source efficiency for numerical apertures $NA = 0.80$ and $NA = 1$. Furthermore, we see some variations in the source efficiency as the height of the nanopost is increased. In the single-mode model, the source efficiency does not depend on the height of the nanopost, since the scattering of the HE11 mode at the top facet is independent of the height. Furthermore, it should be noticed that the single-mode model predicts an efficiency of around 67 % for $NA = 1$, which is significantly less than the prediction by the full model. This is due to the scattering at the top facet, where all backscattered radiation modes (i.e. radiation modes that propagate towards the bottom mirror) are lost in the single-mode model. More details on this will be given in the following subsections, where we will look at the far-field pattern of the nanopost and give simple explanations of the reduced source efficiency for the smallest nanopost, as well as for the observed variations in the source efficiency for the different nanopost heights.

Far-field emission pattern

In the literature, the far-field emission pattern of nanowire structures is usually computed using only the guided modes as in [63]. In [114] the emission into both guided and radiation modes for infinite dielectric nanowires is computed, however not explicitly for truncated nanowires. In Refs. [126] and [127] the far-field radiation pattern from InP nanowires grown on top of an InP substrate are considered. However, as opposed to the study in this chapter Refs. [126] and [127] do not consider a single emitter embedded in the nanowire - instead the whole semiconductor structure is excited, and thus modes with angular momenta $n \neq \pm 1$ are included in the analysis as well as dipoles with orientations along the nanowire direction. Another important difference is that the nanowire is standing on top of a dielectric substrate instead of the bottom mirror in our nanopost structure. The authors do make a modal analysis in [127], however only including the HE11 (guided), TE01 (guided) and TM01 (in the paper it is both a guided mode and a radiation mode depending on the nanowire diameter) modes and do not consider all radiation modes. This is probably unnecessary due to the weak bottom mirror (dielectric substrate). Thus, to our knowledge, a

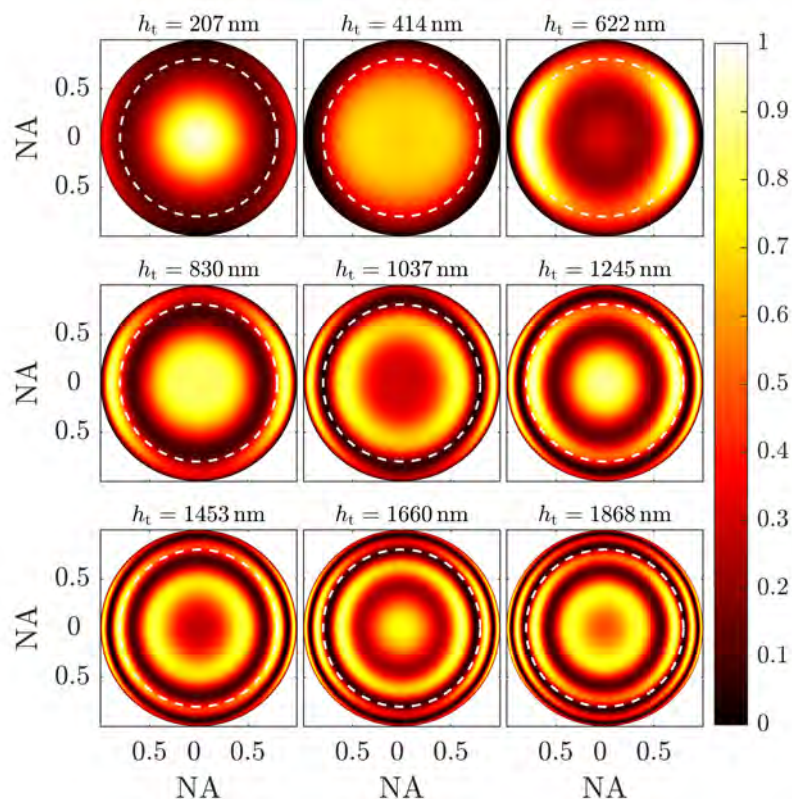


Figure 6.7: Far-field patterns for the 9 shortest nanoposts. The white dashed circle corresponds to a numerical aperture of 0.80. The fields are normalized to the maximum power across the nanopost sizes.

full study on the role of radiation modes has never been investigated except for infinite nanowires. Due to the open boundary conditions in the oFMM formalism, we can correctly account for the contribution of the radiation modes to the far-field emission pattern, and their mutual coupling with the HE11 mode, enabling us to separate the contributions from the radiation modes and the HE11 mode to the far-field radiation pattern.

The far-field patterns of the 9 shortest nanoposts are shown in Fig. 6.7. Here the full model has been used and as seen the far-field includes interference rings - not predicted by a single-mode model. As the height of the nanopost increases additional rings appear. These rings are a consequence of interference between the HE11 mode and the backscattered radiation modes. In [128] it was reported that around 15 % of the intensity of the HE11 mode is backscattered into radiation modes at the top facet of a GaAs nanopost for a diameter of $D = 230$ nm at $\lambda = 920$ nm. The backscattered radiation is reflected by the bottom mirror and thus contribute to the far-field. In Appendix E the far-fields of needle and

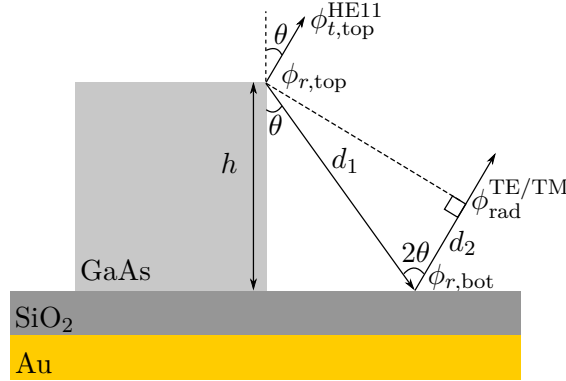


Figure 6.8: As the HE11 mode reflects at the top facet part of the backscattered light goes into radiation modes, that are not confined by the nanopost. These radiation modes gets reflected by the bottom mirror and interferes with the transmitted part of the HE11 mode in the far-field.

trumpet nanowires are found, where the backscattering is reduced due to the out-coupling taper. For those geometries the interference rings in Fig. 6.7 are strongly reduced in accordance with the above explanation.

Fig. 6.8 sketches the interference process between the HE11 mode and the backscattered radiation modes. The part of the HE11 mode that is transmitted into the far-field at an angle θ is phase-shifted by $\phi_{t,top}^{HE11}$ and the part that is backscattered into a radiation mode at the same angle θ obtains a phase-shift of $\phi_{r,top}$. Additionally there are three contributions to the phase of the radiation mode: 1) the propagation of the distances d_1 and d_2 , 2) the reflection at the bottom mirror and 3) the phase due to the conversion of the radiation modes in the nanopost layer into pure TE and TM free space radiation modes (more details on this is found in Appendix D.2). The difference in phase between the two paths is

$$\begin{aligned} \delta\phi &= k_0 (d_1 + d_2) + \phi_{r,top} + \phi_{r,bot} + \phi_{rad}^{TE/TM} - \phi_{t,top}^{HE11} \\ &= \frac{4\pi h \cos\theta}{\lambda} + \phi_{r,top} + \phi_{r,bot} + \phi_{rad}^{TE/TM} - \phi_{t,top}^{HE11}. \end{aligned} \quad (6.6)$$

The bright rings in the far-field appear when there are constructive interference between the two paths meaning that $\delta\phi = 2\pi m$, where $m = 0, 1, 2, \dots$. In Fig. 6.9 the phase difference is plotted for the first, fourth and sixth height in Fig. 6.5, corresponding to the far-fields in Fig. 6.7 with $h_t = 207, 830$ and 1245 nm. Above the plots the far-field along the x -axis from the centre in Fig. 6.7 is shown for visualising the actual location of the far-field rings.

As seen in Fig. 6.9 the phase difference is slightly different for the free space TE and TM modes. However, the difference is too small for two distinct bright rings

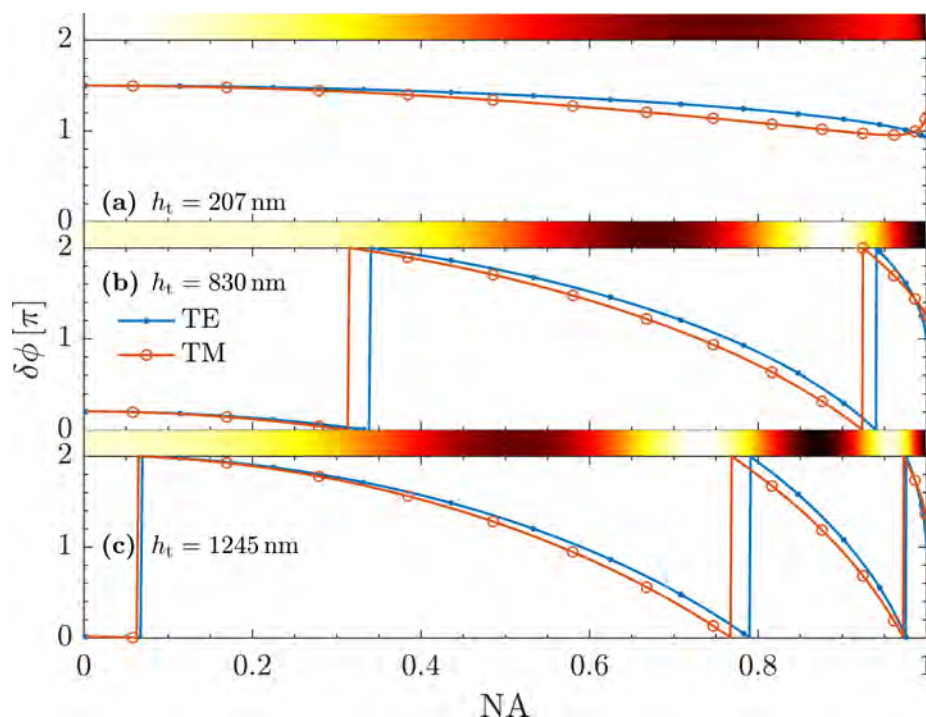


Figure 6.9: Phase difference for the two paths as defined in Fig 6.8 for three different sizes of the nanopost. It is noted that $\delta\phi$ is almost the same for the free space TE and TM modes. Above the plots, the far-field along the x -axis is shown to clarify the position of the rings.

for each polarization to appear. Instead a ring is located near the zero points of the TE/TM phase difference as seen in the far-field slice above the three plots. For $h_t = 207$ nm our model predicts no bright rings in the far-field, for $h_t = 830$ nm our model predicts two rings in the far-field at around $NA = 0.33$ and $NA = 0.93$ and for $h_t = 1245$ nm three rings are predicted to appear at $NA = 0.07$, $NA = 0.78$ and $NA = 0.97$. The predicted rings for all three nanopost heights agree well with the actual location for $NA > 0.4$. However, the simple model generally predicts the rings to be located at a slightly larger NA than the actual location. In order to get an even better description the Gaussian shape of the HE₁₁ mode and the intensity of each of the radiation modes needs to be taken into account at the cost of extra complexity. For $NA < 0.4$ the intensity of the Gaussian HE₁₁ mode is much larger than the intensity of the radiation modes, and thus the predicted rings within this numerical aperture is not seen in the computed far-fields.

It should be noted that for $h_t = 830$ nm the ring is placed outside a numerical aperture of 0.80, which leads to a reduction in source efficiency as seen in Fig. 6.5(b), whereas for $h_t = 1245$ nm the inner ring is located within a numerical

aperture of 0.80 leading to a larger source efficiency. This opens up for the opportunity to tune the source efficiency through the interference between the HE11 mode and the radiation modes in the far-field. In this study, the dipole emitter was kept in an antinode of the HE11 mode relative to both the bottom mirror and the top facet. The source efficiency can be tuned even further if we relax on the condition that the emitter has to sit in an antinode, however, this will be at the cost of some Purcell enhancement. The division of the radiation modes into TE and TM modes in Fig. 6.9 is not straightforward, since the numerically found radiation modes in the nanopost layers are not necessarily the same as those in the air layer. These details are discussed in Appendix D.2.

Source efficiency

In order to explain the reduced source efficiency for the smallest nanopost, we have plotted the source efficiency as function of numerical aperture in Fig. 6.10 computed in four different ways: 1) using only the HE11 mode, 2) using only the radiation modes, 3) using the full model, and 4) using a simple interference model based on the phase difference plotted in Fig. 6.9 - see Eq. (6.7) below. As seen, using only the HE11 mode leads to a very high source efficiency for the smallest nanopost. This is a consequence of the increased Purcell enhancement as compared to the HE11 source efficiency for the other two nanopost heights. However, the total source efficiency including all contributions is in general lower for the smallest nanopost. This indicates that the radiation modes and the HE11 mode interferes destructively. In order to investigate this the following simple equation for computing the far-field power is used [129]

$$P_{\text{Simple}} = P_{\text{HE11}} + P_{\text{Rad}} + 2\sqrt{P_{\text{HE11}}P_{\text{Rad}}} \cos \delta\phi, \quad (6.7)$$

where the source efficiency is obtained by dividing the power in the far-field with the total emitted power as in Eq. (6.4). $\delta\phi$ is obtained from Fig. 6.9, and the power emitted into the HE11 mode (P_{HE11}) and the radiation modes (P_{Rad}) are easily extracted, when using the oFMM formalism. We obtain a good agreement between Eq. (6.7) and the full model as observed in Fig. 6.10 for all three nanopost sizes. The phase difference for the smallest nanopost size is between 1.5π and π (see Fig. 6.9(a)), and thus the interference term in Eq. (6.7) will give a negative contribution. We thus conclude that the reduced source efficiency for the smallest nanopost size observed in Fig. 6.5(b) is due to destructive interference between the HE11 mode and the radiation modes in the far-field. Thus if the phase difference between the HE11 mode and the radiation modes could be engineered to give constructive interference the source efficiency could be improved. How to engineer this phase difference remains unanswered in this study, however, if possible in a realistic design it opens up a new way of enhancing the source efficiency for free space emitting single-photon sources. Regarding what

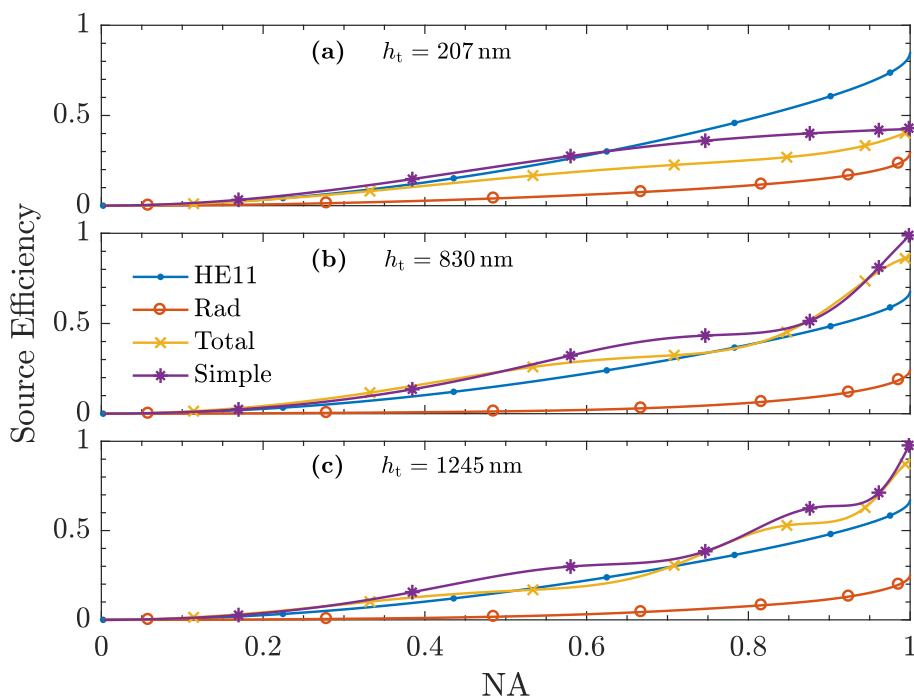


Figure 6.10: Source efficiency as function of numerical aperture for three different nanopost sizes, using only the HE11 mode, only the radiation modes, all modes and a simplified model given in Eq. (6.7).

the interference between the HE11 mode and the backscattered radiation modes means for the indistinguishability has not been investigated in this study.

Broadbandness of nanopost

From an experimental point-of-view, the tolerance of the Purcell enhancement and the source efficiency towards the emission wavelength is important, since the growth method of the QD limits the precision to which the emission wavelength can be engineered. The Purcell enhancement and the source efficiency as function of emission wavelength are plotted in Fig. 6.11 for the four shortest nanoposts. As expected the full-width half-maximum (FWHM) of the Purcell enhancement is largest for the shortest nanopost due to the larger Q -factor, which is the consequence of the small cavity size leading to larger free spectral range (FSR) [130]. The source efficiency is seen to be almost flat across the FWHM of Γ_{HE11} . The nanopost was designed using the single-mode model, such that the largest Purcell enhancement, should be obtained at $\lambda = 920$ nm. However, for the shortest nanopost, where the evanescent modes play a role, the resonance wavelength of the cavity is shifted by ~ 4 nm. This was also observed in Chapter 4 for the PhC

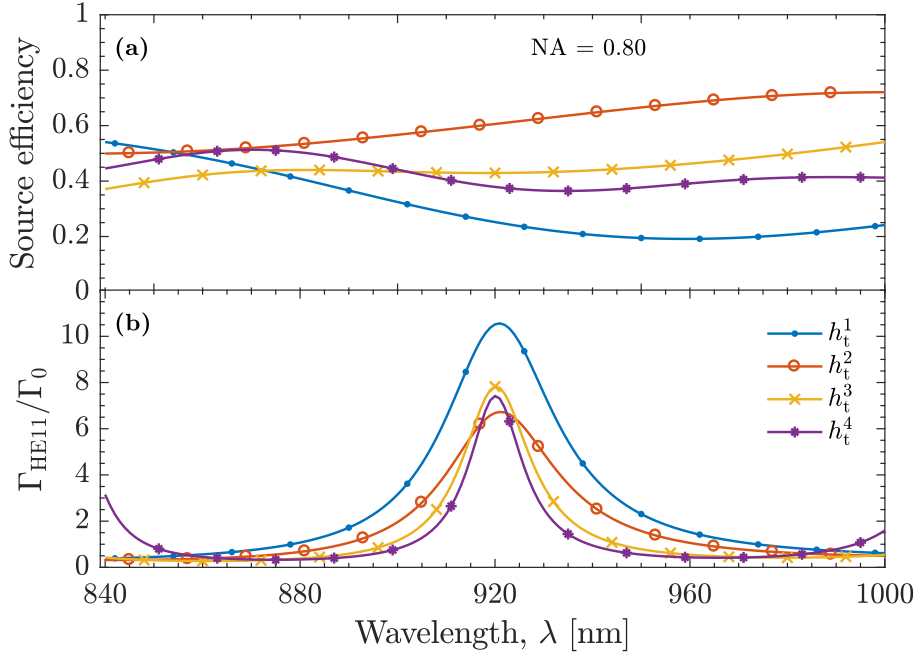


Figure 6.11: (a) The source efficiency for NA = 0.80 and (b) the Purcell enhancement as function of emitter wavelength for the 4 shortest nanopost sizes.

Fano geometry, when the distance between the PTE and the microcavity became small. The shift of the resonance wavelength is a consequence of the coupling between the evanescent modes, and the guided and radiation modes at the top facet and bottom mirror.

6.4 Conclusion

We sought out to study the performance of the simplest nanowire SPS design - the nanopost - using a single-mode model and a full model taking advantage of the modal access provided by the oFMM formalism. The shortest nanopost showed a Purcell enhancement of around 10, whereas all other heights showed a Purcell enhancement of around 7. We found that the source efficiency depends on the nanopost height due to interference between the HE11 mode and the backscattered radiation modes, that are reflected by the bottom mirror into the far-field.

The single-mode model predicted the correct Purcell enhancement for all nanopost heights except for the shortest, where the coupling between HE11, radiation and evanescent modes leads to a breakdown of this model. Regarding the source efficiency and the far-field radiation pattern, the single-mode model proved to be

insufficient, due to the backscattered radiation modes, which are only included in the full model.

Based on the results presented in this chapter, Julien and his co-workers at CEA are currently fabricating and characterizing two samples: 1) the shortest nanopost in order to experimentally verify the additional Purcell enhancement predicted by the full model and 2) the second shortest nanopost due to its predicted source efficiency of around 60 % for $NA = 0.8$ and a Purcell enhancement of 6.5, which are both fairly good numbers for such a simple structure. Unfortunately, they do not have any experimental results yet that could feature in the present thesis.

Cavity–waveguide interplay in lossy resonators and its role in optimal single photon sources

QDs embedded in photonic structures form the basis of modern solid-state quantum optics [12–15], both as single-photon sources, as discussed in the introductions to Chapters 5 and 6, and more generally as light-matter interfaces [131, 132]. In Chapters 5 and 6 we briefly discussed the micropillar and nanowire single-photon sources and how they are fundamentally different. Here we will expand the discussion to include the decoherence processes i.e. the photons interactions with phonons. Furthermore, we have until now treated the dipole as a monochromatic emitter, however, in this chapter, this is no longer the case. The emission spectrum of a QD in a bulk material is seen in Fig. 7.1. The photons emitted in the zero-phonon line (ZPL) are coherent and indistinguishable and roughly 90 % of the emission goes into this line, however, 10 % of the emitted photons are in the phonon sidebands, which makes them incoherent and distinguishable and thus useless for quantum information applications. Furthermore, photons emitted in bulk are emitted in almost random directions, and thus the efficiency is extremely low. Placing the QDs in photonic structures such as the needle or the nanopost investigated in Chapters 5 and 6 enhances the efficiency, since the photons will be emitted in a preferred direction.

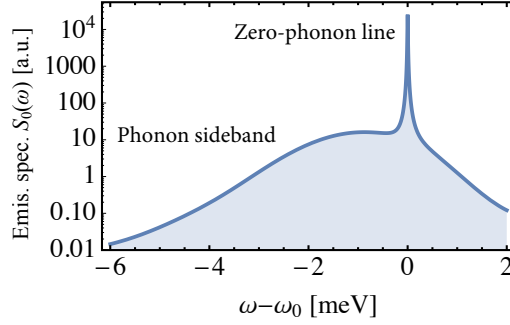


Figure 7.1: Emission spectrum from a quantum dot in a bulk material. The sharp peak is the zero-phonon line, which contains roughly 90 % of the emission, whereas 10 % of the emission goes into the phonon sideband.

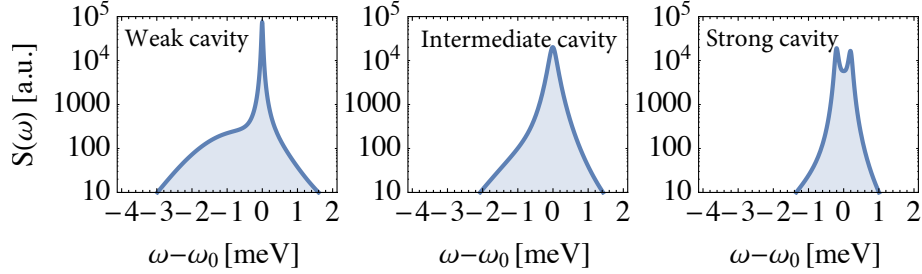


Figure 7.2: Emission spectra for a QD placed in a weak, an intermediate and a strong cavity.

A way to improve the indistinguishability is by enhancing the emission into the zero-phonon line by placing the QD in a cavity, as seen from the emission spectra in Fig. 7.2. However, for cavities with very high Q -factors, we enter the strong-coupling regime, where the zero-phonon line splits, and thus decreases the indistinguishability. The micropillar structures [25, 29, 124, 125] are examples of a nanocavity that enhances the spontaneous emission into a well-defined cavity mode through the Purcell effect, while simultaneously suppressing decoherence mechanisms as theoretically investigated in Refs. [133, 134] and experimentally shown in Ref. [135].

Nanowires do not enhance the emission through cavity effects, however they have an inherently high β -factor (see Section 2.5) due to screening effects meaning most of the emission goes into the desired optical mode [27, 61, 62, 107] (see Fig. 6.2 in Section 6.2), whereas PhC waveguide line defects exploit slow-light effects in order to obtain the same high β -factor [28, 66, 67]. The high β -factor ensures a good spatial overlap between successively emitted photons. The indistinguishability is a measure for the spatial, spectral and polarizational overlap between single photons, and thus a high β -factor is advantageous.

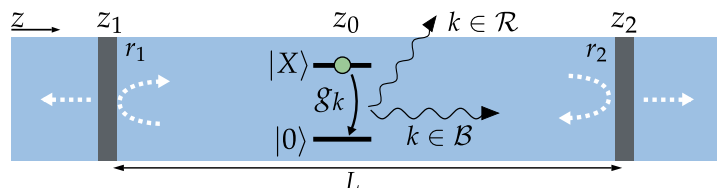


Figure 7.3: Illustration of a two-level emitter in a Fabry-Perot cavity formed by two mirrors embedded in a waveguide structure.

The nanocavities and waveguides are treated very differently in standard quantum optics theory. The first is often modelled using a Jaynes-Cummings model, where the electric field inside the cavity is quantized as a single-mode [136], while the latter are modelled as an unstructured reservoir with a continuum of optical modes with little or no spectral variation [137]. However, in the regime of strongly dissipative cavities¹, neither of the two models provide a good physical description.

This point is illustrated by considering a waveguide structure, where two mirrors are embedded forming a Fabry-Perot cavity as sketched in Fig. 7.3. A smooth transition between a strongly localised single-mode cavity to a standard broadband waveguide is expected when decreasing the mirror reflectivities from 1 to 0, with an intermediate regime at low Q -factors, where the optical local density of states (LDOS) has characteristics from both a cavity and a waveguide [138–140]. However, the Jaynes-Cummings model fails to demonstrate this behaviour, and does not describe the properties of emitters in either a waveguide or a bulk medium for vanishing Q -factors.

The work presented in this chapter is based on our submitted manuscript available on arXiv [141] (J4). In the manuscript, we present a quantum optical model that captures the transition between a high- Q cavity and a waveguide, securing consistent treatment of waveguides, lossy resonators and high quality cavities. Our model bridges highly accurate optical simulations and microscopic quantum dynamical calculations. This enables calculation of the quantum properties of the generated light (such as the indistinguishability), while fully accounting for the electromagnetic properties of the nanostructure. Using our model, we identify an optimal regime of operation for QD single-photon sources, which simultaneously harnesses the high efficiency of a waveguide and the phonon-suppressing spectral structure of a cavity. My contribution to Ref. [141] has been the derivation of the optical Green’s function and the LDOS. Thus this chapter will focus on the classical optical considerations given in our manuscript and only summarize the quantum mechanical model in broader terms. Any reader interested in the details of the quantum optical model are referred to Ref. [141] and its supplementary

¹Meaning cavities having an inherent non-zero β -factor (as in nanowires) and a low Q -factor.

information (SI). Throughout the chapter we will refer to our manuscript, when details has been omitted.

The chapter is organized as follows. In Section 7.1 and 7.2 we derive the LDOS and the Green’s function for the structure sketched in Fig. 7.3, respectively. These both serve as the classical input to our quantum optical master equation describing the dynamical and optical properties of the emitter. We use our model in Section 7.3, and calculate the efficiency and indistinguishability of a single-photon source realized by a high β waveguide with a Fabry-Perot cavity embedded.

7.1 LDOS for Fabry-Perot cavity in waveguide

In this section, we will derive the LDOS, which serve as the input to our quantum mechanical model, and separate the waveguide and cavity contributions. The LDOS is equivalent to the normalised spontaneous emission rate, Γ , which has been used up to this point in the present thesis.

So far in the thesis, an optical mode has been defined by its spatial distribution e.g. the Gaussian shape of the HE11 mode or the doughnut shape of the TE01 mode. However, in this chapter a mode labelled k is defined both from its frequency and from its transverse field profile. We divide our optical modes into two sets: the first set, \mathcal{B} , contains all modes with a certain transverse field profile of interest (e.g. all frequencies for the HE11 mode), and the second set, \mathcal{R} , contains all other modes including radiation modes or potentially other guided modes with a different transverse field profile than the ones in \mathcal{B} (e.g. the TE01 mode). Each mode set is associated with the total LDOS given by the emitter coupling strengths, g_k [56]

$$\mathcal{L}_{\mathcal{S}}(\omega) = \pi \sum_{k \in \mathcal{S}} |g_k|^2 \delta(\omega - \omega_k), \quad \mathcal{S} = \mathcal{B}, \mathcal{R}. \quad (7.1)$$

This expression is completely general, where the dependence on the optical environment is enclosed in the emitter coupling strength, g_k . In the absence of mirrors in the waveguide, the LDOS for both set of modes can be considered constant over the spectrum of the emitter as depicted in Fig. 7.4(a), with $\mathcal{L}_{\mathcal{S}} \simeq \Gamma_{\mathcal{S}}^0$, where $\Gamma_{\mathcal{S}}^0$ is the emission rate normalized to the bulk SE rate into the mode set \mathcal{S} for an emitter in a pure waveguide. When the mirrors has finite amplitude reflectivities r_1 and r_2 , the LDOS into the mode set \mathcal{B} is given as [57]

$$\mathcal{L}_{\mathcal{B}}(\omega) = \Gamma_{\mathcal{B}}^0 \text{Re} \left\{ \frac{[1 + \tilde{r}_1(\omega)][1 + \tilde{r}_2(\omega)]}{1 - \tilde{r}_1(\omega)\tilde{r}_2(\omega)} \right\}, \quad (7.2)$$

where $\Gamma_{\mathcal{B}}^0$ is the emission rate into the waveguide in the absence of mirrors, and where $\tilde{r}_j(\omega) = r_j \exp \left[i \left(\phi_0^j + \beta(\omega)L \right) \right]$ includes the propagation phase in

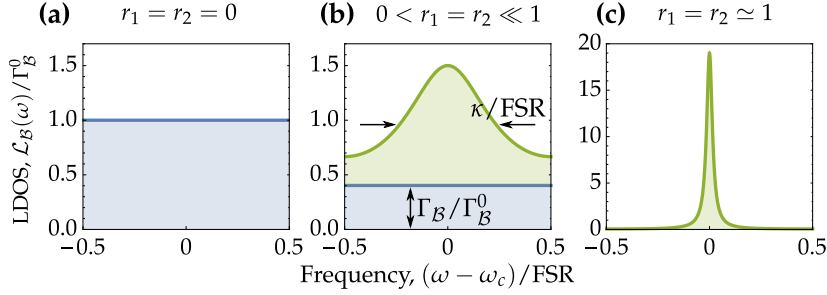


Figure 7.4: Optical LDOS at the emitter position as function of frequency scaled with the free spectral range (FSR) for the Fabry-Perot cavity embedded in a waveguide (see Fig. 7.3) for mirrors with (a) weak, (b) intermediate ($r_1 = r_2 = 0.2$) and (c) high reflectivity. $\Gamma_{\mathcal{B}}$ and $\Gamma_{\mathcal{B}}^0$ is the direct emission into the mode set \mathcal{B} for a waveguide structure with and without mirrors embedded respectively.

the emitter-mirror roundtrip,² where ϕ_0^j is the mirror reflection phase, L is the cavity length and $\beta(\omega) = n_{\text{eff}}\omega/c$ is the propagation constant, which is assumed dispersion-less. n_{eff} is the effective refractive index of the waveguide mode.

In Fig. 7.4(b-c), we plot the LDOS given in Eq. (7.2) for $r_1 = r_2 = 0.2$ and $r_1 = r_2 \simeq 1$ respectively. What should be noted, is that for the intermediate regime in (b) the LDOS features a Lorentzian offset by a constant background. The background contribution stems from the waveguide nature of the dielectric structure, whereas the Lorentzian peak is a signature of the cavity quasi-mode, which becomes the dominant contribution in (c). In order to correctly account for the emitter-cavity dynamics in our optical master equation (see Eq. (7.10)), we need to separate the waveguide and cavity contributions to the LDOS. Doing this separation, allows us to correctly model the quantum properties of the emitted light for the whole range of cavity Q -factors. We approximate the LDOS in Eq. (7.2) as a sum between a spectrally constant background stemming from the waveguide and a Lorentzian originating from the cavity

$$\mathcal{L}_{\mathcal{B}}(\omega) \simeq \bar{\mathcal{L}}_{\mathcal{B}}(\omega) = \ell_{\mathcal{B}}\Gamma_{\mathcal{B}}^0 + \ell_c\Gamma_{\mathcal{B}}^0 \frac{\tilde{\kappa}}{\tilde{\kappa}^2 + \tilde{\omega}^2} \equiv \Gamma_{\mathcal{B}} + \mathcal{L}_c \frac{\tilde{\kappa}}{\tilde{\kappa}^2 + \tilde{\omega}^2}, \quad (7.3)$$

where we have introduced the dimensionless frequency, $\tilde{\omega} = Ln_{\text{eff}}(\omega - \omega_c)/c$ with ω_c being the cavity resonance frequency and linewidth (FWHM), $\tilde{\kappa} = \kappa(Ln_{\text{eff}}/c)$. The contributions to the LDOS from background waveguide modes and the cavity are given by the weights $\ell_{\mathcal{B}}$ and ℓ_c respectively. These and the linewidth $\tilde{\kappa}$ are uniquely determined by the mirror reflectivities r_1 and r_2 as shown in details in the supplementary information (SI) of [141]. In broad terms the relation is determined by requiring the following for $\bar{\mathcal{L}}_{\mathcal{B}}$ and $\mathcal{L}_{\mathcal{B}}$:

²This is similar to Eqs. (6.1) and (6.2)

1 They should be equal at $\tilde{\omega} = 0$:

$$\mathcal{L}_{\mathcal{B}}(0) = \bar{\mathcal{L}}_{\mathcal{B}}(0). \quad (7.4)$$

2 Their second derivatives should be equal at $\tilde{\omega} = 0$:

$$\frac{d^2}{d\tilde{\omega}^2}\mathcal{L}_{\mathcal{B}}(0) = \frac{d^2}{d\tilde{\omega}^2}\bar{\mathcal{L}}_{\mathcal{B}}(0). \quad (7.5)$$

3 Their integrals from $-\pi$ to π should be equal:

$$\int_{-\pi}^{\pi} \mathcal{L}_{\mathcal{B}}(\tilde{\omega})d\tilde{\omega} = \int_{-\pi}^{\pi} \bar{\mathcal{L}}_{\mathcal{B}}(\tilde{\omega})d\tilde{\omega}. \quad (7.6)$$

In the SI of Ref. [141] these equations are solved for two situations: 1) a symmetric cavity with $r_1 = r_2$, and 2) a cavity with a perfect bottom mirror $r_1 = 1$. These requirements ensure a good approximation of the LDOS in Eq. (7.2), which safely allow us to separate the waveguide and cavity contributions. For the case of a symmetric cavity, $r_1 = r_2 = r$, the above requirements lead to the following equations, which uniquely determines $\ell_{\mathcal{B}}$, ℓ_c and $\tilde{\kappa}$ from the mirror reflectivity (see SI of Ref. [141] for details)

$$\ell_{\mathcal{B}} = \frac{1-r^2}{(1-r)^2} \left[1 - \frac{r\tilde{\kappa}^2}{(1-r)^2} \right], \quad (7.7a)$$

$$\ell_c = \frac{r(1-r^2)}{(1-r)^4} \tilde{\kappa}^3, \quad (7.7b)$$

$$\frac{1}{\pi} \tilde{\kappa}^3 \arctan\left(\frac{\pi}{\tilde{\kappa}}\right) - \tilde{\kappa}^2 = \frac{(1-r)^2}{r} \left[\frac{(1-r)^2}{1-r^2} - 1 \right]. \quad (7.7c)$$

Solving the last equation numerically for $\tilde{\kappa}$, and inserting the result in the first two equations determines all three parameters for a particular value of r . On resonance the LDOS in Eq. (7.3) becomes

$$\bar{\mathcal{L}}_{\mathcal{B}}(\omega) = \ell_{\mathcal{B}}\Gamma_{\mathcal{B}}^0 + \frac{\ell_c\Gamma_{\mathcal{B}}^0}{\tilde{\kappa}}. \quad (7.8)$$

The cavity contribution to the LDOS at resonance must correspond to the cavity-enhanced SE rate given by $\Gamma_{\text{cav}} = 4g^2/\kappa$ [142]. This allows us to determine the emitter-cavity coupling strength through ℓ_c and $\Gamma_{\mathcal{B}}^0$ as

$$g = \sqrt{\frac{\Gamma_{\mathcal{B}}^0\ell_c c}{4Ln_{\text{eff}}}}. \quad (7.9)$$

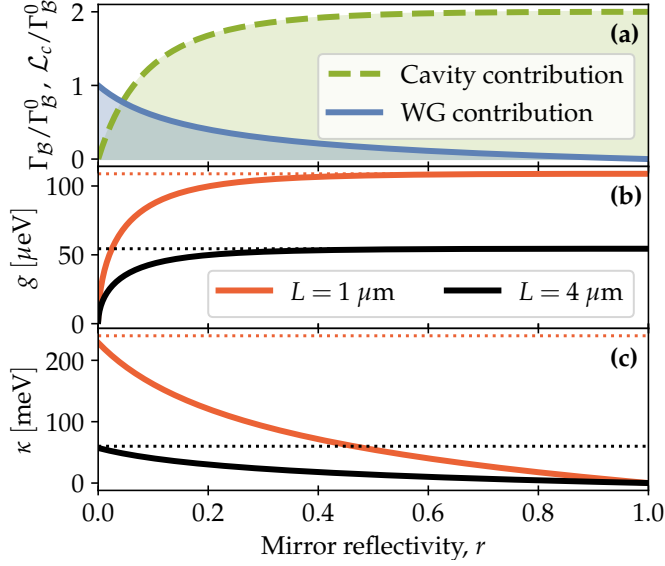


Figure 7.5: The dependence on the mirror reflectivity of (a) the cavity, \mathcal{L}_c , and waveguide, Γ_B , contributions to the LDOS, and (b-c) the emitter-cavity coupling rate, g , and the cavity decay rate, κ , for cavity lengths of $L = 1 \mu\text{m}$ and $L = 4 \mu\text{m}$ with $n_{\text{eff}} = 2.5$. The limiting values of g and κ are indicated by the dashed lines.

Fig 7.5(a) shows the contribution to the LDOS from the background waveguide modes, $\ell_B = \Gamma_B/\Gamma_B^0$, and the cavity quasimode, $\ell_c = \mathcal{L}_c/\Gamma_B^0$, as function of the mirror reflectivity for the symmetric cavity. As seen, the system transforms gradually from being a pure waveguide ($r = 0$) to a cavity ($r \rightarrow 1$) with full suppression of the waveguide background modes. Similarly, the emitter-coupling strength in Eq. (7.9) is shown for two cavity lengths in Fig. 7.5(b), which approaches the value $g_{\text{max}} = \sqrt{\Gamma_B^0 c/2Ln_{\text{eff}}}$ as the reflectivity increases. The linewidth in Fig. 7.5(c) tends to zero as $r \rightarrow 1$, and interestingly it does not diverge as $r \rightarrow 0$, but approaches a value of $\kappa_{\text{max}} \simeq 2.895c/(n_{\text{eff}}L)$. Here it should be noted, that the linewidth only relates to the cavity contribution, which approaches zero as $r \rightarrow 0$. Thus the full LDOS do not have a linewidth, when there is no cavity.

The separated LDOS in Eq. (7.3) allows us to derive a quantum mechanical master equation (details in SI of [141]) describing the dynamical and optical properties of the emitter

$$\dot{\rho}(t) = -i \left[g \left(\hat{a}^\dagger \sigma + \hat{a} \sigma^\dagger \right), \rho(t) \right] + (\Gamma_B + \Gamma_R) \mathcal{D}[\sigma] + \kappa \mathcal{D}[\hat{a}], \quad (7.10)$$

where ρ is the density operator for the cavity-emitter system, $\hat{a}(\hat{a}^\dagger)$ is the annihilation (creation) operator for the cavity mode, and $\mathcal{D}[x] = x\rho(t)x^\dagger - \frac{1}{2} \{x^\dagger x, \rho(t)\}$

is the Lindblad dissipator and $\sigma = |g\rangle\langle e|$. The square brackets $[\hat{x}, \hat{y}] = \hat{x}\hat{y} - \hat{y}\hat{x}$ is the commutator. It should be stressed that at this point, we have not included the influence of phonons, and that the above equation is only presented in order to motivate our division of the LDOS into a waveguide and a cavity contribution. The first term describes the emitter-cavity interaction, where only the cavity contribution to the LDOS has an influence. The second term accounts for the emission into the waveguide background modes and the radiation modes. The last term accounts for the cavity decay rate, i.e. the rate of which the photons escapes the cavity. In the absence of mirrors, $r = 0$, we have $g = 0$, $\Gamma_{\mathcal{B}} = \Gamma_{\mathcal{B}}^0$ and the master equation reduces to the usual waveguide case. For the limit of high reflectivity, $r \rightarrow 1$, the waveguide contribution to the LDOS vanishes, $\Gamma_{\mathcal{B}} \rightarrow 0$, and the master equation describes an emitter coupled to a cavity quasimode and a radiation bath.

For single-mode waveguide structures, the cavity only affects the single guided mode and not the radiation modes. However, for a multimode structure (e.g. a micropillar), the emission rate $\Gamma_{\mathcal{R}}$ includes the emission into both radiation modes and other guided modes, which are not included in the mode set \mathcal{B} . The cavity affects all guided modes, and the total LDOS of the mode set \mathcal{R} becomes

$$\mathcal{L}_{\mathcal{R}}(\omega) = \Gamma_{\text{Rad}} + \sum_m \Gamma_m^0 \text{Re} \left\{ \frac{[1 + \tilde{r}_1^m(\omega)][1 + \tilde{r}_2^m(\omega)]}{1 - \tilde{r}_1^m(\omega)\tilde{r}_2^m(\omega)} \right\}, \quad (7.11)$$

where Γ_{Rad} is the emission rate into radiation modes. The sum runs over all guided modes, which are not included in the mode set \mathcal{B} . From now on, we will consider a single-mode waveguide.

7.2 Green's function

Now that we have derived the LDOS of the waveguide cavity structure, we will determine the Green's function in order to calculate the electromagnetic field, which is coupled to the waveguide to the right in Fig. 7.3. For simplicity, we re-sketch the structure in Fig. 7.6. We derive the Green's function using the Fourier modal method and the scattering matrix formalism, as has already been used throughout this thesis.

Inside the cavity section, we expand the forward propagating part of the field to the right of the emitter in Fig. 7.6 on the cavity section eigenmodes, \mathbf{E}_j^C , as in Eq. (5.1) [46]

$$\mathbf{E}(\mathbf{r}, \omega) = \sum_j a_j^C(\omega, \mathbf{r}_0) \mathbf{E}_j^{C,0}(\mathbf{r}_{\perp}, \omega) \exp[i\beta_j(z - z_0)], \quad (z_0 \leq z \leq z_2), \quad (7.12)$$

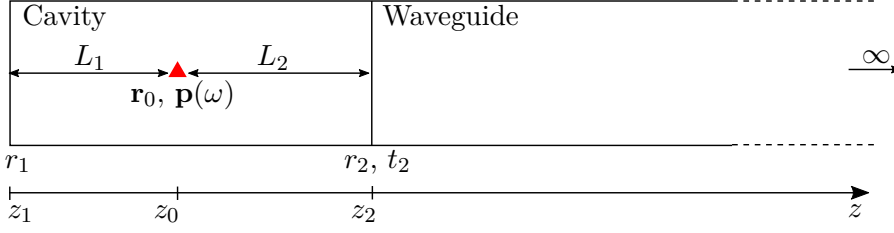


Figure 7.6: Schematic showing a cavity with mirror reflectivities r_1 and r_2 coupled to a waveguide with a transmittivity of t_2 . The point dipole, with dipole moment \mathbf{p} , is placed at \mathbf{r}_0 .

where a_j^C are the modal expansion coefficients for the cavity section and $z_0(z_2)$ is the z -coordinate of the emitter (top mirror). In the single-mode model, the modal expansion coefficients are given by Eq. (6.2) in Section 6.1. For clarity, we restate the equation here with the notation used in this chapter

$$a_{\mathcal{B}}^C(\omega, \mathbf{r}_0) = \frac{1 + \tilde{r}_1(\omega, z_0)}{1 - \tilde{r}_1(\omega, z_0)\tilde{r}_2(\omega, z_0)} a_{\mathcal{B}}^0(\omega, \mathbf{r}_{\perp}^0), \quad (7.13)$$

where $a_{\mathcal{B}}^0 = a_1^0$ is the modal expansion coefficient for the fundamental guided mode of the infinite nanowire, and is given by Eq. (5.2) in Section 5.1 as

$$a_{\mathcal{B}}^0(\omega, \mathbf{r}_{\perp}^0) = \frac{i\omega \mathbf{p} \cdot \mathbf{E}_{\mathcal{B}}^{C,0}(\mathbf{r}_{\perp}^0, \omega)}{2[W]}, \quad (7.14)$$

where \mathbf{p} is the dipole moment of the emitter positioned at $(\mathbf{r}_{\perp}^0, z_0)$. We normalize the mode profiles of the fundamental guided mode of the cavity section and the waveguide, such that they share the same Poynting power (see Eq. (2.7) in Section 2.1)

$$\int_{\mathbf{r}_{\perp}} \text{Re} \left[\mathbf{E}_{\mathcal{B}}^{C,0}(\mathbf{r}, \omega) \times \mathbf{H}_{\mathcal{B}}^{C,0*}(\mathbf{r}, \omega) \right] \cdot \hat{\mathbf{z}} d\mathbf{r}_{\perp} = \int_{\mathbf{r}_{\perp}} \text{Re} \left[\mathbf{E}_{\mathcal{B}}^{\text{WG},0}(\mathbf{r}, \omega) \times \mathbf{H}_{\mathcal{B}}^{\text{WG},0*}(\mathbf{r}, \omega) \right] \cdot \hat{\mathbf{z}} d\mathbf{r}_{\perp}. \quad (7.15)$$

The emitted field by the dipole \mathbf{p} in the cavity is partly transmitted by the second mirror, which leads to an electric field in the waveguide mode \mathcal{B} at z_2 . The field in the waveguide mode is generally given as [44]

$$\begin{aligned} \mathbf{E}_{\mathcal{B}}^{\text{WG}}([\mathbf{r}_{\perp}, z_2], \omega) &= a_{\mathcal{B}}^{\text{WG}} \mathbf{E}_{\mathcal{B}}^{\text{WG},0}(\mathbf{r}_{\perp}, \omega) \\ &= \omega^2 \mu_r \mu_0 \overset{\leftrightarrow}{\mathbf{G}}([\mathbf{r}_{\perp}, z_2], \mathbf{r}_0; \omega) \mathbf{p}(\omega), \end{aligned} \quad (7.16)$$

where $\mu_r = 1$, $a_{\mathcal{B}}^{\text{WG}}$ is the modal excitation coefficient for the \mathcal{B} mode in the waveguide and $\mathbf{E}_{\mathcal{B}}^{\text{WG},0}(\mathbf{r}_{\perp}, \omega)$ is the normalized transversal field profile of the \mathcal{B} waveguide mode. The modal excitation coefficient in the waveguide is given as $a_{\mathcal{B}}^{\text{WG}} = \tilde{t}_2 a_{\mathcal{B}}^C$, where $\tilde{t}_2 = t_2 \exp(i(\phi_t + \beta_{\mathcal{B}} L_2))$. $\overset{\leftrightarrow}{\mathbf{G}}$ is the Green's function (a dyadic tensor) mapping the emitted field at \mathbf{r}_0 to the field in the waveguide at z_2 . We now wish to determine the Green's tensor, using the above expressions. We use the following notation for the Green's tensor

$$\overset{\leftrightarrow}{\mathbf{G}} = \begin{bmatrix} G_{xx} & G_{xy} & G_{xz} \\ G_{yx} & G_{yy} & G_{yz} \\ G_{zx} & G_{zy} & G_{zz} \end{bmatrix} = \begin{bmatrix} \mathbf{G}_x & \mathbf{G}_y & \mathbf{G}_z \end{bmatrix}. \quad (7.17)$$

From Eq. (7.16) we get

$$\overset{\leftrightarrow}{\mathbf{G}}\mathbf{p}(\omega) = \frac{a_{\mathcal{B}}^{\text{WG}} \mathbf{E}_{\mathcal{B}}^{\text{WG},0}(\mathbf{r}_{\perp})}{\omega^2 \mu_0}, \quad (7.18)$$

and insertion of Eqs. (7.13) and (7.14), and using $a_{\mathcal{B}}^{\text{WG}} = \tilde{t}_2 a_{\mathcal{B}}^C$ we arrive at

$$\begin{aligned} \overset{\leftrightarrow}{\mathbf{G}}\mathbf{p} &= \frac{i}{2[W]\omega\mu_0} \frac{\tilde{t}_2(\omega)(1 + \tilde{r}_1(\omega))}{1 - \tilde{r}_1(\omega)\tilde{r}_2(\omega)} \left(\mathbf{p} \cdot \mathbf{E}_{\mathcal{B}}^{C,0}(\mathbf{r}_{\perp}^0, \omega) \right) \mathbf{E}_{\mathcal{B}}^{\text{WG},0}(\mathbf{r}_{\perp}, \omega) \\ &= \frac{i}{2[W]\omega\mu_0} \frac{\tilde{t}_2(\omega)(1 + \tilde{r}_1(\omega))}{1 - \tilde{r}_1(\omega)\tilde{r}_2(\omega)} \left[\mathbf{E}_{\mathcal{B}}^{\text{WG},0}(\mathbf{r}_{\perp}, \omega) \left(\mathbf{E}_{\mathcal{B}}^{C,0}(\mathbf{r}_{\perp}^0, \omega) \right)^T \right] \mathbf{p} \Rightarrow \\ \overset{\leftrightarrow}{\mathbf{G}} &= \frac{i}{2[W]\omega\mu_0} \mathcal{G}(\omega) \mathbf{E}_{\mathcal{B}}^{\text{WG},0}(\mathbf{r}_{\perp}, \omega) \left(\mathbf{E}_{\mathcal{B}}^{C,0}(\mathbf{r}_{\perp}^0, \omega) \right)^T, \end{aligned} \quad (7.19)$$

where T is the transpose and

$$\mathcal{G}(\omega) = \tilde{t}_2(\omega) \frac{1 + \tilde{r}_1(\omega)}{1 - \tilde{r}_1(\omega)\tilde{r}_2(\omega)} \quad (7.20)$$

is the cavity filtering function. Using Eq. (7.16) the field in the waveguide ($z \geq z_2$) is given as

$$\begin{aligned} \mathbf{E}_{\mathcal{B}}^{\text{WG}}(\mathbf{r}, \omega) &= \frac{i\omega}{2} \mathcal{G}(\omega) \exp(i\beta_{\mathcal{B}}(\omega)[z - z_2]) \\ &\quad \mathbf{E}_{\mathcal{B}}^{\text{WG},0}(\mathbf{r}_{\perp}, \omega) \left(\mathbf{E}_{\mathcal{B}}^{C,0}(\mathbf{r}_{\perp}^0, \omega) \right)^T \mathbf{p}(\mathbf{r}_0, \omega). \end{aligned} \quad (7.21)$$

Having determined the Green's function and the electric field in the waveguide, we will now derive a simple expression for the power going through the second mirror. First the power emitted by the point dipole in the absence of mirrors

into mode \mathcal{B} , $P_{\mathcal{B}}^0$, is given by two equivalent expressions: 1) by using Eq. (3.20) and 2) by the time averaged Poynting power in Eq. (2.7). Using these leads to

$$\begin{aligned} P_{\mathcal{B}}^0 &= \frac{\omega}{2} \text{Im} \left[a_{\mathcal{B}}^0 \mathbf{E}_{\mathcal{B}}^{C,0}(\mathbf{r}_{\perp}^0, \omega) \cdot \mathbf{p} \right] \\ &= 2 \left| a_{\mathcal{B}}^0 \right|^2 \frac{1}{2} \int_{\mathbf{r}_{\perp}} \text{Re} \left[\mathbf{E}_{\mathcal{B}}^{C,0}(\mathbf{r}, \omega) \times \mathbf{H}_{\mathcal{B}}^{C,0*}(\mathbf{r}, \omega) \right] \cdot \hat{\mathbf{z}} d\mathbf{r}_{\perp}, \end{aligned} \quad (7.22)$$

where the factor 2 in the second line accounts for the emission in both directions. Thus we get the following expression for the integral

$$\begin{aligned} \int_{\mathbf{r}_{\perp}} \text{Re} \left[\mathbf{E}_{\mathcal{B}}^{C,0}(\mathbf{r}, \omega) \times \mathbf{H}_{\mathcal{B}}^{C,0*}(\mathbf{r}, \omega) \right] \cdot \hat{\mathbf{z}} d\mathbf{r}_{\perp} &= \frac{\omega \text{Im} \left[a_{\mathcal{B}}^0 \mathbf{E}_{\mathcal{B}}^{C,0}(\mathbf{r}_{\perp}^0, \omega) \cdot \mathbf{p} \right]}{2 \left| a_{\mathcal{B}}^0 \right|^2} \\ &= \frac{P_{\mathcal{B}}^0}{\left| a_{\mathcal{B}}^0 \right|^2}. \end{aligned} \quad (7.23)$$

Integrating the time-averaged Poynting vector for the fields in the waveguide, and using the above expression along with Eqs. (7.13) and (7.15) we get

$$\begin{aligned} P_{\mathcal{B}}^{\text{WG}}(\omega) &= \frac{1}{2} \left| a_{\mathcal{B}}^{\text{WG}} \right|^2 \int_{\mathbf{r}_{\perp}} \text{Re} \left[\mathbf{E}_{\mathcal{B}}^{\text{WG},0}(\mathbf{r}, \omega) \times \mathbf{H}_{\mathcal{B}}^{\text{WG},0*}(\mathbf{r}, \omega) \right] d\mathbf{r}_{\perp} \\ &= \frac{\left| a_{\mathcal{B}}^{\text{WG}} \right|^2}{2 \left| a_{\mathcal{B}}^0 \right|^2} P_{\mathcal{B}}^0 = \frac{1}{2} |\mathcal{G}(\omega)|^2 P_{\mathcal{B}}^0 \\ &= \frac{1}{2} |\mathcal{G}(\omega)|^2 \Gamma_{\mathcal{B}}^0(\omega) P_{\text{bulk}}(\omega), \end{aligned} \quad (7.24)$$

where the relation between emitted power and emission rate normalized to their bulk values given in Eq. (2.15) has been used. $\Gamma_{\mathcal{B}}^0(\omega)$ is the normalized emission rate as stated in the beginning of the chapter. The power transmitted to the waveguide is thus simply given by $\mathcal{G}(\omega)$ and the power emitted in the absence of mirrors, which is easily calculated for both ridge and nanowire waveguide structures using the techniques already presented in Chapters 3 and 5. The $\mathcal{G}(\omega)$ -function consists of reflection and transmission scattering coefficients, which are easily calculated using the FMM and the scattering matrix formalism, underlining the strength of the modal methods.

In the following section, we present the results produced by our quantum mechanical model using the LDOS and the Green's function as input.

7.3 Optimal single-photon source

We will now consider a single-photon source composed of a QD in a dielectric waveguide structure with mirrors, where we take one cavity mirror to be perfectly reflecting, $r_1 = 1$, and the other to have a finite reflectivity, $r_2 = r$. Furthermore, we will take the scattering with longitudinal acoustic phonons into account. In order to calculate the exciton-phonon coupling, we use the polaron theory. For details on this theory, we refer any interested reader to the manuscript on arXiv [141] and the SI. Here we will simply state the results from using the quantum mechanical model and provide a discussion of the underlying physics.

The presence of a perfect bottom mirror modulates the LDOS by a sinusoidal variation along the waveguide through interference effects. We now assume that the QD is placed at an antinode of this variation, such that the QD is in perfect resonance with the reflected field. This enhances the SE rate into the \mathcal{B} -mode with a factor of 2: $\Gamma_{\mathcal{B}}^{0*} = 2\Gamma_{\mathcal{B}}^0$ in the absence of the second mirror. In that case the β -factor in the presence of the perfect back mirror is $\beta^* = 2\Gamma_{\mathcal{B}}^0/(\Gamma_{\mathcal{B}}^0 + \Gamma_{\mathcal{R}}^0) = 2\beta/(\beta + 1)$. A waveguide with no mirrors and $\beta = 0.95$, gets an improvement to $\beta^* = 0.974$ in the presence of the perfect back mirror.

Applying our quantum mechanical model as outlined in [141] and the SI, we calculate the indistinguishability and the efficiency as function of the mirror transmittivity of the second mirror. The waveguide is assumed to be single-mode, such that $\Gamma_{\mathcal{R}} = \Gamma_{\text{Rad}}$ is constant and thus not affected by the mirror reflectivities. The efficiency is calculated as the ratio between the power reaching the detector in the waveguide coupled to the cavity and the total emitted power as

$$\mathcal{E} = \frac{\mathcal{P}_{\mathcal{B}}}{\mathcal{P}_{\mathcal{B}} + \mathcal{P}_{\mathcal{R}}}, \quad (7.25)$$

where $\mathcal{P}_{\mathcal{R}} = \Gamma_{\mathcal{R}} \int_{-\infty}^{\infty} P_{\text{bulk}}(\omega) d\omega = \Gamma_{\mathcal{R}} \int_{-\infty}^{\infty} S_0(\omega, \omega) d\omega$. $S_0(\omega, \omega')$ is the two-colour dipole spectrum formally given as

$$S_0(\omega, \omega') = \int_{-\infty}^{\infty} \exp[i(\omega t - \omega' t')] \langle \sigma^\dagger(t) \sigma(t') \rangle dt dt', \quad (7.26)$$

where $\sigma(t) = |g(t)\rangle \langle e(t)|$ and $\langle \sigma^\dagger(t) \sigma(t') \rangle$ is the autocorrelation function. For $\omega = \omega'$, S_0 gives the dipole spectrum for the QD placed in bulk, similar to the spectrum presented in Fig. 7.1. $\mathcal{P}_{\mathcal{B}}$ in Eq. (7.25) is the total power emitted into the fundamental waveguide mode, and is given by integrating Eq. (7.24) over all frequencies as

$$P_{\mathcal{B}} = \frac{\Gamma_{\mathcal{B}}^0}{2} \int_{-\infty}^{\infty} |\mathcal{G}(\omega)|^2 P_{\text{bulk}}(\omega) d\omega = \frac{\Gamma_{\mathcal{B}}^0}{2} \int_{-\infty}^{\infty} |\mathcal{G}(\omega)|^2 S_0(\omega, \omega) d\omega, \quad (7.27)$$

where Γ_B^0 has been assumed constant over the frequency range of interest, and $\mathcal{G}(\omega)$ is given in Eq. (7.20). The expression for the indistinguishability is a bit more complex. Here we will simply state the expression and give an overall physical description of the parameters involved. The indistinguishability is calculated as

$$\begin{aligned} \mathcal{I} &= \frac{\int_{-\infty}^{\infty} |\mathcal{G}^*(\omega)\mathcal{G}(\omega')S_0(\omega, \omega')|^2 d\omega d\omega'}{(2\mathcal{P}_B/\Gamma_B^0)^2} \\ &= \frac{\int_{-\infty}^{\infty} |\mathcal{G}^*(\omega)\mathcal{G}(\omega')S_0(\omega, \omega')|^2 d\omega d\omega'}{\left[\int_{-\infty}^{\infty} |\mathcal{G}(\omega)|^2 S_0(\omega, \omega) d\omega\right]^2}. \end{aligned} \quad (7.28)$$

The details on how to evaluate this expression are found in the SI of Ref. [141]. The numerator gives the total power of coherent photons emitted going through the top mirror and into the waveguide, whereas the denominator is the total power emitted into the waveguide. Thus the indistinguishability is a measure of the fraction of coherent photons we detect in the waveguide. Experimentally the indistinguishability is determined using a Hong-Ou-Mandel setup [143], where two photons incident on a beam splitter will always leave the same output channel if they are indistinguishable [144].

The two-colour spectrum may be separated into two contributions $S_0 = S_{\text{ZPL}} + S_{\text{PSB}}$, where $S_{\text{ZPL}}(S_{\text{PSB}})$ is the emission into the zero-phonon line (phonon sideband) of Fig. 7.1. Thus in broad terms the two-colour dipole spectrum describes the coherence between photons emitted into either of these two channels as

$$\begin{aligned} S_0(\omega, \omega') &= \langle \sigma_{\text{ZPL}}(\omega)\sigma'_{\text{ZPL}}(\omega') \rangle + \langle \sigma_{\text{ZPL}}(\omega)\sigma'_{\text{PSB}}(\omega') \rangle \\ &\quad + \langle \sigma_{\text{PSB}}(\omega)\sigma'_{\text{ZPL}}(\omega') \rangle + \langle \sigma_{\text{PSB}}(\omega)\sigma'_{\text{PSB}}(\omega') \rangle, \end{aligned} \quad (7.29)$$

where the first term gives the primary contribution to the indistinguishability. As seen in Fig. 7.2, introducing a cavity enhances the emission into the zero-phonon line and thus increases the indistinguishability. However, if the cavity becomes too strong, we enter the strong-coupling regime (see Fig. 7.2(c)) and the zero-phonon line split, which reduces the indistinguishability.

In Fig. 7.7 we have plotted (a) the efficiency calculated using Eq. (7.25) and (b) the indistinguishability calculated using Eq. (7.28) as function of the mirror transmittivity of the top mirror for cavities with length $L = \lambda_X/(2n_{\text{eff}})$ and $L = 15\lambda_X/n_{\text{eff}}$, where $\lambda_X = 950 \text{ nm}$ is the QD transition wavelength. In the absence of the second mirror ($t = 1$) the cavity filtering function equals 2 ($\mathcal{G} = 2$) and the efficiency becomes

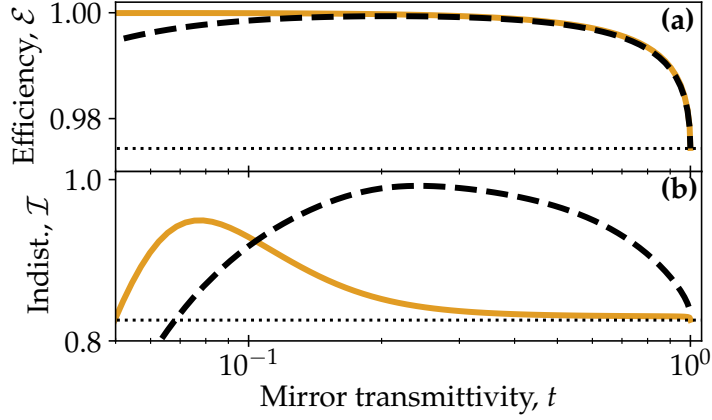


Figure 7.7: (a) Efficiency and (b) indistinguishability of single-photon source as function of the mirror transmittivity of the second mirror for cavities with length $L = \lambda_X / (2n_{\text{eff}})$ (orange solid) and $L = 15\lambda_X / n_{\text{eff}}$ (black dashed). The thin dashed line indicate (a) $\beta^* = 0.974$ and (b) $B^4 = 0.826$. The SE rate into the mirrorless waveguide is $\Gamma_B^0 = 1.1 \mu\text{eV}$.

$$\mathcal{E}_{t=1} = \frac{2\Gamma_B^0}{2\Gamma_B^0 + \Gamma_{\mathcal{R}}} = \beta^*. \quad (7.30)$$

Thus the efficiency converges towards β^* as the top mirror is gradually removed. This is a central result for our model, since if the waveguide mode contribution to the LDOS was ignored, the efficiency would approach zero as $r \rightarrow 0$, which is only a valid approximation if the underlying waveguide structure has a vanishing β -factor, which is the case for micropillar structures. In the same limit, the indistinguishability converges to the Franck-Condon factor (B^2) squared, B^4 , which is the fraction of photons emitted into the ZPL, if the optical LDOS is frequency independent [134]. In the absence of the second mirror, the LDOS is approximately constant across the frequencies of the emitted spectrum.

As seen from Fig. 7.7(a), when lowering the mirror transmittivity the efficiency initially increases due to an increase in the Purcell enhancement. However, the efficiency starts to decrease, when the cavity decay rate becomes small enough such that the photon escapes the cavity by scattering to radiation modes via the QD rather than leaking through the mirror into the waveguide. In the limit $t \rightarrow 0$, we see that the efficiency of the longer cavity is reduced more than for the shorter cavity, which can be explained by the dependence of the cavity decay rate, κ , and the emitter-coupling strength, g , on the cavity length. The cavity decay rate is inverse proportional with the cavity length as $\kappa = \tilde{\kappa}c / (Ln_{\text{eff}})$, where $\tilde{\kappa}$ is found from Eq. (7.7c). The emitter-coupling strength, however, is inversely proportional to the square root of the cavity length as seen in Eq. (7.9). This means that a photon emitted into the longer cavity is more likely to get re-

absorbed by the QD, before dissipating through the mirror to the waveguide, than a photon emitted in the shorter cavity. Whenever the photon is absorbed it will be re-emitted, however, it might be emitted into the radiation modes, which means that it will be lost. Thus for the longer cavity, the photon is exposed to the radiation channel more times than for the shorter cavity in the high Q limit, before it eventually either has leaked to the waveguide or has been scattered into the radiation modes. However, this effect is rather weak as seen from the plot, where the efficiency is well above 0.99 even when t is very close to zero. The efficiency drops to zero, if we have a perfect reflecting second mirror ($t = 0$), since in that case the only escape channel out of the cavity for the photons are through the radiation modes.

We have already discussed that the indistinguishability decreases, when we enter the strong emitter-cavity coupling regime due to the splitting of the ZPL. This regime is reached when $g > \kappa$, and thus for the two different cavity lengths investigated in Fig. 7.7 strong coupling occurs at different transmittivities of the second mirror. As seen from Fig. 7.5(b-c) a longer cavity will enter the strong-coupling regime at lower reflectivity than a shorter cavity. However, the longer cavity will also have a narrower linewidth and thus provide a better filtering of the PSB than the shorter cavity. As seen in Fig. 7.7(b) the best indistinguishability of the longer cavity is obtained for a weaker second mirror than for the shorter cavity, and interestingly the narrower linewidth of the longer cavity provides a better filtering of the PSB than the possible larger Purcell enhancement of the shorter cavity leading to better indistinguishability. We observed the narrowing of the cavity linewidth in the previous chapter in Fig. 6.11 for the nanopost structure. Increasing the cavity length will continuously improve the indistinguishability of the emitted photons until the cavity free spectral range becomes comparable to the width of the PSB, which will then become Purcell enhanced as well. This effect would occur for cavity lengths of 50 – 100 μm . However, for such long single-mode cavities fabrication imperfections will be another source of errors, and will reduce the efficiency and potentially also the indistinguishability.

Our result reveals a new path for obtaining an optimal single-photon source, where it seems advantageous to operate with a single-mode waveguide structure embedded with efficient mirrors forming a long Fabry-Perot cavity. In the plots shown in Fig. 7.7 a perfect bottom mirror ($r_1 = 1$) was assumed, and at the moment the state-of-the-art nanowire mirrors has a reflectance of around 92 % (see Fig. 6.3), which leaves some room for improvement.

7.4 Conclusion

We have developed a quantum mechanical model for calculating the indistinguishability and efficiency of quantum dots embedded in high β waveguide cavities, which correctly accounts for both the cavity effects and the inherent β factor

of the waveguide. Using this model, we have shown that long nanocavities based on high β waveguides represent a promising new platform for realising single-photon sources with simultaneous high efficiency and indistinguishability. Our model predicts, that this structure will beat the numbers predicted in Ref. [134] for the micropillar SPS.

In our model, we have used non-dispersive mirrors, however other mirror types, such as Fano mirrors [9, 35, 101] has lead to interesting dynamics in PhC lasers. Therefore, the frequency response of the mirrors could be another knob for improving the performance of single-photon sources and would thus be an interesting research topic.

Conclusion and outlook

Nanophotonic engineering is key in the development of optical devices with both classical and quantum information applications. A precise and correct description is essential, and a range of different techniques for solving Maxwell's equations are available. The boundary conditions employed on the computational domain are essential for obtaining convergence, and for nanophotonic structures emitting light into free space, open boundaries are the natural choice. Throughout the present thesis, we have used the Fourier modal method (FMM) as the main workhorse due to its easy access to optical modes and their mutual coupling coefficients. Furthermore, open boundary conditions have recently been developed for the FMM in cylindrical coordinates, enabling a correct treatment of radiation into free space from rotationally symmetric structures.

In the present thesis, we have developed implemented and tested an open-boundary condition formalism for the FMM in 3D Cartesian coordinates (3D oFMM). In contrast to the standard FMM formulation, the electromagnetic fields are expanded as Fourier integrals instead of Fourier series. When approximating the integrals as Riemann sums, this allows for a free choice of which in-plane k -values to sample, and as shown in Chapter 3, convergence is obtained much faster for a non-uniform sampling than for a regular equidistant grid. The faster convergence is due to a better description of the radiation modes.

Open boundaries are not always necessary, such as for 2D photonic crystal (PhC) structures, where periodic boundaries are more suitable. Using a Fourier-based

Bloch mode expansion technique, we investigated a 2D PhC waveguide coupled to a microcavity in Chapter 4. We embedded a scattering site in the waveguide, which resulted in a transmission spectrum with a Fano lineshape. The symmetry (parity) of this spectrum, is controlled by the distance between the scattering site and the microcavity. In the limit where these form a Fabry-Perot cavity, it was shown that the roundtrip phase within this cavity is the decisive parameter for the parity. Developing efficient optical switches in PhC waveguides can be realised by Fano geometries, and here the parity decides the direction of the spectral shift needed for switching. Thus further understanding of how to control the shape of the transmission spectrum, might be a first step towards developing energy efficient optical switches.

Semiconductor quantum dots (QDs) embedded in cylindrical nanowire structures has been shown as promising candidates for realising efficient on-demand single-photon sources (SPS). In order to enhance the efficiency of the SPS, the nanowire should be standing on a high-reflective mirror. This is currently only possible for top down fabrication techniques, which depending on the fabrication method can lead to randomly placed QDs in the lateral plane. For these structures, we are well below the diffraction limit, and thus special techniques are needed if one wish to determine the QD position - preferably non-destructively. In Chapter 5, we address this issue by developing a method for mapping the QD position in a needle nanowire using only the far-field radiation pattern. A precise mapping of the QDs could be a first step towards further understanding the potential influence of surface states on the QD properties, which likely depends on the distance to the sidewall.

Single-mode models are easily formulated from the FMM, due to the access to all modes and their scattering coefficients. These often provide additional insight into the physics of specific structures, since analytical expressions are often available. However, as shown in both Chapter 4 and 6 care must be taken, when employing a single-mode model. For both the 2D PhC Fano structure (Chapter 4) and the truncated nanowire (nanopost, Chapter 6), we have identified a breakdown of the single-mode model, when propagation distances become so small that evanescent modes start to influence. For the nanopost geometry, this resulted in a wrong prediction of the Purcell enhancement for the shortest possible nanopost supporting the first harmonic mode of the QD emission wavelength. Furthermore, the source efficiency was in general wrongly predicted by the single-mode model for all lengths of the nanopost, due to the scattering of the fundamental mode at the top facet. The scattering populates downward propagating radiation modes, which are reflected into the far-field by the bottom mirror, where they interfere with the transmitted part of the fundamental mode. A single-mode model does not capture this interference, which can be important for correct calculation of the source efficiency.

In order to correctly account for the solid-state environment surrounding a QD,

quantum mechanical models are needed. Especially, when calculating the indistinguishability of photons emitted by a QD embedded in a photonic structure. Until now, there has mainly been two design strategies for making efficient QD SPSs - either using cavities or single-mode waveguides to enhance the emission into the preferred mode. However, the models used for characterizing cavity SPSs (such as micropillar structures) does not converge towards the models for waveguide SPSs as the reflectivities of the cavity mirrors tends to zero. Thus for a waveguide with mirrors embedded, neither model will correctly predict the properties of the emitted photons. In Chapter 7, we considered such a structure, and developed a quantum mechanical model, which correctly accounts for the inherent high β -factor of the waveguide. Using our model, we identified a new design strategy for realising SPSs with simultaneous high efficiency and indistinguishability, where long cavities in single-mode waveguides seems to be advantageous.

Outlook

Commonly for all chapters is that the FMM has been used in various forms, underlining the diversity of problems, which it is able to solve. However, further development of the FMM is necessary for (a) making it more efficient and (b) expanding the range of structures it can handle. Regarding (a), the staircase approximation needed for treating tapered and photonic crystal structures makes the FMM quite inefficient. For tapers, a possible solution might be found in combining the FMM with the Cross-Section method [122], and describe the propagation through the taper by a differential equation rather than by transmission and reflection matrices coupling the eigenmodes of adjacent staircase layers. Potentially, this could drastically reduce the number of eigenvalue problems to solve.

Regarding (b), we have in the present thesis encountered a needle nanowire with an elliptical cross-section (see Chapter 5), where we treated it as being rotationally symmetric. Currently, we have an in-house code able to solve for the eigenmodes in an elliptical nanowire, however, the transmission and reflection matrices in this framework are still to be derived for structures with changing ellipticity. Elliptical nanowires can be used to enhance the emission into one preferred polarization [145], and thus developing a full FMM able to treat the ellipticity would be a strong tool to investigate this type of nanowires. Our 3D oFMM method developed in Chapter 3 is currently limited to handle structures surrounded by a bulk medium, however, ridge waveguides supported by a substrate are experimentally much more interesting. Thus developing a FMM with open boundary conditions for this type of structure, would be a very strong tool in the development of efficient SPSs integrated on an optical-chip.

As concluded above, a strategy for developing SPSs with simultaneous high efficiency and indistinguishability is to form a long cavity in a high β -waveguide structure. There are numerous ways to realise this. One could be in a PhC waveguide structure, where the mirrors are easily formed by adding holes in the waveguide. The challenge for this platform is how to efficiently couple the photons out into free space or into waveguides with smaller propagation losses. For nanowire waveguides the current state-of-the-art bottom mirror is the metallic mirror covered with a thin film of dielectric material in order to reduce coupling to plasmons. The reflectivity of this mirror is around 92 % [84] and thus developing a better type of bottom mirror is required for increasing the efficiency of the nanowire SPS. The top mirror can be realised as suggested in [57], where a DBR mirror is implemented in the out-coupling trumpet taper. However, an experimental realisation of this structure is still to be demonstrated, and thus poses another research challenge.

Near-field to far-field transformation

A.1 Derivation of Eqs. (2.24)

Below the derivation of Eqs. (2.24) is outlined. Inserting the equivalent currents given in Eqs. (2.23) into Eqs. (2.21) and assuming a plane surface leads to

$$N_\theta = \int_S [J_r \cos \theta \cos (n\phi') \cos (\phi - \phi') + J_\phi \cos \theta \sin (n\phi') \sin (\phi - \phi')] \exp (-ik_0 r' \sin \theta \cos (\phi - \phi')) r' dr' d\phi', \quad (\text{A.1a})$$

$$N_\phi = \int_S [-J_r \cos (n\phi') \sin (\phi - \phi') + J_\phi \sin (n\phi') \cos (\phi - \phi')] \exp (-ik_0 r' \sin \theta \cos (\phi - \phi')) r' dr' d\phi', \quad (\text{A.1b})$$

$$L_\theta = \int_S [M_r \cos \theta \sin (n\phi') \cos (\phi - \phi') + M_\phi \cos \theta \cos (n\phi') \sin (\phi - \phi')] \exp (-ik_0 r' \sin \theta \cos (\phi - \phi')) r' dr' d\phi', \quad (\text{A.1c})$$

$$L_\phi = \int_S [-M_r \sin (n\phi') \sin (\phi - \phi') + M_\phi \cos (n\phi') \cos (\phi - \phi')] \exp (-ik_0 r' \sin \theta \cos (\phi - \phi')) r' dr' d\phi'. \quad (\text{A.1d})$$

These expressions are rewritten using trigonometric relations to

$$N_\theta = \int_S [J_r \cos \theta \cos(n\phi) \cos(n\phi') \cos(\phi') - J_\phi \cos \theta \cos(n\phi) \sin(n\phi') \sin(\phi')] \exp(-ik_0 r' \sin \theta \cos \phi') r' dr' d\phi', \quad (\text{A.2a})$$

$$N_\phi = \int_S [-J_r \sin(n\phi) \sin(n\phi') \sin(\phi') + J_\phi \sin(n\phi) \cos(n\phi') \cos(\phi')] \exp(-ik_0 r' \sin \theta \cos \phi') r' dr' d\phi', \quad (\text{A.2b})$$

$$L_\theta = \int_S [M_r \cos \theta \sin(n\phi) \cos(n\phi') \cos(\phi') + M_\phi \cos \theta \sin(n\phi) \sin(n\phi') \sin(\phi')] \exp(-ik_0 r' \sin \theta \cos \phi') r' dr' d\phi', \quad (\text{A.2c})$$

$$L_\phi = \int_S [-M_r \cos(n\phi) \sin(n\phi') \sin(\phi') + M_\phi \cos(n\phi) \cos(n\phi') \cos(\phi')] \exp(-ik_0 r' \sin \theta \cos \phi') r' dr' d\phi'. \quad (\text{A.2d})$$

Furthermore we have the following relations for the Bessel functions of the first kind

$$2\pi i^n J_n(x) = \int_0^{2\pi} \cos(n\phi) \exp(ix \cos \phi) d\phi, \quad (\text{A.3a})$$

$$\pi i^{n-1} (J_{n-1}(x) - J_{n+1}(x)) = \int_0^{2\pi} \cos \phi \cos(n\phi) \exp(ix \cos \phi) d\phi, \quad (\text{A.3b})$$

$$\pi i^{n-1} (J_{n-1}(x) + J_{n+1}(x)) = \int_0^{2\pi} \sin \phi \sin(n\phi) \exp(ix \cos \phi) d\phi, \quad (\text{A.3c})$$

where J_n is the Bessel function of the first kind of order n ¹. Using these relations

¹Note that J_n is a Bessel function, whereas $J_{r(\phi)}$ is the radial(tangential) component of the equivalent current.

Eqs. A.2 are rewritten to

$$N_\theta = \int \left[\begin{array}{l} (J_r - J_\phi) J_{n-1} (-k_0 r' \sin \theta) \\ - (J_r + J_\phi) J_{n+1} (-k_0 r' \sin \theta) \end{array} \right] \cos \theta \cos (n\phi) i^{n-1} \pi dr', \quad (\text{A.4a})$$

$$N_\phi = \int \left[\begin{array}{l} - (J_r - J_\phi) J_{n-1} (-k_0 r' \sin \theta) \\ - (J_r + J_\phi) J_{n+1} (-k_0 r' \sin \theta) \end{array} \right] \sin (n\phi) i^{n-1} \pi dr', \quad (\text{A.4b})$$

$$L_\theta = \int \left[\begin{array}{l} (M_r + M_\phi) J_{n-1} (-k_0 r' \sin \theta) \\ - (M_r - M_\phi) J_{n+1} (-k_0 r' \sin \theta) \end{array} \right] \cos \theta \sin (n\phi) i^{n-1} \pi dr', \quad (\text{A.4c})$$

$$L_\phi = \int \left[\begin{array}{l} (M_r + M_\phi) J_{n-1} (-k_0 r' \sin \theta) \\ + (M_r - M_\phi) J_{n+1} (-k_0 r' \sin \theta) \end{array} \right] \cos (n\phi) i^{n-1} \pi dr', \quad (\text{A.4d})$$

Using the definitions in Eqs. (2.22) and (2.25) we arrive at the final expressions in Eqs. (2.24)

$$N_\theta = - \int \cos \theta \cos (n\phi) [H_p(r') J_{n-1} (-k_0 r' \sin \theta) + H_m(r') J_{n+1} (-k_0 r' \sin \theta)] i^{n-1} \pi r' dr', \quad (\text{A.5a})$$

$$N_\phi = \int \sin (n\phi) [H_p(r') J_{n-1} (-k_0 r' \sin \theta) - H_m(r') J_{n+1} (-k_0 r' \sin \theta)] i^{n-1} \pi r' dr', \quad (\text{A.5b})$$

$$L_\theta = - \int \cos \theta \sin (n\phi) [E_m(r') J_{n-1} (-k_0 r' \sin \theta) + E_p(r') J_{n+1} (-k_0 r' \sin \theta)] i^{n-1} \pi r' dr', \quad (\text{A.5c})$$

$$L_\phi = \int \cos (n\phi) [-E_m(r') J_{n-1} (-k_0 r' \sin \theta) + E_p(r') J_{n+1} (-k_0 r' \sin \theta)] i^{n-1} \pi r' dr'. \quad (\text{A.5d})$$

Reverting the cosine/sine dependence in Eqs. (2.23) to

$$J_r(r', \phi') = J_r(r') \sin(n\phi'), \quad J_\phi(r', \phi') = J_\phi(r') \cos(n\phi'), \quad (\text{A.6a})$$

$$M_r(r', \phi') = M_r(r') \cos(n\phi'), \quad M_\phi(r', \phi') = M_\phi(r') \sin(n\phi'), \quad (\text{A.6b})$$

and going through similar steps as in the derivation for Eqs. (A.5) leads to

$$N_\theta = \int \cos \theta \sin(n\phi) [H_m(r') J_{n-1}(-k_0 r' \sin \theta) + H_p(r') J_{n+1}(-k_0 r' \sin \theta)] i^{n-1} \pi r' dr', \quad (\text{A.7a})$$

$$N_\phi = \int \cos(n\phi) [H_m(r') J_{n-1}(-k_0 r' \sin \theta) - H_p(r') J_{n+1}(-k_0 r' \sin \theta)] i^{n-1} \pi r' dr', \quad (\text{A.7b})$$

$$L_\theta = \int \cos \theta \cos(n\phi) [E_p(r') J_{n-1}(-k_0 r' \sin \theta) + E_m(r') J_{n+1}(-k_0 r' \sin \theta)] i^{n-1} \pi r' dr', \quad (\text{A.7c})$$

$$L_\phi = \int \sin(n\phi) [-E_p(r') J_{n-1}(-k_0 r' \sin \theta) + E_m(r') J_{n+1}(-k_0 r' \sin \theta)] i^{n-1} \pi r' dr'. \quad (\text{A.7d})$$

A.2 Derivation of Eqs. (5.4) and (5.5)

In this appendix we will derive the near-field to far-field transformation in the oFMM formalism [48] used in Chapters 5 and 6. Using the oFMM formalism with the scattering matrix formalism enables us to compute the near-field of any rotationally symmetric structure. Here, the near-field is assumed to be known in the air layer just on top of the cylindrical structure. The electromagnetic field components for each mode in the near-field are given as [48]

$$F_{r,nj}(r, \phi) = i \sum_{m=1}^M k_m \Delta k_m [b_{n,jm}^F J_{n+1}(k_m r) - c_{n,jm}^F J_{n-1}(k_m r)] \exp(in\phi), \quad (\text{A.8a})$$

$$F_{\phi,nj}(r, \phi) = \sum_{m=1}^M k_m \Delta k_m [b_{n,jm}^F J_{n+1}(k_m r) + c_{n,jm}^F J_{n-1}(k_m r)] \exp(in\phi), \quad (\text{A.8b})$$

where F is either the electric field, E , or the magnetic field, H . $b(c)_{m,nj}^F$ are the expansion coefficients for mode j and angular momentum n in the Bessel basis.

General case - $n \neq 0$

In the general case the EM-field is polarized in both in-plane directions. In the derivation of Eqs. (2.24) a $\cos(n\phi)$ angular dependence on H_ϕ and E_r , and a $\sin(n\phi)$ dependence on H_r and E_ϕ was assumed. However, in Eqs. (5.1), (5.3)

and (A.8) the angular dependence is given as $\exp(in\phi)$. To overcome this we add fields with $\pm n$ angular dependence, where the following relations has been numerically found to hold for the expansion coefficients b^E , c^E , b^H and c^H :

$$b_{-n}^E = (-1)^{n+1}c_n^E \quad b_{-n}^H = (-1)^n c_n^H, \quad (\text{A.9a})$$

$$c_{-n}^E = (-1)^{n+1}b_n^E \quad c_{-n}^H = (-1)^n b_n^H. \quad (\text{A.9b})$$

These relations make sure that the angular dependence of the E_r and H_r components are separated by $\pi/2$ when the $+$ and $-n$ contributions are added - the same applies for the E_ϕ and H_ϕ fields. Using these relations and adding the electric and magnetic fields for $\pm n$ angular momentum in Eqs. (A.8) leads to the desired angular dependence of the electric and magnetic fields. Since the zero point of the phase can be chosen arbitrarily changing between a cosine and sine dependence can be done by shifting the phase by $\pi/2$. Additionally we will use the relation $J_{-n} = (-1)^n J_n$ in the derivations below. We start by considering the radial component of the electric field

$$\begin{aligned} E_{r,nj} &= i \sum_{m=1}^M k_m \Delta k_m \\ &\left[\left(b_{njm}^E J_{n+1}(k_m r) - c_{njm}^E J_{n-1}(k_m r) \right) (\cos(n\phi) + i \sin(n\phi)) + \right. \\ &\left. \left(b_{-njm}^E J_{-n+1}(k_m r) - c_{-njm}^E J_{-n-1}(k_m r) \right) (\cos(n\phi) - i \sin(n\phi)) \right] \quad (\text{A.10a}) \end{aligned}$$

$$\begin{aligned} &= i \sum_{m=1}^M k_m \Delta k_m \\ &\left[\left(b_{njm}^E J_{n+1}(k_m r) - c_{njm}^E J_{n-1}(k_m r) \right) (\cos(n\phi) + i \sin(n\phi)) + \right. \\ &\left((-1)^{n+1} (-1)^{n-1} c_{njm}^E J_{n-1}(k_m r) - \right. \\ &\left. \left. (-1)^{n+1} (-1)^{n+1} b_{njm}^E J_{n+1}(k_m r) \right) (\cos(n\phi) - i \sin(n\phi)) \right] \quad (\text{A.10b}) \end{aligned}$$

$$\begin{aligned} &= i \sum_{m=1}^M k_m \Delta k_m \\ &\left[\left(b_{njm}^E J_{n+1}(k_m r) - c_{njm}^E J_{n-1}(k_m r) \right) (\cos(n\phi) + i \sin(n\phi)) + \right. \\ &\left. \left(c_{njm}^E J_{n-1}(k_m r) - b_{njm}^E J_{n+1}(k_m r) \right) (\cos(n\phi) - i \sin(n\phi)) \right] \quad (\text{A.10c}) \end{aligned}$$

$$E_{r,nj} = -2 \sum_{m=1}^M k_m \Delta k_m \left[b_{njm}^E J_{n+1}(k_m r) - c_{njm}^E J_{n-1}(k_m r) \right] \sin(n\phi) \quad (\text{A.10d})$$

Rotation by $+\pi/2 \quad \Rightarrow$

$$E_{r,nj} = 2 \sum_{m=1}^M k_m \Delta k_m \left[b_{njm}^E J_{n+1}(k_m r) - c_{njm}^E J_{n-1}(k_m r) \right] \cos(n\phi) \quad (\text{A.10e})$$

Next we consider the transverse electric field:

$$E_{\phi,nj} = \sum_{m=1}^M k_m \Delta k_m \left[\left(b_{njm}^E J_{n+1}(k_m r) + c_{njm}^E J_{n-1}(k_m r) \right) (\cos(n\phi) + i \sin(n\phi)) + \left(b_{-njm}^E J_{-n+1}(k_m r) + c_{-njm}^E J_{-n-1}(k_m r) \right) (\cos(n\phi) - i \sin(n\phi)) \right] \quad (\text{A.11a})$$

$$= \sum_{m=1}^M k_m \Delta k_m \left[\left(b_{njm}^E J_{n+1}(k_m r) + c_{njm}^E J_{n-1}(k_m r) \right) (\cos(n\phi) + i \sin(n\phi)) + \left(c_{njm}^E J_{n-1}(k_m r) + b_{njm}^E J_{n+1}(k_m r) \right) (\cos(n\phi) - i \sin(n\phi)) \right] \quad (\text{A.11b})$$

$$E_{\phi,nj} = 2 \sum_{m=1}^M k_m \Delta k_m \left[b_{njm}^E J_{n+1}(k_m r) + c_{njm}^E J_{n-1}(k_m r) \right] \cos(n\phi) \quad (\text{A.11c})$$

Rotation by $+\pi/2 \quad \Rightarrow$

$$E_{\phi,nj} = 2 \sum_{m=1}^M k_m \Delta k_m \left[b_{njm}^E J_{n+1}(k_m r) + c_{njm}^E J_{n-1}(k_m r) \right] \sin(n\phi) \quad (\text{A.11d})$$

For the radial magnetic field we get:

$$H_{r,nj} = i \sum_{m=1}^M k_m \Delta k_m \left[\left(b_{njm}^H J_{n+1}(k_m r) - c_{njm}^H J_{n-1}(k_m r) \right) (\cos(n\phi) + i \sin(n\phi)) + \left(b_{-njm}^H J_{-n+1}(k_m r) - c_{-njm}^H J_{-n-1}(k_m r) \right) (\cos(n\phi) - i \sin(n\phi)) \right] \quad (\text{A.12a})$$

$$H_{r,nj} = 2i \sum_{m=1}^M k_m \Delta k_m \left[b_{njm}^H J_{n+1}(k_m r) - c_{njm}^H J_{n-1}(k_m r) \right] \cos(n\phi) \quad (\text{A.12b})$$

Rotation by $+\pi/2 \quad \Rightarrow$

$$H_{r,nj} = 2i \sum_{m=1}^M k_m \Delta k_m \left[b_{njm}^H J_{n+1}(k_m r) - c_{njm}^H J_{n-1}(k_m r) \right] \sin(n\phi) \quad (\text{A.12c})$$

And finally for the tangential magnetic field we have:

$$H_{\phi,nj} = \sum_{m=1}^M k_m \Delta k_m \left[\left(b_{njm}^H J_{n+1}(k_m r) + c_{njm}^H J_{n-1}(k_m r) \right) (\cos(n\phi) + i \sin(n\phi)) + \left(b_{-njm}^H J_{-n+1}(k_m r) + c_{-njm}^H J_{-n-1}(k_m r) \right) (\cos(n\phi) - i \sin(n\phi)) \right] \quad (\text{A.13a})$$

$$H_{\phi,nj} = 2i \sum_{m=1}^M k_m \Delta k_m \left[b_{njm}^H J_{n+1}(k_m r) + c_{njm}^H J_{n-1}(k_m r) \right] \sin(n\phi) \quad (\text{A.13b})$$

Rotation by $+\pi/2 \Rightarrow$

$$H_{\phi,nj} = -2i \sum_{m=1}^M k_m \Delta k_m \left[b_{njm}^H J_{n+1}(k_m r) + c_{njm}^H J_{n-1}(k_m r) \right] \cos(n\phi) \quad (\text{A.13c})$$

Inserting Eqs. (A.10e), (A.11d), (A.12c) and (A.13c) into Eqs. (2.25) and leaving out the angular dependence leads to the following expressions

$$H_- = H_{r,nj} - H_{\phi,nj} = 4i \sum_{m=1}^M k_m \Delta k_m b_{njm}^H J_{n+1}(k_m r), \quad (\text{A.14a})$$

$$H_+ = H_{r,nj} + H_{\phi,nj} = -4i \sum_{m=1}^M k_m \Delta k_m c_{njm}^H J_{n-1}(k_m r), \quad (\text{A.14b})$$

$$E_- = E_{r,nj} - E_{\phi,nj} = -4 \sum_{m=1}^M k_m \Delta k_m c_{njm}^E J_{n-1}(k_m r), \quad (\text{A.14c})$$

$$E_+ = E_{r,nj} + E_{\phi,nj} = 4 \sum_{m=1}^M k_m \Delta k_m b_{njm}^E J_{n+1}(k_m r). \quad (\text{A.14d})$$

Insertion of Eqs. (A.14) into Eqs. (A.5) gives the needed quantities for calculating the far field using Eqs. (2.20). Now we are exploiting the open boundaries

in the oFMM formalism, such that the integration limits in Eqs. (A.5) are 0 and ∞ . First we take a look at $N_{\theta,nj}$

$$N_{\theta,nj} = - \int_0^\infty \cos \theta \cos(n\phi) (H_+(r')J_{n-1}(-k_0r' \sin \theta) + H_-(r')J_{n+1}(-k_0r' \sin \theta)) i^{n-1} \pi r' dr' \quad (\text{A.15a})$$

$$= - \int_0^\infty \cos \theta \cos(n\phi) 4i \sum_{m=1}^M k_m \Delta k_m \left[-c_{njm}^H J_{n-1}(k_m r') J_{n-1}(-k_0 r' \sin \theta) + b_{njm}^H J_{n+1}(k_m r') J_{n+1}(-k_0 r' \sin \theta) \right] i^{n-1} \pi r' dr' \quad (\text{A.15b})$$

$$= -4i^n \pi \cos \theta \cos(n\phi) \sum_{m=1}^M k_m \Delta k_m \int_0^\infty \left[-c_{njm}^H J_{n-1}(k_m r') (-1)^{n-1} J_{n-1}(k_0 r' \sin \theta) + b_{njm}^H J_{n+1}(k_m r') (-1)^{n+1} J_{n+1}(k_0 r' \sin \theta) \right] r' dr' \quad (\text{A.15c})$$

$$\boxed{N_{\theta,nj} = 4(-i)^n \pi \cos \theta \cos(n\phi) \sum_{m=1}^M \Delta k_m (b_{njm}^H - c_{njm}^H) \delta(k_m - k_0 \sin \theta)} \quad (\text{A.15d})$$

Here we have used the Bessel function closure equation [146]

$$\int_0^\infty J_\alpha(kr) J_\alpha(k'r) r dr = \frac{1}{k} \delta(k - k'). \quad (\text{A.16})$$

Similarly for $N_{\phi,nj}$ we get

$$N_{\phi,nj} = \int_0^\infty \sin(n\phi) (H_+(r')J_{n-1}(-k_0r' \sin \theta) - H_-(r')J_{n+1}(-k_0r' \sin \theta)) i^{n-1} \pi r' dr' \quad (\text{A.17a})$$

$$= \int_0^\infty \sin(n\phi) 4i \sum_{m=1}^M k_m \Delta k_m \left[-c_{njm}^H J_{n-1}(k_m r') J_{n-1}(-k_0 r' \sin \theta) - b_{njm}^H J_{n+1}(k_m r') J_{n+1}(-k_0 r' \sin \theta) \right] i^{n-1} \pi r' dr' \quad (\text{A.17b})$$

$$\boxed{N_{\phi,nj} = 4(-i)^n \pi \sin(n\phi) \sum_{m=1}^M \Delta k_m (b_{njm}^H + c_{njm}^H) \delta(k_m - k_0 \sin \theta)} \quad (\text{A.17c})$$

$L_{\theta,j,n}$ and $L_{\phi,j,n}$ are derived in a similar way and the final form of these are

$$\boxed{L_{\theta,nj} = -4(-i)^{n-1}\pi \cos \theta \sin(n\phi) \sum_{m=1}^M \Delta k_m (b_{njm}^E - c_{njm}^E) \delta(k_m - k_0 \sin \theta)} \quad (\text{A.18})$$

$$\boxed{L_{\phi,nj} = 4(-i)^{n-1}\pi \cos(n\phi) \sum_{m=1}^M \Delta k_m (b_{njm}^E + c_{njm}^E) \delta(k_m - k_0 \sin \theta)} \quad (\text{A.19})$$

The above equations only applies for $n \neq 0$. In the two following sections the equations will be derived for $n = 0$ for the two polarizations TE and TM.

TM polarization

For TM polarization Eqs. (A.5) applies, however the fields given in Eqs. (A.10e), (A.11d), (A.12c) and (A.13c) are no longer valid, since these were constructed by adding fields with $\pm n$ angular momentum. For TM polarization $n = 0$, and thus we return to Eqs. (A.8) to find the electric and magnetic fields for TM polarization. TM polarization is defined as having $H_r = H_z = E_\phi = 0$. So the electric and magnetic fields are

$$\begin{aligned} E_{r,j}^{\text{TM}} &= i \sum_{m=1}^M k_m \Delta k_m \left[b_{m,j}^E J_1(k_m r) - c_{m,j}^E J_{-1}(k_m r) \right] \\ &= i \sum_{m=1}^M k_m \Delta k_m \left[b_{m,j}^E + c_{m,j}^E \right] J_1(k_m r) = E_+ = E_- \end{aligned} \quad (\text{A.20a})$$

$$\begin{aligned} H_{\phi,j}^{\text{TM}} &= \sum_{m=1}^M k_m \Delta k_m \left[b_{m,j}^H J_1(k_m r) + c_{m,j}^H J_{-1}(k_m r) \right] \\ &= \sum_{m=1}^M k_m \Delta k_m \left[b_{m,j}^H - c_{m,j}^H \right] J_1(k_m r) = H_+ = -H_- \end{aligned} \quad (\text{A.20b})$$

Using these fields in Eqs. (A.7) and setting $n = 0$ leads to:

$$N_{\theta,j,\text{TM}} = - \int_0^\infty \cos \theta (H_+ J_{-1}(-k_0 r' \sin \theta) + H_- J_1(-k_0 r' \sin \theta)) i^{-1} \pi r' dr' \quad (\text{A.21a})$$

$$= i\pi \cos \theta \int_0^\infty (H_{\phi,j} J_1(k_0 r' \sin \theta) + H_{\phi,j} J_1(k_0 r' \sin \theta)) r' dr' \quad (\text{A.21b})$$

$$N_{\theta,j,\text{TM}} = 2i\pi \cos \theta \sum_{m=1}^M \Delta k_m [b_{m,j}^H - c_{m,j}^H] \delta(k_m - k_0 \sin \theta) \quad (\text{A.21c})$$

$$N_{\phi,j,\text{TM}} = 0 \quad (\text{A.22})$$

$$L_{\theta,j,\text{TM}} = 0 \quad (\text{A.23})$$

$$L_{\phi,j,\text{TM}} = \int_0^\infty (-E_- J_{-1}(-k_0 r' \sin \theta) + E_+ J_1(-k_0 r' \sin \theta)) i^{-1} \pi r' dr' \quad (\text{A.24a})$$

$$= i^{-1} \pi \int_0^\infty (-E_{r,j} J_1(k_0 r' \sin \theta) - E_{r,j} J_1(k_0 r' \sin \theta)) r' dr' \quad (\text{A.24b})$$

$$L_{\phi,j,\text{TM}} = -2\pi \sum_{m=1}^M \Delta k_m [b_{m,j}^E + c_{m,j}^E] \delta(k_m - k_0 \sin \theta) \quad (\text{A.24c})$$

TE polarization

For TE polarization Eqs. (A.5) are used for calculating the far field. As for the TM case we start from Eqs. (A.8) for determining the field components, where $E_r = E_z = H_\phi = 0$, which leads to the following electric and magnetic fields

$$\begin{aligned} E_{\phi,j}^{\text{TE}} &= \sum_{m=1}^M k_m \Delta k_m [b_{m,j}^E J_1(k_m r) + c_{m,j}^E J_{-1}(k_m r)] \\ &= \sum_{m=1}^M k_m \Delta k_m [b_{m,j}^E - c_{m,j}^E] J_1(k_m r) = E_+ = -E_- \end{aligned} \quad (\text{A.25a})$$

$$\begin{aligned} H_{r,j}^{\text{TE}} &= \sum_{m=1}^M k_m \Delta k_m [b_{m,j}^H J_1(k_m r) - c_{m,j}^H J_{-1}(k_m r)] \\ &= \sum_{m=1}^M k_m \Delta k_m [b_{m,j}^H + c_{m,j}^H] J_1(k_m r) = H_+ = H_- \end{aligned} \quad (\text{A.25b})$$

Insertion of these fields into Eqs. (A.7), setting $n = 0$, and following the same steps as for TM polarization, we arrive at the final expressions

$$\boxed{N_{\theta,j,\text{TE}} = 0} \quad (\text{A.26})$$

$$\boxed{N_{\phi,j,\text{TE}} = 2\pi \sum_{m=1}^M \Delta k_m \left[b_{m,j}^H + c_{m,j}^H \right] \delta(k_m - k_0 \sin \theta)} \quad (\text{A.27})$$

$$\boxed{L_{\phi,j,\text{TE}} = -2i\pi \cos \theta \sum_{m=1}^M \Delta k_m \left[b_{m,j}^E - c_{m,j}^E \right] \delta(k_m - k_0 \sin \theta)} \quad (\text{A.28})$$

$$\boxed{L_{\theta,j,\text{TE}} = 0} \quad (\text{A.29})$$

Modelling open nanophotonic systems using the Fourier modal method: Generalization to 3D Cartesian coordinates

In this appendix additional derivations for Chapter 3 are provided.

B.1 Direct factorization rule

We start by factorizing Eqs. (3.2)-(3.7) and writing them in a matrix form one-by-one. Inserting the function expansion in Eq. (3.8) into Eq. (3.2) leads to

$$\int \int [k_y c_{E_z}(k_x, k_y) - \beta c_{E_y}(k_x, k_y)] g(k_x, k_y, x, y) dk_x dk_y = \omega \mu_0 \int \int c_{H_x}(k_x, k_y) g(k_x, k_y, x, y) dk_x dk_y, \quad (\text{B.1})$$

where the integration limits (from $-\infty$ to ∞) have been omitted for notational clarity. Multiplying with $g^*(k'_x, k'_y)$, integrating over x and y and using the orthogonality relation (3.9) lead to

$$\begin{aligned} (2\pi)^2 \int \int [k_y c_{Ez}(k_x, k_y) - \beta c_{Ey}(k_x, k_y)] \delta(k_x - k'_x) \delta(k_y - k'_y) dk_x dk_y \\ = (2\pi)^2 \omega \mu_0 \int \int c_{Hx}(k_x, k_y) \delta(k_x - k'_x) \delta(k_y - k'_y) dk_x dk_y. \end{aligned} \quad (\text{B.2})$$

Performing the integrations in Eq. (B.2) we arrive at

$$k_y c_{Ez}(k_x, k_y) - \beta c_{Ey}(k_x, k_y) = \omega \mu_0 c_{Hx}(k_x, k_y), \quad (\text{B.3})$$

which after discretization of the k space is written in matrix form as

$$\mathbf{k}_y \mathbf{e}_z - \beta \mathbf{e}_y = \omega \mu_0 \mathbf{h}_x, \quad (\text{B.4})$$

where \mathbf{e}_y is a vector with c_{Ey}^ξ as elements. \mathbf{k}_x and \mathbf{k}_y are diagonal matrices with elements k_x^ξ and k_y^ξ .

Using a similar approach, Eqs. (3.3) and (3.4) are written in matrix form as

$$\beta \mathbf{e}_x - \mathbf{k}_x \mathbf{e}_z = \omega \mu_0 \mathbf{h}_y, \quad (\text{B.5})$$

$$\mathbf{k}_x \mathbf{e}_y - \mathbf{k}_y \mathbf{e}_x = \omega \mu_0 \mathbf{h}_z. \quad (\text{B.6})$$

In order to eliminate \mathbf{e}_z from Eqs. (B.4) and (B.5), we prepare Eq. (3.7) in a discretized form, for which the direct factorization rule applies. Expanding the field components, using Eqs. (3.14)-(3.15) and performing a change of variables $\hat{k}_{x,y} = k_{x,y} + k'_{x,y}$ lead to

$$\begin{aligned} \int \int [k_x c_{Hy}(k_x, k_y) - k_y c_{Hx}(k_x, k_y)] \exp[i(k_x x + k_y y)] dk_x dk_y \\ = -\omega \varepsilon_0 \int \int \int \int \left[\begin{array}{c} \varepsilon_B \delta(\hat{k}_x - k_x) \delta(\hat{k}_y - k_y) + \\ c_{\Delta\varepsilon}(\hat{k}_x - k_x, \hat{k}_y - k_y) \end{array} \right] c_{Ez}(k_x, k_y) \\ \times \exp[i(\hat{k}_x x + \hat{k}_y y)] dk_x dk_y d\hat{k}_x d\hat{k}_y. \end{aligned} \quad (\text{B.7})$$

We then multiply with $\exp[-i(k'_x x + k'_y y)]$, integrate over x and y and employ the orthogonality condition (3.9) and obtain

$$\begin{aligned}
 k'_x c_{Hy}(k'_x, k'_y) - k'_y c_{Hx}(k'_x, k'_y) = -\omega \varepsilon_0 \int \int \left[\varepsilon_B \delta(k'_x - k_x) \delta(k'_y - k_y) \right. \\
 \left. + c_{\Delta\varepsilon}(k'_x - k_x, k'_y - k_y) \right] c_{Ez}(k_x, k_y) dk_x dk_y. \quad (\text{B.8})
 \end{aligned}$$

In discretized form Eq. (B.8) is written as

$$\mathbf{k}_x \mathbf{h}_y - \mathbf{k}_y \mathbf{h}_x = -\omega \varepsilon_0 [\mathbf{\Delta\varepsilon} \mathbf{\Delta k} + \varepsilon_B \mathbf{I}] \mathbf{e}_z, \quad (\text{B.9})$$

where $\mathbf{\Delta\varepsilon}$ is the Toeplitz matrix containing the elements $c_{\Delta\varepsilon}^\xi = c_{\Delta\varepsilon}(k_x^\xi, k_y^\xi)$, \mathbf{I} is the identity matrix and $\mathbf{\Delta k}$ is the diagonal matrix containing the discretized area elements Δk_ξ in k space. Thus, \mathbf{e}_z equals to

$$\mathbf{e}_z = -\frac{1}{\omega \varepsilon_0} [\mathbf{\Delta\varepsilon} \mathbf{\Delta k} + \varepsilon_B \mathbf{I}]^{-1} [\mathbf{k}_x \mathbf{h}_y - \mathbf{k}_y \mathbf{h}_x]. \quad (\text{B.10})$$

allowing us to write Eqs. (B.4) and (B.5) in the form of an eigenvalue problem that couples the lateral electric field components to the lateral magnetic field components as

$$\begin{bmatrix} \mathbf{k}_x \varepsilon_{\text{Tot}}^{-1} \mathbf{k}_y & -\mathbf{k}_x \varepsilon_{\text{Tot}}^{-1} \mathbf{k}_x + k_0^2 \mathbf{I} \\ \mathbf{k}_y \varepsilon_{\text{Tot}}^{-1} \mathbf{k}_y - k_0^2 \mathbf{I} & -\mathbf{k}_y \varepsilon_{\text{Tot}}^{-1} \mathbf{k}_x \end{bmatrix} \begin{bmatrix} \mathbf{h}_x \\ \mathbf{h}_y \end{bmatrix} = \omega \varepsilon_0 \beta \begin{bmatrix} \mathbf{e}_x \\ \mathbf{e}_y \end{bmatrix}, \quad (\text{B.11})$$

where $\varepsilon_{\text{Tot}} = \mathbf{\Delta\varepsilon} \mathbf{\Delta k} + \varepsilon_B \mathbf{I}$.

From Eqs. (3.5) and (3.6) we write similar set of equations that couples the lateral components so that Eqs. (3.5) and (3.6) together with Eq. (B.11) allows us to eliminate the magnetic field components and form an eigenvalue problem for the lateral electric field components (or vice versa). However, Eqs. (3.5) and (3.6) need special treatment due to the product $\varepsilon E_{x,y}$.

B.2 Inverse factorization rule

In the following the application of the inverse rule for open boundaries with a separable discretization grid in k space will be presented. As discussed in Appendix B.3, an equidistant discretization with an open BC is mathematically equivalent to implementing a periodic BC and a Fourier series expansion. Furthermore, as will become apparent in the course of deriving the inverse factorization for the separable discretization, the inverse factorization approach is not applicable for our dartboard discretization scheme defined in Section 3.2.

The factorization will be performed on Eq. (3.5) to illustrate how the inverse rule is implemented for the product εE_x . The matrix representation for the ε function

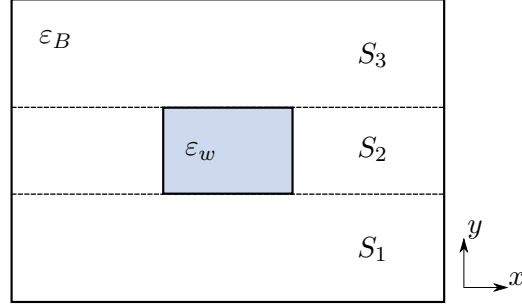


Figure B.1: A waveguide in air is divided into three sections separated by the y interfaces of the permittivity function. Here the background permittivity is ε_B and in the waveguide region $\Delta\varepsilon(x, y) = \varepsilon_w - \varepsilon_B$. The permittivity is y independent inside each of the three sections.

used in the product εE_x will be denoted ε_x , indicating that it accommodates for continuity of the product along the x direction, where the inverse rule is applied as in [71, 73]. Now, E_x is discontinuous in the x direction but continuous in the y direction. ε is discontinuous in both the x and y direction. Their product, εE_x , is continuous in the x direction and discontinuous in the y direction, thus the inverse rule is used for the x direction and the direct rule for the y direction. The way this is done computationally is to divide the structure into sections separated by the interfaces in the y direction and apply the inverse rule to each of these sections. This is illustrated in Figure B.1.

In general the expansion coefficients for all (x, y) -dependent functions are given as in Eq. (3.10). The integration over the y coordinate is then separated into sections where the function is uniform along the y axis. Using Figure B.1 as the example, the y integration is separated into three parts

$$\begin{aligned}
 c_f(k_x, k_y) &= \frac{1}{2\pi} \int_{S_1} f_{x,S_1}(k_x) \exp(-ik_y y) dy \\
 &\quad + \frac{1}{2\pi} \int_{S_2} f_{x,S_2}(k_x) \exp(-ik_y y) dy \\
 &\quad + \frac{1}{2\pi} \int_{S_3} f_{x,S_3}(k_x) \exp(-ik_y y) dy,
 \end{aligned} \tag{B.12}$$

where

$$f_{x,S_i}(k_x) = \frac{1}{2\pi} \int f(x, y_{S_i}) \exp(-ik_x x) dx. \tag{B.13}$$

Here the notation $f(x, y_{S_i})$ means that the function is evaluated within section S_i and is only dependent on the x coordinate within that section. With this separation, it is possible to factorize ε using the correct factorization rules *provided*

that the discretized basis set features separable k_x and k_y dependency as in Eq. (3.24). If this is the case, we can index the k_x and k_y contributions to the basis mode k vector as (k_x^m, k_y^l) using separate indices m and l . It is then possible to apply the inverse rule to the product $\varepsilon_x E_x$ factorized along the x direction by first preparing the Fourier transform along the x axis of the inverse permittivity as

$$\eta_{x,S_i}(k_x) = \frac{1}{2\pi} \int_{-\infty}^{\infty} \Delta\eta(x, y_{S_i}) \exp(-ik_x x) dx + \eta_B \delta(k_x). \quad (\text{B.14})$$

We then form the Toeplitz matrix for the η_{x,S_i} function discretized on the k_x^m grid. Since the product of the expansions of ε and E_x involves an integration over k space as in B.8, the Toeplitz matrix is given by

$$\boldsymbol{\eta}_{x,S_i,\text{Tot}} = \boldsymbol{\Delta}\boldsymbol{\eta}_{x,S_i} \boldsymbol{\Delta}\mathbf{k}_x + \eta_B \mathbf{I}, \quad (\text{B.15})$$

where $\boldsymbol{\Delta}\boldsymbol{\eta}_{x,S_i}$ is the Toeplitz matrix containing the elements $\Delta\eta_{x,S_i}^m = \Delta\eta_{x,S_i}(k_x^m)$ and $\boldsymbol{\Delta}\mathbf{k}_x$ is the diagonal matrix with Δk_x^m as elements. According to the inverse rule, we then take the inverse of this matrix and Fourier transform the resulting elements along the y axis as

$$\begin{aligned} \varepsilon_{x,mn}(k_y) &= \frac{1}{2\pi} \int_{-\infty}^{\infty} (\boldsymbol{\Delta}\boldsymbol{\eta}_{x,\text{Tot}}^{\text{Inv}})_{mn}(y) \exp(-ik_y y) dy \\ &+ \varepsilon_B \delta_{mn} \delta(k_y), \end{aligned} \quad (\text{B.16})$$

where $\boldsymbol{\Delta}\boldsymbol{\eta}_{x,\text{Tot}}^{\text{Inv}}(y) = \boldsymbol{\eta}_{x,S_i,\text{Tot}}^{-1} - \varepsilon_B \mathbf{I}$, which is piece-wise constant over the various regions S_i as discussed above.

The final Toeplitz matrix $\boldsymbol{\varepsilon}_x$ is then obtained by introducing the discretization on the k_y^l grid, and its elements are given by

$$\begin{aligned} (\boldsymbol{\varepsilon}_x)_{mn,lj} &= \frac{1}{2\pi} \int_{-\infty}^{\infty} (\boldsymbol{\Delta}\boldsymbol{\eta}_{x,\text{Tot}}^{\text{Inv}})_{mn}(y) \exp(-i(k_y^l - k_y^j)y) dy \Delta k_y^j \\ &+ \delta_{mn} \delta_{lj} \varepsilon_B. \end{aligned} \quad (\text{B.17})$$

Similarly for the product $\varepsilon_y E_y$ we obtain

$$\begin{aligned} (\boldsymbol{\varepsilon}_y)_{mn,lj} &= \frac{1}{2\pi} \int_{-\infty}^{\infty} (\boldsymbol{\Delta}\boldsymbol{\eta}_{y,\text{Tot}}^{\text{Inv}})_{lj}(x) \exp(-i(k_x^m - k_x^n)x) dx \Delta k_x^n \\ &+ \delta_{mn} \delta_{lj} \varepsilon_B. \end{aligned} \quad (\text{B.18})$$

The integrals in Eqs. (B.17) and (B.18) can be carried out analytically when the matrix $\Delta\boldsymbol{\eta}_{x(y),\text{Tot}}^{\text{Inv}}$ has been found for each $y(x)$ -independent section.

The factorization of Eqs. (3.5)–(3.6) thus become

$$ik_y \mathbf{h}_z - i\beta \mathbf{h}_y = -i\omega\varepsilon_0 \boldsymbol{\varepsilon}_x \mathbf{e}_x \quad (\text{B.19})$$

$$-i\beta \mathbf{h}_x - ik_x \mathbf{h}_z = -i\omega\varepsilon_0 \boldsymbol{\varepsilon}_y \mathbf{e}_y. \quad (\text{B.20})$$

Eliminating \mathbf{h}_z using Eq. (B.6) finally leads to the following eigenvalue problem

$$\begin{bmatrix} -\mathbf{k}_x \mathbf{k}_y & \mathbf{k}_x^2 - k_0^2 \boldsymbol{\varepsilon}_y \\ k_0^2 \boldsymbol{\varepsilon}_x - \mathbf{k}_y^2 & \mathbf{k}_y \mathbf{k}_x \end{bmatrix} \begin{bmatrix} \mathbf{e}_x \\ \mathbf{e}_y \end{bmatrix} = \omega\mu_0\beta \begin{bmatrix} \mathbf{h}_x \\ \mathbf{h}_y \end{bmatrix}. \quad (\text{B.21})$$

The splitting of the factorization along the x and y axes such that the inverse rule can be used along the x axis and the direct rule along the y axis relies on the separability of the k_x and k_y dependencies of the discretization grid such that the discretization in B.15 can be performed in a well-defined manner. However, for our dartboard discretization scheme, this separation is not possible, and for this reason, we simply use the direct rule for the factorization with $\boldsymbol{\varepsilon}_x = \boldsymbol{\varepsilon}_y = \boldsymbol{\varepsilon}_{\text{Tot}}$.

B.3 Relationship between open and periodic boundary conditions

To understand the equivalence between the open BC formalism with equidistant discretization and the periodic BC formalism, let us consider the representation of a function $f(x)$ with compact support such that $f(x) = 0$ for $|x| > L/2$. The continuous integral expansion of this function is given by

$$f(x) = \int F(k) \exp(ikx) dk \quad (\text{B.22})$$

$$F(k) = \frac{1}{2\pi} \int_{-L/2}^{L/2} f(x) \exp(-ikx) dx, \quad (\text{B.23})$$

where the integration domain in (B.23) has been reduced from $[-\infty, \infty]$ to $[-L/2, L/2]$ since $f(x) = 0$ outside this range.

We now implement the equidistant discretisation scheme with a discretization step Δk such that (B.22) becomes

$$f(x) = \sum_n F(k_n) \exp(ik_n x) \Delta k, \quad (\text{B.24})$$

where $k_n = n\Delta k$.

Let us compare this equation to the Fourier series expansion of the same function over the interval $[-L/2, L/2]$ given by

$$f(x) = \sum_n c_n \exp(ik_n x) \quad (\text{B.25})$$

$$c_n = \frac{1}{L} \int_{-L/2}^{L/2} f(x) \exp(-ik_n x) dx. \quad (\text{B.26})$$

where $k_n = n2\pi/L$. Now, the integral expansion (B.22)-(B.23) should ideally reproduce a function $f(x)$ for which $f(x) = 0$ for $|x| > L/2$. However, we observe that the representation in (B.24) implementing the equidistant discretization is mathematically equivalent to the standard Fourier series representation (B.25)-(B.26) of a periodic function $f(x) = f(x + L)$, where the periodicity is given by

$$L = \frac{2\pi}{\Delta k}. \quad (\text{B.27})$$

When representing the optical fields using an open BC and equidistant discretization, we are thus in practice reintroducing a periodic BC with the associated numerical artifacts due to the presence of the neighboring elements. The artifacts can be suppressed by decreasing Δk , in which case the Riemann sum representation of the Fourier transform approaches the exact value of the integral. However, this occurs at the expense of significant computational cost, and a non-uniform discretization scheme is thus strongly preferred.

B.4 Field emitted by a point dipole

In this section we derive the expression for the dipole coupling coefficient used in Eq. (3.18). The derivation follows the same procedure as in Ref. [46] for a 2D Fourier modal method. The starting point is the Lorentz reciprocity theorem in Eq. (2.8). Since we are interested in the field emitted by a single point dipole, only one current source is present, thus $\mathbf{J}_2 = 0$ and $\mathbf{J}_1 = \mathbf{J}_{\text{PD}}\delta(\mathbf{r}_{\text{PD}} - \mathbf{r})$, and Eq. (2.8) simplifies to

$$\int_S (\mathbf{E} \times \mathbf{H}_2 - \mathbf{E}_2 \times \mathbf{H}) \cdot \hat{\mathbf{n}} dS = \mathbf{J}_{\text{PD}} \cdot \mathbf{E}_2(\mathbf{r}_{\text{PD}}), \quad (\text{B.28})$$

where $[\mathbf{E}, \mathbf{H}]$ are the emitted dipole fields, which we wish to determine and $\hat{\mathbf{n}}$ is the normal unit vector to the surface S . $[\mathbf{E}_2, \mathbf{H}_2]$ is set to be the fields of a forward (backward) propagating eigenmode m , such that

$$[\mathbf{E}_2, \mathbf{H}_2] = [\mathbf{e}_m^\pm, \mathbf{h}_m^\pm] \exp[\pm i\beta_m(z^\pm - z_{\text{PD}})], \quad (\text{B.29})$$

where $z^+ > z_{\text{PD}}$ and $z^- < z_{\text{PD}}$. Furthermore the forward (backward) propagating dipole fields are expanded using the dipole coupling coefficient $\mathbf{a}_{\text{PD}}(\mathbf{b}_{\text{PD}})$ as

$$\mathbf{E}^\pm(\mathbf{H}^\pm)(\mathbf{r}_\perp, z > z_{\text{PD}}) = \sum_j a(b)_{\text{PD}}^j \mathbf{e}(\mathbf{h})_j^\pm(\mathbf{r}_\perp) \exp[i\beta(z^\pm - z_{\text{PD}})], \quad (\text{B.30})$$

where $a(b)$ is used for the $+(-)$ index, and $\mathbf{e}(\mathbf{h})_j$ are the j 'th electric(magnetic) eigenmode expanded as Fourier integrals as in Eq. (3.8).

Due to our open boundary conditions the surface integral in Eq. (B.28) is over an infinite surface in the (x, y) -plane. For the forward (backward) propagating dipole field the surface S is placed at $z_{1(2)}$ just above (below) the dipole position, such that the normal unit vectors are $\hat{\mathbf{n}}_1 = -\hat{\mathbf{n}}_2 = \hat{\mathbf{z}}$. Inserting Eq. (B.30) into Eq. (B.28) for the forward and backward propagating dipole fields and using that $\mathbf{e}^+ = \mathbf{e}^- = \mathbf{e}$ and $\mathbf{h}^+ = -\mathbf{h}^- = \mathbf{h}$ [39] leads to

$$\begin{aligned} & - \sum_j b_{\text{PD}}^j \int_{S_2} (\pm \mathbf{e}_j \times \mathbf{h}_m + \mathbf{e}_m \times \mathbf{h}_j) \exp[i(\pm\beta_m - \beta_j)(z_2 - z_{\text{PD}})] \cdot \hat{\mathbf{z}} dS \\ & + \sum_j a_{\text{PD}}^j \int_{S_1} (\pm \mathbf{e}_j \times \mathbf{h}_m - \mathbf{e}_m \times \mathbf{h}_j) \exp[i(\pm\beta_m + \beta_j)(z_1 - z_{\text{PD}})] \cdot \hat{\mathbf{z}} dS \\ & = \mathbf{J}_{\text{PD}} \mathbf{e}_m^\pm. \end{aligned} \quad (\text{B.31})$$

The integral over the products between the electric and magnetic eigenmode components will be carried out by using the expansion of the eigenmodes given in the first line of Eq. (3.8).

$$\begin{aligned} & \iint_{-\infty}^{\infty} e_{j,x(y)} h_{m,y(x)} dx dy = \\ & \iint_{-\infty}^{\infty} \iint_{-\infty}^{\infty} c_{e_x(y),j}(k_x, k_y) c_{h_y(x),m}(k'_x, k'_y) \\ & \times \exp\left[i\left((k_x + k'_x)x + (k_y + k'_y)y\right)\right] dk_\perp dk'_\perp dx dy \\ & = (2\pi)^2 \iint_{-\infty}^{\infty} c_{e_x(y),j}(k_x, k_y) c_{h_y(x),m}(k'_x, k'_y) \\ & \times \delta(k_x + k'_x) \delta(k_y + k'_y) dk_\perp dk'_\perp \\ & = (2\pi)^2 \int_{-\infty}^{\infty} c_{e_x(y),j}(k_x, k_y) c_{h_y(x),m}(-k_x, -k_y) dk_\perp \\ & \simeq (2\pi)^2 \sum_{l,p} c_{e_x(y),j}(k_x^l, k_y^p) c_{h_y(x),m}(-k_x^l, -k_y^p) \Delta k_\perp^{lp}, \end{aligned} \quad (\text{B.32})$$

where c_f are the expansion coefficients defined in Eq. (3.10), and are found by solving Eqs. (3.16) and (3.17). Inserting Eq. (B.32) into Eq. (B.31) leads to the following matrix equation for the dipole coupling coefficients

$$\begin{bmatrix} \mathbf{M}^{++} & \mathbf{M}^{+-} \\ \mathbf{M}^{-+} & \mathbf{M}^{--} \end{bmatrix} \begin{bmatrix} \mathbf{a}_{\text{PD}}^{(x,y,z)} \\ \mathbf{b}_{\text{PD}}^{(x,y,z)} \end{bmatrix} = \begin{bmatrix} J_{\text{PD}}^{(x,y,z)} \mathbf{e}_{(x,y,z)}^+(\mathbf{r}_{\text{PD}}) \\ J_{\text{PD}}^{(x,y,z)} \mathbf{e}_{(x,y,z)}^-(\mathbf{r}_{\text{PD}}) \end{bmatrix}, \quad (\text{B.33})$$

where (x, y, z) is either orientation of the dipole. The \mathbf{M} matrices are

$$\mathbf{M}^{++} = (2\pi)^2 \left(\mathbf{C}_{h_y, \uparrow}^T \mathbf{C}_{e_x} - \mathbf{C}_{h_x, \uparrow}^T \mathbf{C}_{e_y} - \mathbf{C}_{e_x, \downarrow}^T \mathbf{C}_{h_y} + \mathbf{C}_{e_y, \downarrow}^T \mathbf{C}_{h_x} \right) \Delta \mathbf{k}_{\perp}, \quad (\text{B.34a})$$

$$\mathbf{M}^{+-} = -(2\pi)^2 \left(\mathbf{C}_{h_y, \uparrow}^T \mathbf{C}_{e_x} - \mathbf{C}_{h_x, \uparrow}^T \mathbf{C}_{e_y} + \mathbf{C}_{e_x, \downarrow}^T \mathbf{C}_{h_y} - \mathbf{C}_{e_y, \downarrow}^T \mathbf{C}_{h_x} \right) \Delta \mathbf{k}_{\perp}, \quad (\text{B.34b})$$

$$\mathbf{M}^{-+} = (2\pi)^2 \left(-\mathbf{C}_{h_y, \uparrow}^T \mathbf{C}_{e_x} + \mathbf{C}_{h_x, \uparrow}^T \mathbf{C}_{e_y} - \mathbf{C}_{e_x, \downarrow}^T \mathbf{C}_{h_y} + \mathbf{C}_{e_y, \downarrow}^T \mathbf{C}_{h_x} \right) \Delta \mathbf{k}_{\perp}, \quad (\text{B.34c})$$

$$\mathbf{M}^{--} = -(2\pi)^2 \left(-\mathbf{C}_{h_y, \uparrow}^T \mathbf{C}_{e_x} + \mathbf{C}_{h_x, \uparrow}^T \mathbf{C}_{e_y} + \mathbf{C}_{e_x, \downarrow}^T \mathbf{C}_{h_y} - \mathbf{C}_{e_y, \downarrow}^T \mathbf{C}_{h_x} \right) \Delta \mathbf{k}_{\perp}, \quad (\text{B.34d})$$

where each column of matrix \mathbf{C} contains the expansion coefficient for the eigenmode. \mathbf{C}^T is the transpose of \mathbf{C} and \mathbf{C}_{\downarrow} means that the rows has been mirrored, such that the first row is now the last row of the matrix.

The eigenmodes are in principal orthogonal, such that \mathbf{M}^{+-} and \mathbf{M}^{-+} are diagonal and \mathbf{M}^{++} and \mathbf{M}^{--} are zero. This orthogonality is found numerically to hold approximately, however with non-vanishing elements possibly stemming from numerical rounding errors.

B.5 Waveguide on substrate

The results presented in Chapter 3 are for free standing square waveguides, however it is experimentally much more interesting to investigate waveguides supported by a dielectric substrate, since these enables on-chip optical systems due to their very low transmission loss [87]. Furthermore, they have reasonably large β -factors for one dipole orientation [88], which makes them a candidate for realising an efficient on-chip single-photon source.

For a ridge waveguide on a substrate (see Fig. B.2) the dielectric function can be described as

$$\varepsilon(x, y) = \Delta \varepsilon_w \text{rect}(x/w_w) \text{rect}(y/h_w - 1/2) + \varepsilon_B + \Theta(-y) \Delta \varepsilon_S, \quad (\text{B.35})$$

where $\Delta\varepsilon_w = \varepsilon_w - \varepsilon_B$ within the waveguide region and $\Delta\varepsilon_S = \varepsilon_S - \varepsilon_B$. $\Theta(y)$ is the Heaviside step function and $\text{rect}(t)$ is the rectangular function defined as

$$\Theta(y) = \begin{cases} 1 & \text{if } y > 0 \\ 0 & \text{if } y \leq 0. \end{cases} \quad (\text{B.36a})$$

$$\text{rect}(t) = \begin{cases} 0 & \text{if } |t| > 1/2 \\ 1 & \text{if } |t| \leq 1/2. \end{cases} \quad (\text{B.36b})$$

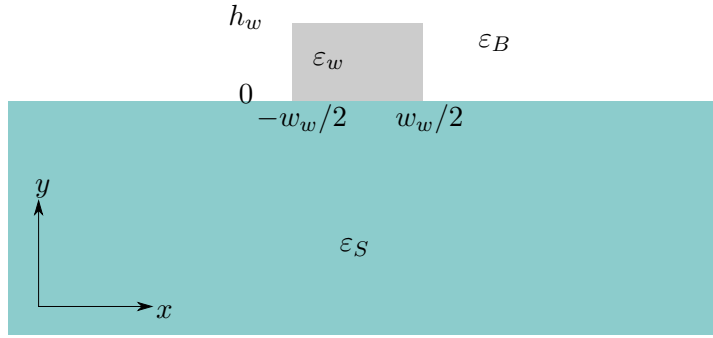


Figure B.2: Ridge waveguide on substrate.

The expansion coefficients for the dielectric function are given by Eq. (3.10)

$$\begin{aligned} c_\varepsilon(k_x, k_y) &= \frac{1}{(2\pi)^2} \int \int \varepsilon(x, y) \exp[-i(k_x x + k_y y)] dx dy \\ &= \frac{1}{(2\pi)^2} \int \int (\Delta\varepsilon_w \text{rect}(x, y) + \varepsilon_B + \Delta\varepsilon_S \Theta(-y)) \\ &\quad \exp[-i(k_x x + k_y y)] dx dy. \end{aligned} \quad (\text{B.37})$$

In the following the Fourier transform \mathcal{F} of a function $f(x, y)$ will be denoted as

$$\mathcal{F}[f(x, y)] = \frac{1}{(2\pi)^2} \int_{-\infty}^{\infty} \int_{-\infty}^{\infty} f(x, y) \exp[-i(k_x x + k_y y)] dx dy. \quad (\text{B.38})$$

The expansion coefficients in Eq. (B.37) are given by three Fourier transforms:

$$c_\varepsilon(k_x, k_y) = \mathcal{F}[\Delta\varepsilon_w \text{rect}(x/w_w) \text{rect}(y/h_w - 1/2)] + \mathcal{F}[\varepsilon_B] + \mathcal{F}[\Delta\varepsilon_S \Theta(-y)]. \quad (\text{B.39})$$

The above Fourier transforms are:

$$\mathcal{F}[\Delta\varepsilon_w \text{rect}(x/w_w) \text{rect}(y/h_w - 1/2)] = \frac{1}{(2\pi)^2} \Delta\varepsilon_w h_w w_w \text{sinc}(w_w k_x/2) \text{sinc}(h_w k_y/2) \exp(-ih_w k_y/2), \quad (\text{B.40a})$$

$$\mathcal{F}[\varepsilon_B] = \varepsilon_B \delta(k_y) \delta(k_x) \quad (\text{B.40b})$$

$$\mathcal{F}[\Delta\varepsilon_S \Theta(-y)] = \Delta\varepsilon_S \frac{1}{2\pi} \delta(k_x) \left(\pi \delta(k_y) + \frac{i}{k_y} \right), \quad (\text{B.40c})$$

where $\text{sinc}(x) = \sin(x)/x$. In the Fourier transform of the Heaviside step function the term $1/k_y$ gives us an issue, since we risk dividing with zero. Thus our developed 3D oFMM is not suitable for handling ridge waveguides on infinite substrates with open BCs. For these structures the substrate has to be surrounded by air, which can be a reasonably good description, however not ideal.

All-optical mapping of the position of single quantum dots embedded in a nanowire antenna

This appendix supports Chapter 5 with various experimental and computational results. The appendix will be referred to throughout the chapter.

C.1 Photoluminescence spectrum

In Fig. C.1 the PL spectrum of the investigated needle nanowire is shown. As seen there are quite many peaks in the spectrum at different wavelengths, which originates from different transitions in the QDs. The QDs we have chosen to focus this study on are QD1, QD2 and QD3, since these produce three very different far-field patterns. The emission wavelengths of the three QDs under study are 891.5 nm, 907 nm and 912 nm.

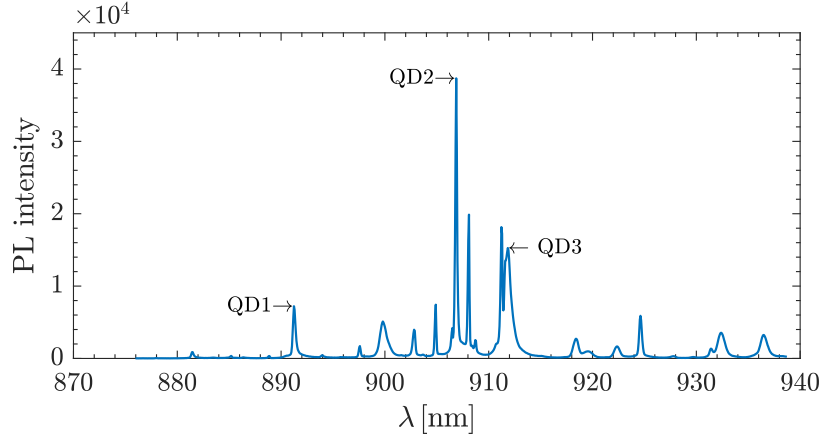


Figure C.1: PL spectrum of the needle nanowire. As seen several QD transitions are visible in the spectrum. We have chosen to focus this study on QD1, QD2 and QD3.

C.2 Polarization study

In order to investigate which state transitions the peaks in Fig. C.1 are due to, we measure the PL spectrum at different polarizations. If the transition is from a neutral exciton, the fine structure splitting (fss) might be present as a shift in the peak position in the PL spectrum as the polarizer is rotated. This study has been performed on QD1, QD2 and QD3, and the results are seen in Figs. C.2-C.4 below. A fss is observed in the polarization spectra for QD1 and QD2, indicating that these are likely from a neutral exciton transition. There is no fss for QD3, and thus it cannot be concluded that this transition is from a neutral exciton.

C.3 Lifetime measurement

Having concluded that QD1 (891.5 nm) and QD2 (907 nm) are neutral excitons, the quantum state of QD3 can be determined by comparison of the radiative lifetime. For a trion state the radiative lifetime is smaller than for a neutral exciton in InGaAs QDs [119]. After excitation of the QDs the emission intensity stemming from a neutral exciton can be described by a biexponential curve as [147]

$$I = C_0 \gamma_r [A_1 \exp(-t/\tau_1) + A_2 \exp(-t/\tau_2)], \quad (\text{C.1})$$

where C_0 is proportional to the collection efficiency of the experimental setup and the term in the brackets is the population of the bright exciton state. The lifetimes τ_1 and τ_2 are given by the radiative decay rate γ_r , the non-radiative

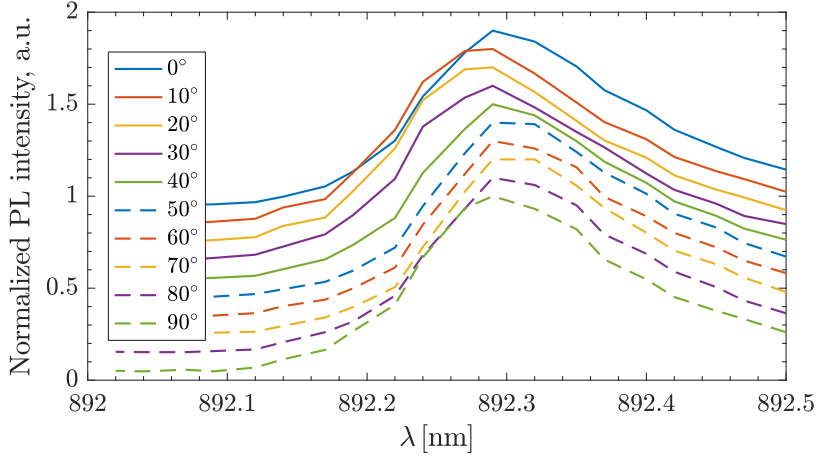


Figure C.2: PL spectrum around the QD1 emission wavelength for different rotations of the polarizer. As seen the location of the peak shifts as the polarizer is rotated, which indicates that the transition is from a neutral exciton. The shift is due to the fine structure splitting.

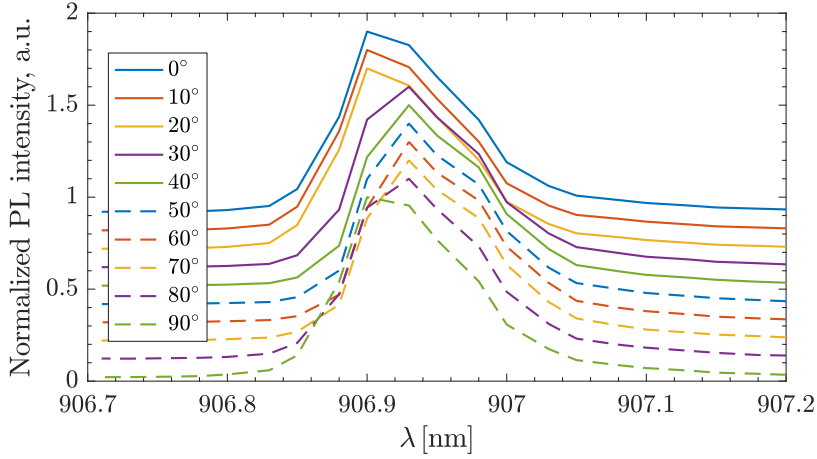


Figure C.3: PL spectrum around the QD2 emission wavelength for different rotations of the polarizer. As seen the location of the peak shifts as the polarizer is rotated, which indicates that the transition is from a neutral exciton. The shift is due to the fine structure splitting.

decay rate γ_{nr} , and the spin-flip rates between the dark and bright exciton γ_{db} and γ_{bd} as [120, 147]

$$\tau_1^{-1} = \gamma_1 = \frac{A + B}{2}, \quad (\text{C.2a})$$

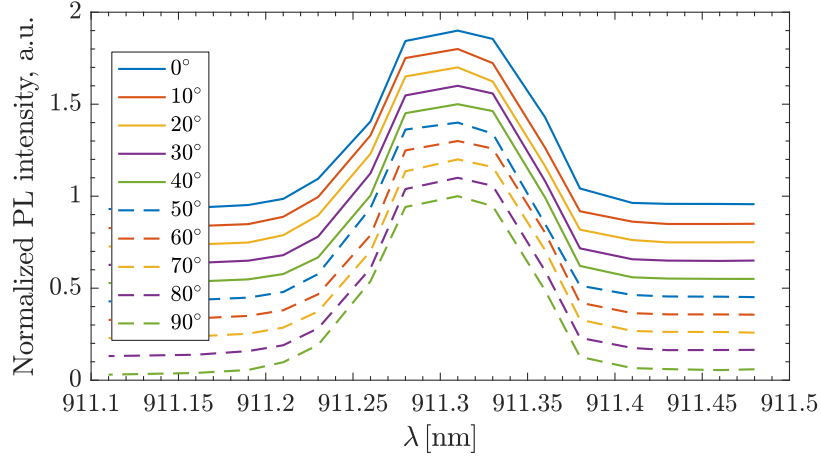


Figure C.4: PL spectrum around the QD3 emission wavelength for different rotations of the polarizer. As seen the location of the peak does not shift as the polarizer is rotated, which could indicate that the transition is from a charged trion state or that there is no fss in the QD.

$$\tau_2^{-1} = \gamma_2 = \frac{A - B}{2}, \quad (\text{C.2b})$$

where

$$A = \gamma_r + 2\gamma_{nr} + \gamma_{db} + \gamma_{bd} = \gamma_r + 2\gamma_{nr} + 2\gamma_{db}, \quad (\text{C.3a})$$

$$B = \sqrt{\gamma_r^2 + 2\gamma_r(\gamma_{bd} - \gamma_{db}) + (\gamma_{db} + \gamma_{bd})^2} = \sqrt{\gamma_r^2 + 4\gamma_{db}^2}. \quad (\text{C.3b})$$

All the rates are illustrated in the three-level scheme in Fig. C.5. In principle the $|X\rangle$ and $|Y\rangle$ excitons also couple to each other through spin-flip processes, however this coupling is not important for the analysis here, since it has been shown to occur with a time constant smaller than 100 ps for InAs/GaAs QDs [118]. Furthermore, we collect both polarizations in the time-resolved PL measurement in Fig. C.6, and thus the simplified three-level scheme is sufficient for determining the quantum state of QD1, QD2 and QD3. Including the coupling between the $|X\rangle$ and $|Y\rangle$ excitons would be important for a polarization study of the emitted field. Assuming an equal population of the bright and dark exciton state after the non-resonant excitation, the amplitudes of the two decay rates in Eq. (C.1), $A_{1(2)}$, are given as [147]

$$A_1 = \frac{1}{4} \left[1 + \frac{\gamma_r}{\gamma_1 - \gamma_2} \right] - \frac{1}{2} \frac{\gamma_{db}}{\gamma_1 - \gamma_2}, \quad (\text{C.4a})$$

$$A_2 = \frac{1}{4} \left[1 - \frac{\gamma_r}{\gamma_1 - \gamma_2} \right] + \frac{1}{2} \frac{\gamma_{db}}{\gamma_1 - \gamma_2}. \quad (\text{C.4b})$$

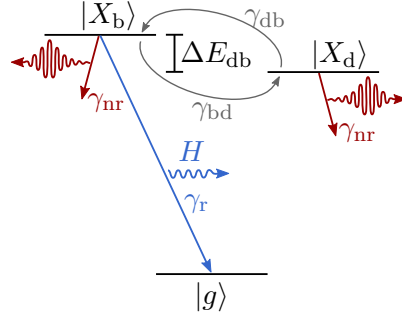


Figure C.5: Three-level scheme used for describing the biexponential trend of the time-resolved PL measurement in Fig. C.6. The bright exciton couples through spin-flip processes to the dark exciton with rates γ_{db} and γ_{bd} , and both excitons decay through non-radiating processes at the rate γ_{nr} . The recombination rate of the bright exciton is γ_r , and leads to the emission of a photon. An identical three-level scheme applies for the $|Y\rangle$ excitons.

There exist no dark trion state and the radiative decay rate for a trion is larger than for a neutral exciton. Thus a trion state should show a significantly shorter lifetime in a measurement than a neutral exciton. The lifetime measurements of the QD1, QD2 and QD3 are shown in Fig. C.6, where the experimental data has been fitted to Eq. (C.1) and the extracted lifetimes are shown in the plots. As seen the lifetime of QD3 is more than a factor 2 larger than the lifetime of QD1 and QD2, which does not point towards QD3 being a trion state. However, QD3 does not show a clear biexponential behaviour as is expected for a neutral exciton. We attribute the lack of a clear biexponential trend to a fast spin-flip process between the bright and the dark exciton within QD3 (i.e. large γ_{db}), which reduces the intensity of the fast decay rate relative to the slow as seen from Eqs. (C.4). Thus in the experiment only the slow decay channel will be visible leading to larger lifetimes and hiding the biexponential behaviour, as reported in Ref. [118, 120].

Based on the lifetime measurements and the PL polarization spectra in Figs. C.2-C.4, we conclude that all three QD emissions originates from recombination of a neutral exciton.

C.4 The role of the emitter type for the far-field radiation pattern

In this appendix we will investigate the role of the emitter type for an emitter placed in a nanowire supporting three guided modes: HE_{11}^r , HE_{11}^ϕ and TE_{01} . The superscript on the HE_{11} mode denotes the dominant in-plane linear polarization. We will consider two types of emitters: trion states and neutral exciton

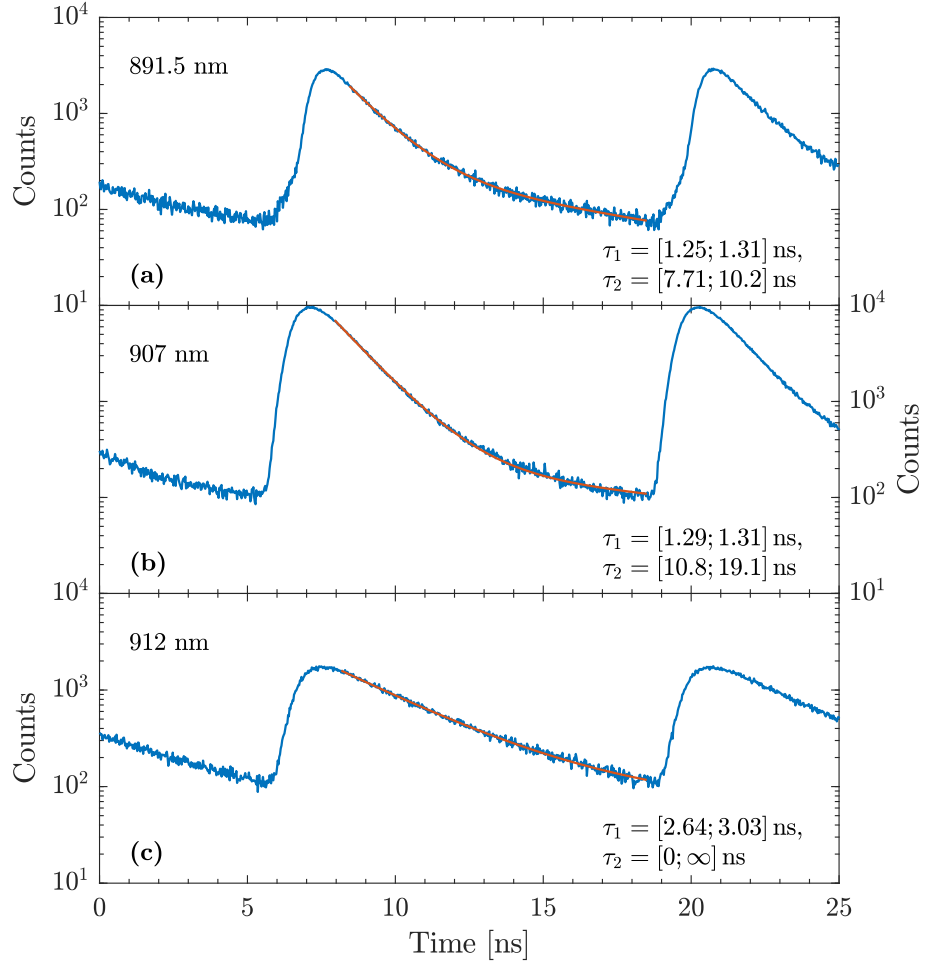


Figure C.6: Measured decay curves of QD1, QD2 and QD3. The curves are fitted to Eq. (C.1) and the extracted lifetimes are given in their 95 % confidence interval.

states, producing circularly and linearly polarized light respectively. Depending on the spin of the additional carrier in the trion state it will produce either right or left circularly polarized light, which in the oFMM formalism is described as a point dipole with its components 90 degree out of phase as

$$\sigma^+ = \frac{p}{\sqrt{2}} (\hat{\mathbf{r}} + i\hat{\phi}) \quad \left(X_{\pm}^{|\alpha_{e(h)}} \right), \quad (\text{C.5a})$$

$$\sigma^- = \frac{p}{\sqrt{2}} (\hat{\mathbf{r}} - i\hat{\phi}) \quad \left(X_{\pm}^{|\alpha_{e(h)}} \right), \quad (\text{C.5b})$$

where $\hat{\mathbf{r}}$ and $\hat{\phi}$ are the unit vectors for the radial and tangential coordinates. The neutral exciton will produce either horizontally or vertically polarized light as

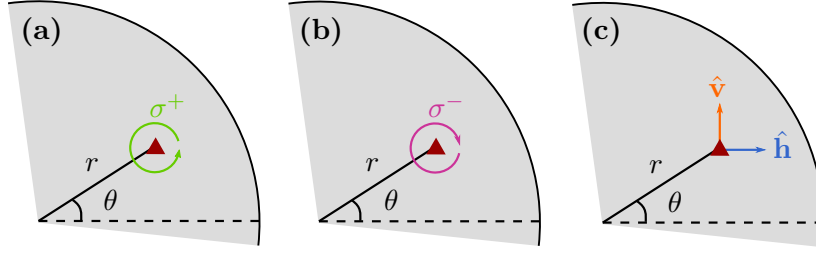


Figure C.7: Quantum dot placed in a nanowire producing either circularly (a,b) or linearly (c) polarized light.

$$\mathbf{p}^H = p\hat{\mathbf{h}} = p \begin{pmatrix} \cos\theta\hat{\mathbf{r}} - \sin\theta\hat{\phi} \\ X^b \end{pmatrix}, \quad (\text{C.6a})$$

$$\mathbf{p}^V = p\hat{\mathbf{v}} = p \begin{pmatrix} \sin\theta\hat{\mathbf{r}} + \cos\theta\hat{\phi} \\ Y^b \end{pmatrix}, \quad (\text{C.6b})$$

where θ is defined in Fig. C.7.

The HE₁₁ mode has contributions from angular momentum $n = \pm 1$, and for a linear dipole these are coupled to equally, however a circular dipole will mainly couple to one of these, which can be derived using Eqs. (5.2) and (5.3) for an on-axis dipole, where $E_{r,n,j} = \pm iE_{\phi,n,j}$ in Eq. (5.3)¹. For the circular dipole in Eq. (C.5a) at $r = 0$ and $n = \pm 1$ we have the following relation between the electric field components

$$E_{r,n=1,j}(r=0) = -i \sum_{m=1}^M k_m \Delta k_m c_{n,jm}^E = -iE_{\phi,n=1,j}(r=0), \quad (\text{C.7a})$$

$$E_{r,n=-1,j}(r=0) = i \sum_{m=1}^M k_m \Delta k_m b_{n,jm}^E = iE_{\phi,n=-1,j}(r=0). \quad (\text{C.7b})$$

By performing the dot product in Eq. (5.2) and using the circular dipole in Eq. (C.5a) we get

$$a_{n=1,j}^{\sigma^+}(0) = \frac{i\omega}{2[W]} \frac{p}{\sqrt{2}} [E_{r,n=1,j}(0) + iE_{\phi,n=1,j}(0)] = 0, \quad (\text{C.8a})$$

$$a_{n=-1,j}^{\sigma^+}(0) = \frac{i\omega}{2[W]} \frac{p}{\sqrt{2}} [E_{r,n=-1,j}(0) + iE_{\phi,n=-1,j}(0)] \equiv a_{\text{HE11},-1}^{\sigma^+}. \quad (\text{C.8b})$$

¹For an off-axis dipole the circular dipole will couple to both angular momenta, due to the non-equal emission rate into the radial and tangential component of the HE₁₁ mode as seen in Fig. 5.3

Correspondingly, we have the dipole coupling coefficient $a_{\text{HE11},+1}^{\sigma^-}$ for the other circular dipole given in Eq. (C.5b). However, in the following we consider an off-axis dipole, such that it also couples to the TE01 mode keeping in mind that the circular dipoles will mainly couple to either angular momenta.

The generated electric field for the off-axis dipoles in Eqs. (C.5) and (C.6) in the nanowire after propagation along the z -axis are

$$E_r^{\sigma^\pm} = \left[a_{\text{HE11},+1}^{\sigma^\pm} E_{r,\text{HE11},+1} + a_{\text{HE11},-1}^{\sigma^\pm} E_{r,\text{HE11},-1} \right] \exp(i\beta_{\text{HE11}} z), \quad (\text{C.9a})$$

$$E_\phi^{\sigma^\pm} = \left[a_{\text{HE11},+1}^{\sigma^\pm} E_{\phi,\text{HE11},+1} + a_{\text{HE11},-1}^{\sigma^\pm} E_{\phi,\text{HE11},-1} \right] \exp(i\beta_{\text{HE11}} z) + a_{\text{TE01}}^{\sigma^\pm} E_{\phi,\text{TE01},1} \exp(i\beta_{\text{TE01}} z), \quad (\text{C.9b})$$

$$E_r^{p^{HV}} = a_{\text{HE11}}^{p^{HV}} E_{r,\text{HE11}} \exp(i\beta_{\text{HE11}} z), \quad (\text{C.9c})$$

$$E_\phi^{p^{HV}} = a_{\text{HE11}}^{p^{HV}} E_{\phi,\text{HE11}} \exp(i\beta_{\text{HE11}} z) + a_{\text{TE01}}^{p^{HV}} E_{\phi,\text{TE01},1} \exp(i\beta_{\text{TE01}} z), \quad (\text{C.9d})$$

and by replacing E with H and swap r and ϕ the generated magnetic fields are given with the same expressions.

The dipole coupling coefficients are given by Eq. (5.2) as

$$a_{\text{HE11}}^{p^{r(\phi)}} = E_{r(\phi),\text{HE11}} = E_{r(\phi),\text{HE11},-1} + E_{r(\phi),\text{HE11},+1}, \quad (\text{C.10a})$$

$$a_{\text{TE01}}^{p^\phi} = E_{\phi,\text{TE01}}, \quad (\text{C.10b})$$

$$a_{\text{HE11},-1}^{\sigma^\pm} = \frac{1}{\sqrt{2}} [E_{r,\text{HE11},-1} \pm iE_{\phi,\text{HE11},-1}], \quad (\text{C.10c})$$

$$a_{\text{HE11},+1}^{\sigma^\pm} = \frac{1}{\sqrt{2}} [E_{r,\text{HE11},+1} \pm iE_{\phi,\text{HE11},+1}], \quad (\text{C.10d})$$

$$a_{\text{TE01}}^{\sigma^\pm} = \pm \frac{1}{\sqrt{2}} iE_{\phi,\text{TE01}} \quad (\text{C.10e})$$

$$a_{\text{HE11},\pm 1}^{p^H} = [\cos \theta E_{r,\text{HE11},\pm 1} - \sin \theta E_{\phi,\text{HE11},\pm 1}], \quad (\text{C.10f})$$

$$a_{\text{HE11},\pm 1}^{p^V} = [\sin \theta E_{r,\text{HE11},\pm 1} + \cos \theta E_{\phi,\text{HE11},\pm 1}], \quad (\text{C.10g})$$

$$a_{\text{TE01}}^{p^H} = -\sin \theta E_{\phi,\text{TE01}}, \quad (\text{C.10h})$$

$$a_{\text{TE01}}^{p^V} = \cos \theta E_{\phi,\text{TE01}}, \quad (\text{C.10i})$$

where the common pre-factor $\frac{i\omega}{2} p$ has been omitted. Before computing the power in the nanowire emitted by each dipole we will state the power emitted by the

tangentially and radially oriented dipoles using the time averaged Poynting vector in Eq. (2.7)

$$P^{p^r} = \frac{1}{2} \text{Re} \left\{ \left| a_{\text{HE11}}^{p^r} \right|^2 \left[E_{r,\text{HE11}} H_{\phi,\text{HE11}}^* - E_{\phi,\text{HE11}} H_{r,\text{HE11}}^* \right] \right\} = P_{\text{HE11}}^{p^r}, \quad (\text{C.11a})$$

$$\begin{aligned} P^{p^\phi} &= \frac{1}{2} \text{Re} \left\{ \left[\left| a_{\text{HE11}}^{p^\phi} \right|^2 E_{r,\text{HE11}} H_{\phi,\text{HE11}}^* - \right. \right. \\ &\quad \left. \left(a_{\text{HE11}}^{p^\phi} E_{\phi,\text{HE11}} \exp(i\beta_{\text{HE11}} z) + a_{\text{TE01}}^{p^\phi} E_{\phi,\text{TE01}} \exp(i\beta_{\text{TE01}} z) \right) \right. \\ &\quad \left. \left(a_{\text{HE11}}^{p^{\phi*}} H_{r,\text{HE11}}^* \exp(-i\beta_{\text{HE11}} z) + a_{\text{TE01}}^{p^{\phi*}} H_{r,\text{TE01}}^* \exp(-i\beta_{\text{TE01}} z) \right) \right] \right\} \\ &= \frac{1}{2} \text{Re} \left\{ \left[\left| a_{\text{HE11}}^{p^\phi} \right|^2 \left(E_{r,\text{HE11}} H_{\phi,\text{HE11}}^* - E_{\phi,\text{HE11}} H_{r,\text{HE11}}^* \right) \right. \right. \\ &\quad - a_{\text{HE11}}^{p^\phi} a_{\text{TE01}}^{p^{\phi*}} E_{\phi,\text{HE11}} H_{r,\text{TE01}}^* \exp(i\Delta_\beta z) \\ &\quad - a_{\text{TE01}}^{p^\phi} a_{\text{HE11}}^{p^{\phi*}} E_{\phi,\text{TE01}} H_{r,\text{HE11}}^* \exp(-i\Delta_\beta z) \\ &\quad \left. \left. - \left| a_{\text{TE01}}^{p^\phi} \right|^2 E_{\phi,\text{TE01}} H_{r,\text{TE01}}^* \right] \right\} \\ &= P_{\text{HE11}}^{p^\phi} + P_{\text{TE01}}^{p^\phi} - \frac{1}{2} \text{Re} \left\{ \left[a_{\text{HE11}}^{p^\phi} a_{\text{TE01}}^{p^{\phi*}} E_{\phi,\text{HE11}} H_{r,\text{TE01}}^* \exp(i\Delta_\beta z) \right. \right. \\ &\quad \left. \left. + a_{\text{TE01}}^{p^\phi} a_{\text{HE11}}^{p^{\phi*}} E_{\phi,\text{TE01}} H_{r,\text{HE11}}^* \exp(-i\Delta_\beta z) \right] \right\}, \quad (\text{C.11b}) \end{aligned}$$

where $\Delta_\beta = \beta_{\text{HE11}} - \beta_{\text{TE01}}$. As above the power in the nanowire for the circular and linear dipoles is given by the time averaged Poynting vector in Eq. (2.7). For the circular dipoles we get

$$\begin{aligned} P^{\sigma^\pm} &= \frac{1}{2} \text{Re} \left\{ \left[a_{\text{HE11},+1}^{\sigma^\pm} E_{r,\text{HE11},+1} + a_{\text{HE11},-1}^{\sigma^\pm} E_{r,\text{HE11},-1} \right] \right. \\ &\quad \left[a_{\text{HE11},+1}^{\sigma^{\pm*}} H_{\phi,\text{HE11},+1}^* + a_{\text{HE11},-1}^{\sigma^{\pm*}} H_{\phi,\text{HE11},-1}^* \right] \\ &\quad - \left[\left(a_{\text{HE11},+1}^{\sigma^\pm} E_{\phi,\text{HE11},+1} + a_{\text{HE11},-1}^{\sigma^\pm} E_{\phi,\text{HE11},-1} \right) \exp(i\beta_{\text{HE11}} z) \right. \\ &\quad \left. + a_{\text{TE01}}^{\sigma^\pm} E_{\phi,\text{TE01}} \exp(i\beta_{\text{TE01}} z) \right] \\ &\quad \left[\left(a_{\text{HE11},+1}^{\sigma^{\pm*}} H_{r,\text{HE11},+1}^* + a_{\text{HE11},-1}^{\sigma^{\pm*}} H_{r,\text{HE11},-1}^* \right) \exp(-i\beta_{\text{HE11}} z) \right. \\ &\quad \left. + a_{\text{TE01}}^{\sigma^{\pm*}} H_{r,\text{TE01}}^* \exp(-i\beta_{\text{TE01}} z) \right] \left. \right\} \\ &= \frac{1}{2} \text{Re} \left\{ \left| a_{\text{HE11},+1}^{\sigma^\pm} \right|^2 E_{r,\text{HE11},+1} H_{\phi,\text{HE11},+1}^* \right. \\ &\quad + \left| a_{\text{HE11},-1}^{\sigma^\pm} \right|^2 E_{r,\text{HE11},-1} H_{\phi,\text{HE11},-1}^* \\ &\quad + a_{\text{HE11},+1}^{\sigma^\pm} a_{\text{HE11},-1}^{\sigma^{\pm*}} E_{r,\text{HE11},+1} H_{\phi,\text{HE11},-1}^* \\ &\quad \left. + a_{\text{HE11},+1}^{\sigma^{\pm*}} a_{\text{HE11},-1}^{\sigma^\pm} E_{r,\text{HE11},-1} H_{\phi,\text{HE11},+1}^* \right\} \quad (\text{C.12a}) \end{aligned}$$

$$\begin{aligned}
& - \left| a_{\text{HE11},+1}^{\sigma^\pm} \right|^2 E_{\phi,\text{HE11},+1} H_{r,\text{HE11},+1}^* \\
& - \left| a_{\text{HE11},-1}^{\sigma^\pm} \right|^2 E_{\phi,\text{HE11},-1} H_{r,\text{HE11},-1}^* \\
& - a_{\text{HE11},+1}^{\sigma^\pm} a_{\text{HE11},-1}^{\sigma^{\pm*}} E_{\phi,\text{HE11},+1} H_{r,\text{HE11},-1}^* \\
& - a_{\text{HE11},+1}^{\sigma^{\pm*}} a_{\text{HE11},-1}^{\sigma^\pm} E_{\phi,\text{HE11},-1} H_{r,\text{HE11},+1}^* \\
& - a_{\text{TE01}}^{\sigma^\pm} H_{r,\text{TE01}}^* \left(a_{\text{HE11},+1}^{\sigma^\pm} E_{\phi,\text{HE11},+1} + a_{\text{HE11},-1}^{\sigma^\pm} E_{\phi,\text{HE11},-1} \right) \exp(i\Delta_\beta z) \\
& - a_{\text{TE01}}^{\sigma^{\pm*}} E_{\phi,\text{TE01}} \left(a_{\text{HE11},+1}^{\sigma^{\pm*}} H_{r,\text{HE11},+1}^* + a_{\text{HE11},-1}^{\sigma^{\pm*}} H_{r,\text{HE11},-1}^* \right) \exp(-i\Delta_\beta z) \\
& - \left\{ \left| a_{\text{TE01}}^{\sigma^\pm} \right|^2 E_{\phi,\text{TE01}} H_{r,\text{TE01}}^* \right\} \tag{C.12b}
\end{aligned}$$

We will show that the incoherent sum of the circular dipoles are equal to the incoherent sum of the linear dipoles. In order to show this we first add the power emitted by the circular dipoles. In the derivation we need the following relations between the dipole coupling coefficients

$$\begin{aligned}
& \left| a_{\text{HE11}}^{p^{r(\phi)}} \right|^2 E_{r(\phi),\text{HE11}} H_{\phi(r),\text{HE11}}^* = \\
& \left[a_{\text{HE11},+1}^{p^{r(\phi)}} E_{r(\phi),\text{HE11},+1} + a_{\text{HE11},-1}^{p^{r(\phi)}} E_{r(\phi),\text{HE11},-1} \right] \\
& \left[a_{\text{HE11},+1}^{p^{r(\phi)*}} H_{r(\phi),\text{HE11},+1}^* + a_{\text{HE11},-1}^{p^{r(\phi)*}} H_{r(\phi),\text{HE11},-1}^* \right], \tag{C.13a}
\end{aligned}$$

$$a_{\text{HE11},-1}^{\sigma^\pm} = \frac{1}{\sqrt{2}} \left[a_{\text{HE11},-1}^{p^r} \pm i a_{\text{HE11},-1}^{p^\phi} \right], \tag{C.13b}$$

$$a_{\text{HE11},+1}^{\sigma^\pm} = \frac{1}{\sqrt{2}} \left[a_{\text{HE11},+1}^{p^r} \pm i a_{\text{HE11},+1}^{p^\phi} \right], \tag{C.13c}$$

$$\left| a_{\text{HE11},-1}^{\sigma^\pm} \right|^2 = \frac{1}{2} \left[\left| a_{\text{HE11},-1}^{p^r} \right|^2 + \left| a_{\text{HE11},-1}^{p^\phi} \right|^2 \right], \tag{C.13d}$$

$$\left| a_{\text{HE11},+1}^{\sigma^\pm} \right|^2 = \frac{1}{2} \left[\left| a_{\text{HE11},+1}^{p^r} \right|^2 + \left| a_{\text{HE11},+1}^{p^\phi} \right|^2 \right], \tag{C.13e}$$

$$\begin{aligned}
a_{\text{HE11},+1}^{\sigma^\pm} a_{\text{HE11},-1}^{\sigma^{\pm*}} &= \frac{1}{2} \left[a_{\text{HE11},+1}^{p^r} a_{\text{HE11},-1}^{p^{r*}} + a_{\text{HE11},+1}^{p^\phi} a_{\text{HE11},-1}^{p^{\phi*}} \right. \\
& \quad \mp i a_{\text{HE11},+1}^{p^r} a_{\text{HE11},-1}^{p^{\phi*}} \mp i a_{\text{HE11},+1}^{p^\phi} a_{\text{HE11},-1}^{p^{r*}} \left. \right], \tag{C.13f}
\end{aligned}$$

$$\begin{aligned}
a_{\text{HE11},+1}^{\sigma^{\pm*}} a_{\text{HE11},-1}^{\sigma^\pm} &= \frac{1}{2} \left[a_{\text{HE11},+1}^{p^{r*}} a_{\text{HE11},-1}^{p^r} + a_{\text{HE11},+1}^{p^{\phi*}} a_{\text{HE11},-1}^{p^\phi} \right. \\
& \quad \mp i a_{\text{HE11},+1}^{p^{r*}} a_{\text{HE11},-1}^{p^\phi} \mp i a_{\text{HE11},+1}^{p^{\phi*}} a_{\text{HE11},-1}^{p^r} \left. \right], \tag{C.13g}
\end{aligned}$$

$$a_{\text{TE01}}^{\sigma^\pm} = \pm \frac{1}{\sqrt{2}} i a_{\text{TE01}}^{p^\phi}. \tag{C.13h}$$

Now we will compute the incoherent sum of the power emitted by the two circular

dipoles using the above relations.

$$\begin{aligned}
P^\sigma &= P^{\sigma^+} + P^{\sigma^-} \\
&= \frac{1}{2} \text{Re} \left\{ \left(\left| a_{\text{HE}11,+1}^{\sigma^+} \right|^2 + \left| a_{\text{HE}11,+1}^{\sigma^-} \right|^2 \right) \right. \\
&\quad \left(E_{r,\text{HE}11,+1} H_{\phi,\text{HE}11,+1}^* - E_{\phi,\text{HE}11,+1} H_{r,\text{HE}11,+1}^* \right) \\
&\quad + \left(\left| a_{\text{HE}11,-1}^{\sigma^+} \right|^2 + \left| a_{\text{HE}11,-1}^{\sigma^-} \right|^2 \right) \\
&\quad \left(E_{r,\text{HE}11,-1} H_{\phi,\text{HE}11,-1}^* - E_{\phi,\text{HE}11,-1} H_{r,\text{HE}11,-1}^* \right) \\
&\quad + \left(a_{\text{HE}11,+1}^{\sigma^+} a_{\text{HE}11,-1}^{\sigma^+*} + a_{\text{HE}11,+1}^{\sigma^-} a_{\text{HE}11,-1}^{\sigma^-*} \right) \\
&\quad \left(E_{r,\text{HE}11,+1} H_{\phi,\text{HE}11,-1}^* - E_{\phi,\text{HE}11,+1} H_{r,\text{HE}11,-1}^* \right) \\
&\quad + \left(a_{\text{HE}11,+1}^{\sigma^+*} a_{\text{HE}11,-1}^{\sigma^+} + a_{\text{HE}11,+1}^{\sigma^-*} a_{\text{HE}11,-1}^{\sigma^-} \right) \\
&\quad \left(E_{r,\text{HE}11,-1} H_{\phi,\text{HE}11,+1}^* - E_{\phi,\text{HE}11,-1} H_{r,\text{HE}11,+1}^* \right) \\
&\quad - a_{\text{TE}01}^{\sigma^+*} H_{r,\text{TE}01}^* \left(a_{\text{HE}11,+1}^{\sigma^+} E_{\phi,\text{HE}11,+1} + a_{\text{HE}11,-1}^{\sigma^+} E_{\phi,\text{HE}11,-1} \right) \exp(i\Delta\beta z) \\
&\quad - a_{\text{TE}01}^{\sigma^-*} H_{r,\text{TE}01}^* \left(a_{\text{HE}11,+1}^{\sigma^-} E_{\phi,\text{HE}11,+1} + a_{\text{HE}11,-1}^{\sigma^-} E_{\phi,\text{HE}11,-1} \right) \exp(i\Delta\beta z) \\
&\quad - a_{\text{TE}01}^{\sigma^+} E_{\phi,\text{TE}01} \left(a_{\text{HE}11,+1}^{\sigma^+*} H_{r,\text{HE}11,+1}^* + a_{\text{HE}11,-1}^{\sigma^+*} H_{r,\text{HE}11,-1}^* \right) \exp(-i\Delta\beta z) \\
&\quad - a_{\text{TE}01}^{\sigma^-} E_{\phi,\text{TE}01} \left(a_{\text{HE}11,+1}^{\sigma^-*} H_{r,\text{HE}11,+1}^* + a_{\text{HE}11,-1}^{\sigma^-*} H_{r,\text{HE}11,-1}^* \right) \exp(-i\Delta\beta z) \\
&\quad \left. - \left(\left| a_{\text{TE}01}^{\sigma^+} \right|^2 + \left| a_{\text{TE}01}^{\sigma^-} \right|^2 \right) E_{\phi,\text{TE}01} H_{r,\text{TE}01}^* \right\} \quad (\text{C.14a}) \\
&= \frac{1}{2} \text{Re} \left\{ \left(\left| a_{\text{HE}11,+1}^{p^r} \right|^2 + \left| a_{\text{HE}11,+1}^{p^\phi} \right|^2 \right) \right. \\
&\quad \left(E_{r,\text{HE}11,+1} H_{\phi,\text{HE}11,+1}^* - E_{\phi,\text{HE}11,+1} H_{r,\text{HE}11,+1}^* \right) \\
&\quad + \left(\left| a_{\text{HE}11,-1}^{p^r} \right|^2 + \left| a_{\text{HE}11,-1}^{p^\phi} \right|^2 \right) \\
&\quad \left(E_{r,\text{HE}11,-1} H_{\phi,\text{HE}11,-1}^* - E_{\phi,\text{HE}11,-1} H_{r,\text{HE}11,-1}^* \right) \\
&\quad + \left(a_{\text{HE}11,+1}^{p^r} a_{\text{HE}11,-1}^{p^r*} + a_{\text{HE}11,+1}^{p^\phi} a_{\text{HE}11,-1}^{p^\phi*} \right) \\
&\quad \left(E_{r,\text{HE}11,+1} H_{\phi,\text{HE}11,-1}^* - E_{\phi,\text{HE}11,+1} H_{r,\text{HE}11,-1}^* \right) \\
&\quad + \left(a_{\text{HE}11,+1}^{p^r*} a_{\text{HE}11,-1}^{p^r} + a_{\text{HE}11,+1}^{p^\phi*} a_{\text{HE}11,-1}^{p^\phi} \right) \\
&\quad \left(E_{r,\text{HE}11,-1} H_{\phi,\text{HE}11,+1}^* - E_{\phi,\text{HE}11,-1} H_{r,\text{HE}11,+1}^* \right) \\
&\quad \left. + i \frac{1}{\sqrt{2}} a_{\text{TE}01}^{p^\phi*} H_{r,\text{TE}01}^* \left(\left(a_{\text{HE}11,+1}^{\sigma^+} - a_{\text{HE}11,+1}^{\sigma^-} \right) E_{\phi,\text{HE}11,+1} + \right. \right.
\end{aligned}$$

$$\begin{aligned}
& \left(a_{\text{HE11},-1}^{\sigma^+} - a_{\text{HE11},-1}^{\sigma^-} \right) E_{\phi,\text{HE11},-1} \exp(i\Delta_\beta z) \\
& - i \frac{1}{\sqrt{2}} a_{\text{TE01}}^{p^\phi} E_{\phi,\text{TE01}} \left(\left(a_{\text{HE11},+1}^{\sigma^{+*}} - a_{\text{HE11},+1}^{\sigma^{-*}} \right) H_{r,\text{HE11},+1}^* + \right. \\
& \quad \left. \left(a_{\text{HE11},-1}^{\sigma^{+*}} - a_{\text{HE11},-1}^{\sigma^{-*}} \right) H_{r,\text{HE11},-1}^* \right) \exp(-i\Delta_\beta z) \\
& - \left| a_{\text{TE01}}^{p^\phi} \right|^2 E_{\phi,\text{TE01}} H_{r,\text{TE01}}^* \} \tag{C.14b} \\
= & P_{\text{HE11}}^{p^r} + P_{\text{HE11}}^{p^\phi} + P_{\text{TE01}}^{p^\phi} \\
& - \frac{1}{2} \text{Re} \left\{ \left[a_{\text{HE11}}^{p^\phi} a_{\text{TE01}}^{p^{\phi*}} E_{\phi,\text{HE11}} H_{r,\text{TE01}}^* \exp(i\Delta_\beta z) \right. \right. \\
& \quad \left. \left. + a_{\text{TE01}}^{p^\phi} a_{\text{HE11}}^{p^{\phi*}} E_{\phi,\text{TE01}} H_{r,\text{HE11}}^* \exp(-i\Delta_\beta z) \right] \right\} \\
= & P^{p^r} + P^{p^\phi}. \tag{C.14c}
\end{aligned}$$

Thus the incoherent sum of the two circular dipoles equals the incoherent sum of the radially and tangentially oriented dipoles, when we only consider the HE11 and the TE01 modes. We will do the same derivation for the horizontally and vertically oriented dipoles defined in Eq. (C.6). The approach is exactly the same as above. We will need the following relations for the dipole coupling coefficients

$$a_{\text{HE11}}^{p^H} = \cos \theta a_{\text{HE11}}^{p^r} - \sin \theta a_{\text{HE11}}^{p^\phi} \tag{C.15a}$$

$$a_{\text{HE11}}^{p^V} = \sin \theta a_{\text{HE11}}^{p^r} + \cos \theta a_{\text{HE11}}^{p^\phi} \tag{C.15b}$$

$$\begin{aligned}
\left| a_{\text{HE11}}^{p^H} \right|^2 &= \cos^2 \theta \left| a_{\text{HE11}}^{p^r} \right|^2 + \sin^2 \theta \left| a_{\text{HE11}}^{p^\phi} \right|^2 \\
&\quad - \cos \theta \sin \theta \left(a_{\text{HE11}}^{p^r} a_{\text{HE11}}^{p^{\phi*}} - a_{\text{HE11}}^{p^{r*}} a_{\text{HE11}}^{p^\phi} \right) \tag{C.15c}
\end{aligned}$$

$$\begin{aligned}
\left| a_{\text{HE11}}^{p^V} \right|^2 &= \sin^2 \theta \left| a_{\text{HE11}}^{p^r} \right|^2 + \cos^2 \theta \left| a_{\text{HE11}}^{p^\phi} \right|^2 \\
&\quad + \cos \theta \sin \theta \left(a_{\text{HE11}}^{p^r} a_{\text{HE11}}^{p^{\phi*}} - a_{\text{HE11}}^{p^{r*}} a_{\text{HE11}}^{p^\phi} \right) \tag{C.15d}
\end{aligned}$$

$$\left| a_{\text{HE11}}^{p^H} \right|^2 + \left| a_{\text{HE11}}^{p^V} \right|^2 = \left| a_{\text{HE11}}^{p^r} \right|^2 + \left| a_{\text{HE11}}^{p^\phi} \right|^2 \tag{C.15e}$$

$$a_{\text{TE01}}^{p^H} = -\sin \theta a_{\text{TE01}}^{p^\phi} \tag{C.15f}$$

$$a_{\text{TE01}}^{p^V} = \cos \theta a_{\text{TE01}}^{p^\phi} \tag{C.15g}$$

Using the above relations between the dipole coupling coefficients the total power emitted by the horizontally and vertically oriented dipoles are

$$\begin{aligned}
P^p &= P^{p^H} + P^{p^V} \\
&= \frac{1}{2} \text{Re} \left\{ E_r^{p^H} H_\phi^{p^{H*}} + E_r^{p^V} H_\phi^{p^{V*}} - E_\phi^{p^H} H_r^{p^{H*}} - E_\phi^{p^V} H_r^{p^{V*}} \right\} \tag{C.16a}
\end{aligned}$$

$$\begin{aligned}
&= \frac{1}{2} \text{Re} \left\{ \left(\left| a_{\text{HE11}}^{p^H} \right|^2 + \left| a_{\text{HE11}}^{p^V} \right|^2 \right) E_{r,\text{HE11}} H_{\phi,\text{HE11}}^* \right. \\
&\quad - \left(a_{\text{HE11}}^{p^H} E_{\phi,\text{HE11}} \exp(i\beta_{\text{HE11}} z) + a_{\text{TE01}}^{p^H} E_{\phi,\text{TE01}} \exp(i\beta_{\text{TE01}} z) \right) \\
&\quad \left(a_{\text{HE11}}^{p^{H*}} H_{r,\text{HE11}}^* \exp(-i\beta_{\text{HE11}} z) + a_{\text{TE01}}^{p^{H*}} H_{r,\text{TE01}}^* \exp(-i\beta_{\text{TE01}} z) \right) \\
&\quad - \left(a_{\text{HE11}}^{p^V} E_{\phi,\text{HE11}} \exp(i\beta_{\text{HE11}} z) + a_{\text{TE01}}^{p^V} E_{\phi,\text{TE01}} \exp(i\beta_{\text{TE01}} z) \right) \\
&\quad \left. \left(a_{\text{HE11}}^{p^{V*}} H_{r,\text{HE11}}^* \exp(-i\beta_{\text{HE11}} z) + a_{\text{TE01}}^{p^{V*}} H_{r,\text{TE01}}^* \exp(-i\beta_{\text{TE01}} z) \right) \right\} \\
&\hspace{15em} \text{(C.16b)}
\end{aligned}$$

$$\begin{aligned}
&= \frac{1}{2} \text{Re} \left\{ \left(\left| a_{\text{HE11}}^{p^r} \right|^2 + \left| a_{\text{HE11}}^{p^\phi} \right|^2 \right) E_{r,\text{HE11}} H_{\phi,\text{HE11}}^* \right. \\
&\quad - \left(\left| a_{\text{HE11}}^{p^r} \right|^2 + \left| a_{\text{HE11}}^{p^\phi} \right|^2 \right) E_{\phi,\text{HE11}} H_{r,\text{HE11}}^* \\
&\quad - \left(a_{\text{HE11}}^{p^H} a_{\text{TE01}}^{p^{H*}} + a_{\text{HE11}}^{p^V} a_{\text{TE01}}^{p^{V*}} \right) E_{\phi,\text{HE11}} H_{r,\text{TE01}}^* \exp(i\Delta_\beta z) \\
&\quad - \left(a_{\text{HE11}}^{p^{H*}} a_{\text{TE01}}^{p^H} + a_{\text{HE11}}^{p^{V*}} a_{\text{TE01}}^{p^V} \right) E_{\phi,\text{TE01}} H_{r,\text{HE11}}^* \exp(-i\Delta_\beta z) \\
&\quad \left. - \left| a_{\text{TE01}}^{p^\phi} \right|^2 E_{\phi,\text{TE01}} H_{r,\text{TE01}}^* \right\} \\
&\hspace{15em} \text{(C.16c)}
\end{aligned}$$

$$\begin{aligned}
&= P_{\text{HE11}}^{p^r} + P_{\text{HE11}}^{p^\phi} + P_{\text{TE01}}^{p^\phi} \\
&\quad - \frac{1}{2} \text{Re} \left\{ a_{\text{HE11}}^{p^\phi} a_{\text{TE01}}^{p^{\phi*}} E_{\phi,\text{HE11}} H_{r,\text{TE01}}^* \exp(i\Delta_\beta z) \right. \\
&\quad \quad \left. + a_{\text{HE11}}^{p^{\phi*}} a_{\text{TE01}}^{p^\phi} E_{\phi,\text{TE01}} H_{r,\text{HE11}}^* \exp(-i\Delta_\beta z) \right\} \\
&\hspace{15em} \text{(C.16d)}
\end{aligned}$$

$$= P^{p^r} + P^{p^\phi}. \hspace{15em} \text{(C.16e)}$$

Thus the incoherent sum of the linear dipoles equals the incoherent sum of the circular dipoles, which means we can treat emissions from neutral excitons and trion states in the same way by adding the far-field power from the radial and tangential dipoles incoherently. The above derivation only included the HE11 and TE01 modes, however, in reality we have all modes. Thus in order to confirm the above relation we performed the full simulation with the two circular dipoles in Eqs. (C.5) and the radial and tangential dipoles and computed their power distribution in an infinite nanowire on a gold mirror - i.e. the structure sketched in Fig. 5.8b without the out-coupling taper. We have placed the circular and linear dipoles at different positions along the radial axis of the nanowire 80 nm above the bottom mirror as for the experimental structure. For each radial position we have evaluated the emitted power distribution at different cross-sections along the nanowire. In Fig. C.8 we evaluate the power distribution at $z = 1800, 2000, 2200$ nm above the bottom mirror emitted by the dipoles placed at $r_{\text{PD}} = 0.6R_{\text{NW}}$. The nanowire used in Fig. C.8 has a diameter of 230 nm instead of 200 nm. The conclusion is exactly the same for 200 nm, however, due to the better confinement of the TE01 mode the interference effects become more apparent and thus the

comparison between the two incoherent sums is more convincing. The top part of Fig. C.8a-c shows the power distribution for the two circular dipoles given in Eq. (C.5) and the radially and tangentially oriented dipoles. The bottom part shows the sum of the emitted powers by the circular and linear dipoles. The take home message from this figure is that the two figures in the bottom are close to identical in all three cases - a closer analysis shows minute differences, however these are so small that they will not be resolved in an experiment. The differences are due to the inclusion of all modes and not only the HE11 and TE01 modes in the calculation. So as long as the HE11 and the TE01 modes are the dominant modes in the nanowire the incoherent sum of the circular dipoles and the linear dipoles yields the same result.

C.5 Simulated far-fields of the needle nanowire

Here we present the simulated far-fields for the needle nanowire sketched in Fig. 5.8b for nanowire section heights of 1900 nm, 1950 nm and 2000 nm. In Fig. C.9 the emission wavelength is 891.5 nm corresponding to QD1, whereas in Figs. C.10 and C.11 the emission wavelengths are 907 and 912 nm respectively corresponding to QD2 and QD3 in the experimental structure. As seen both the QD position and the height of the straight nanowire section is important for the far-field radiation pattern. The position of the QD controls the power emitted into the HE11 and the TE01-like radiation modes as seen in Fig. 5.3, whereas the nanowire height determines the phase difference between the two modes as seen in Fig. C.8, where the power distribution in the nanowire depends on the propagation distance along the nanowire.

As seen by comparing Figs. C.10 and C.11 a difference in emission wavelength of only 5 nm leads to visibly different far-field patterns. The emission wavelength plays the same role for the radiation pattern as the height of the nanowire, since changing the wavelength changes the propagation constants and thus the phase difference between the two modes.

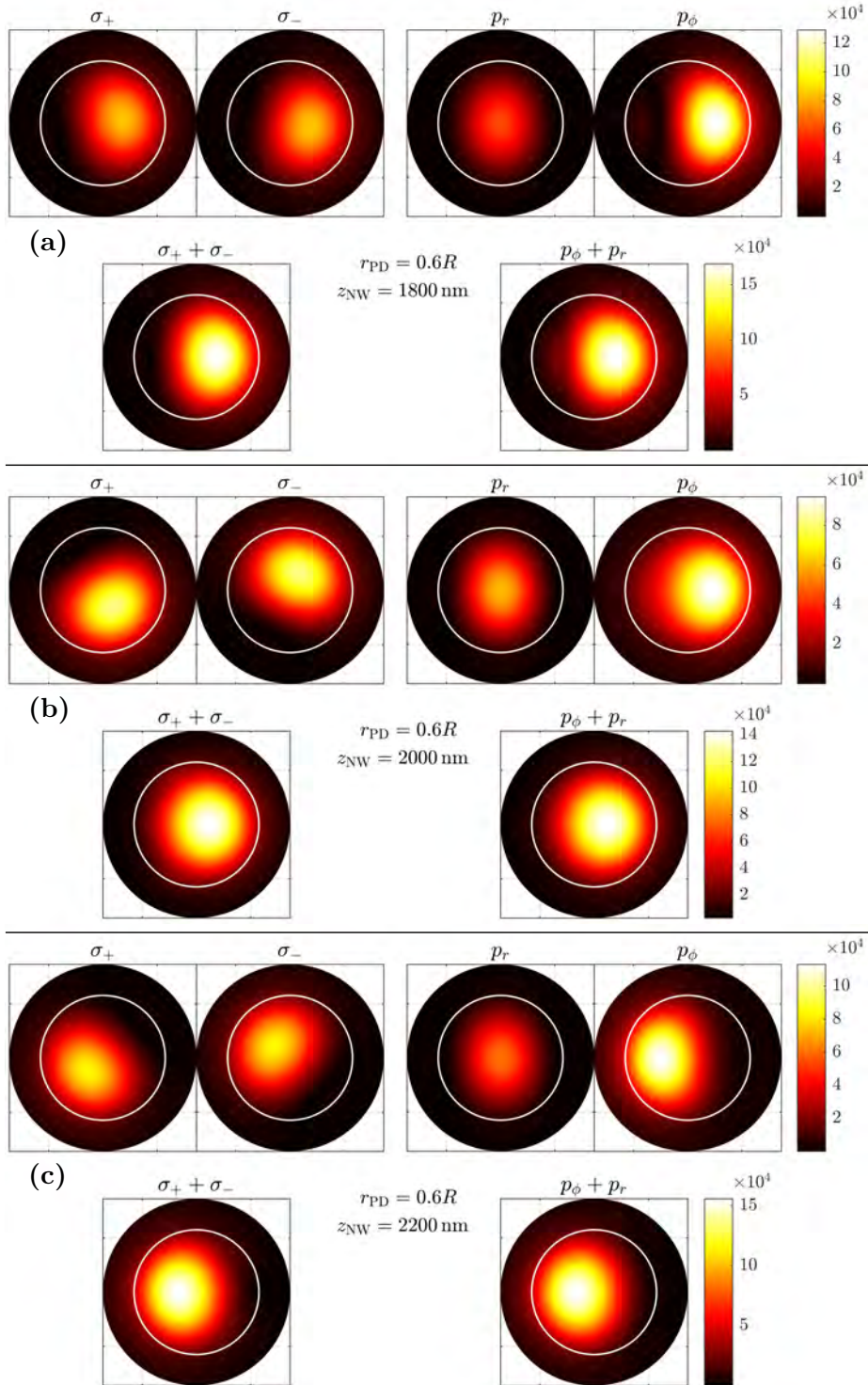


Figure C.8: Power distribution in an infinite nanowire on the silica-gold mirror emitted (top) by the two circular dipoles σ_{\pm} and the two linear dipoles $p_{r(\phi)}$. (bottom) The incoherent sum of the circular and linear dipoles. The dipoles are all placed on the x -axis and displaced $0.6 R_{\text{NW}}$ from the centrum. The power is evaluated at (a) 1800 nm, (b) 2000 nm and (c) 2200 nm.

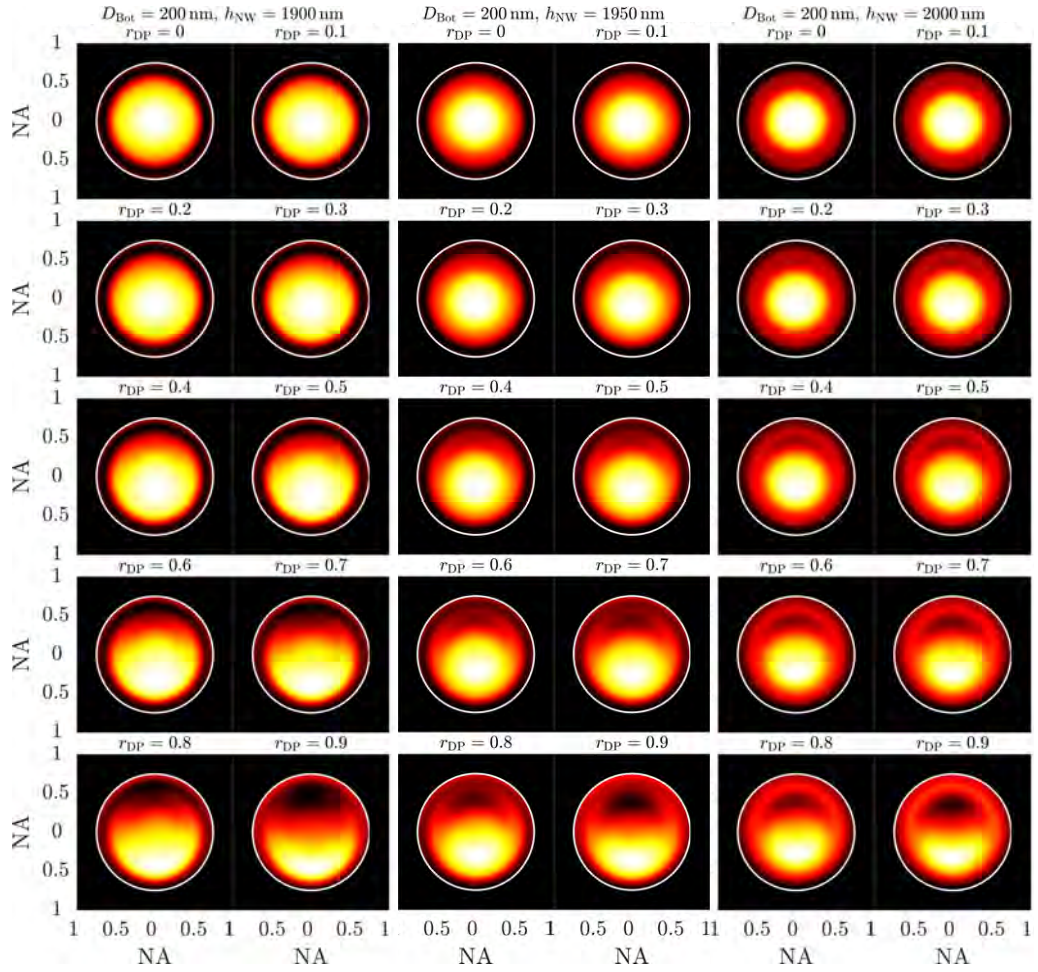


Figure C.9: The simulated far-fields for the needle nanowire sketched in Fig. 5.8b with $h_{NW} = 1900$ nm (left), 1950 nm (middle) and 2000 nm (right) for 10 different positions of the point dipole along the y -axis from the center to the edge of the nanowire with $\lambda = 891.5$ nm.

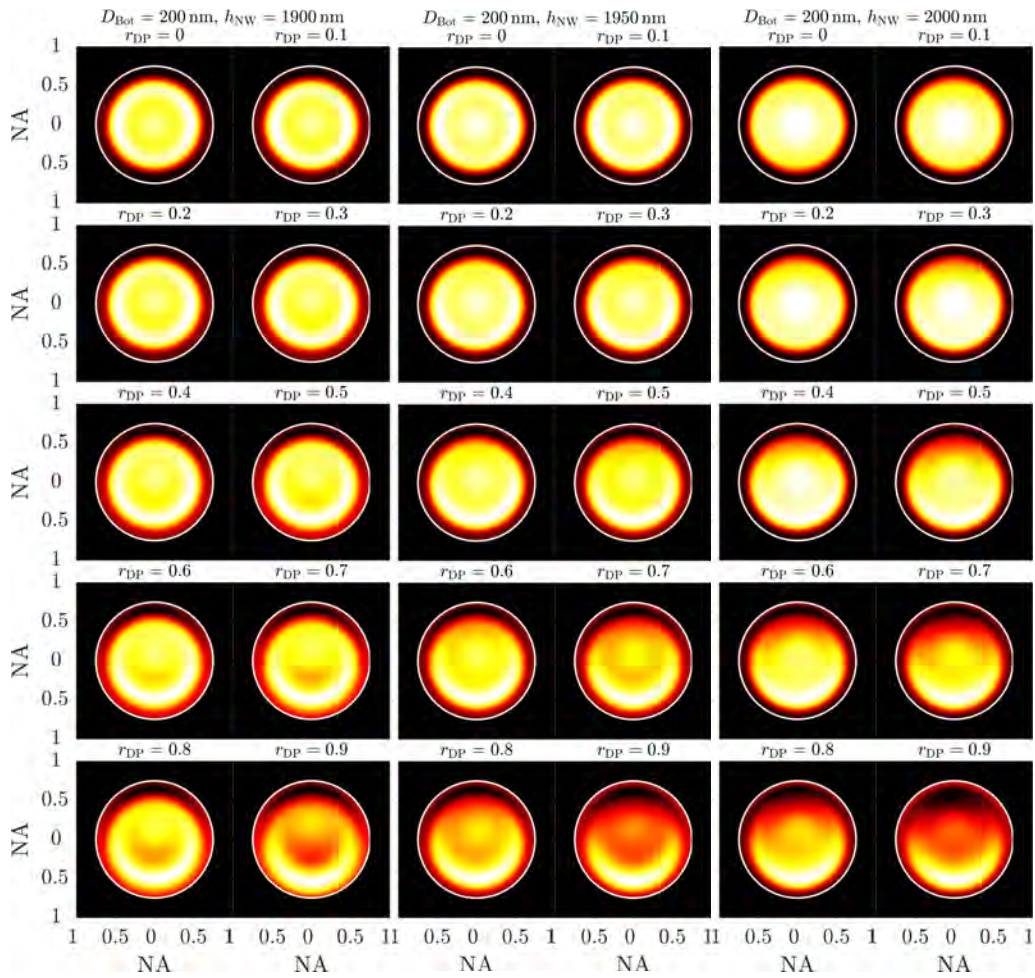


Figure C.10: The simulated far-fields for the needle nanowire sketched in Fig. 5.8b with $h_{\text{NW}} = 1900$ nm (left), 1950 nm (middle) and 2000 nm (right) for 10 different positions of the point dipole along the y -axis from the center to the edge of the nanowire with $\lambda = 907$ nm.

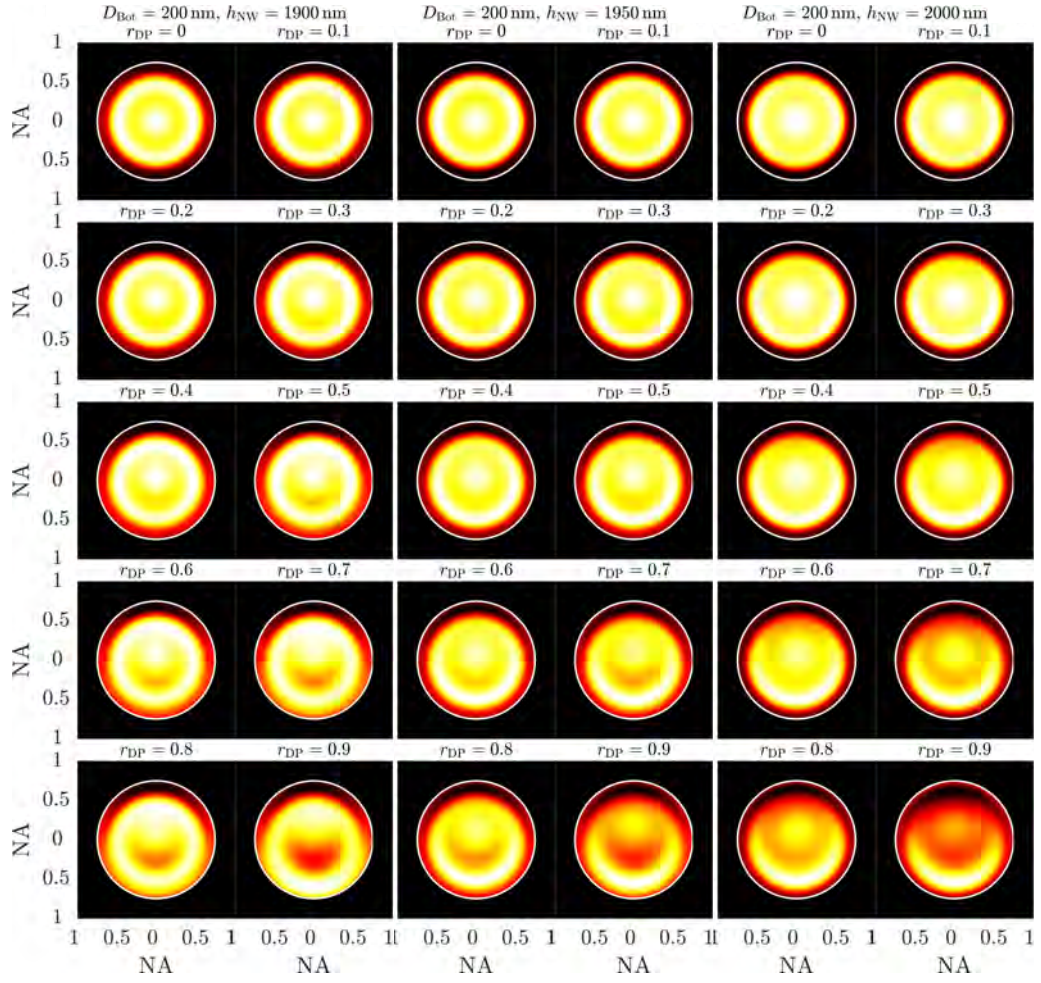


Figure C.11: The simulated far-fields for the needle nanowire sketched in Fig. 5.8b with $h_{NW} = 1900$ nm (left), 1950 nm (middle) and 2000 nm (right) for 10 different positions of the point dipole along the y -axis from the center to the edge of the nanowire with $\lambda = 912$ nm.

Breakdown of single-mode model for computing source efficiency and Purcell enhancement for nanopost structures

D.1 Convergence study of Purcell enhancement

The discretization strategy of the k -values is similar to the one presented in Section 3.2 in Chapter 3, where a dense sampling around k_0 leads to faster convergence [48]. However, we only need to sample radial k -values due to the cylindrical symmetry. The total number of k -points are divided, such that half of the k -values are between 0 and k_0 , and half are between k_0 and $k_{\text{cut-off}}k_0$. The points in these two intervals are distributed in the following way in order to obtain a dense sampling around k_0

$$k_{m,1} = k_0 \sin\left(n_{k,1} \frac{\pi}{\text{NP} + 1}\right), \quad n_{k,1} = 1, \dots, \frac{\text{NP}}{2}, \quad (\text{D.1a})$$

$$k_{m,2} = k_0 \left[k_{\text{cut-off}} - \sin\left(n_{k,2} \frac{\pi}{\text{NP} + 1}\right) (k_{\text{cut-off}} - 1) \right], \quad (\text{D.1b})$$

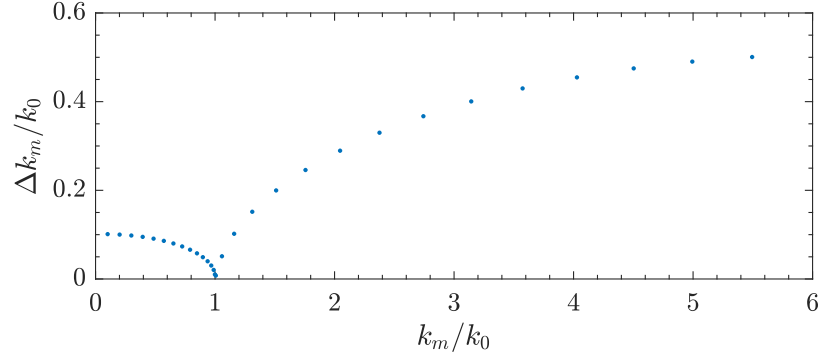


Figure D.1: Example of the k -sampling step size used for the computations in Chapter 6 with $k_{\text{cutoff}} = 6$ and $\text{NP} = 30$.

$$n_{k,2} = \frac{\text{NP}}{2} + 1, \dots, \text{NP}, \quad (\text{D.1c})$$

where NP is the total number of k -points and $k_{\text{cut-off}}k_0$ is the maximum k -value in the sampling. An example of our k -sampling is seen in Fig. D.1.

In Fig. D.2 the convergence of the Purcell enhancement computed using (a) the full model and (b) the single-mode model is studied for the shortest nanopost size - $D = 230$ nm, $h_b = 73$ nm and $h_t = 207$ nm. The number of k -points on the x -axis corresponds to the number of modes used in the calculation as in Chapter 3, and $k_{\text{cut-off}}$ is the largest in-plane k -value included in the approximation of the Fourier integral.

From Fig. D.2 it is seen that the full model and the single-mode model converges towards two different values. However, the full model has a hard time converging for the smallest nanopost size, which we attribute to the influence of the evanescent modes. It should be stated that increasing the cut-off value does not necessarily increase the numerical accuracy in our discretization strategy. In fact increasing the cut-off value actually reduces the k -sampling density around k_0 . The convergence plot for the full model thus serve as a way to estimate the numerical uncertainty, and we conclude that the SE rate predicted by the full model is $\Gamma_{\text{HE11}} = 10 \pm 2$ and the single-mode model converges towards $\Gamma_{\text{HE11}} = 7.3 \pm 0.3$, and thus the two models do not agree within the estimated numerical uncertainty. For all calculations in Chapter 6, we use 1400 k -points and $k_{\text{cut-off}} = 40k_0$, since these parameters predict a Purcell enhancement in the middle of the numerical uncertainty interval for the full model. It is only for the smallest nanopost, that we observe such a large numerical uncertainty on the Purcell enhancement.

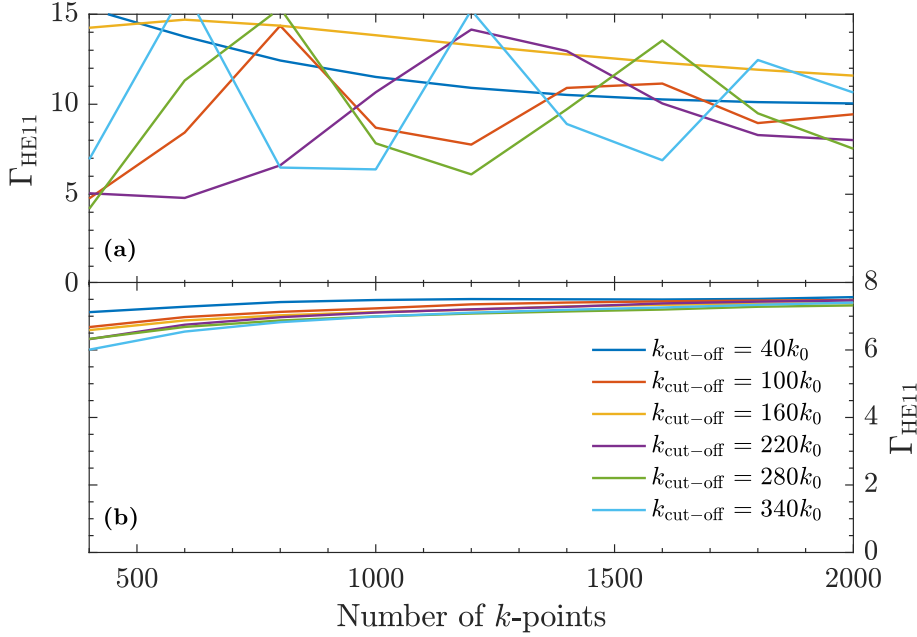


Figure D.2: Convergence study of the Purcell enhancement in the nanopost geometry in Fig. 6.1 with $D = 230$ nm and $h_t = 207$ nm computed using (a) the full model and (b) the single-mode model.

D.2 Division of radiation modes into TE and TM polarization

The lateral electromagnetic field in the oFMM formalism is given by Eqs. (5.3), which are repeated here for clarity

$$F_{r,nj}(r) = i \sum_{m=1}^M k_m \Delta k_m [b_{njm}^F J_{n+1}(k_m r) - c_{njm}^F J_{n-1}(k_m r)], \quad (\text{D.2a})$$

$$F_{\phi,nj}(r) = \sum_{m=1}^M k_m \Delta k_m [b_{njm}^F J_{n+1}(k_m r) + c_{njm}^F J_{n-1}(k_m r)], \quad (\text{D.2b})$$

where F is either the electric field E or the magnetic field H , and additionally the z -components of the electromagnetic field are [48]

$$E_{z,nj}(r) = \frac{i}{\omega \varepsilon(r)} \sum_{m=1}^M k_m^2 \Delta k_m [b_{njm}^H - c_{njm}^H] J_n(k_m r), \quad (\text{D.3a})$$

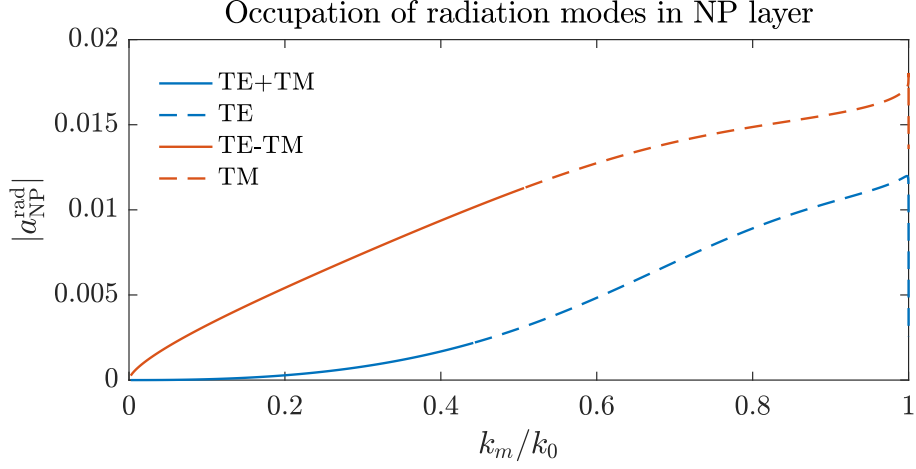


Figure D.3: The occupation of radiation modes in the nanopost layer as function of in-plane k_m -value. Each radiation mode is classified as being either TE, TM or a linear combination of these.

$$H_{z,nj}(r) = \frac{-i}{\omega\mu_0} \sum_{m=1}^M k_m^2 \Delta k_m \left[b_{njm}^E - c_{njm}^E \right] J_n(k_m r). \quad (\text{D.3b})$$

In air (or any bulk medium) the natural solutions are TE ($E_z = 0$) and TM ($H_z = 0$) polarized light. From the above equations we can classify modes by their Bessel function expansion coefficients b and c as

$$b_{njm}^E = c_{njm}^E \quad \& \quad b_{njm}^H = -c_{njm}^H \quad \text{TM}, \quad (\text{D.4a})$$

$$b_{njm}^H = c_{njm}^H \quad \& \quad b_{njm}^E = -c_{njm}^E \quad \text{TE}, \quad (\text{D.4b})$$

and thus in the air layer of the nanopost structure we can split the modes into pure TE and TM modes by writing the Bessel function expansion coefficients for the electric field as

$$b_{njm}^{E,\text{TE}} = -c_{njm}^{E,\text{TE}} = \frac{1}{\sqrt{2}} \delta_{jm}, \quad (\text{D.5a})$$

$$b_{njm}^{E,\text{TM}} = c_{njm}^{E,\text{TM}} = \frac{1}{\sqrt{2}} \delta_{jm}, \quad (\text{D.5b})$$

where $n = \pm 1$, j is the mode index and m is the index for the in-plane k -value.

In the nanopost layer, we have to solve for the Bessel function expansion coefficients numerically as outlined in [48] and [75]. The radiation modes are minimally affected by the nanopost itself and are close to being free space air modes, where

a single in-plane k_m -value dominates in each mode. However, these are not necessarily divided into pure TE and TM modes, but could also be linear combinations of these as TE+TM and TE-TM. In Fig. D.3 the occupation of radiation modes in the nanopost layer is plotted as function of the dominant in-plane k_m -value. Each mode is classified as being a TE or TM mode, or a linear combination by their coupling to the pure TE and TM modes in the air layer. The coupling is given by the transmission matrix and each radiation mode mainly couples to the free space air modes, that has the same k_m -value as the dominant k_m -value in the nanopost radiation mode. Thus, if a radiation mode mainly couples to a free space TE(TM) mode, the radiation mode is categorized as being a TE(TM) mode. If it couples to both TE and TM modes it is categorized as being a linear combination of the two. This classification of radiation modes in the nanopost layer is not deterministic and the radiation modes with small forward propagation constants in general have contributions from a few dominant in-plane k_m -values and are thus harder to categorize. However, the approach outlined here works quite well for determining the phase difference in Fig. 6.9, and the simple model provides good predictions of the location of the far-field interference rings as described in Section 6.3.

Far-field of tapered nanowires

In this appendix we present the far-field from on-axis quantum dots placed in 3 different tapered nanowire geometries illustrated in Fig. E.1.

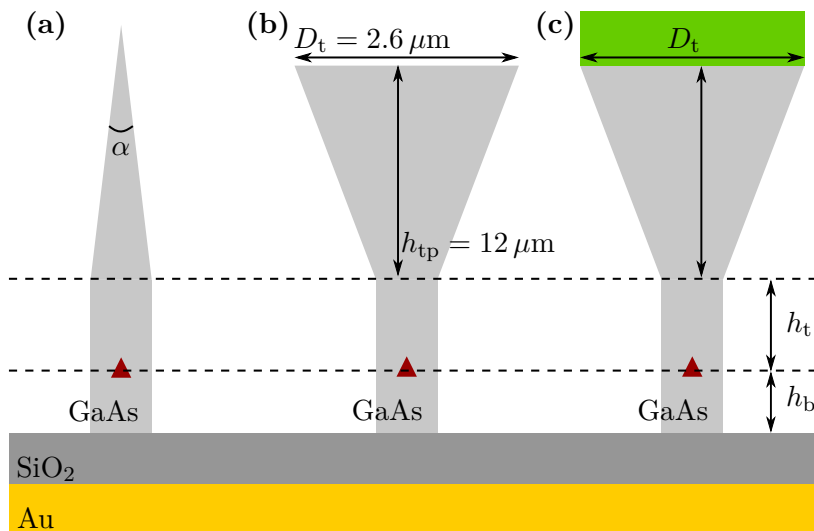


Figure E.1: Sketch of three nanowires with a tapered out-coupling section: (a) Needle with $\alpha = 5^\circ$, (b) trumpet without and (c) with AR coating. The bottom diameter is 250 nm.

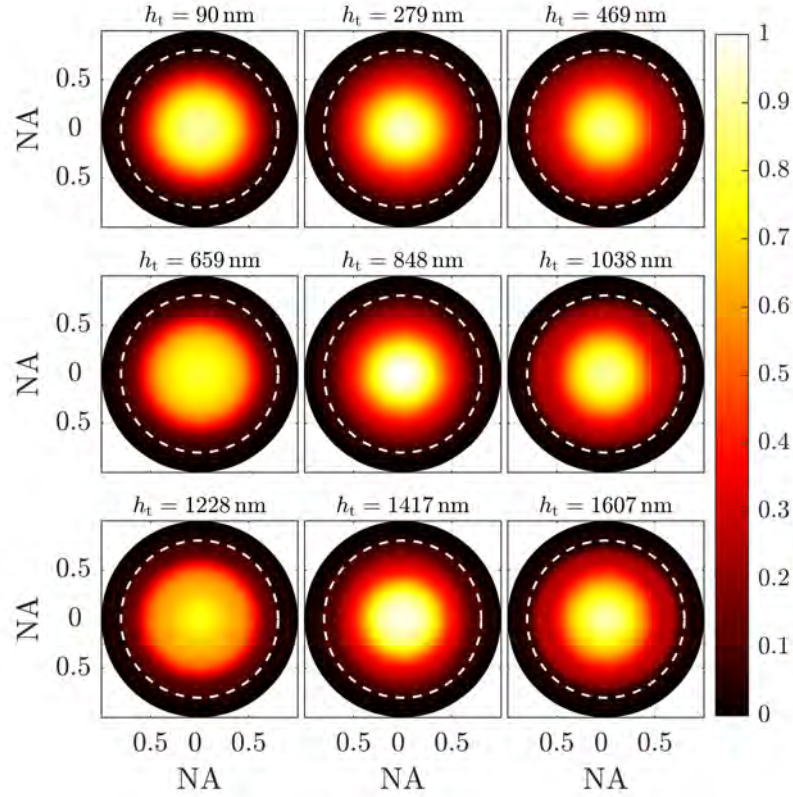


Figure E.2: Far-field of the needle nanowire sketched in Fig. E.1(a) for the 9 first h_t supporting an anti-node at the QD position. The dashed circle indicates $\text{NA} = 0.8$.

The QD is placed in an anti-node, and the distance between the QD and the bottom mirror is kept fixed at $h_b = 63$ nm. The distance to the start of the tapering section, h_t , is varied discretely in order to satisfy the phase condition, such that the QD is placed in an anti-node. Even though the needle taper and the trumpet taper with the anti-reflective (AR) coating have a negligible backscattering from the tapering section back into the nanowire, there is a finite reflection coefficient, which is used to determine the discrete values of h_t supporting an anti-node. This approach is used in order to get a fair comparison between the tapered nanowire far-fields and the nanopost far-fields presented in Chapter 6.

In Fig. E.2 the far-fields of the needle nanowire in Fig. E.1(a) is shown for the 9 shortest nanowire sections. As seen the interference rings, which appeared in the nanopost far-field (see Fig. 6.7) are completely gone as expected. In general the far-field pattern looks Gaussian shaped, which enables coupling into an optical fibre [62].

Fig. E.3 shows the far-fields of the trumpet nanowire without AR coating for

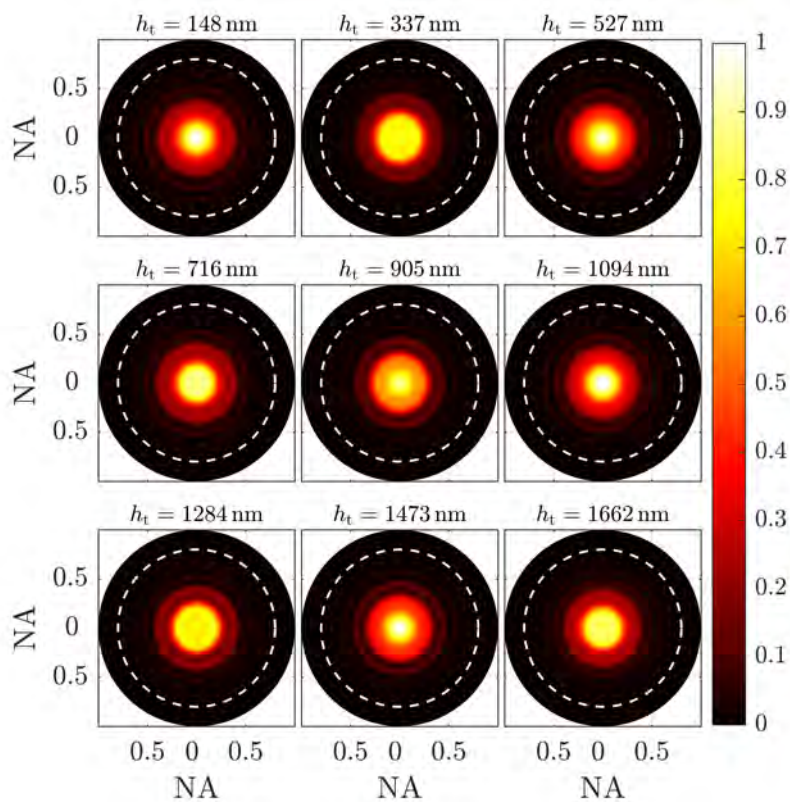


Figure E.3: Far-field of the trumpet nanowire with no AR coating sketched in Fig. E.1(b) for the 9 first h_t supporting an anti-node at the QD position. The dashed circle indicates $\text{NA} = 0.8$.

the 9 shortest nanowire sections. Here we observe some interference rings in the far-field as for the nanopost structure, however they are not as evident. This is due to the more directive Gaussian profile of the HE₁₁ mode in the far-field.

Finally, Fig. E.4 shows the far-fields of the trumpet nanowire with AR coating, and now all interference fringes are completely gone. It should also be noted, that the far-field seem to be almost unchanging with the length of the nanowire section. Furthermore, the far-field is very directional and most of the power lies within $\text{NA} = 0.5$.

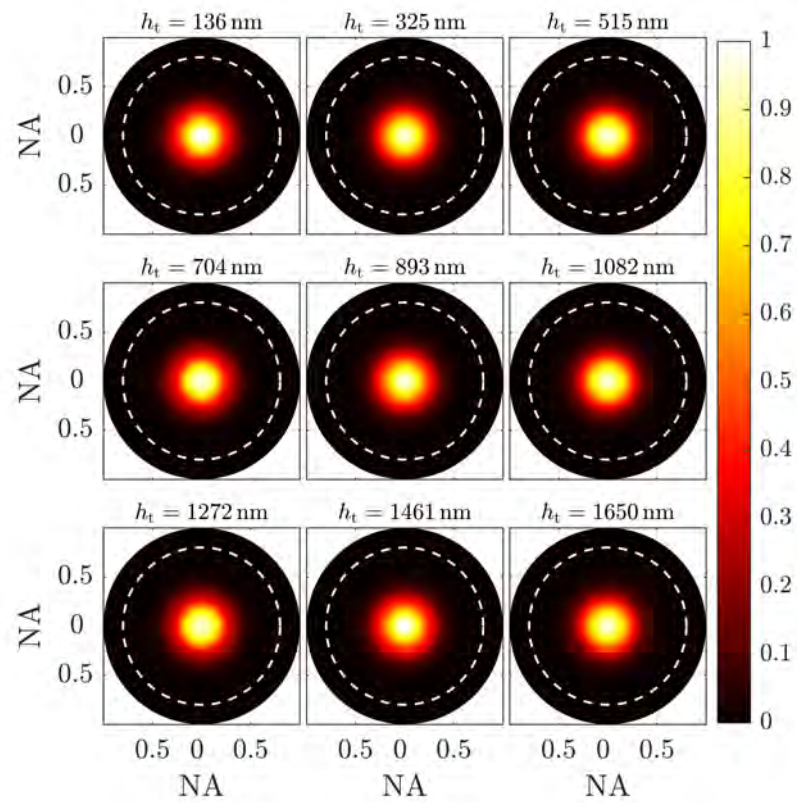


Figure E.4: Far-field of the trumpet nanowire with AR coating sketched in Fig. E.1(c) for the 9 first h_t supporting an anti-node at the QD position. The dashed circle indicates $NA = 0.8$.

Bibliography

- [1] J. C. Maxwell, “A Dynamical Theory of the Electromagnetic Field,” *Philosophical Transactions of the Royal Society of London* **155**, 459–512 (1865).
- [2] B. J. Hunt, “Oliver Heaviside: A first-rate oddity,” *Phys. Today* **65**, 48 (2012).
- [3] A. Einstein, “Über einen die Erzeugung und Verwandlung des Lichtes betreffenden heuristischen Gesichtspunkt,” *Annalen der Physik* **322**, 132–148 (1905).
- [4] C. J. Chang-Hasnain, “Tunable VCSEL,” *IEEE J. Sel. Top. Quantum Electron.* **6**, 978–987 (2000).
- [5] I.-S. Chung and J. Mørk, “Silicon-photonics light source realized by III–V/Si-grating-mirror laser,” *Appl. Phys. Lett.* **97**, 151113 (2010).
- [6] T. Ansbaek, I.-S. Chung, E. S. Semenova, O. Hansen, and K. Yvind, “Resonant MEMS tunable VCSEL,” *IEEE J. Sel. Top. Quantum Electron.* **19**, 1702306–1702306 (2013).
- [7] O. Painter, R. K. Lee, A. Scherer, A. Yariv, J. D. O’Brien, P. D. Dapkus, and I. Kim, “Two-Dimensional Photonic Band-Gap Defect Mode Laser,” *Science* **284**, 1819–1821 (1999).
- [8] M. Lončar, T. Yoshie, A. Scherer, P. Gogna, and Y. Qiu, “Low-threshold photonic crystal laser,” *Applied Physics Letters* **81**, 2680–2682 (2002).
- [9] Y. Yu, W. Xue, E. Semenova, K. Yvind, and J. Mork, “Demonstration of a self-pulsing photonic crystal Fano laser,” *Nat. Phot.* **11**, 81–84 (2016).
- [10] Y. Yu, M. Heuck, H. Hu, W. Xue, C. Peucheret, Y. Chen, L. K. Oxenløwe, K. Yvind, and J. Mørk, “Fano resonance control in a photonic crystal structure and its application to ultrafast switching,” *Appl. Phys. Lett.* **105**, 061117 (2014).

- [11] D. A. Bekele, Y. Yu, H. Hu, P. Guan, L. Ottaviano, M. Galili, L. K. Oxenløwe, K. Yvind, and J. Mørk, “Pulse carving using nanocavity-enhanced nonlinear effects in photonic crystal Fano structures,” *Opt. Lett.* **43**, 955 (2018).
- [12] P. Lodahl, S. Mahmoodian, and S. Stobbe, “Interfacing single photons and single quantum dots with photonic nanostructures,” *Rev. Mod. Phys.* **87**, 347–400 (2015).
- [13] P. Kok, W. J. Munro, K. Nemoto, T. C. Ralph, J. P. Dowling, and G. J. Millburn, “Linear optical quantum computing with photonic qubits,” *Rev. Mod. Phys.* **79**, 135–174 (2007).
- [14] I. Aharonovich, D. Englund, and M. Toth, “Solid-state single-photon emitters,” *Nat. Photonics* **10**, 631–641 (2016).
- [15] J. L. O’Brien, A. Furusawa, and J. Vučković, “Photonic quantum technologies,” *Nat. Photonics* **3**, 687–695 (2009).
- [16] E. Knill, R. Laflamme, and G. J. Millburn, “A scheme for efficient quantum computation with linear optics,” *Nature* **409**, 46–52 (2001).
- [17] C. H. Bennett and G. Brassard, “Quantum Cryptography: Public Key Distribution and Coin Tossing,” *Proceedings of IEEE International Conference on Computers, Systems and Signal Processing* **1**, 175–179 (1984).
- [18] T. Huber, A. Predojević, M. Khoshnegar, D. Dalacu, P. J. Poole, H. Majedi, and G. Weihs, “Polarization Entangled Photons from Quantum Dots Embedded in Nanowires,” *Nano Lett.* **14**, 7107–7114 (2014).
- [19] M. Müller, S. Bounouar, K. D. Jöns, M. Glässl, and P. Michler, “On-demand generation of indistinguishable polarization-entangled photon pairs,” *Nat. Photonics* **8**, 224–228 (2014).
- [20] D. Huber, M. Reindl, Y. Huo, H. Huang, J. S. Wildmann, O. G. Schmidt, A. Rastelli, and R. Trotta, “Highly indistinguishable and strongly entangled photons from symmetric GaAs quantum dots,” *Nat. Comm.* **8**, 15506 (2017).
- [21] H. J. Kimble, “The quantum internet,” *Nature* **453**, 1023–1030 (2008).
- [22] N. Gregersen, P. Kaer, and J. Mørk, “Modeling and Design of High-Efficiency Single-Photon Sources,” *IEEE J. Sel. Top. Quantum Electron.* **19**, 9000516 (2013).
- [23] N. Gregersen, T. R. Nielsen, J. Mørk, J. Claudon, Jean, and M. Gérard, “Designs for high-efficiency electrically pumped photonic nanowire single-photon sources,” *Opt. Express* **18**, 21204–21218 (2010).

- [24] M. Ikezawa, L. Zhang, Y. Sakuma, and Y. Masumoto, “Quantum interference of two photons emitted from a luminescence center in GaAs:N,” *Appl. Phys. Lett.* **110**, 152102 (2017).
- [25] N. Somaschi, V. Giesz, L. D. Santis, J. C. Loredó, M. P. Almeida, G. Hornecker, S. L. Portalupi, T. Grange, C. Antón, J. Demory, C. Gómez, I. Sagnes, N. D. Lanzillotti-Kimura, A. Lemaître, A. Auffeves, A. G. White, L. Lanco, , and P. Senellart, “Near-optimal single-photon sources in the solid state,” *Nat. Photonics* **10**, 340–345 (2016).
- [26] X.-L. Chu, S. Götzinger, and V. Sandoghar, “A single molecule as a high-fidelity photon gun for producing intensity-squeezed light,” *Nat. Photonics* **11**, 58–62 (2017).
- [27] J. Claudon, J. Bleuse, N. S. Malik, M. Bazin, P. Jaffrennou, N. Gregersen, C. Sauvan, P. Lalanne, and J.-M. Gérard, “A highly efficient single-photon source based on a quantum dot in a photonic nanowire,” *Nat. Photonics* **4** (2010).
- [28] M. Arcari, I. Söllner, A. Javadi, S. L. Hansen, S. Mahmoodian, J. Liu, H. Thyrrestrup, E. H. Lee, J. D. Song, S. Stobbe, and P. Lodahl, “Near-Unity Coupling Efficiency of a Quantum Emitter to a Photonic Crystal Waveguide,” *Phys. Rev. Lett.* **113**, 093603 (2014).
- [29] X. Ding, Y. He, Z.-C. Duan, N. Gregersen, M.-C. Chen, S. Unsleber, S. Maier, C. Schneider, M. Kamp, S. Höfling, C.-Y. Lu, and J.-W. Pan, “On-Demand Single Photons with High Extraction Efficiency and Near-Unity Indistinguishability from a Resonantly Driven Quantum Dot in a Micropillar,” *Phys. Rev. Lett.* **116** (2016).
- [30] T. M. Babinec, B. J. M. Hausmann, M. Khan, Y. Zhang, J. R. Maze, P. R. Hemmer, and M. Lončar, “A diamond nanowire single-photon source,” *Nat. Nanotechnol.* **5**, 195–199 (2010).
- [31] Y. Shih, “Entangled biphoton source - property and preparation,” *Rep. Prog. Phys.* (2003).
- [32] M. Munsch, N. S. Malik, E. Dupuy, A. Delga, J. Bleuse, J.-M. Gérard, J. Claudon, N. Gregersen, and J. Mørk, “Dielectric GaAs Antenna Ensuring an Efficient Broadband Coupling between an InAs Quantum Dot and a Gaussian Optical Beam,” *Phys. Rev. Lett.* **110** (2013).
- [33] K. G. Lee, X. W. Chen, H. Eghlidi, P. Kukura, R. Lettow, A. Renn, V. Sandoghdar, and S. Götzinger, “A planar dielectric antenna for directional single-photon emission and near-unity collection efficiency,” *Nat. Photonics* **5**, 166–169 (2011).

- [34] Y. Akahane, T. Asano, B.-S. Song, and S. Noda, “High-Q photonic nanocavity in a two-dimensional photonic crystal,” *Nature* **425**, 944–947 (2003).
- [35] J. Mork, Y. Chen, and M. Heuck, “Photonic Crystal Fano Laser: Terahertz Modulation and Ultrashort Pulse Generation,” *Phys. Rev. Lett.* **113**, 163901 (2014).
- [36] L. F. Frellsen, Y. Ding, O. Sigmund, and L. H. Frandsen, “Topology optimized mode multiplexing in silicon-on-insulator photonic wire waveguides,” *Opt. Express* **24**, 16866–16873 (2016).
- [37] J. R. de Lasson, L. H. Frandsen, P. Gutsche, S. Burger, O. S. Kim, O. Breinbjerg, A. Ivinskaya, F. Wang, O. Sigmund, T. Häyrynen, A. V. Lavrinenko, J. Mørk, and N. Gregersen, “Benchmarking five numerical simulation techniques for computing resonance wavelengths and quality factors in photonic crystal membrane line defect cavities,” *Opt. Express* **26**, 11366 (2018).
- [38] D. J. Griffiths, *Introduction to electrodynamics* (Pearson, 2008), chap. 7.3, pp. 321–342, 3rd ed.
- [39] A. V. Lavrinenko, J. Lægsgaard, N. Gregersen, F. Schmidt, and T. Søndergaard, *Numerical methods in photonics* (CRC Press, 2015), chap. 2, pp. 5–22.
- [40] D. J. Griffiths, *Introduction to electrodynamics* (Pearson, 2008), chap. 8, pp. 345–363, 3rd ed.
- [41] D. J. Griffiths, *Introduction to electrodynamics* (Pearson, 2008), chap. 9, pp. 364–415, 3rd ed.
- [42] A. V. Lavrinenko, J. Lægsgaard, N. Gregersen, F. Schmidt, and T. Søndergaard, *Numerical methods in photonics* (CRC Press, 2015), chap. 3, pp. 23–75.
- [43] A. V. Lavrinenko, J. Lægsgaard, N. Gregersen, F. Schmidt, and T. Søndergaard, *Numerical methods in photonics* (CRC Press, 2015), chap. 8, pp. 251–326.
- [44] L. Novotny and B. Hecht, *Principles of Nano-Optics* (Cambridge University Press, 2012), chap. 2, pp. 12–44, 2nd ed.
- [45] A. V. Lavrinenko, J. Lægsgaard, N. Gregersen, F. Schmidt, and T. Søndergaard, *Numerical methods in photonics* (CRC Press, 2015), chap. 7, pp. 197–249.

- [46] A. V. Lavrinenko, J. Lægsgaard, N. Gregersen, F. Schmidt, and T. Søndergaard, *Numerical methods in photonics* (CRC Press, 2015), chap. 6, pp. 139–194.
- [47] P. Bienstman and R. Baets, “Optical modelling of photonic crystal and VCSELs using eigenmode expansion and perfectly matched layers,” *Opt. Quantum. Electron.* **33**, 327–341 (2001).
- [48] T. Häyrynen, J. R. de Lasson, and N. Gregersen, “Open-geometry Fourier modal method: modeling nanophotonic structures in infinite domains,” *J. Opt. Soc. Am. A* **33**, 1298 (2016).
- [49] F. Bloch, “Über die Quantenmechanik der Elektronen in Kristallgittern,” *Z. Physik* **52**, 555–600 (1929).
- [50] J. R. de Lasson, “Modeling and simulations of light emission and propagation in open nanophotonic systems,” Ph.D. thesis, Technical University of Denmark (2015).
- [51] J.-P. Berenger, “A Perfectly and Matched Layer and for the Absorption and of Electromagnetic and Waves,” *J. Comput. Phys.* **114**, 185–200 (1994).
- [52] P. Bienstman and R. Baets, “Advanced boundary conditions for eigenmode expansion models,” *Opt. Quantum. Electron.* **34**, 523–540 (2002).
- [53] J. P. Hugonin and P. Lalanne, “Perfectly matched layer as nonlinear coordinate transforms: a generalized formalization,” *J. Opt. Soc. Am. A* **22**, 1844–1849 (2005).
- [54] N. Gregersen and J. Mørk, “An improved perfectly matched layer for the eigenmode expansion technique,” *Opt. Quantum. Electron.* **40**, 957–966 (2008).
- [55] E. M. Purcell, “Spontaneous emission probabilities at radio frequencies,” *Phys. Rev.* **69** (1946).
- [56] L. Novotny and B. Hecht, *Principles of Nano-Optics* (Cambridge University Press, 2012), chap. 8, pp. 224–281, 2nd ed.
- [57] N. Gregersen, D. P. S. McCutcheon, J. Mørk, J.-M. Gérard, and J. Claudon, “A broadband tapered nanocavity for efficient nonclassical light emission,” *Opt. Express* **24**, 20904 (2016).
- [58] L. E. Ballentine, *Quantum mechanics - A modern development* (World scientific, 1998), chap. 12, pp. 332–369.
- [59] C. C. Gerry and P. L. Knight, *Introductory Quantum Optics* (Cambridge University Press, 2005), chap. 4, pp. 74–114.

- [60] J. P. Dowling, “Spontaneous Emission in Cavities: How Much More Classical can You Get?” *Found. Phys.* **23** (1993).
- [61] P. Stepanov, A. Delga, N. Gregersen, E. Peinke, M. Munsch, J. Teissier, J. Mørk, M. Richard, J. Bleuse, J.-M. Gérard, and J. Claudon, “Highly directive and Gaussian far-field emission from "giant" photonic trumpets,” *Appl. Phys. Lett.* **107**, 141106 (2015).
- [62] G. Bulgarini, M. E. Reimer, M. B. Bavinck, K. D. Jöns, D. Dalacu, P. J. Poole, E. P. A. M. Bakkers, and V. Zwiller, “Nanowire Waveguides Launching Single Photons in a Gaussian Mode for Ideal Fiber Coupling,” *Nano Lett.* **14**, 4102–4106 (2014).
- [63] N. Gregersen, T. R. Nielsen, J. Claudon, J.-M. Gérard, and J. Mørk, “Controlling the emission profile of a nanowire with a conical taper,” *Opt. Lett.* **33**, 1693 (2008).
- [64] C. A. Balanis, *Advanced Engineering Electromagnetics* (Wiley, 1989), vol. 1, chap. 6.
- [65] K. J. Vahala, “Optical microcavities,” *Nature* **424**, 839–846 (2003).
- [66] G. Lecamp, P. Lalanne, and J. P. Hugonin, “Very Large Spontaneous-Emission β Factors in Photonic-Crystal Waveguides,” *Phys. Rev. Lett.* **99**, 023902 (2007).
- [67] V. S. C. Manga Rao and S. Hughes, “Single quantum-dot Purcell factor and β factor in a photonic crystal waveguide,” *Phys. Rev. B* **75**, 205437 (2007).
- [68] J. Mørk, F. Öhman, M. van der Poel, Y. Chen, P. Lunnemann, and K. Yvind, “Slow and fast light: Controlling the speed of light using semiconductor waveguides,” *Laser Photon. Rev.* **3**, 30–44 (2009).
- [69] A. Taflove and S. C. Hagness, *Computational Electrodynamics: The Finite-Difference Time-Domain Method* (Artech House, 2004), 3rd ed.
- [70] N. Gregersen, S. Reitzenstein, C. Kistner, M. Strauss, C. Schneider, S. Höfling, L. Worschech, A. Forchel, T. R. Nielsen, J. Mørk, and J.-M. Gérard, “Numerical and Experimental Study of the Q Factor of High-Q Micropillar Cavities,” *IEEE J. Quantum Electron.* **46**, 1470–1483 (2010).
- [71] L. Li, “New formulation of the Fourier modal method for crcross surface-relief gratings,” *J. Opt. Soc. Am. A* **14**, 2758–2767 (1997).
- [72] L. Li, “Use of Fourier series in the analysis of discontinuous periodic structures,” *J. Opt. Soc. Am. A* **13**, 1870–1876 (1996).

- [73] P. Lalanne, “Effective properties and band structures of lamellar subwavelength crystals: Plane-wave method revisited,” *Physical Review B* **58**, 9801–9807 (1998).
- [74] B. Guizal, D. Barchiesi, and D. Felbacq, “Electromagnetic beam diffraction by a finite lamellar structure: an aperiodic coupled-wave method,” *J. Opt. Soc. Am. A* **20**, 2274–2280 (2003).
- [75] N. Bonod, E. Popov, and M. Nevière, “Differential theory of diffraction by finite cylindrical objects,” *J. Opt. Soc. Am. A* **22**, 481–490 (2005).
- [76] G. P. Bava, P. Debernardi, and L. Fratta, “Three-dimensional model for vectorial fields in vertical-cavity surface-emitting lasers,” *Phys. Rev. A* **63**, 023816 (2001).
- [77] M. Dems, I.-S. Chung, P. Nyakas, S. Bischoff, and K. Panajotov, “Numerical Methods for modeling Photonic-Crystal VCSELs,” *Opt. Express* **18**, 16042–16054 (2010).
- [78] J. P. Boyd, *Chebyshev and Fourier Spectral Methods* (DOVER Publications, 2000), 2nd ed.
- [79] J. R. de Lasson, T. Christensen, J. Mørk, and N. Gregersen, “Modeling of cavities using the analytic modal method and an open geometry formalism,” *J. Opt. Soc. Am. A* **29**, 1237–1246 (2012).
- [80] T. Häyrynen, A. D. Osterkryger, J. R. de Lasson, and N. Gregersen, “Modeling open nanophotonic systems using the Fourier modal method: generalization to 3D Cartesian coordinates,” *J. Opt. Soc. Am. A* **34**, 1632–1641 (2017).
- [81] L. Li, “Formulation and comparison of two recursive matrix algorithms for modeling layered diffraction gratings,” *J. Opt. Soc. Am. A* **13**, 1024–1035 (1996).
- [82] A. W. Snyder and J. D. Love, *Optical Waveguide Theory* (Chapman and Hall, 1983).
- [83] G. Lecamp, P. Lalanne, and J. P. Hugonin, “The electromagnetic properties of light emission into semiconductor waveguides,” *Proc. of SPIE* **6195**, 61950E (2006).
- [84] I. Friedler, P. Lalanne, J. P. Hugonin, J. Claudon, J. M. Gérard, A. Beveratos, and I. Robert-Philip, “Efficient photonic mirrors for semiconductor nanowires,” *Opt. Lett.* **33**, 2635–2637 (2008).
- [85] S. Essig and K. Busch, “Generation of adaptive coordinates and their use in the Fourier Modal Method,” *Opt. Express* **18**, 23258–23274 (2010).

- [86] S. K. Raghuwanshi and S. Talabattula, “Analytical approximation solutions for 3-D optical waveguides: Review,” *Indian J. Phys.* **83**, 127–151 (2009).
- [87] H. Inoue, K. Hiruma, K. Ishida, T. Asai, and H. Matsumura, “Low Loss GaAs Optical Waveguides,” *IEEE Trans. Electron Devices* **32**, 2662–2668 (1985).
- [88] P. Stepanov, A. Delga, X. Zang, J. Bleuse, E. Dupuy, E. Peinke, P. Lalanne, J.-M. Gérard, and J. Claudon, “Quantum dot spontaneous emission control in a ridge waveguide,” *Appl. Phys. Lett.* **106**, 041112 (2015).
- [89] H.-Y. Ryu, M. Notomi, and Y.-H. Lee, “High-quality-factor and small-mode-volume hexapole modes in photonic-crystal-slab nanocavities,” *Appl. Phys. Lett.* **83**, 4294–4296 (2003).
- [90] K. Nozaki, T. Tanabe, A. Shinya, S. Matsuo, T. Sato, H. Taniyama, and M. Notomi, “Sub-femtojoule all-optical switching using a photonic-crystal nanocavity,” *Nat. Photonics* **4**, 477–483 (2010).
- [91] C. Fenzl, T. Hirsch, and O. S. Wolfbeis, “Photonic Crystals for Chemical Sensing and Biosensing,” *Angew. Chem. Int. Ed.* **53**, 3318–3335 (2014).
- [92] S. Fan, “Sharp asymmetric line shapes in side-coupled waveguide-cavity systems,” *Appl. Phys. Lett.* **80**, 908 (2002).
- [93] U. Fano, “Effects of Configuration and Interaction on Intensities and Phase Shifts,” *Phys. Rev.* **124**, 1866–1878 (1961).
- [94] K. Nozaki, A. Shinya, S. Matsuo, T. Sato, E. Kuramochi, and M. Notomi, “Ultralow-energy and high-contrast all-optical switch involving Fano resonance based on coupled photonic crystal nanocavities,” *Opt. Express* **21**, 11877 (2013).
- [95] M. Heuck, P. T. Kristensen, Y. Elesin, and J. Mørk, “Improved switching using Fano resonances in photonic crystal structures,” *Opt. Lett.* **38**, 2466–2468 (2013).
- [96] A. D. Osterkryger, J. R. de Lasson, M. Heuck, Y. Yu, J. Mørk, and N. Gregersen, “Spectral symmetry of Fano resonances in a waveguide coupled to a microcavity,” *Opt. Lett.* **41**, 2065–2068 (2016).
- [97] A. D. Østerkryger, “Optical properties of photonic crystal microcavities and waveguides,” Master’s thesis, DTU Fotonik, Technical University of Denmark (2015).
- [98] J. R. de Lasson, P. T. Kristensen, J. Mørk, and N. Gregersen, “A Bloch modal approach for engineering waveguide and cavity modes in two-dimensional photonic crystals,” *Proc. of SPIE* **9127**, 91270F (2014).

- [99] J. R. de Lasson, P. T. Kristensen, J. Mørk, and N. Gregersen, “Roundtrip matrix method for calculating the leaky resonant modes of open nanophotonic structures,” *J. Opt. Soc. Am. A* **31**, 2142–2151 (2014).
- [100] T. S. Rasmussen, Y. Yu, and J. Mork, “Modes, stability, and small-signal response of photonic crystal Fano lasers,” *Opt. Express* **26**, 16365 (2018).
- [101] T. S. Rasmussen, Y. Yu, and J. Mork, “Theory of Self-pulsing in Photonic Crystal Fano Lasers,” *Laser Photon. Rev.* **11** (2017).
- [102] J. P. Hugonin, P. Lalanne, T. P. White, and T. Krauss, “Coupling into slow-mode photonic crystal waveguides,” *Opt. Lett.* **32**, 2638–2640 (2007).
- [103] C. Sauvan, P. Lalanne, and J. P. Hugonin, “Slow-wave effect and mode-profile matching in photonic crystal microcavities,” *Phys. Rev. B* **71** (2005).
- [104] Y. Tanaka, J. Upham, T. Nagashima, T. Sugiya, T. Asano, and S. Noda, “Dynamic control of the Q factor in a photonic crystal nanocavity,” *Nat. Mater.* **6**, 862–865 (2007).
- [105] P. E. Kremer, A. C. Dada, P. Kumar, Y. Ma, S. Kumar, E. Clarke, and B. D. Gerardot, “Strain-tunable quantum dot embedded in a nanowire antenna,” *Phys. Rev. B* **90**, 201408 (2014).
- [106] J. Heinrich, A. Huggenberger, T. Heindel, S. Reitzenstein, S. Höfling, L. Worschech, and A. Forchel, “Single photon emission from positioned GaAs/AlGaAs photonic nanowires,” *Appl. Phys. Lett.* **96**, 211117 (2010).
- [107] M. E. Reimer, G. Bulgarini, N. Akopian, M. Hocevar, M. B. Bavinck, M. A. Verheijen, E. P. Bakkers, L. P. Kouwenhoven, and V. Zwiller, “Bright single-photon sources in bottom-up tailored nanowires,” *Nat. Commun.* **3** (2012).
- [108] D. Tumanov, N. Vaish, H. A. Nguyen, Y. Curé, J.-M. Gérard, J. Claudon, F. Donatini, and J.-P. Poizat, “Static strain tuning of quantum dots embedded in a photonic wire,” *Appl. Phys. Lett.* **112**, 123102 (2018).
- [109] M. A. M. Versteegh, M. E. Reimer, K. D. Jöns, D. Dalacu, P. J. Poole, A. Gulinatti, A. Giudice, and V. Zwiller, “Observation of strongly entangled photon pairs from a nanowire quantum dot,” *Nat. Commun.* **5** (2014).
- [110] D. Cadeddu, J. Teissier, F. R. Braakman, N. Gregersen, P. Stepanov, J.-M. Gérard, J. Claudon, R. J. Warburton, M. Poggio, and M. Munsch, “A fiber-coupled quantum-dot on a photonic tip,” *Appl. Phys. Lett.* **108**, 011112 (2016).
- [111] M. Munsch, A. V. Kuhlmann, D. Cadeddu, J.-M. Gérard, J. Claudon, M. Poggio, and R. J. Warburton, “Resonant driving of a single photon emitter embedded in a mechanical oscillator,” *Nat. Commun.* **8** (2017).

- [112] P.-L. de Assis, I. Yeo, A. Gloppe, H. A. Nguyen, D. Tumanov, E. Dupont-Ferrier, N. S. Malik, E. Dupuy, J. Claudon, J.-M. Gérard, A. Auffèves, O. Arcizet, M. Richard, and J.-P. Poizat, “Strain-Gradient Position Mapping of Semiconductor Quantum Dots,” *Phys. Rev. Lett.* **118** (2017).
- [113] A. Yariv, *Optical electronics in modern communications* (Oxford University Press, 1997), chap. 3, pp. 55–75, 5th ed.
- [114] A. V. Maslov, M. I. Bakunov, and C. Z. Ning, “Distribution of optical emission between guided modes and free space in a semiconductor nanowire,” *J. Appl. Phys.* **99**, 024314 (2006).
- [115] T. Nobis, E. M. Kaidashev, A. Rahm, M. Lorenz, and M. Grundmann, “Whispering Gallery Modes in Nanosized Dielectric Resonators with Hexagonal Cross Section,” *Phys. Rev. Lett.* **93** (2004).
- [116] L. Novotny and B. Hecht, *Principles of Nano-Optics* (Cambridge University Press, 2012), chap. 9, pp. 282–312, 2nd ed.
- [117] R. J. Warburton, “Single spin in self-assembled quantum dots,” *Nat. Mater.* **12**, 483–493 (2013).
- [118] I. Favero, G. Cassabois, C. Voisin, C. Delalande, P. Roussignol, R. Ferreira, C. Couteau, J. P. Poizat, and J. M. Gérard, “Fast exciton spin relaxation in single quantum dots,” *Phys. Rev. B* **71**, 233304 (2005).
- [119] G. A. Narvaez, G. Bester, and A. Zunger, “Excitons, biexcitons, and trions in self-assembled (In, Ga)As/GaAs quantum dots: Recombination energies, polarization, and radiative lifetimes versus dot height,” *Phys. Rev. B* **72**, 245318 (2005).
- [120] J. M. Smith, P. A. Dalgarno, R. J. Warburton, A. O. Govorov, K. Karrai, B. D. Gerardot, and P. M. Petroff, “Voltage Control of the Spin Dynamics of an Exciton in a Semiconductor Quantum Dot,” *Phys. Rev. Lett.* **94**, 197402 (2005).
- [121] A. D. Osterkryger and N. Gregersen, “Efficient formalism for treating tapered structures using the Fourier modal method,” *Proc. SPIE* **9889** (2016).
- [122] B. Z. Katsenelenbaum, L. M. del Rio, M. Pereyaslavets, M. S. Ayza, and M. Thumm, *Theory of Nonuniform Waveguides: the cross-section method*, vol. 44 of *IEE Electromagnetic Waves series* (The Institution of Electrical Engineers, London, United Kingdom, 1998).
- [123] I. Ederra, M. S. Ayza, M. Thumm, and B. Z. Katsenelenbaum, “Comparative Analysis of Mode Reflection and Transmission in Presence of a

- Cutoff Cross Section of Nonuniform Waveguide by Using the Cross Section and the Mode-Matching and General Scattering-Matrix Methods,” *IEEE Transactions on Microwave Theory and Techniques* **49**, 637–645 (2001).
- [124] Y.-M. He, Y. He, Y.-J. Wei, D. Wu, M. Atatüre, C. Schneider, S. Höfling, M. Kamp, C.-Y. Lu, and J.-W. Pan, “On-demand semiconductor single-photon source with near-unity indistinguishability,” *Nat. Nanotechnol.* **8**, 213–217 (2013).
- [125] O. Gazzano, S. Michaelis de Vasconcellos, C. Arnold, A. Nowak, E. Galopin, I. Sagnes, L. Lanco, A. Lemaître, and P. Senellart, “Bright solid-state sources of indistinguishable single photons,” *Nat. Comm.* **4**, 1425 (2013).
- [126] G. Grzela, R. Paniagua-Domínguez, T. Barten, Y. Fontana, J. A. Sánchez-Gil, and J. G. Rivas, “Nanowire Antenna Emission,” *Nano Lett.* **12**, 5481–5486 (2012).
- [127] D. van Dam, D. R. Abujetas, R. Paniagua-Domínguez, J. A. Sánchez-Gil, E. P. A. M. Bakkers, J. E. M. Haverkort, and J. G. Rivas, “Directional and Polarized Emission from Nanowire Arrays,” *Nano Lett.* **15**, 4557–4563 (2015).
- [128] I. Friedler, C. Sauvan, J. P. Hugonin, P. Lalanne, J. Claudon, and J. M. Gérard, “Solid-state single photon sources: the nanowire antenna,” *Opt. Express* **17**, 2095–2110 (2009).
- [129] L. Novotny and B. Hecht, *Principles of Nano-Optics* (Cambridge University Press, 2012), chap. 5, pp. 131–164, 2nd ed.
- [130] L. Novotny and B. Hecht, *Principles of Nano-Optics* (Cambridge University Press, 2012), chap. 11, pp. 338–368, 2nd ed.
- [131] C. Arnold, J. Demory, V. Loo, A. Lemaître, I. Sagnes, M. Glazov, O. Krebs, P. Voisin, P. Senellart, and L. Lanco, “Macroscopic rotation of photon polarization induced by a single spin,” *Nat. Commun.* **6** (2015).
- [132] C. Y. Hu, A. Young, J. L. O’Brien, W. J. Munro, and J. G. Rarity, “Giant optical Faraday rotation induced by a single-electron spin in a quantum dot: Applications to entangling remote spins via a single photon,” *Phys. Rev. B* **78** (2008).
- [133] P. Kaer, P. Lodahl, A.-P. Jauho, and J. Mork, “Microscopic theory of indistinguishable single-photon emission from a quantum dot coupled to a cavity: The role of non-Markovian phonon-induced decoherence,” *Phys. Rev. B* **87** (2013).

- [134] J. Iles-Smith, D. P. S. McCutcheon, A. Nazir, and J. Mørk, “Phonon scattering inhibits simultaneous near-unity efficiency and indistinguishability in semiconductor single-photon sources,” *Nat. Photonics* **11**, 521–526 (2017).
- [135] T. Grange, N. Somaschi, C. Antón, L. D. Santis, G. Coppola, V. Giesz, A. Lemaître, I. Sagnes, A. Auffèves, and P. Senellart, “Reducing Phonon-Induced Decoherence in Solid-State Single-Photon Sources with Cavity Quantum Electrodynamics,” *Phys. Rev. Lett.* **118** (2017).
- [136] E. T. Jaynes and F. W. Cummings, “Comparison of Quantum and Semiclassical Radiation Theories with Application to the Beam Maser,” *Proceedings of the IEEE* **51**, 89–109 (1963).
- [137] V. V. Weisskopf and E. Wigner, “Berechnung der natürlichen Linienbreite auf Grund der Diraschen Lichttheorie,” *Z. Physik* **63** (1930).
- [138] N. Ismail, C. C. Kores, D. Geskus, and M. Pollnau, “Fabry-Pérot resonator: spectral line shapes, generic and related Airy distributions, linewidths, finesses, and performance at low or frequency-dependent reflectivity,” *Opt. Express* **24**, 16366 (2016).
- [139] P. T. Kristensen and S. Hughes, “Modes and Mode Volumes of Leaky Optical Cavities and Plasmonic Nanoresonators,” *ACS Photonics* **1**, 2–10 (2013).
- [140] S. M. Barnett and P. M. Radmore, “Quantum theory of cavity quasimodes,” *Opt. Commun.* **68**, 364–368 (1988).
- [141] E. V. Denning, J. Iles-Smith, A. D. Osterkryger, N. Gregersen, and J. Mork, “Fundamental cavity-waveguide interplay in cavity QED,” arXiv:1804.01364 [quant-ph] (2018).
- [142] P. Meystre and M. Sargent III, *Elements of Quantum Nano-Optics* (Springer-Verlag, Berlin, 2007), chap. 18, pp. 427–444, 4th ed.
- [143] C. K. Hong, Z. Y. Ou, and L. Mandel, “Measurement of Subpicosecond Time Intervals between Two Photons by interference,” *Phys. Rev. Lett.* **59**, 2044–2046 (1987).
- [144] P. Kaer, N. Gregersen, and J. Mork, “The role of phonon scattering in the indistinguishability of photons emitted from semiconductor cavity QED systems,” *New J. Phys.* **15** (2013).
- [145] J. Claudon, N. Gregersen, P. Lalanne, and J.-M. Gérard, “Harnessing Light with Photonic Nanowires: Fundamentals and Applications to Quantum Optics,” *ChemPhysChem* **14**, 2393–2402 (2013).

- [146] G. B. Arfken and H. J. Weber, *Mathematical Methods for Physicists* (Elsevier, 2005), chap. 11, pp. 675–740, sixth ed.
- [147] Q. Wang, S. Stobbe, and P. Lodahl, “Mapping the Local Density of Optical States of a Photonic Crystal with Single Quantum Dots,” *Phys. Rev. Lett.* **107**, 167404 (2011).

Andreas Dyhl Østerkryger received the BSc Eng (2012) and MSc Eng (2015) degrees in Physics and Nanotechnology from the Technical University of Denmark (DTU). Dr. Østerkryger's research interests are within simulating and modelling nanophotonic structures, developing simulation tools for solving Maxwell's equations and single-photon sources based on quantum dots.

Dr. Østerkryger's PhD studies has been conducted at DTU Fotonik. During his studies he visited CEA in Grenoble from February 2017 to May 2017 under the supervision of researcher Julien Claudon. He defended his PhD Thesis in August 2018, where the evaluation board consisted of Assoc. Prof. Andrei Lavrinenko, Postdoc Phillip Trøst Kristensen and Head of Research Group Sven Burger.



Department of Photonics Engineering

Ørsteds Plads, Building 343
2800 Kgs. Lyngby
Tlf. 45256352

www.fotonik.dtu.dk